Transactions of the ASME

The Journal of FLUIDS ENGINEERING (USPS 278-480) is edited and published quarterly at the offices of The American Society of Mechanical Engineers, United Engineering Center, 345 E. 47th St., New York, N. Y. 10017. Cable Address, "Mechaneer," New York. **Second-class** postage paid at New York, **CHANGES OF ADDRESS** must be received at Society headquarters seven weeks before they are to be effective. Please send old label and new address. **PRICES:** To members, $36.00, annually: to nonmembers, $72.00. Single copies, $24.00 each. Add $5.00 for postage to countries outside the United States and Canada. **STATEMENT** from By-Laws. The Society shall not be responsible for statements or opinions advanced in papers or . . . printed in its publications (B7.1, Par. 3),

INDEXED by the Engineering Index, Inc.

Journal of Fluids Engineering

Published Quarterly by The American Society of Mechanical Engineers

VOLUME 104 • NUMBER 4 • DECEMBER 1982

Fluid Dynamics of Inducers—A Review

B. Lakshminarayana

Director of Computational Fluid Dynamics Studies and Professor of Aerospace Engineering, Department of Aerospace Engineering, The Pennsylvania State University, University Park, Pa. 16802

The objective of this paper is to review the experimental and analytical investigations on the fluid dynamic aspects of noncavitating inducers. Various analyses available for the prediction of the flow field, starting from the simple radial equilibrium analysis to the numerical solution of exact three-dimensional inviscid and viscid flow equations, are reviewed. The experimental data on the overall inducer performance, rotor blade passage measurements, and boundary layer on rotor blades are critically examined. Some of the available data have been reinterpreted to provide suitable guidance to the designer. The review and the concluding remarks include a global view of the state-of-the-art and applicability of the research to design, and some viewpoints on the analysis and design of inducers.

1 Inducers

Inducers are employed in rocket pump feed systems, water jet propulsion, centrifugal impeller, and various other applications. The aerospace industry has made substantial contribution to the current state-of-the-art of inducers used in rocket pump feed systems [1–3]. The inducer technology had found new application in the commerical market, such as high-speed ships (in excess of 50 knots) [4, 5], and auxiliary power units for aircraft [6]. Inducers are also used in centrifugal impellers and aircraft fuel feed systems.

The turbopumps used in liquid rocket feed systems operate at high speeds so as to minimize weight and size of the system – an important design criteria for an aerospace vehicle. Conventional pumps cavitate at suction-specific speeds (SS) in excess of 8000. The need to increase the speed led to the development of a cavitation-resistant inducer, which is essentially an axial-flow pump with high-solidity blades used in front of the main pump. The value of the suction specific speed (SS) can be improved by fitting the inducer blade to the pump, thus decreasing the pump size for application in water jet propulsion of ships, hydrofoil craft, chemical pumps, and rocket turbopumps.

The inducer usually contains fewer blades (usually 3 to 4) than conventional pumps. Long and narrow passages provide the time and space for the collapse of the cavitation bubbles and for the gradual addition of energy. The blades in most practical inducers used in rocket pumps wrap around almost 360 deg. The purpose of the inducer is to pressurize the flow sufficiently to enable the main pump to operate satisfactorily. The physical reasoning for the selection of such unconventional pumps is described by Acosta [7]. Inducers have operated successfully at suction-specific (SS) speeds in excess of 70,000. Various types of inducers used in rocket application are described in [8] and shown in Fig. 1. A design and performance summary of typical rocket pump inducers is tabulated in [8].

The major characteristic features of the inducer are low flow coefficient (0.05 to 0.2), large stagger angle (70 to 85 deg), and high-solidity blades (few blades of very long chord length as opposed to short chords of a many-bladed com-

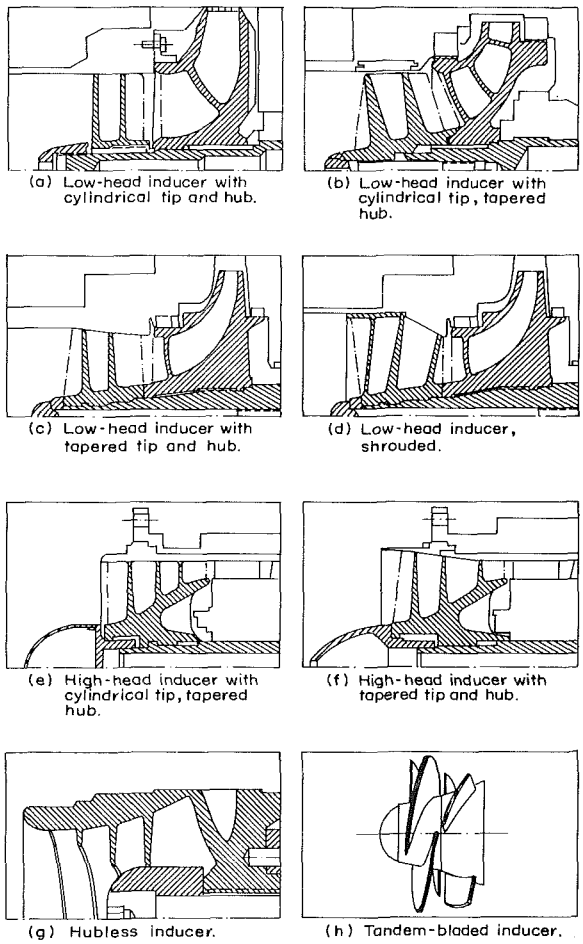

Fig. 1 Basic inducer types (updated version of reference [1])

Contributed by the Fluids Engineering Division for publication in the JOURNAL OF FLUIDS ENGINEERING. Manuscript received by the Fluids Engineering Division, April 6, 1981.

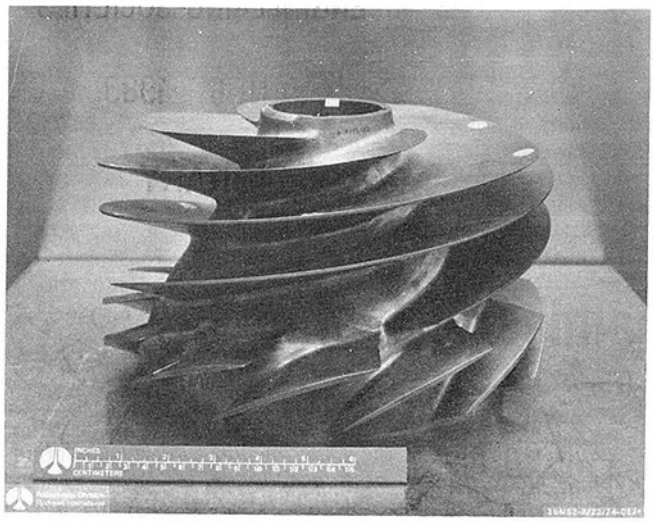

Fig. 2 Photograph of the low pressure oxidizer turbopump inducer impeller used in space shuttle main engine ϕ = 0.07, SS = 70,000 (photograph courtesy of Rocketdyne Division of Rockwell Corporation)

pressor rotor) of little or no camber. The resulting configuration, even though beneficial from the point of view of cavitation, results in highly viscous, turbulent, and, almost invariably, fully developed flow inside these passages. This results in a large departure from indealized and design fluid dynamic performance. The inducers for pumps are designed to keep the cavity thickness to a minimum and provide part of the pressure rise (as high as 6000 psi in space shuttle engines). Extreme compactness and light weight are required to obtain the maximum payload in the rocket vehicle. The light weight is achieved by high rotational speeds. The low pressure oxidizer turbopump inducer used in the space shuttle main rocket engine (470,000 lb thrust each) is shown in Fig. 2. The turbomachinery (oxidizer, fuel pumps, and turbines) in the space shuttle engine has the highest power-to-weight ratio (75,840 hp with a weight of 760 lb) of any turbomachinery known. Details of this engine can be found in [2] and [3].

In view of these cavitation requirements, the blades are designed to be very thin and the passages very long. Jakobsen [8] provided the most comprehensive review of the rocket pump inducer design, with specific details on the blading and passage design, including hub size and shape, inlet diameter and contour, blade profile, leading edge, sweep, cant, lead, thickness of blades, solidity, and other aspects. Details of the design can be found in references [2–16]. Ross and Benerian [14] provided the analytical base for the design of inducers.

2 Scope of This Review and Nature of Flow Field

The investigations reviewed [1–73] here are mainly concerned with the effect of viscosity, not the effects of cavitation. The papers dealing with cavitation and cavitation-induced instability are listed under "uncited bibliography" [75–113] at the end of the paper.

In any research involving an understanding of the complex flow phenomena in a real evironment, one has to resort to a "building block approach" and study the phenomena individually first and collectively later. This is the only approach that will lead to eventual solution and improvement of the flow in inducers. Inducer flow are dominated by viscous and turbulence effects and cavitation. The regions in which the primary or inviscid flow exists are very small. Therefore, the group at Penn State studied one aspect of this complex machinery, viscous and turbulent flow, in great detail. A thorough understanding of the viscous and turbulent effects only (in the absence of cavitation) will eventually lead to better design (e.g., viscous design), a more systematic approach, and an understanding of this complex flow. The objective of this review is to review all aspects of this viscous flow phenomenon so that the designers and analysts in industry can include these effects in a systematic manner. This will also lay the ground work for the future investigation of the flow field inside the rotor passages of a cavitating inducer.

The experimental aspects of cavitation in inducers are not reviewed in this paper as the information available on this topic is related mainly to the overall performance and visualization of the cavitation phenomena [75–95]. The work on unsteady cavitation and stability of inducers has been reviewed by Greitzer [113]. The analytical part of the cavitating flow is incorporated in section 3 of this paper. Hopefully, this review paper will stimulate a systematic investigation of the research, such as the Penn State effort, to study the detailed flow phenomena in cavitating inducers. The availability of nonintrusive measurement technique (laser doppler velocimeter) would make such a study an attractive one at the present time. This review paper, as well as Penn State's work on inducers, will then form important ground work for such a study.

A review of the experimental data acquired inside the passage and at the exit of the rotor, tested with air and water, is covered. Various analytical, numerical analyses available for the prediction of the flow field are described. Attempts are made to emphasize significance and application of these results to inducer design. Advantages of tandem and hubless inducers are also briefly discussed. There has been no state-of-the-art review on fluid dynamic aspects of inducers and,

Nomenclature

C = chord length
C_f = skin-friction coefficient ($2\tau_0/\rho W_e^2$)
d_h = hydraulic mean diameter
H = stagnation head rise (in absolute flow)
H_E = head rise derived from Euler's equation (UV_θ/g)
H_{loss} = $H_E - H_m$
H_m = measured stagnation head rise (in absolute flow)
H_{sv} = net positive suction head, ft
h = static head
L = lead of the helix
N = number of blades
p,P_0 = static and stagnation pressure
P_{OR} = stagnation pressure of the relative flow
Q = flow rate, gpm
R = r/r_t
R_e = Reynolds number based on blade tip speed ($U_t r_t/\nu$)
R_{ht} = hub/tip ratio
R_N = Reynolds number, $\bar{W} d_h/\nu$
r,θ,z = radial, tangential, and axial coordinates
SS = suction specific speed, $N\sqrt{Q}/H_{sv}^{3/4}$, r p m $\sqrt{\text{GPM}}/(\text{ft})^{3/4}$
S = blade spacing
U = blade speed
V,v = resultant and fluctuating components of absolute velocity
V_r,V_θ,V_z = radial, tangential, and axial components of absolute velocity
W,w = resultant and fluctuating components of relative velocity
W_r,W_θ,W_z = radial, tangential, and axial components of relative velocity
x,y = coordinates parallel to and perpendicular to blade camber line and

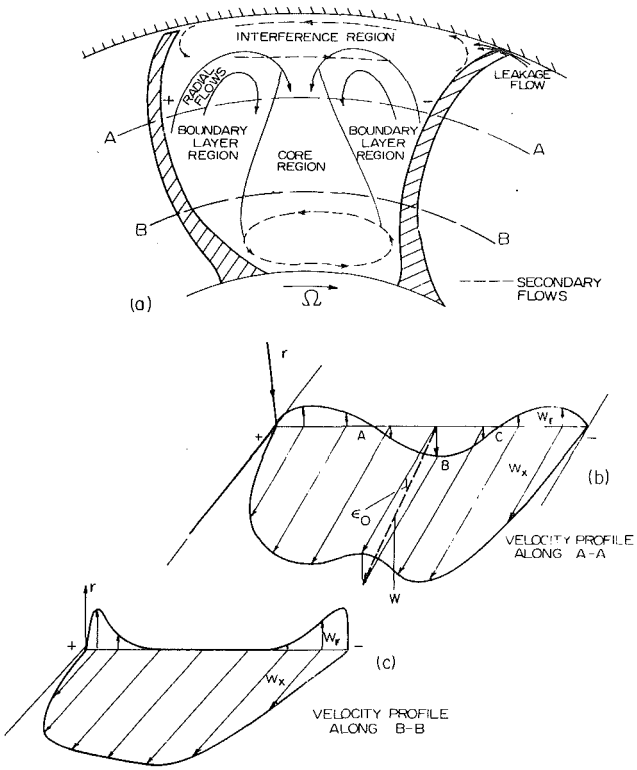

Fig. 3 Nature of flows in inducers

therefore, a review of this field is long overdue. This is the major objective of the paper.

The mechanism by which the stagnation-static-pressure rise takes place in inducers is due to a curious combination of inviscid turning effects and shear forces. While the former has a dominant influence in conventional machinery such as compressors and pumps, the shear forces dominate the flow in inducers, at least near the tip. The viscous and turbulence effects in these blade rows are not confined to thin regions at the blades and in the end zones, but extend over the entire cross section of the flow. It is hoped that the data, analysis, and correlations reviewed in this paper will serve to establish analytical methods for the analysis and modeling of turbomachinery flows dominated by viscous, turbulent, and secondary flow effects and under conditions where the real fluid effects are at least as important as the ideal effects which form the basis of the existing design.

The boundary layers that develop on the blades of rotating machinery such as compressors, pumps, inducer, propellers, and turbines are not two-dimensional. The rotation of the blade produces spanwise flow, resulting in a skewed or three-dimensional boundary layer. The extent of three-dimensionality depends on the angular velocity, flow coefficient, space/chord ratio, aspect ratio, stagger angle of the blade, etc. A basic understanding of the effects of centrifugal and Coriolis forces on the boundary-layer behavior is essential for the improved analysis and performance of such rotating fluid machinery. The radial flow inside the boundary layer, when encountered by the annulus wall, produces a complex flow near the tip, resulting in radially inward flow. These and other interaction effects result in extremely complex boundary-layer characteristics, as shown in Fig. 3. It is one of the additional objectives of this paper to review the state-of-the-art of the understanding of boundary-layer phenomena on these inducer blades.

3 Analysis of the Inducer Flow Field

Many of the analyses carried out for the prediction of the inducer flow field are equally applicable to both cavitating and noncavitating flow; hence, a brief review of the two-phase flow analysis is included, even though this paper primarily is restricted to noncavitating flows. The reader is referred to books by Horlock [44], Wislicenus [45], and Vavra [46] for several techniques available for the prediction of inviscid flow fields in axial flow turbomachinery. These techniques are equally applicable in the computation of inviscid flow fields in inducers. A word of caution is in order. The inducer flow field is dominated by viscous and turbulence effects and, therefore, the inviscid theories are at best qualitative.

The analyses avaliable can be classified as:

1 Analyses based on simplified radial equilibrium ($V_r = W_r = 0$) and Euler's equation.
2 Meridional flow solution including viscous effects.
3 Approximate viscid analysis based on shear pumping effect.
4 Three-dimensional inviscid analyses (exact).
5 Three-dimensional viscid analysis.

3.1 Analyses Based on Simplified Radial Equilibrium Analysis and Euler's Equation. In this section, the analyses based on one- and two-dimensional blade-to-blade solutions, coupled with the complementary solution based on the simplified radial equilibrium ($V_r = W_r = 0$) analyses, are described.

Earlier analyses [14, 48–55] were mainly concerned with the

Nomenclature (cont.)

lying on a cylindrical surface
x_t = location of transition point
ϵ = angle between limiting streamline and x direction
β = relative air angle measured from axial direction
λ_R = friction coefficient for a rotating channel
ν = kinematic viscosity
ρ = density
ϕ = flow coefficient, $W_z/\Omega r_t$
ψ_E = $2gH_E/U_t^2$
ψ_{loss} = $2gH_{loss}/U_t^2$
ψ_S = $2gH/U_t^2$ (static head rise coefficient)
ψ_t = stagnation headrise coefficient, $2gH/U_t{}^2$
ψ_R = stagnation head coefficient of relative flow, $2P_{OR}/\rho U_t^2$
Ω = angular velocity
η = hydraulic efficiency, ψ_t/ψ_E
ζ = $\psi_E - \psi_t$
θ_{11} = momentum thickness in chordwise direction

$$\left[\int_0^h \frac{W_x}{W_0}\left(1-\frac{W_x}{W_0}\right)\right]$$

$R\theta_{11}$ = $W_e\theta_{11}/\nu$
σ = solidity (C/S)
τ = shear stress

Subscripts

h,t = hub, tip
m = values at mid-passage, free stream
r,θ,z = components along r,θ,z directions
x,y = components along x,y directions
1,2 = inlet, outlet
e = edge of the boundary layer

Superscript

$-$ = mass-averaged over the entire passage/circumferential average

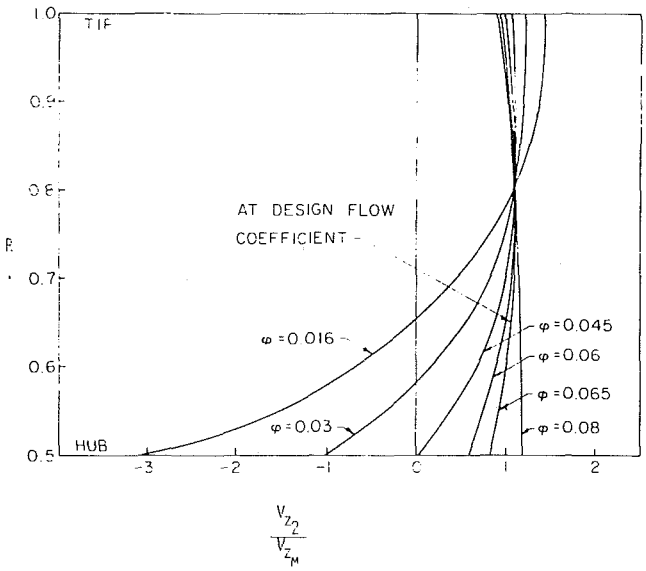

Fig. 4 Predicted radial variation of outlet axial velocity for the Penn State four-bladed inducer [52, 71]

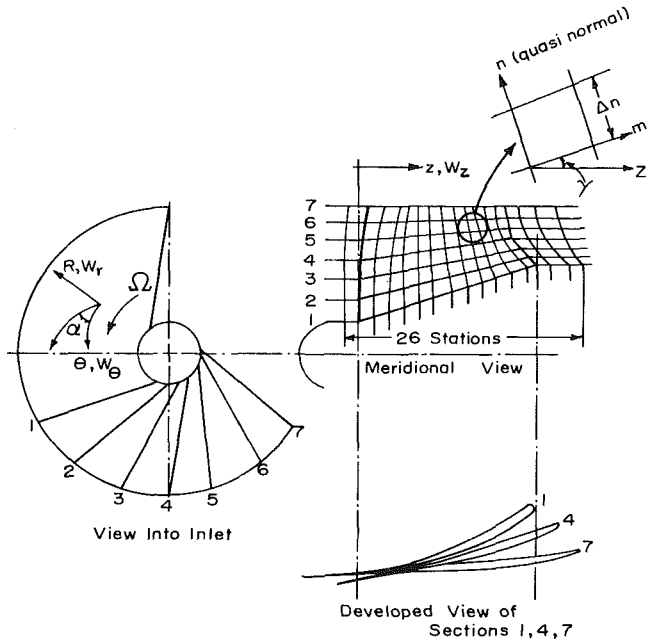

Fig. 5 Inducer geometry, coordinate system, and grid for numerical analysis

calculation of the pressure head rise characteristics using one-dimensional equations. The analyses are mainly based on the Euler's equation, with the tangential velocity computed from the inlet and outlet blade angles. Mirolyubov [48] allowed for the losses in the channel through an empirical loss based on the friction loss in a pipe. Similar analysis was carried out by Dumov [49]. They both conducted a series of experiments (in water and fuel) with space/chord ratios varying from 0.70 to 1.5, and correlated these results and the analysis to prove that the ratio of actual to theoretical head rise is given by (for the range of values of $k = 0.2$ to 0.8):

$$\frac{H_A}{H_i} = \frac{1}{0.4+(S/C)}\left(1-\frac{k}{(S/C)}\right) \tag{1}$$

where $k = \bar{V}_{m_2}/\Omega r \tan\beta$ is the meridional velocity, and β is the helix angle. The equation is valid for a flat-plate helical inducer ($r\tan\beta$ = const).

The theoretical head rise was calculated using a simplified radial equilibrium equation ($\partial p/\partial r = \rho V_\theta^2/r$) and the Euler's equation ($H = U V_\theta/g$). The theoretical head is predicted to be

$$H_i = \frac{\Omega^2}{g}\left(\frac{\Omega L}{2\pi V_{z_m}} - 1\right)\left[k_1 + \left(1 - \frac{2\pi \bar{V}_{z_m}}{\Omega L}\right)k_2\right] \tag{2}$$

where k_1 and k_2 are functions of r_h, r_t, and L. The measured data shows good agreement with equation (1). It should be remarked here that the theory is based on two-dimensional flows, while the correlation (equation (1)) based on the experimental data includes the three-dimensional effects. The good agreement between predictions and data may be somewhat fortuitous.

Some of the early work in this area is due to Rains [51]. His analysis is valid for a flat-plate helical inducer ($r\tan\beta$ = const) with a constant hub/tip ratio, without any inlet swirl. The outlet flow angle is assumed to be equal to the blade angle, and the flow is assumed to be in simple radial equilibrium ($V_r = W_r = 0$). The axial velocity predicted from this analysis is given by

$$\frac{V_z}{U_t} = \frac{R^2\tan\beta_t + C}{R^2 + \tan^2\beta_t}$$

The continuity equation is used to evaluate the constant C. Two expressions are given for the head rise coefficient (ψ_E), one based on the area-averaged values of $\psi(r)$ and the other based on the flow averaged quantity. The agreement between the experiments of Newoz [53] and Rains is found to be poor at off-design conditions where hub flow shows to tendency to separate.

Analyses similar to Rain's have been carried out by Huppert [47] and Montgomery [55]. The latter included the viscous effects (through constant as well as radially varying loss correlations) and provided a comprehensive set of predictions for various inducers tested at the NASA Lewis Research Center [17–20]. The analysis [55] included inducers with varying hub/tip ratios, radially constant loss correlation, and radially varying loss correlation. The analysis is valid for a flat-plate helical inducer. Unlike Rain's [51], Montgomery's analysis included the effects of the deviation angle.

The simplified radial equilibrium equation, in combination with the integral form of the continuity equation, is used to derive an expression for the radial distribution of the axial velocity at various off-design conditions for the four-bladed inducer used in Penn State's investigation [31]. It is an extension of Huppert's [47] analysis for a flat-plate inducer, where $r\tan\beta$ = constant. This has been extended in reference [52] for an inducer based on aerodynamic design [31], where $r^2\tan\beta$ is nearly constant. The axial velocity distribution for this case is given by

$$\frac{V_{z_2}}{V_{z_m}} = \frac{1}{Y}\left[Y_m + \frac{\tan\beta_t}{\phi}\frac{V_{z_1}}{V_{z_m}}\left(R^2 - R_m^2\right)\right] \tag{3}$$

$$\frac{\bar{V}_{z_1}}{V_{z_m}} = \frac{2KY_m\int_{R_h}^{1.0}(R/Y)dR}{1-2\tan\beta_t/\phi\left[\int_{R_h}^{1.0}(R^3/Y)dR - R_m^2\int_{R_h}^{1.0}(R/Y)dR\right]} \tag{4}$$

where $\phi = \bar{V}_{z_1}/\Omega r_t$, $Y = (\tan^2\beta_t + R^4)^{3/4}$,

$$Y_m = (\tan^2\beta_t + R_m^4)^{3/4},\ r_m = \sqrt{(r_t^2 + r_h^2)/2}$$

k is a blockage factor to allow for blade thickness and boundary-layer growth, and V_{z_m} is the axial velocity at the hydraulic mean radius, r_m.

For any given flow coefficient, $\bar{V}_{z_1}/V_{z_m}$ is calculated using equation (4), which is then substituted in equation (3) to

predict the axial velocity at various radii. The prediction for the four-blade inducer, shown in Fig. 4, confirms the results from flow visualization and measurements reported later. It should be recognized that the above analysis does not take into account the viscous effects: hence, the tendency for the backflow to occur near hub at the design condition is not predicted. The tendency for flow reversal at the root at flow coefficients lower than the design value is, however, correctly predicted.

3.2 Meridional Flow Solution ($V_r = W_r \neq 0$) Including Viscous Effects. Cooper [56] included losses as well as two-phase flow (cavitation) effects and utilized approximate momentum equations to solve the flow field in an inducer with an annulus of varying area. The viscous effects are included through a loss term in the streamwise momentum equation. The momentum equation is written in the meridional (m) and quasi-normal directions shown in the insert of Fig. 5. The basic assumptions made are as follows: (1) The fluid is assumed to be either liquid or a variable-density homogeneous two-phase medium. (2) Fluid flows in annuli (Fig. 5) formed by stream surfaces of revolution generated by revolving meridional streamlines about the axis of rotation. (3) Average flow conditions exist at the mid-passage. These are determined from the meridional flow solutions, which are then utilized in the blade-to-blade solution. (4) The relative flow follows the blade mean line, and the exit deviation angles are based on specified values. (5) The blade-to-blade relative velocity variation is linear.

The meridional streamlines and the quasi-normals are derived using the method developed by Katsanis [54]. The approximate equations employed in the m, n and θ directions are given, respectively, by

$$\frac{dP}{\rho} = d\left(\frac{\Omega^2 r^2}{2}\right) - d\left(\frac{W^2}{2}\right) - dL \tag{5}$$

$$\frac{dP}{dn} = \frac{\rho V_\theta^2 \cos\gamma}{r} \tag{6}$$

$$\frac{(p_p - p_s)}{(\theta_p - \theta_s)} = \rho V_m \frac{d}{dm}(rV_\theta) \tag{7}$$

$$dL = f\frac{x}{d_h}\frac{W^2}{2} - \zeta d\left(\frac{W^2}{2}\right) \tag{8}$$

$$\rho = \begin{cases} \rho_f & p \geq p_{\text{sat}} \\ \rho_f\left[\dfrac{1}{1 + (B/\rho_f)(p_{\text{sat}} - P)}\right] & p < p_{\text{sat}} \end{cases} \tag{9}$$

where γ is the meridional angle, dL is the work done by the friction force, f is the friction coefficient, ζ is the diffusion loss factor (due to the pressure gradient and bubble collapse), and B is a fluid thermodynamic vaporization constant [56].

Equations (5) through (9) and the continuity equation are solved interatively for pressure, the overall pressure coefficient, and efficiency. The simplifying assumptions made (especially for the blade-to-blade solution) are serious limitations on the application of the analysis. The overall performance (ψ and η) can be predicted reasonably accurately provided the loss correlation (including its radial variation) is accurate. The analysis described in the next section is based on the three-dimensional form of the radial equilibrium equation and a more accurate loss model.

Davis et al. [57] and Cool et al. [59] utilized a channel approach for the blade-to-blade solution (including cavity bubbles) and the following radial equilibrium equation with

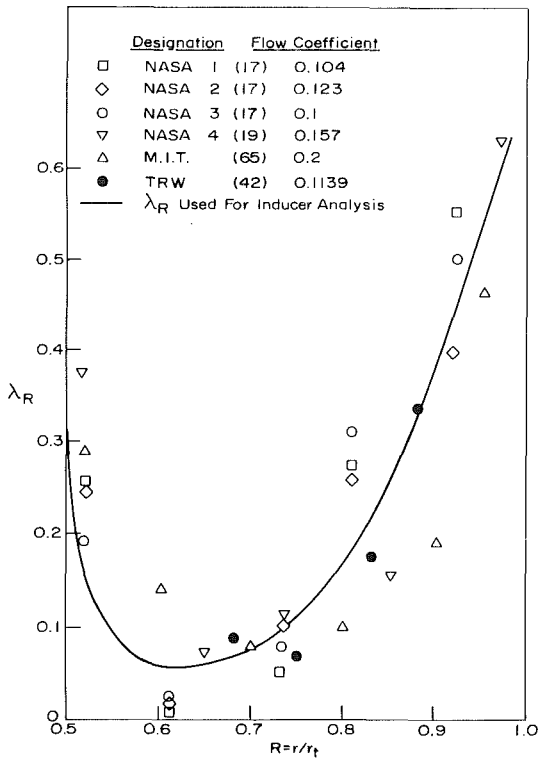

Fig. 6 Radial variation of the modified friction loss coefficient λ_R for various inducers calculated from equation (10) [31]

streamline curvature in the meridional plane:

$$\frac{1}{\rho}\frac{\partial p}{\partial r} = \frac{V_\theta^2}{r} - V_m^2 \cos^2_\gamma \frac{\partial \gamma}{\partial z} - V_m \sin\gamma \cos\gamma \frac{\partial V_m}{\partial z}$$

where V_m is the meridional velocity. The boundary layer growth is calculated from a two-dimensional momentum integral equation. This analysis is at best qualitative in view of the approximations used in the blade-to-blade solution (both viscous and inviscid). The analysis was mainly directed towards computation of aerodynamic loads for the stress and vibration analysis of the blade [58].

3.3 Viscid Analysis Based on the Empirical Loss Coefficient. An approximate analysis of the inducer flow, based on an empirically derived friction-loss coefficient, was carried out by Lakshminarayana [31]. The salient points of this analysis are discussed below.

Inducer data collected from various sources (NASA, M.I.T., TRW, etc.) indicate that the measured friction losses are several times higher than those of an equivalent stationary inducer channel, especially near the tip. The friction losses in an inducer are strongly dependent on the rotation factor (inverse of flow coefficient). A new friction-loss coefficient applicable to inducers operating in the range of flow coefficients $\phi = 0.065$ to 0.2 is defined and derived. The frictional losses estimated from this newly defined friction-loss coefficient agree well with the measured values for the Penn State inducer.

The loss coefficient is given by

$$\psi_{\text{loss}} = \frac{2gH_{\text{loss}}}{U_t^2} = \lambda_R \frac{R_{ht}}{\phi}\frac{1}{R_N^{1/4}}\frac{C}{d_h}\left(\frac{\bar{W}}{U_t}\right)^2 \tag{10}$$

where λ_R is a function of radius, as shown in Fig. 6.

A circumferentially averaged radial equilibrium equation is used to predict the relative and absolute tangential velocities. The analysis is based on suitable assumptions for the radial and main-flow velocity profiles (based on the existing three-dimensional turbulent boundary-layer data available) and loss coefficients discussed above. The circumferentially averaged

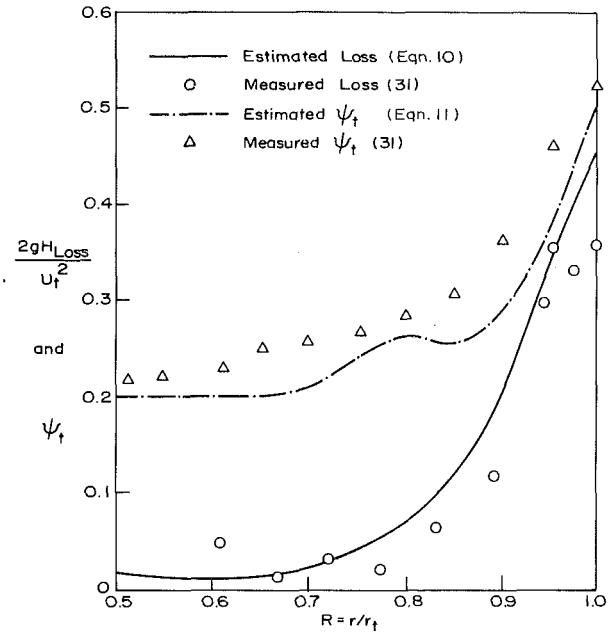

Fig. 7 Estimated and measured friction losses and stagnation pressure coefficient for the four-bladed inducer [31]

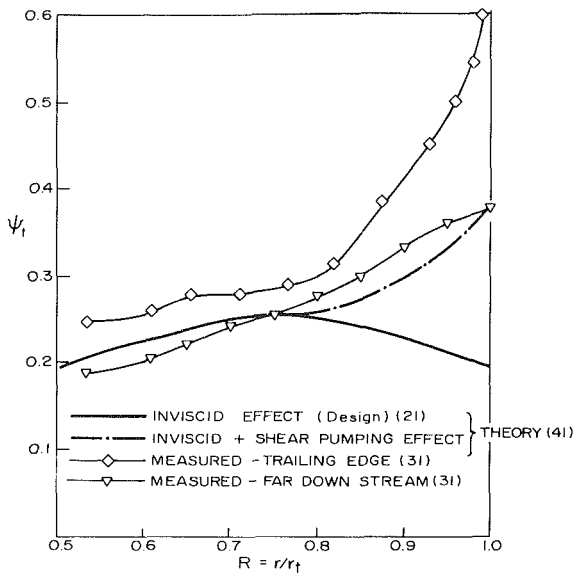

Fig. 8 Predicted and measured radial variation of absolute stagnation-pressure rise coefficient (ψ_t) for the Penn State inducer [41]

radial equilibrium equation valid for inducers operating at low flow coefficients is given by,

$$\frac{-0.275}{\sin^2\beta}\bar{W}_\theta\left(\tan\alpha\frac{\partial\bar{W}_\theta}{\partial x}+\bar{W}_\theta\sec^2\epsilon\frac{\partial\epsilon}{\partial x}\right)+1.015\,\bar{W}_\theta\frac{\partial\bar{W}_\theta}{\partial r}+1.015\frac{\bar{W}_\theta^2}{r}-2\Omega\bar{W}_\theta+\frac{\partial}{\partial r}\left(\frac{\lambda_R}{R_N^{1/4}}\frac{R_{ht}}{\phi}\frac{C}{d_h}\frac{\bar{W}^2}{2}\right)=0. \quad (11)$$

This equation was solved with the assumption that W_θ varies linearly with x, (chord-wise distance) and by using experimental values for ϵ. The pressure rise coefficient was computed from the predicted $\bar{W}_\theta$. This predicted and measured values of ψ_t for the Penn State inducer (four-bladed inducer) is shown in Fig. 7. Predicted values for three- and two-bladed inducers are shown in references [33] and [27], respectively. The losses and efficiencies predicted from the empirical loss correlation are also in good agreement (Fig. 7). Hence, it is evident that if the frictional effects are known either empirically or analytically, the flow properties at the exit of the inducer can be predicted quite accurately. The very purpose of the boundary-layer investigation on the helical blade and a channel described later is to provide the most important missing link in the frictional effects, which are otherwise based on empiricism, and hence not universally valid.

The axial velocities predicted, using the continuity and axial momentum equations with assumed radial velocity profiles and the derived tangential velocity distribution, agree qualitatively with the value measured from a stationary probe at the exit of a four-bladed inducer [31].

3.4 Approximate Viscid Analysis Based on Shear Pumping Effect. The investigations carried out at Penn State [23-41] have revealed that the flow field inside these rotating passages is highly complex and three-dimensional in nature. The flow is highly turbulent and viscous both inside and outside of the rotor. Even though the inducers are designed as axial flow machinery, the radial velocities generated by viscous, Coriolis, and centrifugal forces inside the blade boundary layers are found to be of the same order of magnitude as the axial velocity. The energy exchange process is complicated in terms of physical phenomena as well as mathematical description.

The conventional design and analysis procedure used in other types of pumps or compressors have to be supplemented by some innovative technique to include major viscous effects (both direct and indirect) responsible for the energy addition. The pump has to be treated as a mixed-flow pump. The axial velocity has the same effect (inviscid) as in the conventional pump. The pressure rise due to this effect is caused by incidence and camber and both static- and stagnation-head increases through the blade row.

The other contribution to the energy addition comes from the radial component of velocity arising from the Coriolis and centrifugal forces in the boundary layers. These boundary layers are found to cover the entire passage, and hence the radial velocity occurs across the entire passage width. Therefore, the effect of radial velocity on head rise may be significant. The radial velocity provides a vehicle for momentum exhange between the fluid and the rotor via the shear stress. This phenomenon will be referred to here as "shear pumping effect." Because of the shear stresses exerted on the flow, it is accelerated tangentially during the radial path, thus providing an additional head rise. It should be recognized here that this phenomenon involves no potential flow effect or flow turning. Even though explored in connection wilth multiple-disk shear pumps or compressors, it has never been recognized as a source of pressure rise in an axial flow inducer which has very long and narrow passages. The major purpose of the analysis carried out by Lakshminarayana [41] was to explore this effect analytically and provide for the first time an estimate of the "direct" effect of shear stresses in providing a head rise. In this analysis, the flow is assumed to be an incompressible single phase. Blade camber and normal shear stresses as well as pressure gradient normal to the blade inside the blade boundary layer are neglected. The passage is assumed to have fully developed flow.

The equations of motion in a rotating coordinate system are integrated normal to the blade, with suitable assumptions for the velocity profiles and the skin-friction coefficient, to derive the following equation [41]:

$$\frac{d\bar{W}}{dr}-2.2\Omega-0.254\Omega\frac{\sin\beta}{\epsilon^2}+\frac{\bar{W}}{r}\left[0.127r\frac{\partial\beta}{\partial r}\tan\beta+\sin^2\beta\right.$$

$$+0.259\frac{\sin\beta}{\epsilon^2}-0.254+\frac{0.075}{\epsilon\cos\beta}N\left(\frac{W_e r}{\nu}\right)^{-1/5}\Bigg]=0 \qquad (12)$$

where W is the passage-averaged velocity given by

$$\bar{W}=\frac{1}{\delta}\int_0^{\delta} u\,dy=\frac{7}{8}W_e.$$

Equation (12) is a first-order nonlinear differential equation and can be solved from known values of $\epsilon(r)$, Ω, $\beta(r)$, and ν.

The above expression provides an estimate for the reduction in relative velocity due to the shear pumping effect alone. It can be used to calculate the stagnation-pressure rise due to this shear pumping effect. An estimate of the total-pressure-rise coefficient can be made by the addition of the head rise due to inviscid and shear pumping effects. The predicted pressure-rise coefficient for the four-bladed inducer with aerodynamically designed blades operating at $\phi = 0.065$ is shown compared with the measured values in Fig. 8. It is evident that the steep head rise characteristics observed are partly due to the shear pumping effect. The agreement between the theory and the experiment, shown in Fig. 8, is only reasonable. The discrepancy may well be due to the three-dimensional inviscid effects, which are not accounted for in the "mean streamline method," used in the design, as well as leakage and secondary flows that exist in this region.

3.5 Three-Dimensional Inviscid Analysis (Exact). A thorough knowledge of all significant inviscid effects (blade blockage, flow turning, finite hub/tip ratio, etc.) and viscid effects (boundary-layer growth, energy dissipation, etc.) is essential in the accurate prediction of the flow in all turbomachinery. Relevant to this, the availability of modern computers with large storage capacities and fast computation times greatly enhance the possibility of numerically solving the complete equations of motion. One of the early investigations in this area was made by Cooper and Bosch [42] and Bosch et al. [43] for the three-dimensional inviscid flow through axial flow inducers. Application and extension of this method of analysis was carried out in references [30], [33], [34], and [37]. Modifications to the Cooper-Bosch method have been attempted to reduce convergence time of the solution and to provide a viscid solution capability based on the empirically determined blade skin-friction coefficients. A method of initializing the blade flow parameters as input to the Cooper-Bosch method has also been attempted in a search for a faster convergence to the solution. A new technique for satisfying the Kutta condition at the trailing edge has been incorporated into the program.

This method developed by Cooper and Bosch [42] solves the momentum and continuity equations iteratively in three dimensions for a finite grid of points representing the channel between the blades. The nonlinear partial differential equations governing the flow in a rotating cylindrical coordinate system r, θ, z are:

r momentum

$$\frac{g_0}{\rho}\frac{\partial p}{\partial r}+W_r\frac{\partial W_r}{\partial r}+\frac{W_\theta}{r}\frac{\partial W_r}{\partial\theta}+W_z\frac{\partial W_r}{\partial z}-\frac{1}{r}(W_\theta+r\Omega)^2+F_r=0 \qquad (13)$$

θ momentum

$$\frac{g_0}{\rho}\frac{\partial p}{\partial\theta}+W_r\frac{\partial W_\theta}{\partial r}+\frac{W_\theta}{r}\frac{\partial W_\theta}{\partial\theta}+W_z\frac{\partial W_\theta}{\partial z}+\frac{W_r W_\theta}{r}+2W_r\Omega+F_\theta=0 \qquad (14)$$

z momentum

$$\frac{g_0}{\rho}\frac{\partial p}{\partial z}+W_r\frac{\partial W_z}{\partial r}+\frac{W_\theta}{r}\frac{\partial W_z}{\partial\theta}+W_z\frac{\partial W_z}{\partial z}+F_z=0 \qquad (15)$$

continuity

$$\frac{W_r}{r}\frac{\partial W_r}{\partial\theta}+\frac{1}{r}\frac{\partial W_\theta}{\partial\theta}+\frac{\partial W_z}{\partial z}+\frac{1}{\rho}\left(W_r\frac{\partial\rho}{\partial r}+\frac{W_\theta}{r}\frac{\partial\rho}{\partial\theta}+W_z\frac{\partial\rho}{\partial z}\right)=0 \qquad (16)$$

where W_z, W_θ, and W_r are relative velocities in the axial, tangential, and radial directions, respectively. F_r, F_θ, and F_z are the components of the viscous forces and are zero for the inviscid case considered in this section. The boundary condition to be satisfied on the hub, annulus walls, and blade surfaces in $\mathbf{W}_R \cdot \mathbf{n} = 0$, where $\mathbf{n}$ is the direction normal to the channel boundaries and $\mathbf{W}_R$ is the total relative velocity. In the Cooper-Bosch method, the above equations are rearranged to give residuals, which are reduced to zero by a relaxation procedure. The total residual (RT) of one relaxation cycle is calculated by

$$RT=\sum_{i=1}^{IMAX}\sum_{j=1}^{JMAX}\sum_{k=1}^{KMAX}[(R1)^2+(R2)^2+(R3)^2+(R4)^2]_{i,j,k} \qquad (17)$$

where $R1$, $R2$, $R3$, and $R4$ are the residuals calculated for the three momentum equations (13)–(15) and the continuity equation (16), and IMAX, JMAX, and KMAX are the number of grid stations in the radial, tangential, and axial directions, respectively, which are used in the numerical analysis.

The initial estimation for the velocity and static pressure distribution throughout the inducer flow passage is calculated by the two-dimensional Douglas-Neumann program for a cascade, described in detail in reference [60]. This solution was modified to include three-dimensional effects, approximately, using the solution of Lakshminarayana and White [61] for the effects of converging or diverging ducts on the airfoil performance.

Since the extension of the stagnation stream surfaces downstream have been constructed to be uniformly periodic with a spacing of $2\pi/N$ (N being the number of blades), the values of velocity and pressure at the downstream tangential channel boundaries should be equal. This condition is applied at the blade trailing edge after each iteration cycle. If the pressure and suction surface parameters differ from each other at the trailing-edge grid point, the average value is used in the residual calculations. Changes made to the original Cooper-Bosch program are given in Appendix B of reference [34] and are concentrated in subroutine "MAIN." This program was run for the three-bladed configuration tested at Penn State. Some of the results and their interpretation are discussed in a later section.

3.6 Three-Dimensional Viscid Analysis Based on Empirical Wall Shear Stress. A method incorporating some of the major effects of viscosity was presented in references [34] and [37]. In this formulation, the major viscous terms in equations (13) through (16) are retained and modeled. The expressions for F_r, F_θ, and F_z are given by

$$F_r = -\frac{1}{\rho}\left[\frac{\partial\tau_{r\theta}}{r\partial\theta}+\frac{\partial\tau_{rz}}{\partial z}+\frac{\partial\sigma_{rr}}{\partial r}+\frac{(\sigma_{rr}-\sigma_{\theta\theta})}{r}\right]$$

$$F_\theta = -\frac{1}{\rho}\left[\frac{\partial\sigma_{\theta\theta}}{r\partial\theta}+\frac{\partial\tau_{\theta z}}{\partial z}+\frac{\partial\tau_{\theta r}}{\partial r}+\frac{2}{r}\tau_{\theta r}\right]$$

$$F_z = -\frac{1}{\rho}\left[\frac{\partial\tau_{z\theta}}{r\partial\theta}+\frac{\partial\sigma_{zz}}{\partial z}+\frac{\partial\tau_{rz}}{\partial r}+\frac{\tau_{rz}}{r}\right]$$

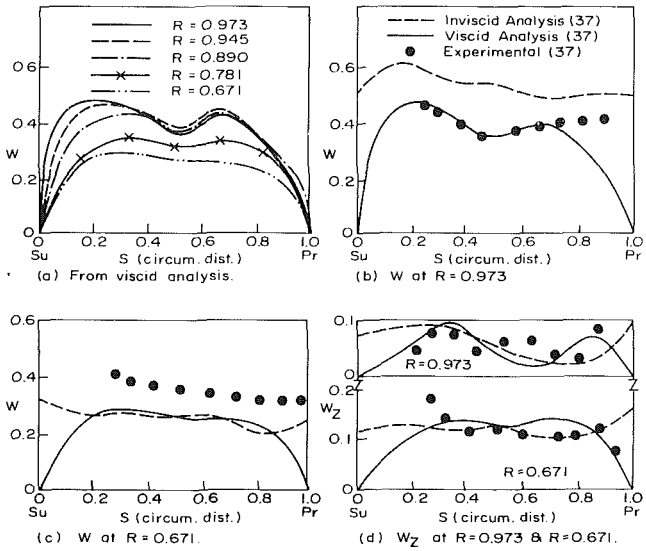

Fig. 9 Comparison between theory and experiment of the blade-to-blade distribution of total relative velocity and axial velocity near the trailing edge for the Penn State inducer [37]

where τ is the shear stress and σ is the normal stress. For example, τ_{r_θ} is the shear stress in the r direction in a plane perpendicular to θ. σ_{rr} is the normal stress in a plane normal to the r direction.

Since the stagger angle is very large, these viscous terms can be approximated by retaining the dominant terms as well as neglecting the normal shear stress, resulting in:

$$F_r = -\frac{1}{\rho}\frac{\partial \tau_{rz}}{\partial z}$$

$$F_\theta = -\frac{1}{\rho}\frac{\partial \tau_{\theta z}}{\partial z}$$

$$F_z = -\frac{1}{\rho}\frac{\partial \tau_{z\theta}}{r\partial \theta}$$

The distribution of shear stress is assumed to be linear across the flow passage from the pressure surface to the suction surface. The values of wall shear stresses are assumed to be known from the empirical skin-friction coefficient (C_f) data for a four-blade flat-plate helical channel presented in reference [38]. Details of incorporating this into the main program are discussed in references [34] and [37].

An additional requirement placed on the viscid analysis is to satisfy the viscid boundary condition, which requires that all components of velocity are zero at the blade surface.

The geometry and the grid system used are shown in Fig. 5. The comparison of blade static pressure is given in reference [37]. Inviscid and viscid analysis results for the total relative velocity distribution near the trailing edge for a three-bladed inducer are plotted in Fig. 9. Magnitudes of W near the tip are comparable to those found experimentally, whereas near the hub, the inviscid velocities are significantly lower than the predicted results. The viscid analysis prediction for the total relative velocity distribution is also shown in Fig. 9. It is a striking departure from the inviscid analysis distribution, expecially near the tip where the viscous effects are known to be appreciable. The viscid analysis also provides crude approximations for the suction and pressure surface boundary layers. A large velocity deficiency near the tip is predicted at approximately 50 percent passage width and agrees favorably with the experimental W profiles plotted in Fig. 9.

The prediction of radial velocity is at best qualitative. The reasons for this are discussed in references [34] and [37].

The viscid analysis is approximate due to the various assumptions and simplifications made. In particular, the viscid boundary conditions imposed on the solution are rather drastic, since the grid geometry spacing used in the exact analysis is relatively large. More tangential grid stations would be needed, especially close to the blade surface, to better define the shape of the blade boundary layer.

4 Inducer Overall Performance (Noncavitating)

4.1 Flat-Plate Inducers Tested in Water and Cryogenic Liquids. For the experimental aspects of the flow, many authors have studied the overall inducer performance with different configurations and inlet angles, and in various fluids such as water, liquid hydrogen, or nitrogen, under a wide range of flow parameters [4, 5, 7, 12, 14, 17–20, 42, 43, 48, 49, 53, 56, 57, 62–68, 72, 73]. Cavitating inducer performance has been studied by investigators listed in the uncited bibliography. However, in most cases these studies are very specific and deal with cavitation performance, overall efficiency, and radial distribution of flow properties rather than with a general and basic investigation of the flow phenomena in inducers. The cavitating and noncavitating performance of 84, 81, and 78 deg inducers under different flow coefficients has been studied by Acosta [7]. Acosta observed a deterioration in the radial distribution of the axial velocity and head rise at the exit for $\phi = 0.07$ under a noncavitating condition, with a backflow near the hub and a sharp positive gradient in head rise near the tip. These results are similar to those obtained by many investigators. Acosta attributed the large departure from design values based on the Simplified Radial Equilibrium Equation (SRE) to strong three-dimensional and viscous effects. Acosta also noticed a decrease in efficiency at large solidity, which is confirmed by the results obtained for the four- and three-bladed inducers tested at Penn State [27]. This effect can be attributed to the influence of blade blockage on the flow characteristics and an increase in viscous and turbulent mixing losses due to decrease in channel width.

Mullan [65] tested two inducers, one designed on the basis of radial equilibrium consideration [11] and the other with a constant pitch angle (simple helix). Both inducers were tested at various flow coefficients. The inducer designed on the basis of radial equilibrium equations had superior performance. The axial velocities were found to be low at the hub and high at the tip even at design condition, and this trend is reversed at flow coefficients higher than design. At flow coefficients lower than design however, the performance deteriorates with the presence of the back-flow at $\phi = 0.17$ and 0.14. Steep head rise near the tip is observed at a low flow coefficient ($\phi = 0.12$). The peak efficiencies of the inducers were 80 percent and 72 percent, for the aerodynamically designed inducer and the flat-plate inducer, respectively.

R. F. Soltis et al. [19] also measured steep head rise near the blade tip of a noncavitating 78 deg axial inducer under various flow coefficients. Using the simplified radial equilibrium equation which relates the static head rise gradient and the tangential velocity

$$\frac{1}{\rho}\frac{\partial p}{\partial r} = \frac{V_\theta^2}{r}$$

they derived the outlet axial velocity profile using experimental values for the total pressure and outlet flow angles. However, at their station of measurement, located about 1/5 diameter downstream of the rotor, the radial velocities are likely to be very small and the flow nearly axisymmetric, since the wake diffusion in such inducers is very rapid.

This analysis serves to establish that the flow is axisymmetric at small axial distances downstream of the trailing edge, which may correspond to large distances along the

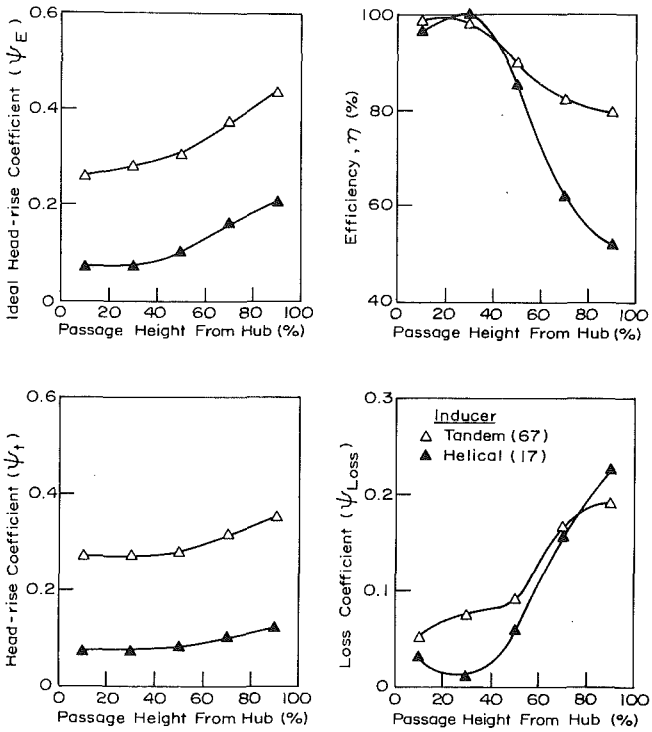

Fig. 10 Comparison of blade element parameters for tandem-bladed inducer and 80.6 deg helical inducer [67]

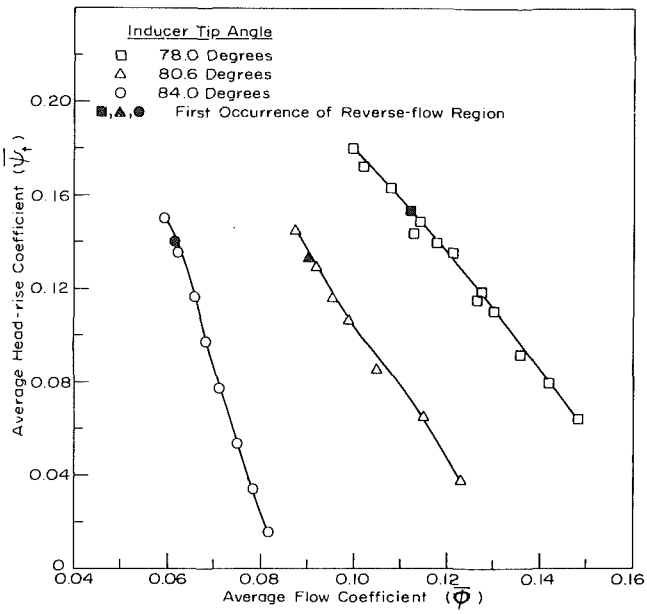

Fig. 11 Comparison of overall performance of 78, 80.6, and 84 deg helix angle inducers [20]

streamline path (since the streamlines follow tightly wound helical paths). However, the existence of large head rise near the tip cannot be accounted for in this analysis.

Three flat-plate inducers of 78, 80.6, and 84 deg were tested, respectively, by Soltis et al. [19], Sandercock et al. [17], and Anderson et al. [20] at the NASA Lewis Research Center. The rotors had three blades with a tip diameter of 127 mm, hub/tip of 0.5, and a solidity ranging from approximately 1.8 for the 78 deg inducer to 3.0 for the 86 deg inducer. The investigation was carried out in the Center's water tunnel, powered by a 3000 hp variable-frequency motor. The rotor was tested at various speeds. Details of this tunnel are given in reference [67]. They carried out overall performance measurements at both non-cavitating and cavitating conditions, including a radial survey at the exit. The following properties were derived from these measurements: pressure rise coefficient, efficiency, axial velocity at the exit, deviation angle, loss coefficient, and ideal head rise coefficient. In addition, flow visualization was carried out to determine the extent of cavitation. The radial distribution of outlet parameters for the 80.6 deg inducer [17] is shown in Fig. 10. The performance is similar to those of Mullan [65], who reported a deterioration in exit velocity distribution with a decrease in the flow coefficient. The overall pressure (or head) rise and efficiency showed marked improvement at the lowest flow coefficient ($\phi = 0.107$) tested. This is an improvement over the data reported by Mullan [65] at low flow coefficients. The noncavitating performance showed nearly linear variation of the head rise coefficient with the flow coefficient with a maximum efficiency of 82 percent. A very sharp increase in the loss coefficient towards the tip region was observed at all flow coefficients tested. Other conclusions are similar to those of Mullan [65] described earlier.

Overall noncavitating performance of the inducers with 78, 80.6, and 84 deg stagger angles at the tip is shown in Fig. 11 for the range of rotor speeds from 9000 to 15,000 rpm. The solid symbols on the performance curves for each inducer locate the operating conditions at which zero axial velocities are first observed at the hub outlet measuring stations. The slope of the ψ-ϕ curve increases as the stagger angle is increased. The NASA Lewis Research Center personnel have thus demonstrated successful operational of the inducer at very low flow coefficients.

The inducers tested by other investigations [4, 5, 7, 12, 14, 42, 43, 53, 57, 62–68, 72, 73] showed trends similar to those measured by the NASA Lewis group [17, 19, 20] and hence will not be described here.

Oshima [64] tested two-bladed inducers with two different tip clearances (0.5 mm and 10 mm), a stagger angle of 75 deg at the tip, and a tip diameter of 206 mm, and found that the suction performance deteriorates with an increase in tip clearance height when the eye diameter of the main impeller is nearly equal to the normal inducer diameter. Other configurations tested showed that the behavior is less sensitive to the tip clearance.

The main conclusions of the various studies described above are:

1 The overall head rise coefficient increases when the operating flow coefficient decreases. The head rise coefficient is very high near the tip (two to three times the design values) and nearly uniform from the hub to mid-radius.

2 The total head rise coefficient increases when the solidity of the blades is decreased in the practical range of solidities used in inducers.

3 The radial distribution of outlet velocity tends to deteriorate when the flow coefficient is decreased. At low flow coefficients and for most inducer configurations, there is a large positive radial gradient in the exit axial velocity with a backflow near the hub. This is dictated by the radial equilibrium as described in Section 3.1. Another probable cause of this backflow is the large redistribution of the flow as it leaves the trailing edge, the radial velocity decaying from positive values inside the blade passage to zero as the flow becomes axisymmetric downstream.

4 The radial loss distribution shows substantially higher losses from mid-radius to the tip. The efficiency is maximum near the hub and reaches very low values near the tip of the blade.

4.2 Tandem and Hubless Inducers. Soltis et al. [62, 67] tried to improve the performance of flat-plate inducers by employing a tandem rotor, as shown in Fig. 1. In this approach,

the high blade loading is distributed between two or more closely coupled blade sections so that the blade surface boundary-layer separation is prevented on any of the individual blades. The comparison between the flat-plate inducer and the tandem inducer tested by Soltis et al. [62, 67] is shown in Fig. 10. The average flow coefficient ($\bar{\phi}$) and head rise coefficient ($\bar{\psi}$) of the flat-plate inducer were 0.107 and 0.085, respectively. These values for the tandem rotor were 0.109 and 0.303, respectively. The comparison indicates that the efficiency and head rise are generally higher and the losses lower near the tip for a tandem rotor. Substantial improvement near the tip section (η and ψ_{loss}) indicates that the tandem rotor prevents a large accumulation of low-energy fluid in the tip region. The tandem rotor tested by Soltis et al. [62, 67] also maintained great efficiency over a large portion of the flow range.

Another concept which is tried to improve the performance of these inducers is to utilize a hubless inducer, shown schematically in Fig. 1. The entire shroud-blade assembly rotates. The advantages of this design configuration are: (1) the elimination of tip vortices: (2) the centrifuging effect on the cavitation bubbles, causing them to cluster around the center of the inducer where they collapse without causing material damage; and (3) the achievement of high suction speed by employing high sweepback in the vanes. This concept is orginally due to Jekat [15, 73] and has been explored further by Miller and Gross [18] and Lindley and Martinson [72]. Jekat observed all the advantages mentioned earlier. The tip vortex cavitation was eliminated, and the inlet vane cavitation was reduced by large sweep back in the vanes. The predicted centrifuging of the cavitation bubble and its collapse (without causing material damage) was confirmed. The peak efficiencies measured by Miller and Gross [18] indicate that their value did not exceed 65 percent, while a flat-plate inducer (with hub) tested by Sandercock et al. [17] has a peak efficiency of 82 percent, and the corresponding tandem inducer [67] had a peak efficiency of 85 percent. Even though hubless inducers have better cavitation characteristics, their poor overall efficiency makes them less attractive for commerical application. Lindley and Martinson [72] concluded from a full-scale test that the cavitation performance of a hubless inducer is not significantly better than the conventional inducer.

Since no information is available on the exit flow properties, such as the radial distribution of the axial and tangential velocities and the pressure rise characteristics, it is difficult to conclude from the available data that the hubless inducer has better overall performance and flow characteristics. It is not clear how the core flow near the center would affect the performance of the main pump.

5 Penn State's Results From Inducers Tested in Air

The experimental investigation of the flow phenomena in rocket pump inducers carried out at the Pennsylvania State University is summarized here. All the experimental investigations were conducted with air as the test medium. Details can be found in references [21] through [41] and summary in reference [71]. Rocketdyne [74] tested pumps with air as the working fluid and found that a very good correlation exists between air test data and the liquid test data. While the characteristic form of the inducer is dictated by cavitation requirements, the flow is subjected to major effects of viscosity and turbulence in the long and narrow passages. The investigation reported here are concerned with the effects of viscosity, not the effects of cavitation.

One of the major objectives of this investigation was to understand the flow phenomena in these inducers through flow visualization and conventional and hot-wire probe measurement inside and at the exit of the blade passage, and to provide analytical methods for the prediction of flow through inducers. To achieve the objectives mentioned above, the experimental work was carried out using four-, three-, and two-bladed inducers with aerodynamically designed blades. The blades were identical in all these cases. Wislicenus and Lakshminarayana [21] made the first attempt to design inducers on the basis of rational aerodynamic concepts. Extensive data is available for this inducer.

The basic research and boundary-layer investigation was carried out using a helical flat plate of (of same dimensions as the inducer blades tested), and a flat-plate helical inducer (four-bladed). The flow measurements were carried out using

Table 1 Summary of the Inducer Investigation at the Pennsylvania State University: Tip Diameter = 0.915 m, Reynolds number based on radius and blade speed at tip = 6.6×10^5

Configuration	Design	C^* in.	(C^*/S^*)	β_1^* degrees	(β_1)hub degrees	ϕ	Measurements and analysis carried out	Refs. where reported
Four-bladed inducer	Cambered blades-free vortex design	83	2.86	86°15′	75°30′	0.065	Flow visualization inside the passage; exit, entry, and passage flow measured with a pitot probe. Approximate analyses.	[21,22,23,27, 28,31,32,41]
Four-bladed inducer	Flat plate	95	3.4	84°	78°	0.04 to 0.067 and open throttle	Exit flow measurement; extensive hot-wire measurement at 1600 locations inside the passage to define mean velocity, turbulence intensity, and stress; blade static-pressure and skin-friction stress. Boundary-layer analysis.	[26,30,38,39, 40]
Three-bladed inducer	Cambered blades	83	2.14	86°15′	75°30′	0.065	Exit and entry flow using both hot-wire and pitot probe; hot-wire probe measurements inside the passage. Numerical solution of inviscid and viscid equations.	[26,27,30,32, 33,34,35,36, 37,41]
Two-bladed inducer	Cambered blades	83	2.14	86°15′	75°30′	0.065	Exit and entry flow measurements.	[27]
Single blade	Flat plate	95		84°	78°	open throttle	Mostly three-dimensional turbulent boundary-layer measurements.	[24,25,26,29]

*Values at the tip

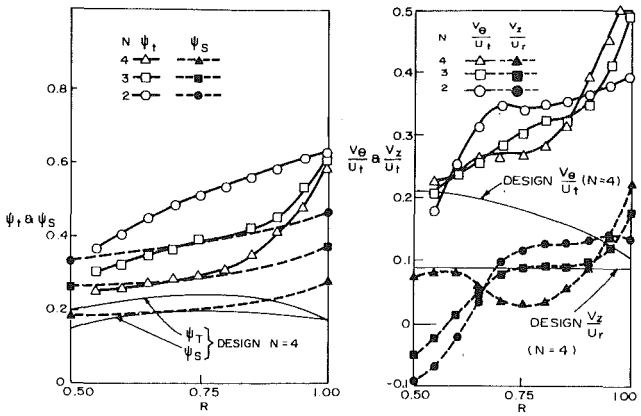

Fig. 12 Radial variation of flow properties for four-, three-, and two-bladed inducers

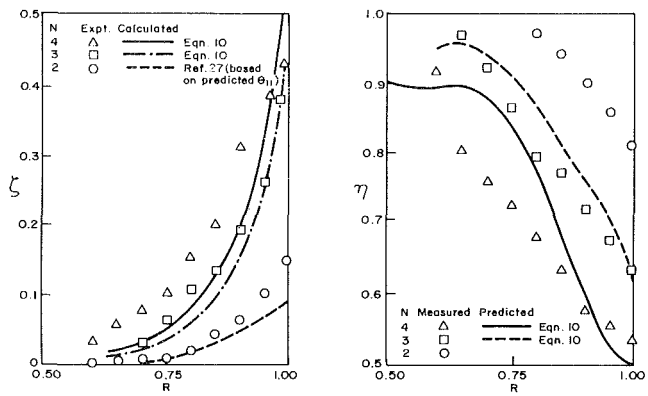

Fig. 13 Calculated and measured distribution of loss coefficient (ζ) and efficiency η for Penn State inducers

triaxial hot-wire probes and pitot probes. Details of the measurement technique are given in reference [69]. Detailed mean and turbulence flow fields inside the passage as well as at the exit of the rotor were derived from these measurements.

The boundary layer, end-wall, and other passage data revealed the extremely complex nature of the flow, in particular the major effects of viscosity present across the entire passage. A summary of the configurations used, the nature of measurements taken, and the references where they are reported is tabulated in Table 1. The inducer characteristics and the design of the inducer are described in references [21] and [31]. Both the published and the unpublished results from the Penn State program are reviewed here.

A visualization study of the flow through the four-bladed inducer configuration is reported in references [28] and [52]. The flow was found to be highly three-dimensional, with appreciable radial velocity throughout the passage. At or near the design flow coefficient, no backflow is observed upstream of the inducer. A separated region of the flow exists near the hub at the discharge of the inducer. The extent of the backflow increases considerably, both at inlet and at exit, for flow coefficients lower than the design value. The radial velocities within the blade passage appear to be quite strong at all radii. The radial movement inside the blade boundary layer, when enountered by the annulus wall, tends to deflect towards the mid-passage and then radially inward. These radial flows exist near the outer radius (midradius to tip) and are found to be large (Fig. 3).

5.1 Measurements Downstream of the Aerodynamically Designed and Flat-Plate Inducers. The flow measurement carried out at several stations downstream of the four-, three-, and two-bladed inducer blade row tested at the same flow coefficient are reported in references [22, 23, 25–28, 30–41]. The major conclusions from the four-bladed inducer results are presented here.

The test inducer, designed approximately for uniform head distribution over its discharge area, actually produces a very nonuniform head near the tip, as shown in Fig. 12. The axial velocity distribution shows maximum departure from design, as shown in Fig. 12. The velocity near the hub shows a tendency to separate, with maximum values occurring near the tip. Measurements very close to the trailing edge reveal a different trend, with minimum velocity occurring at midradius [27]. The measured tangential velocity (absolute) is substantially higher than the design, especially from the midradius to the tip (Fig. 12).

The loss coefficient (ζ) calculated from the measured Euler head coefficient ($\psi_E = 2U\ V_\theta/U_t^2$) and measured pressure coefficient (ψ_t) is plotted in Fig. 13. The losses are much higher than for any other conventional turbomachinery, especially in the outer radii. The hydraulic efficiency, $\eta = \psi_t/\psi_E$, plotted in Fig. 13, shows near-normal efficiencies (90 percent) near the root and 50 percent efficiency near the tip for the four-bladed inducer. The mass-averaged efficiency given by

$$\bar{\eta} = \int_{r_h}^{r_t} \eta V_z r dr \Big/ \int_{r_h}^{r_t} V_z r dr \tag{18}$$

is found to be 64 percent for the four-bladed inducer, 76 percent for the three-bladed inducer, and 88.5 percent for the two-bladed inducer.

5.1.1 Effect of Solidity (or Number of Blades) on Overall Performances. Major conclusions derived by comparison of the measurements at the exit of the two-, three-, and four-bladed inducer are as follows (Figs. 12 and 13).

The results indicate that the performance, both pressure rise and efficiency, improve continuously with a decrease in solidity (at the same flow coefficient ϕ). The two-bladed inducer shows the best performance, even though the backflow region near the hub at the exit is increased with a decrease in solidity. The static-pressure (or head) rise increases continuously, at all radii, with the decrease in solidity (Fig. 12).

The radii distribution of stagnation-pressure rise coefficient indicate that strong real fluid effects are evident at all solidities. ψ_t increase continuously with the decrease in solidity. The frictional effects play a dual role here. The energy exchange or head rise is the desirable part. Associated with friction is the energy dissipation of the fluid flowing through the pump. These losses arise from (in addition to secondary and leakage flow near the annulus and hub walls): (*a*) skin friction on the blade surface, and (*b*) interaction between pressure surface and suction surface boundary layers, especially near the outer wall. The radial movement inside the blade boundary layer, when encountered by the annulus wall, tends to deflect towards midpassage and then radially inward. Intense turbulence and mixing in this region give rise to considerable flow loss. Both of these losses are reduced when the spacing is increased, even though the effect of spacing on energy transfer is not to appreciable. The net effect is a larger pressure rise, at all the radii, as the blade spacing is increased. It can also be seen in Fig. 12 that a steep rise in ψ_t (towards the tip), observed in the case of three- and four-bladed inducers, is substantially reduced for $N = 2$, thus indicating minimization of the interaction effects near the tip as the solidity is decreased. Observed increase in ψ_t, with the decrease in solidity, is a result of major significance, indicating that the frictional losses are reduced substantially with the increased spacing, even though energy transfer due to inviscid and shear pumping effects show no appreciable

change with the spacing. The mass-averaged stagnation-pressure (or head) rise coefficient, defined by,

$$\bar{\psi}_t = \int_{r_h}^{r_t} \psi_t V_z r dr \Big/ \int_{r_h}^{r_t} V_z r dr \tag{19}$$

and shown in Fig. 14, indicates that ψ_t increases continuously with a decrease in blade number at all the radii.

The axial velocity profiles are found to be similar, qualitatively, downstream of all the inducers tested, as shown in Fig. 12. The steep rise in axial velocity toward the tip observed in the case of three- and four-bladed inducers is absent in the case of the two-bladed configuration, but the extent of the separated zone (or back-flow region) near the hub increases continuously with the decrease in solidity. Thus, the axial velocity profile deteriorates with the decrease in the solidity.

The steep gradient in ζ that exists near the tip for $N = 4$ and 3 is reduced drastically for the two-bladed case (Fig. 13). There is a drastic reduction in loss between a three- and two-bladed inducer, thus indicating that the boundary layers in a two-bladed inducer do not cover the entire passage. The hydraulic efficiency for the inducer can be derived from $\eta = \psi_t/\psi_E$, where ψ_E is the ideal or Euler head rise coefficient (Fig. 13). This clearly indicates that the efficiency improves, at all the radii, as the solidity is decreased. It is surprising that the local efficiencies improve as much as 30 to 50 percent when the solidity is halved. Even though efficiency is not a major consideration in the selection of inducers for the present-day spacecraft, it would assume added importance when space travel becomes a commercial venture.

The mass-averaged efficiency derived from equation (18) are shown plotted in Fig. 14 and compared with those of Acosta [7], Iura [70], and Soltis et al. [19]; the latter measurements correspond to non-cavitating conditions. Appreciable decrease in $\bar{\eta}$ is observed with the increase in solidity, the trend being the same for all of the inducers shown. A physical reasoning for the observed trend in the variation of overall efficiency ($\bar{\eta}$) with σ is as follows: consider inducers operating as the same flow and blade parameters, except for the change in blade spacing S. Since the average loss coefficient ($\bar{\zeta}$) is proportional to C/d_h or C/S, the solidity, the overall efficiency is

$$\eta = 1 - \frac{k\sigma}{\bar{\psi}_e}$$

where k is a constant. Since $\bar{\psi}_E$, the average Euler head rise coefficient, is nearly the same for all the inducers tested in this program (see Fig. 14), overall efficiency ($\bar{\eta}$) can be expressed as

$$\bar{\eta} = 1 - k_1 \sigma. \tag{20}$$

The values of $\bar{\eta}$ derived from equation (20) with $k_1 = 0.107$ agree reasonably well with the measured efficiencies (Fig. 14). This adequately explains the decrease in efficiency for increased solidity.

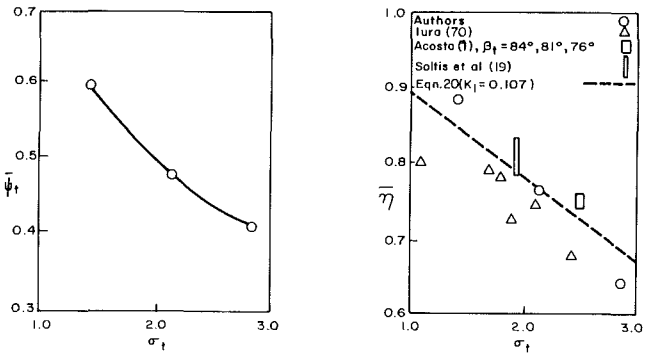

Fig. 14 Variation of mass-averaged stagnation pressure rise coefficient ($\bar{\psi}_t$) and ($\bar{\eta}$) with solidity for Penn State inducers

5.1.2 Flat Plate Inducer. A flat-plate inducer, whose details are shown in Table 1 and described in reference [39], was tested in air. The stagnation-pressure rise for the flat-plate inducer exhibits characteristics which are very similar to an aerodynamically designed inducer. Steep rise in stagnation pressure was observed near the tip even in the case of the flat-plate inducer with an open throttle (no inviscid effects). This provides a convincing argument that the tip of the inducer blade behaves as a shear pump, where the pressure or head rise is brought about entirely by the viscous effects. The absolute tangential velocity distribution [71], even in the absence of inviscid turning effects, is very similar to the distribution observed for the aerodynamically designed inducer.

For the purpose of comparison, the flat-plate inducer data at $\phi = 0.05$ and the data from the aerodynamically designed inducer ($\phi = 0.065$) are chosen. This choice is based on nearly identical pressure rise across the inducers from hub to tip [71, 41]. The static-pressure and stagnation-pressure rise coefficients, plotted in Fig. 15, indicate nearly similar characteristics, even though the stagnation-pressure rise near tip is about 50 percent lower for the flat-plate inducer near the trailing edge. From mid-radius to the tip, the aerodynamically

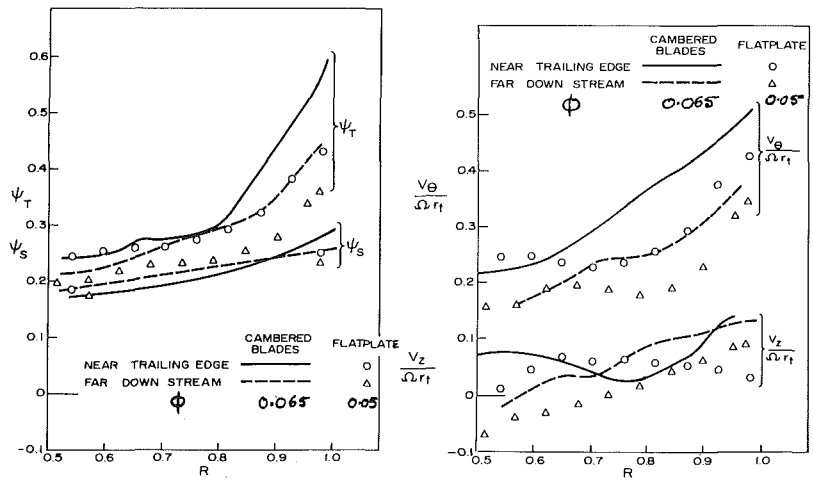

Fig. 15 Radial variation of flow preperties for the flat-plate inducer and cambered-bladed inducers tested at Penn State [41]

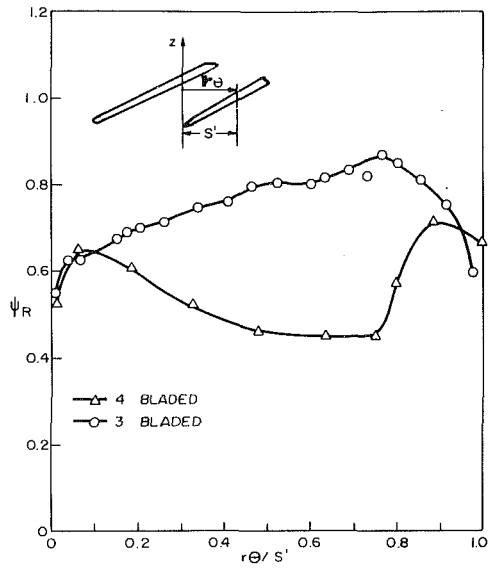

Fig. 16 Stagnation pressure coefficient of the relative flow at 1/3 blade chord from the leading edge for R = 0.975 for four- and three-bladed inducers

designed inducer shows as much steeper gradient in the head rise coefficient. The major cause of this is probably due to the "shear pumping effect."

The radial distribution of the absolute tangential velocity and the axial velocity are also compared in Fig. 15. The tangential velocity follows the same trend as the stagnation head rise coefficient, but the major discrepancy occurs in the axial velocity distribution. Near the trailing-edge location, the flow in the flat-plate inducer shows a tendency to separate near the hub, while the flow in the aerodynamically designed inducer does not. The axial velocity near the tip for the aerodynamically designed inducer is higher, a consequence of higher radial velocity [41]. Both inducers show the same trend far downstream, with a larger backflow region observed for the flat-plate inducer.

5.1.3 Blade-to-Blade Distribution of Flow Properties at the Exit of the Inducer. Pitot probes, wedge probes, and three-sensor hot-wire probe (with ensemble-averaging technique) were utilized at the exit of the inducers to drive flow properties at the exit. Details of these measurements are given in references [22, 33, 35]. These results are summarized in reference [71]. The relative stagnation-pressure coefficient (ψ_R) is found to be nearly uniform across the passage near the hub and mid-radius. The measurements near the tip indicate considerable boundary-layer thickening. This confirms the presence of severe radial flows and, hence, the blade boundary-layer transport towards the tip.

The radial velocities obtained from the hot-wire measurements are found to be of the same order of magnitude as the axial velocities throughout the flow passage. The turbulence-intensity components in the radial, axial, tangential, and relative directions (based on local mean-velocity component) are found to be about 75 percent, 45 percent, 20 percent, and 15 percent, respectively. The turbulence intensities are found to be nearly uniform in the entire flow passage at the exit. These measurements reveal the highly turbulent nature of the flow in inducers.

The distribution of axial, tangential, and relative velocities are similar for both the four- and the three-bladed inducers even though the tangential velocities are higher for the three-bladed inducers.

5.2 Measurments Inside the Blade Row. Some of the blade static pressures and the limiting streamline angles for the four-bladed inducer are reported in references [28] and [32],

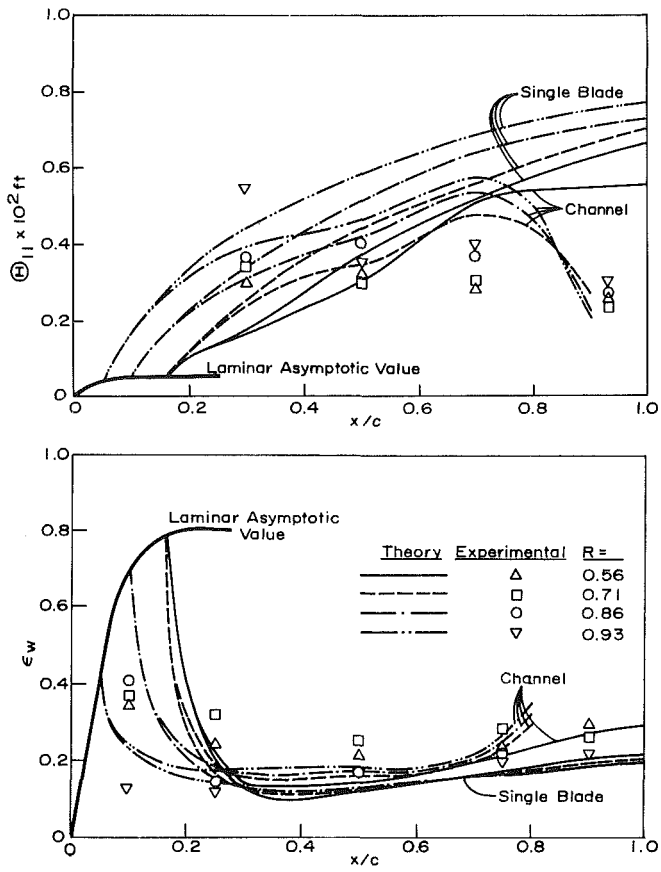

Fig. 17 Predicted and measured variations of momentum thickness and limiting streamline angle on the leading surface of the Penn State flat-plate inducer rotor (open throttle), reference [38].

respectively. Most extensive blade-pressure distribution was carried out for the three-bladed inducer and is reported in references [34], [36], and [37].

The ammonia trace technique provides a satisfactory method for determining blade limiting streamline angles on the inducer rotor blade. The blade limiting streamline angle measurements provide several observations which have either been noted in previous investigations or have been found from other experimental results quoted in references [25] through [41]. These include: an increase in ϵ from the leading edge to the trailing edge, indicating the existence of higher radial velocities as the flow proceeds downstream within the inducer channel; higher values of ϵ near the hub indicating higher radial velocities in this region; negative values of ϵ at the pressure surface tip (up to 45 percent chord) indicating radially inward flow due to the presence of the annulus-wall boundary-layer scraping effect; and values of α_w (arc tan ϵ) greater than 90 deg near the hub trailing edge indicating the existence of a backflow region in this area.

The magnitude of blade static pressure distributions are found to be considerably higher than the design values.

In order to understand the flow behavior inside the inducer passages, experimental investigation of the relative flow (blade-to-blade) inside the inducer passages was undertaken using rotating probes and the pressure-transfer device. Pressure-probe measurements inside the four bladed inducer are reported in references [22], [23], and [32], and for the three-bladed inducer in references [25, 26, 30, 32, 33, and 37]. The flow was surveyed in one passage and at several radial locations. Some of the major conclusions derived from measurements in four-bladed inducers as presented in references [22], [23], and [32] are described below.

1 The measurement of relative flow near the trailing edge

reveals the presence of a loss core located slightly inward from the tip. The mid-passage at this radius is found to have minimum relative stagnation pressure and, hence, maximum loss. A substantial portion of total flow losses occurs near the leading edge. The losses near the tip are found to be about five times those at other radii (see Fig. 11 in reference [32]).

2 The blade boundary layers are found to be quite thin near hub. The boundary-layer thickness near the mid-radius is about 25 percent of the blade passage, being thicker on the suction surface than on the blade pressure surface. A conventional boundary-layer type of profile exists from hub to mid-radius; whereas, the velocity profile near the tip (mid-radius to tip) is of conventional type near the blade surfaces and "wake" type near the mid-passage. Qualitative reasons for the existence of this type to profile are discussed in references [32].

3 Near the trailing-edge station, the passage-averaged values of relative velocity have a maximum value at mid-radius, being considerably lower than the design values from mid-radius to tip. The diffusion of relative flow is caused mainly by the inviscid turning effects from the hub to mid-radius; whereas, the diffusion from mid-radius to the tip is dominantly influenced by the viscid and "shear pumping" effect.

The following conclusions are derived by comparing the relative flow measurements taken in the three-bladed inducer with those of the four-bladed configuration [32, 33]. Measurements taken near the leading edge show marked reduction in boundary-layer growth, flow losses, and radial inward velocity in the case of the three-bladed inducer. The losses near the tip are nearly halved from those of the four-bladed inducer, and the "wake" type of profile observed near the mid-passage of the tip disappears in the case of the four-bladed inducer, as shown in Fig. 16. There is appreciable improvement in hub and wall static-pressure distributions in the case of the three-bladed inducer.

5.3 Measurements Inside the Blade Passage of a Three-Bladed Inducer Using Hot-Wire Probes. Detailed measurements of mean velocity and turbulent flow field inside the three-bladed inducer were carried out using the rotating hot-wire technique described in references [30, 34, 36, and 37]. The flow was measured at various radii and across the blade at axial stations approximately at 1/3 blade chord and trailing edge.

Total relative velocity profiles, derived from the rotating triaxial hot-wire measurements, indicate a substantial velocity deficiency near the tip at mid-passage which expands significantly as the flow proceeds downstream toward the inducer trailing edge (Fig. 9). The higher values of axial velocity near the hub, shown in Fig. 9, indicate the significant effect of blade blockage within the inducer flow passage. A slight backflow was found to exist at the extreme tip location at 1/3 blade chord from the leading edge and can be attributed to the annulus-wall boundary-layer scraping effect identified in the limiting streamline angle (ϵ) measurements. The measured magnitudes of radial velocity are found to be the same order as those of axial velocity within the inducer passage. The large values of radial velocity confirm the highly three-dimensional characteristics of the inducer flow and emphasize the necessity for a three-dimensional theory for accurate flow analysis. Turbulence levels within the blade passage, indicated from the experimental results, are generally high near the tip regions. The radial component of turbulence intensities appears to have the largest magnitudes, reaching values of up to 24 percent in the mixing region.

5.4 Boundary Layer and Related Phenomena on Inducer Blades and Passages. A systematic study of the boundary layer on a rotating blade and inside a rotating channel was undertaken by the Penn State group. In the first phase of the program, the boundary layer on a simpler configuration, namely, a rotating helical blade of large chord length enclosed in an annulus, was studied [24, 26, 29]. In the absence of chordwise pressure gradients, the effect of rotation on the boundary layer can be discerned.

The interference due to adjoining blades ("channel effect") that exists in turbomachinery passages is not simulated in the above model. With this as an objective, studies of the influence of the rotation and "channel effects" as well as pressure gradient effects were carried out in a rotating channel, with the geometry of a four-bladed flat-plate inducer [30, 38, 39, 40]. In both of these experiments, air was employed as the test medium.

The following conclusions may be drawn from the theoretical and analytical investigations carried out on a single rotating helical blade [24, 29]: (1) The solution of the momentum integral equations predict, accurately, the boundary-layer growth and the limiting streamline angle ϵ at various locations on the rotating-blade surface. (2) About 100 skin-friction measurements carried out at various radial and tangential locations of the blade and at several rotational speeds indicate that the skin-friction coefficient on a rotating blade can be represented by

$$\frac{c_f}{c_{fo}} = 1 + 0.85\, R_o^{1/2}$$

where $R_o = \epsilon\theta$, the theoretically derived rotation number (ratio of the Coriolis force to the inertial force inside the boundary layer), and c_{fo} = skin-friction coefficient for a flat plate at zero pressure gradient. A similar expression is given for the developed region of the flow.

5.4.1 Boundary Layer Development in a Flat-Plate Channel. In an axial flow inducer, the interaction between pressure surface and suction surface boundary layers would result in an extremely complex flow, especially near the outer half of the blade span. These effects were studied in a helical flat-plate inducer specifically designed and fully instrumented for this purpose. Details of the program and the Reynolds equation valid for this flow are given in reference [25], and velocity-profile analysis and details of instrumentation in reference [26]. Details on the velocity profiles carried out with mild and strong pressure gradients, as well as detailed analyses, are described in references [38–40].

A boundary-layer flow analysis was carried out using the momentum integral technique, which employs three-dimensional equations of motion in the rotating coordinate system [38–40]. The measurements of the boundary-layer characteristics (three components of velocity, turbulence intensities, Reynolds stresses, skin-friction coefficient, and limiting streamline angle) were carried out utilizing the conventional and tri-axial hot-wire probes rotating with the rotor inside the passage [38, 40].

The inducer was tested with open throttle [38, 39] and at $\phi = 0.05$ [39, 40]. The momentum thickness and the limiting streamline angle on the leading surface predicted from a three-dimensional momentum integral analysis is shown in Fig. 17. The momentum thickness increases rapidly near the leading edge, reaching an asymptotic value at nearly 1/3 chord from the leading edge. It starts to decrease near the trailing edge. As expected, the momentum thickness increases toward the tip. The predictions are quite good, except near the blade tip. The limiting streamline angle, shown plotted in Fig. 17, indicates that the radial velocities are large in the laminar region and lower in the turbulent region. The limiting streamline angle decreases as the outer wall is approached. The predictions from the momentum integral analysis are quite good.

The skin-friction coefficient for the rotating channel is

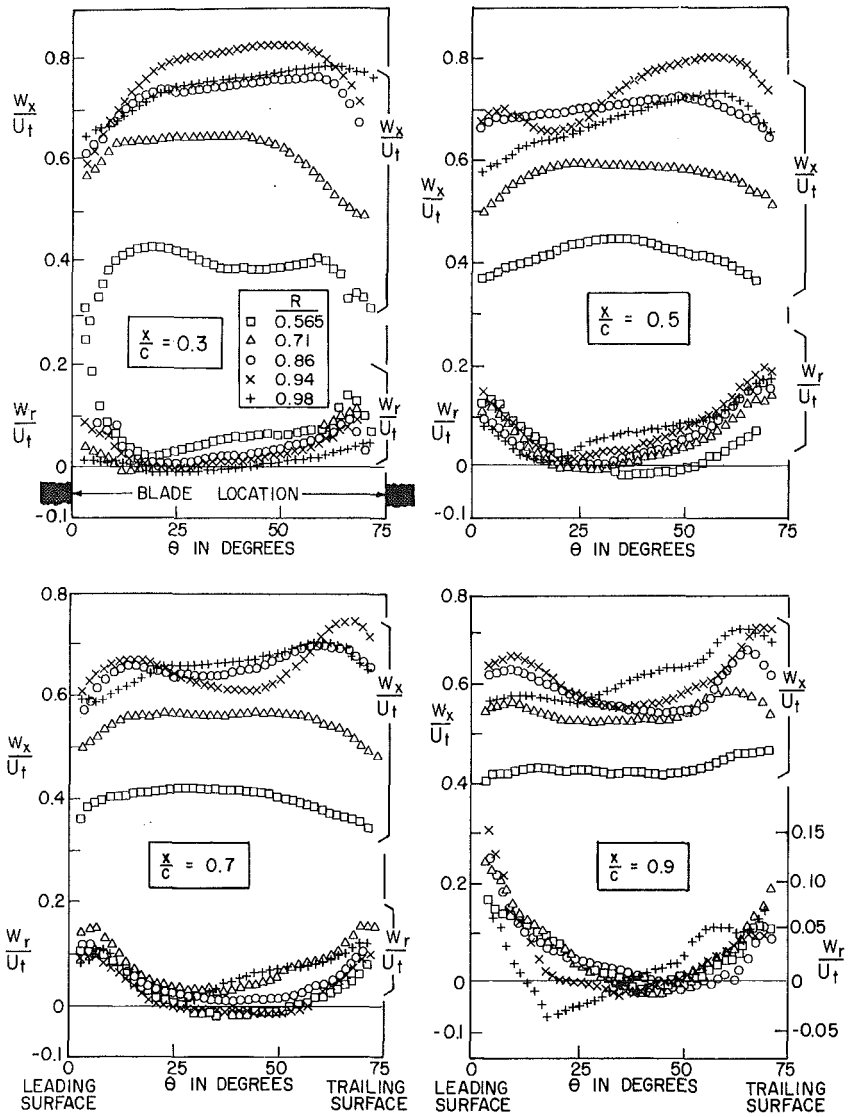

Fig. 18 Blade-to-blade variation of streamwise and radial velocity profile for the Penn State flat-plate inducer at $\phi = 0.05$, reference [40].

found to vary with three important three-dimensional boundary-layer parameters, θ_{11}, ϵ, and H. The proposed correlation for the skin-friction coefficient, based on the limited data in the rotating channel with mild pressure gradients, is

$$C_f = 0.172 R_{\theta_{11}}{}^{-0.268} 10^{-0.678H}[1 + 0.52\sqrt{\epsilon_w(x - x_t)/C}].$$

The term in the brackets is due to three-dimensional effects. Variation with $R_{\theta_{11}}$ and H is found to be the same as that for a stationary channel.

The streamwise and radial velocity profiles inside the four-bladed flat-plate inducer at $\phi = 0.05$ measured by a triaxial hot wire probe are shown in Fig. 18. The boundary layers are thin near the hub ($R = 0.565$) and show a substantial increase as the tip is approached. As the flow proceeds downstream the hub boundary layer is thrown outwards, resulting in a complex flow near the tip. Turbulent shear stress measurements [40] show that in three-dimensional rotating turbulent layers, all three of the velocity cross-correlations are of the same order of magnitude inside the boundary layer.

6 Concluding Remarks

The major significance of the research carried out hitherto is that it has provided a good understanding of the flow in inducers where the real fluid effects are at least equally important to the ideal fluid effects which form the basis of existing design methods of turbomachinery. It is hoped that the results reviewed will help establish a theoretical model for the eventual analysis and design of turbomachinery dominated not only by viscous and turbulence effects inside the turbomachinery passages, but also by the secondary flow and other interaction effects near the end-wall regions. Technique have been developed for the solution of three-dimensional inviscid equations of turbomachinery. It is anticipated that the analytical and experimental investigations reviewed here will lead to the eventual development of a three-dimensional viscid program that will include all the dominant viscous and turbulence terms. The Penn State research program has provided a large amount of accurate data for the boundary layer on rotating blades and in rotating channels. These could be utilized by investigators presently involved in the development of computer codes.

The radial velocities are of the same order of magnitude as the axial velocities; hence, inclusion of these as well as the dominant turbulence terms is essential for the accurate prediction of the flow. The inner part of the rotor (hub to mid-radius) could be designed from inviscid considerations, but the design of the outer part (mid-radius to tip) should take

into account the "drag or shear" pumping effect. The semiempirical friction loss coefficient developed and used for the prediction of head rise characteristics, even though unsatisfactory in view of our better insight into the loss mechanism, could serve as a useful tool in the preliminary design or analysis of inducers. The performance deteriorates with an increase in the number of blades. These results provide a design criteria in the selection of solidity in inducers.

Acknowledgments

The author wishes to acknowledge the National Aeronautics and Space Administration for sponsoring (NASA Grant NGL 39-009-007) the research carried out at The Pennsylvania State University on inducer flows. Comments, criticism, and encouragement by Werner R. Britisch of the NASA Lewis Research Center and George F. Wislicenus of The Pennsylvania State University are gratefully acknowledged.

References

1 Ross, C. C., "Some Historical Notes on Turbopump Systems for Liquid Rockets," ASME Paper 64WA/FE22, 1964.

2 Rothe, K., "Turbopump Configuration Selection for the Space Shuttle Main Engine," ASME Paper 74-FE-33, 1974.

3 Johnson, J., and Colbo, H., "Update of the Space Shuttle Main Engine (SSME)," AIAA Paper 78-1001, 1978.

4 Susuda, S., and Kitamura, N., "Experimental Studies on Centrifugal Pump with Inducer for Water Jetted Propulsion," Inst. Mech. Engrs. (London), Paper C165/74, 1974.

5 Arcand, L., "The Performance of Two Axial Flow Water Jet Pumps," ASME Symp. on Pumping Machinery for Marine Propulsion, Mar. 1968.

6 Luscher, W. P., "Commercial Application of Rocket Turbopump Technology," NASA SP 5030 (Symposium on Technology Status and Trends), Apr. 1965, pp. 21–35.

7 Acosta, A. J., "An Experimental Study of Cavitating Inducers," *Proc. Second Symposium on Naval Hydrodynamics*, Washington, D.C., Aug. 1958, pp. 553–557.

8 Jacobsen, J. K., "Liquid Rocket Engine Turbopump Inducers," Series on NASA Space Vehicle Design Criteria, NASA SP 8052, May 1971.

9 King, A. L., "References on Inducers for Rotodynamic Pumps," British Hydromechanics Research Association Report B1B24, Sept. 1967.

10 Wislicenus, G. F., "Preliminary Design of Turbopumps and Related Machinery," NASA Reference Publication (RP) (to be published 1982).

11 Stenning, A. H., "The Design of Axial Inducers for Turbopumps," M.I.T. Gas Turbine Lab Rept. 44, Feb. 1958.

12 Wright, M. K., "Design Comments and Experimental Results for Cavitation Resistant Inducers Up to 40,000 Suction Specific Space," *Trans. ASME*, Apr. 1964, pp. 176–180.

13 Janigro, A., and Ferrini, F., "Recent Progress in Pump Research," Von Karman Inst. Lecture Series 61, 1973.

14 Ross, C. C., and Benerian, G., "Some Aspects of High Suction Speed Pump Inducers," *Trans. ASME*, Nov. 1956, pp. 1715–1721.

15 Jekat, W. K., "The Worthington Inducer," NASA Final Report on Contract NAS8-2680, 1964.

16 Farquahr, T., and Lindley, B. K., "Hydraulic Design of the M-1 Liquid Hydrogen Turbopump," NASA CR 54822, 1966.

17 Sandercock, D. M., Soltis, R. F., and Anderson, D. A., "Cavitation and Non-Cavitation Performance of 80.6° Flat Plate Helical Inducer at Three Rotational Speeds," NASA Technical Note D-1439, Nov. 1962.

18 Miller, C. D., and Gross, L. A., "A Performance Investigation of an Eight-Inch Hubless Pump Inducer in Water and Liquid Nitrogen," NASA TN D-3807, Mar. 1967.

19 Soltis, R. F., Anderson, D. A., and Sandercock, D. M., "Investigation of the Performance of a 78° Flat Plate Helical Inducer," NASA Technical Note D-1170, Mar. 1962.

20 Anderson, D. A., Soltis, R. F., and Sandercock, D. M., "Performance of an 84° Flat Plate Helical Inducer and Comparison with Performance of a Similar 78° and 80.6° Inducers," NASA TN D-2553, Dec. 1964.

21 Wislicenus, G. F., and Lakshiminarayana, B., "Design of a Test Inducer," NASA CR-67129, 1965.

22 McCafferty, H. G., "Errors in Measuring the Fluctuating Flow at the Discharge of an Inducer," M.S. thesis, Dept. of Aerospace Engineering, The Pennsylvania State University, 1967.

23 Lakshminarayana, B., "Investigations and Analysis of Flow Phenomena of Secondary Motions in Axial Flow Inducers," NASA CR-103291, June 1969, pp. 1–23.

24 Jabbari, A., "Turbulent Boundary Layer Characteristics on a Rotating Helical Blade," M.S. thesis, Dept. of Aerospace Engineering, The Pennsylvania State University, 1969 (also as NASA CR-105649, NASA Star Index N69-36288, Sept. 1969).

25 Poncet, A., Yamaoka, H., and Lakshminarayana, B., "Investigations and Analysis of Flow Phenomena of Secondary Motions in Axial Flow Inducers," NASA CR-107267, July 1970, pp. 1–115.

26 Yamaoka, H., Lakshminarayana, B., and Anand, A. K., "Investigations and Analysis of Flow Phenomena of Secondary Motions in Axial Flow Inducers," Report to NASA, July 1971, 97 pp.

27 Lakshminarayana, B., and Anand, A. K., "Solidity Effects in Axial Flow Inducers," *Proc. Second International J.S.M.E. Conf. on Fluid Machinery and Fluidics*, Tokyo, Sept. 1972, pp. 157–166.

28 Lakshminarayana, B., "Visualization Study of Flow in Axial Flow Inducers," ASME Journal of Basic Engineering, Dec. 1972, pp. 777–787.

29 Lakshminarayana, B., Jabbari, A., and Yamaoka, H., "Turbulent Boundary Layer on a Rotating Helical Blade," *Journal of Fluid Mechanics*, Vol. 51, Part 3, 1972, pp. 545–569.

30 Anand, A. K., Gorton, C. A., Lakshminarayana, B., and Yamaoka, H., "Investigation of Boundary Layer and Turbulence Characteristics Inside the Passages of an Axial Flow Inducer," NASA CR-121248, July 1973, pp. 1–220.

31 Lakshminarayana, B., "Experimental and Analytical Investigation of Flow Through a Rocket Pump Inducer," *Fluid Mechanics, Design, and Acoustics of Turbomachinery*, NASA SP 304, Part II, 1974, pp. 690–731.

32 Lakshminarayana, B., "Three Dimensional Flow in Rocket Pump Inducers, Part 1: Measured Flow Field Inside the Rotating Blade Passage and at the Exit," ASME Journal of Fluids Engineering, Vol. 95, Dec. 1973, pp. 567–578.

33 Poncet, A., and Lakshminarayana, B., "Investigations of Three Dimensional Flow Characteristics in a Three Bladed Rocket Pump inducer," NASA CR-2290, 1973.

34 Gorton, C. A., and Lakshminarayana, B., "Analytical and Experimental Study of the Three-Dimensional Mean Flow and Turbulence Characteristics Inside the Passage of an Axial Flow Inducer," NASA CR 3333, 1980, pp. 1–170.

35 Lakshminarayana, B., and Poncet, A., "A Method of Measuring Three-Dimensional Wakes in Turbomachinery," ASME Journal of Fluids Engineering, Vol. 96, No. 2, June 1974, pp. 87–91 (discussion in Journal of Fluids Engineering, Vol. 97, No. 4, Dec. 1975, pp. 627–628).

36 Gorton, C. A., and Lakshminarayana, B., "A Method of Measuring the Three Dimensional Mean Flow and Turbulence Characteristics Inside a Rotating Turbomachinery Passage," ASME *Journal of Engineering for Power*, Vol. 98, No. 2, Apr. 1976, pp. 137–146.

37 Lakshminarayana, B., and Gorton, C. A., "Three Dimensional Flow Field in Rocket Pump Inducers, Part 2: Three Dimensional Viscid Flow Analysis and Hot Wire Data on Three Dimensional Mean Flow and Turbulence Inside the Rotor Passage," ASME Journal of Fluids Engineering, Vol. 99, No. 1, Mar. 1977, pp. 176–186.

38 Anand, A. K., and Lakshminarayana, B., "Three Dimensional Turbulent Boundary Layer in a Rotating Channel," ASME Journal of Fluids Engineering, Vol. 97, June 1975, pp. 197–210.

39 Anand, A. K., and Lakshminarayana, B., "An Experimental and Theoretical Investigation of Three Dimensional Turbulent Boundary Layer Inside the Passage of a Turbomachinery Rotor," NASA CR 2888, 1977.

40 Anand, A. K., and Lakshminarayana, B., "An Experimental Study of Three Dimensional Boundary Layers and Turbulence Characteristics Inside a Rotating Channel," ASME *Journal of Engineering for Power*, Vol. 100, No. 4, 1978, pp. 676–690.

41 Lakshminarayana, B., "On the Shear Pumping Effect in Rocket Pump Inducers," book chapter in *Pump—Analysis, Design and Application*, Vol. 1, Worthington Pump Inc., 1978, pp. 49–68.

42 Cooper, P., and Bosch, H., "Three Dimensional Analysis of Inducer Fluid Flow," NASA Report CR-54836, TRW ER-6673A, Feb. 1966.

43 Bosch, H. B., Cooper, P., and Stoermer, W. P., "Advanced Inducer Study," TRW ER-5288, May 1963.

44 Horlock, J. H., *Axial Flow Compressors*, Butterworth, Inc., 1958.

45 Wislicenus, G. F., *Fluid Mechanics of Turbomachinery*, Dover, Vol. II, 1965, pp. 646–683.

46 Vavra, M. H., *Aerothermodynamics of Turbomachines*, Wiley, 1960.

47 Huppert, M. C. et al., "Some Cavitation Problems in Rocket Propellant Pumps," unpublished report, Rocketdyne.

48 Mirolyubov, I. V., "Calculations of the Characteristics of Axial Flow Force Pumps," *Aviattsionnaya Teknika*, No. 1, 1959, pp. 81–88 (English translation AFSC, FTD TT 63-418).

49 Dumov, V. I., "Calculation of Pressure Head Characteristics of Axial Helical Impellers," *Taploenergetika*, Vol 11, 1962, pp. 23–27 (English translation AFSC-FTD-TT 63-407).

50 Roelke, R. J., "Analytical Investigation of Three Turbopump Feed Systems Suitable for High Pressure Hydrogen Oxygen Rocket Engine Applications," NASA TN D-2974, Aug. 1965.

51 Rains, D. A., "Head Flow Characteristics of Axial Flow Inducers," *Jet Propulsion*, Aug. 1958, pp. 557–558.

52 Lakshminarayana, B., and Wislicenus, G. F., "Investigations and Analysis of Flow Phenomena in Axial Flow Inducers," Report to NASA, Aug. 1965.

53 Newoj, H. J., "Cavitation Studies in Axial Inducers," Professional Degree Thesis, Calif. Inst. Tech., 1956.

54 Katsanis, T., "Use of Arbitrary Quasi-Orthogonals for Calculating Flow Distribution in the Meridional Plane of a Turbomachine," NASA TN D-2546, 1964.

55 Montgomery, J. C., "Analytical Performance Characteristics and

Outlet Flow Constant and Variable Lead Helical Inducers for Cryogenic Pumps," NASA TN D-583, March 1961.

56 Cooper, P., "Analysis of Single and Two Phase Flows in Turbopump Inducers," ASME *Journal of Engineering for Power*, Vol. 89, 1967.

57 Davis, R. E., Coons, L. L., and Scheer, D. D., "Internal Streamline Flow Analysis for Turbopump Inducers Under Cavitating and Non-Cavitating Conditions," AIAA Paper 70-629, 1970.

58 Cool, L. L., Reddecliff, J., Wemmel, A. E., and Young, W. E., "Study of Inducer Load and Stress," NASA CR 72712, Vol. 1 (1970), Vol. 2 (1972), Vol. 3 (1972).

59 Barten, H. J., Scheurenbrand, J. A., and Scheer, D. D., "Stress and Vibration Analysis of Inducer Blades Using Finite Element Technique," AIAA Paper 70-630, 1970.

60 Giesing, J. P., "Extension of the Douglas-Neumann Program to Problems of Lifting, Infinite Cascades," Douglas Aircraft Division Report LB-31653, July 1964.

61 Lakshminarayana, B., and White, M. T., "Airfoil in a Contracting or Diverging Stream" *J. Aircraft*, Vol. 9, No. 5, May 1972, pp. 354-360.

62 Soltis, R. F., Urasek, D. L., and Miller, M. J., "Overall Performance of a Tandem Bladed Inducer Tested in Water," NASA TN D-5134, May 1969.

63 Moore, R. D., and Meng, P. R., "Comparison of Non Cavitation Performance for 78°, 80.6°, and 84° Helical Inducers Operated in Hydrogen," NASA TN D-6361, May 1971.

64 Oshima, M., "The Effect of Inducer Tip Clearance on Suction Performance," *Bull. JSME*, Vol. 13, No. 58, 1970, pp. 555-581.

65 Mullan, P. J., "An Investigation of Cavitating Inducers for Turbopumps," Gas Turbine Laboratory, M.I.T., Report No. 53, May 1959.

66 Osborn, W. M., "Investigation of a Liquid-Fluorine Inducer and Main-Stage Pump Combination Designed for a Suction Specific Speed of 20.000," NASA TM X-1070, Mar. 1965.

67 Soltis, R. F., Urasek, D. C., and Miller, M. J., "Blade Element Performance of a Tandem-Bladed Inducer Tested in Water," NASA Technical Note D-5562, Nov. 1969.

68 Crouse, J. E., Montgomery, J. C., and Soltis, R. F., "Investigation of the Performance of an Axial Flow Pump Designed by the Blade Element Theory—Design and Overall Performance," NASA TN D-5915, 1961.

69 Lakshminarayana, B., "Techniques for the Measurement of Rotor Flow in Turbomachinery," *Proc. ASME Symposium on Measurement Methods in Rotating Components of Turbomachinery*, Edited by B. Lakshminarayana and P. Runstadler, Jr., 1980 (to be published in ASME *Journal of Engineering for Power*, April 1981).

70 Iura, T., Discussion of reference [6], p. 554.

71 Lakshminarayana, B., "Analytical and Experimental Study of Flow Phenomena in Non-Cavitating Rocket Pump Inducers," NASA CR. 3471, Oct. 1981.

72 Lindley, B. K., and Martinson, A. R., "An Evaluation of a Hubless Inducer and a Full Flow Hydraulic Turbine Driven Inducer Boost Pump," NASA CR 72995, 1971.

73 Jekat, "A New Approach to the Reduction of Pump Cavitation, The Hubless Inducer," ASME *Journal of Basic Engineering*, Vol. 89, 1967, pp. 125-139.

74 King, J. A., "Testing Pumps in Air," ASME *Journal of Engineering for Power*, 1968 (ASME Paper No. 67-WA/FE-4).

Uncited References

Cavitation Performance

Also see references [4-20, 43, 53, 55-58, 63-67, 73] for cavitating aspects of inducers.

75 Stripling, L. B., and Acosta, A. J., "Cavitation in Turbopumps, Part 1," ASME *Journal of Basic Engineering*, Vol. 84, No. 3, Sept. 1962, p. 326.

76 Stripling, L. B., "Cavitation in Turbopumps, Part 2," ASME *Journal of Basic Engineering*, Vol. 84, No. 3, Sept. 1962, p. 329.

77 Jekat, W. K., "Reynolds Number and Incidence-Angle Effects on Inducer Cavitation," ASME Paper 66-WA/FE-31, 1966.

78 Oshima, M., "A Study on Suction Performance of a Centrifugal Pump With an Inducer," *Bulletin, JSME*, Vol. 10, No. 42, 1967, pp. 959-965.

79 Lewis, G. W., and Tysl, E. R., "Cavitation Performance of an 83° Helical Inducer Operated in Liquid Hydrogen," NASA TM X-419, Mar. 1961.

80 Jakobsen, J. K., "On the Mechanism of Head Breakdown in Cavitating Inducers," ASME *Journal of Basic Engineering*, Vol. 86, June 1964, pp. 291-304.

81 Bisell, W. R., Wong, G. S., and Winstead, T. W., "An Analysis of Two Phase Flow in LH_2 Pumps for O_2/H_2 Rocket Engines," AIAA Paper 69-549, 1969.

82 Deeprose, W. M., et al., "Cavitation Noise, Flow Noise, and Erosion," *Proc. Conf. and Cavitation*, Inst. Mech. Engrs. London, 1974.

83 Moore, R. D., and Meng, P. R., "Cavitation Performance of Line Mounted 80.6° Helical Inducer in Hydrogen," NASA TM X-1854, Aug. 1969.

84 Meng, P. R., and Moore, R. D., "Hydrogen Cavitation Performance of 80.6° Helical Inducer with Blunt Leading Edges," NASA TM X-2022, July 1970.

85 Meng, P. R., and Moore, R. D., "Hydrogen Cavitation Performance of 80.6° Helical Inducer Mounted in Line with Stationary Center Body," NASA TM X-1935, Jan. 1970.

86 Kovich, G., "Experimental and Predicted Cavitation Performance of 80.6° Helical Inducer in High Temperature Water," NASA TN D-6809, May 1972.

87 Kovich, G., "Comparison of Predicted and Experimental Cavitation Performance of 84° Helical Inducer in Water and Hydrogen," NASA TN D-7016, Dec. 1970.

88 Ball, C. L., Meng, P. R., and Reid, L., "Cavitation Performance of an 84° Helical Pump Inducer Operated in 37° and 42° R Liquid Hydrogen," NASA TM X-1360, 1967.

89 Moore, R. D., and Meng, P. R., "Thermodynamic Effects of Cavitation of an 80.6° Helical Inducer Operated in Hydrogen," NASA TN D-5614, 1970.

90 Meng, P. R., "Change in Inducer Net Positive Suction Head Requirement with Flow Coefficient in Low Temperture Hydrogen (27.9° to 36.6°R)," NASA TN D-4423, 1968.

91 Meng, P. R., and Moore, R. D., "Cavitation Performance of 80.6° Helical Inducer in Liquid Hydrogen," NASA TM X-1808, 1969.

92 Meng, P. R., and Connelly, R. E., "Investigation of Effects of Simulated Nuclear Radiation on Inducer Performance in Liquid Hydrogen," NASA TM X-1359, 1967.

93 Moore, R. D., and Meng, P. K., "Effect of Blade Loading Edge Thickness on Cavitation Performance of 80.6° Helical Inducer in Hydrogen," NASA TN D-6855, 1970.

94 Sutton, M., "Improving the Cavitation Performance of Centrifugal Pumps with Helical Inducer," Brit. Hydromechanics Res. Assoc., TN 814, 1964.

95 Jacobsen, J. K., "Computer Program to Calculate Cavity on Inducer Blades," NASA Tech. Brief NAR 53852, 1968.

Unsteady Cavitation, Instability and Oscillations

96 Kim, J. H., and Acosta, A. J., "Unsteady Flow in Cavitating Turbopumps," ASME *Journal of Fluids Engineering*, Vol. 97, 1975, pp. 413-418.

97 Rubin, S., "Longitudinal Instability of Liquid Rockets Due to Propulsion Feedback (POGO)," *Journal Spacecraft and Rockets*, Vol. 3, No. 8, 1966, pp. 1188-1195.

98 Sack, L. E., and Nottage, H. B., "System Oscillations Associated with Cavitating Inducers," ASME *Journal of Basic Engineering*, Vol. 87, No. 4, 1965, pp. 917-925.

99 Natanzon, M. S., and Baltsev, N. I., Bazhanov, V. V., and Leyderuarger, M. R., "Experimental Investigation of Cavitation Induced Oscillations in Helical Inducers," *Fluid Mech.—Soviet Research*, Vol. 3, 1974, pp. 38-45.

100 Brennen, C. and Acosta, A. J., "Theoretical Quasi-Static Analysis of Cavitation Compliance in Turbopumps," *Journal Spacecraft and Rockets*, Vol. 10, No. 3, 1973, pp. 175-180.

101 Ghahremani, F. G., and Rubin, S., "Empirical Evaluation of Pump Inlet Compliance," Final Report No. ATR-73 (7257)-1, Aerospace Corp., El Segundo, Calif., July 1972.

102 Kolesnikov, K. S., and Kinelev, V. G., "Mathematical Model of Cavitation Phenomena in Helico Centrifugal Pumps," *Soviet Aeronautics*, Vol. 16, No. 4, 1973, pp. 64-68.

103 Brennen, C. Acosta, A. J., "The Dynamic Transfer Function for a Cavitation Inducer," ASME JOURNAL OF FLUIDS ENGINEERING, Vol. 98, 1976, pp. 182-191.

104 Jackson, E. D., "Summary: Study of Pump Discharge Oscillations," Rocketdyne Report R-6693-1, Oct. 1966.

105 Wong, G. S., MacGregor, C., and Hoshide, R. K., "Suppression of Cavitation and Unstable Flow in Throttled Pumps," *Journal Spacecraft*, Vol. 2, No. 1, Jan.-Feb. 1965, pp. 73-80.

106 Kamijo, K., Shimura, T., and Watanabe, M., "An Experimental Investigation of Cavitating Inducer Instability," ASME Paper 77-WA/FE-44, 1977.

107 Ng, S. L., "Dynamic Response of Cavitating Turbomachines," Ph.D. thesis, Cal. Tech., 1976.

108 Young, W. E., et al., "Study of Cavitating Inducer Instabilities," NASA CR-123939, 1972.

109 Badowski, H. R., "An Explanation for Inducer Instability in Cavitating Inducer," ASME Forum on Cavitation, 1969.

110 Watanabe, T., and Kawata, Y., "Research on the Oscillation in Cavitating Inducer," IAHR, 1979, pp. 265-276.

111 Jackson, E. D., "Study of Pump Discharge Oscillations," (Final Report) NASA CR 80153, 1968.

112 Kamijo, K., Shimura, T., and Watanabe, M., "A Visual Observation of Cavitating Inducer Instability," National Aerospace Laboratory (Japan) Report NAL TR 598T, May 1980.

113 Greitzer, E., "Stability of Pumping Systems," ASME JOURNAL OF FLUIDS ENGINEERING, Vol. 103, No. 2, June 1981.

C. E. Brennen

Professor of Mechanical Engineering.

C. Meissner

E. Y. Lo

G. S. Hoffman

Former Undergraduates.

California Institute of Technology,
Pasadena, Calif. 91125

Scale Effects in the Dynamic Transfer Functions for Cavitating Inducers

Dynamic transfer functions for two cavitating inducers of the same geometry but different size are presented, compared, and discussed. The transfer functions for each inducer indicate similar trends as the cavitation number is decreased. The nondimensional results for the two sizes are compared with themselves and with theoretical calculations based on the Bubbly Flow Model (reference [2]). All three sets of results compare well and lend further credance to the theoretical model. The best values of the two parameters in the model (K and M) are evaluated and recommended for use in applications.

1 Introduction

The purpose of this paper is to present further data on the dynamic transfer functions for cavitating inducers. The earlier experiments of Ng and Brennen [1] presented measured transfer functions for a 7.6 cm diameter model of the low pressure oxidizer turbopump in the Space Shuttle Main Engine (SSME). In a later paper [2] a theoretical model of the unsteady cavitating flow in an inducer was presented which, despite many approximations, yielded transfer functions which exhibited many of the qualitative dynamic characteristics of the experimental measurements. For the purpose of more detailed quantitative rather than qualitative comparison, it was necessary to assume values for two scalar quantities which are crucial to the model. One of these (K in reference [2]) essentially represents the mean compressibility of the bubbly cavitating flow; the other (M in reference [2]) is the factor of proportionality between the fluctuating angle of attack at the inducer inlet and the fluctuating rate of production of cavitating bubbles in the neighborhood of inlet.

This paper presents further experimental measurements of transfer functions specifically for larger, 10.2 cm diameter inducers. A number of inducers were used but presentation here will be confined to the results for a 10.2 cm model of the SSME inducer. Comparison with the results for the geometrically similar 7.6 cm inducer allows some limited evaluation of the effects of scale on the transfer function elements (and on K and M). Furthermore, the more extensive data base and the improvement in the quality of the data permit a more critical examination of the theoretical "bubbly-flow" model and lead to a more definitive recommendation for the empirical constants K and M.

Like the previous experiments, the present results were obtained in the Dynamic Pump Test Facility which has been previously described in reference [1]. For the present experiments an alternative working section was constructed to accommodate 10.2 cm impellers. However, the same volute was used for both impeller sizes. Furthermore, new dynamic instrumentation was added in the form of electromagnetic meters to supplement the earlier measurements of fluctuating flow rate (see Fig. 1). As previously discussed (references [1] and [11]) the measurement of the fluctuating flow rates (2 to 4 percent of the mean flow rate) into and out of the pump are the most critical aspect of these kinds of experiments. As described in reference [11], the modified Foxboro electromagnetic meters (EMM) provided significant improvement in the dynamic data over that obtained with the laser doppler velocimeters (LDV). This was due primarily to the fact that the EM meters provide a true integrated measure of the instantaneous volume flow rate [3] in these unsteady flows. Such a measure is difficult to achieve with the point velocity measurements using the LDV, particularly in the presence of oscillating flow boundary layers. Some details on both the steady calibration of the EM meters and an in-line comparison of the dynamic performance of the EMM and LDV are included in reference [11].

2 Steady State Inducer Pump Performance

The difference in performance between the two geometrically similar inducers was investigated and found to be caused by differences in the efficiency of pressure recovery in the volute. The latter was not scaled up but merely modified at inlet to accommodate the 10.2 cm impellers. The resulting difference in the slope of the performance curves at a flow coefficient, $\phi = 0.07$ (for which dynamic transfer matrices were obtained) causes some difference in the "resistance" component (real part of Z_{12}) of the transfer matrices for the two impellers; further discussion on this is delayed until Section 5.

The cavitation performance of the 10.2 cm impeller is presented in Fig. 3. Comparison of this data with the

Contributed by the Fluids Engineering Division for publication in the JOURNAL OF FLUIDS ENGINEERING. Manuscript received by the Fluid Engineering Division, September 26, 1979.

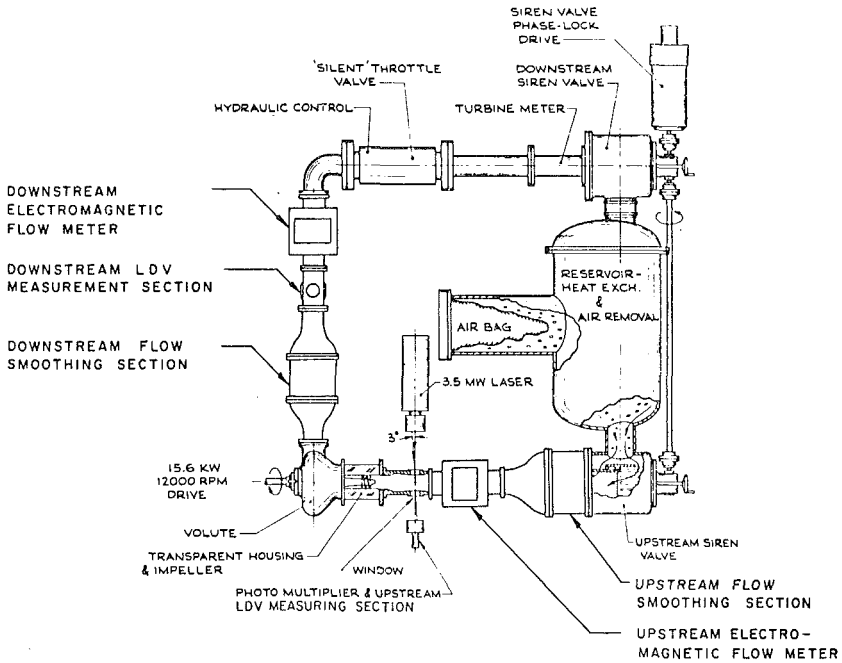

Fig. 1 Schematic plan view of the modified Dynamic Pump Test Facility

cavitation performance of the 7.6 cm impeller (see Fig. 4 of reference [1]) indicates that the curves are merely displaced vertically due to the differences in pressure recovery in the volute and that the essential nature of the cavitation effect is unchanged. Also shown in Fig. 3 are the mean flow conditions at which dynamic transfer matrices were obtained; these are identified by letters which will be used for identification in later figures.

Both steady state performance data and dynamic transfer functions were also obtained with various prerotation inhibiting devices installed several diameters upstream of the inducers. The effects of these devices are reported briefly in reference [11].

3 Dynamic Transfer Matrices

The dynamic transfer matrices reported here use the definition described previously ([1], [2])

$$\begin{Bmatrix} \tilde{h}_2 - \tilde{h}_1 \\ \tilde{m}_2 - \tilde{m}_1 \end{Bmatrix} = \begin{Bmatrix} ZP_{11} & ZP_{12} \\ ZP_{21} & ZP_{22} \end{Bmatrix} \begin{Bmatrix} \tilde{h}_1 \\ \tilde{m}_1 \end{Bmatrix}$$

where $\tilde{h}$, $\tilde{m}$ are nondimensional fluctuating total pressure and mass flow rate quantities which are complex in general. Subscripts 1 and 2 refer to inlet and discharge quantities. The transfer matrix $[ZP]$ is a complex function of the mean flow conditions (ϕ, σ) and the reduced frequency, ω.

The experimental and data reduction methods used to obtain $[ZP]$ matrices between the inducer inlet and the volute discharge were similar to those described by Ng and Brennen [1]. However, two differences should be noted. First, the addition of the electromagnetic flow meters allowed separate evaluation of transfer matrices using the simultaneous measurements from either the EM meters or the laser doppler velocimeters. Second, in order to accommodate the discharge EM meter, the downstream smoothing section between the volute discharge and the downstream LDV was considerably shortened and strengthened. This significantly reduced the corrections which were originally used by Ng and Brennen [1] to obtain the pump transfer matrix, $[ZP]$, from the overall measured $[Z]$ matrix. Furthermore, all the corrections described in that previous paper are smaller in relative magnitude for the 10.2 cm impellers than for the 7.6 cm impellers. The net result is a substantial improvement in accuracy over the transfer functions previously presented for the 7.6 cm impellers.

The presentation of the transfer functions is similar to that employed previously. The real and imaginary parts of the elements of $[ZP]$ are plotted as solid and dashed lines, respectively, in graphs against reduced frequency, ω. All of the transfer functions presented here for the 10.2 cm impeller

Nomenclature

a_{NIJ} = coefficients in the polynomial fits to the transfer matrices
A_i = inducer inlet area
F = blade passage frictional resistance parameter
h = inducer blade tip spacing
$\tilde{h}$ = nondimensional fluctuating total pressure, $\tilde{h}^*/1/2\rho U_T^2$
$\tilde{h}^*$ = fluctuating total pressure
I, J = dummy subscripts equal to 1 or 2
j = imaginary unit
K = parameter of bubbly flow model
M = parameter of bubbly flow model
$\tilde{m}$ = nondimensional fluctuating mass flow rate, $\tilde{m}^*/\rho U_T A_i$
$\tilde{m}^*$ = fluctuating mass flow rate
N = integer power and subscript
U_A = mean axial velocity at inducer inlet
U_T = inducer tip speed
ZP_{IJ} = inducer pump transfer matrix
γ = blade angle at inducer inlet tip
ϵ = fractional length of blade passage containing bubbly mixture
ϕ = flow coefficient, U_A/U_T
ψ = head coefficient, total pressure rise $\div \rho U_T^2$
ρ = water density
σ = cavitation number, inlet pressure minus vapor pressure $\div 1/2\,\rho U_T^2$
τ = ratio of inducer axial length to blade tip spacing
Ω = radian frequency of perturbations
ω = reduced frequency $\Omega h/U_T$

Subscripts 1 and 2 on $\tilde{h}$ and $\tilde{m}$ refer to the inlet and discharge quantities.

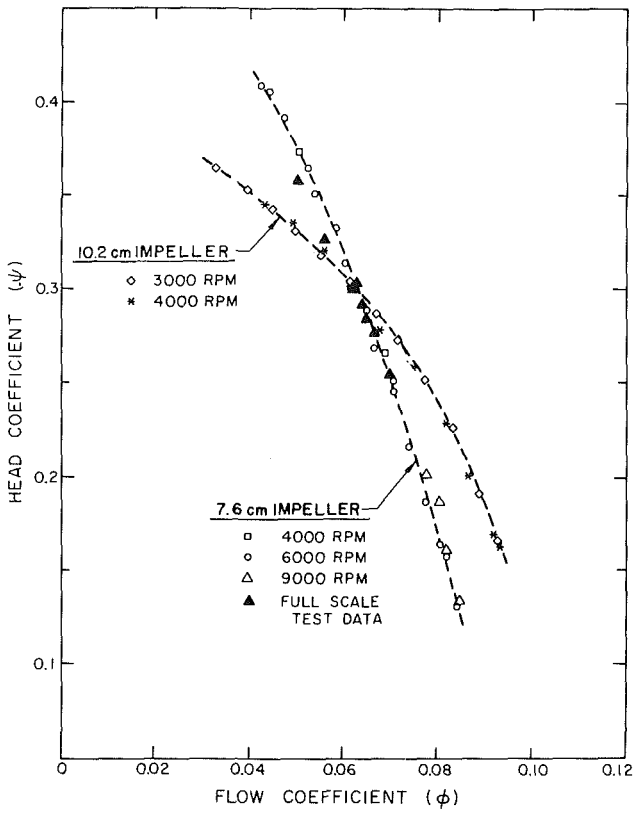

Fig. 2 Noncavitating performance of the 7.6 cm and 10.2 cm diameter models of the low pressure oxidizer inducer pump in the SSME at various rotating speeds. Also shown are some full scale data [4]. Uncertainties are about ±0.002 on the ordinate and ±0.001 on the abscissa.

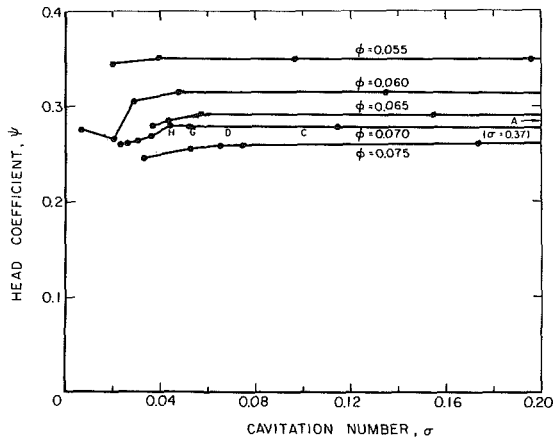

Fig. 3 Cavitation performance at the 10.2 cm diameter model at various flow coefficients taken with a uniform honeycomb in the inlet flow. The points at which transfer functions were obtained are indicated by the letters, A, C, D, G, and H. Uncertainties are about ±0.002 on the ordinate and abscissa.

were obtained from the EMM flow rate measurements, though simultaneous LDV transfer functions were also obtained in all cases. As discussed previously, the EMM transfer functions were believed to be superior; one comparison of EMM and LDV transfer functions is included in reference [11].

4 Comparison of the Transfer Matrices for the Two Sizes of Impeller

Figure 4 presents the measured transfer functions for the 10.2 cm impeller at $\phi = 0.07$ and various cavitation numbers. The latter range from $\sigma = 0.37$ for the point A at which there

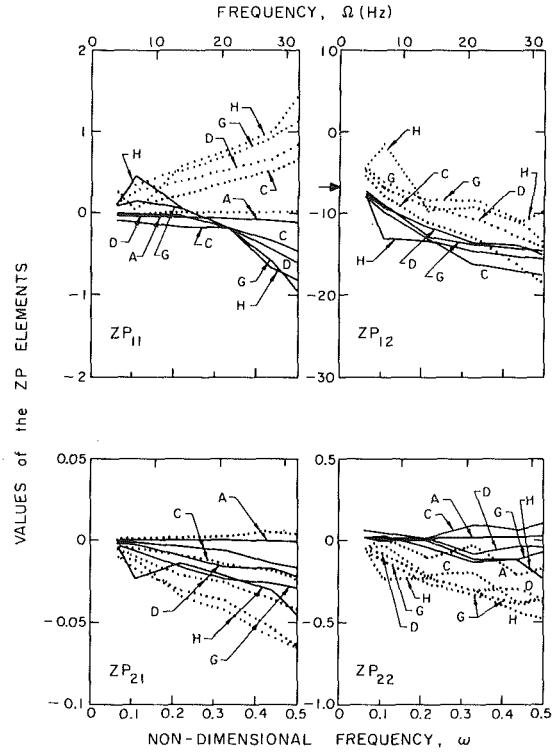

Fig. 4 Transfer matrices for the 10.2 cm impeller at $\phi = 0.07$, a rotating speed of 6000 rpm and various cavitation numbers as follows: (A) 0.37, (C) 0.10, (D) 0.069, (G) 0.052, and (H) 0.044. The real and imaginary parts are denoted by the solid and dashed lines, respectively. The quasistatic resistance from the slope in Fig. 2 is indicated by the arrow.

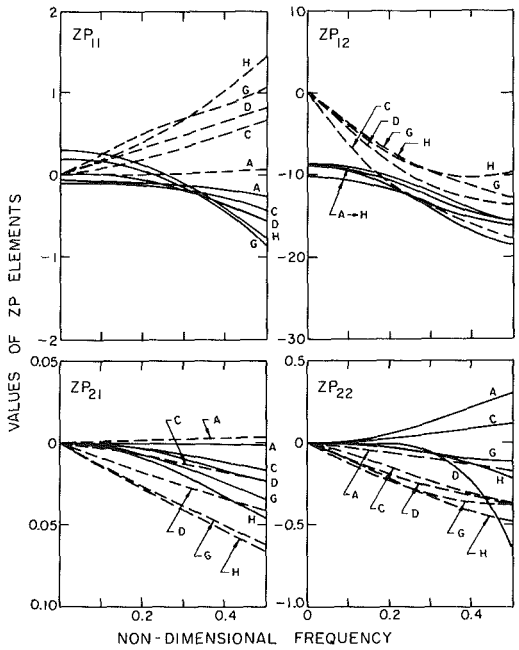

Fig. 5 Polynomial curve fits to the 10.2 cm impeller transfer matrices of Fig. 4

was little cavitation, down to $\sigma = 0.045$ for the pont H at which there was extensive cavitation and the impeller was on the verge of breakdown. For purposes of clarification and comparison with similar graph for the 7.6 cm impellers (Brennen [2]), polynomial fits were made to these data of the form

$$ZP_{IJ} = \sum_{N=0}^{N_{IJ}} a_{NIJ} (j\omega)^N \qquad (1)$$

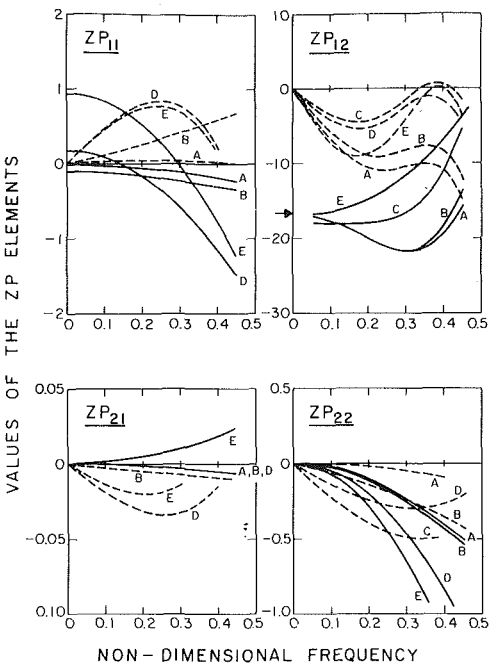

Fig. 6 Polynomial curve fits to the 7.6 cm impeller transfer matrices obtained at ϕ = 0.07 and a rotating speed of 9000 rpm by Ng and Brennen [1]. The cavitation numbers are (A) 0.51, (B) 0.11, (C) 0.046, (D) 0.040, and (E) 0.023. The quasistatic resistance from the slope in Fig. 2 is indicated by the arrow. (Reproduced from reference [2]).

where $N_{11} = N_{21} = N_{22} = 3$, $N_{12} = 5$, and a_{021} and a_{022} were set to zero in order to satisfy quasistatic continuity of mass [9]. Some of the resulting smoothed transfer functions are presented in Fig. 5. The comparable figure for the 7.6 cm impellers was included in reference [2] and is reproduced here as Fig. 6. In that figure the letters do not refer to the points in Fig. 3, but to those in Fig. 4 of reference [1].

The trends with cavitation number which were discussed in references [1] and [2] are similar for the two impellers. It is quite clear that in both cases a quasistatic model would only be appropriate for reduced frequencies less than about 0.1. Though a more detailed comparison will be included as part of the correlation with theory in Section 7, the following comments should be made on each of the ZP elements. Beginning with the impedance, ZP_{12}, it is clear from Figs. 5 and 6 that the trend of the resistance (or negative of the real part of ZP_{12}) correlates fairly well in both cases with the quasistatic resistance which can be obtained from the slope of the performance curves in Fig. 2. However these initial values differ in the two cases, not because of scale, but due to differences in pressure recovery in the volute as discussed in Section 2. Furthermore, it is apparent that under non-cavitating conditions the resistance in the 10.2 cm impeller increases more dramatically with frequency than in the 7.6 cm impeller. The reason for this is not clear but it may be a property of the flow at discharge and in the volute rather than a property of the inducer itself. Incrementally, cavitation causes a decrease in the resistance at higher frequencies although this is more marked with the 7.6 cm impeller. The inertial component of the impedance (negative of the imaginary part of ZP_{12}) is larger for the larger impeller. Cavitation causes incremental decreases in this component at higher frequencies which are similar for the two impellers.

Turning to the other three components, it should be stressed that in theory all of them should be zero for a completely rigid system, an incompressible fluid, and no cavitation. Apart from some unexplained discrepancies in ZP_{22}, this appears to be the case for both impellers. For example, nonzero values for ZP_{11} and ZP_{21} can be attributed entirely to the presence of cavitation. The comparison of Figs. 5 and 6 indicates good

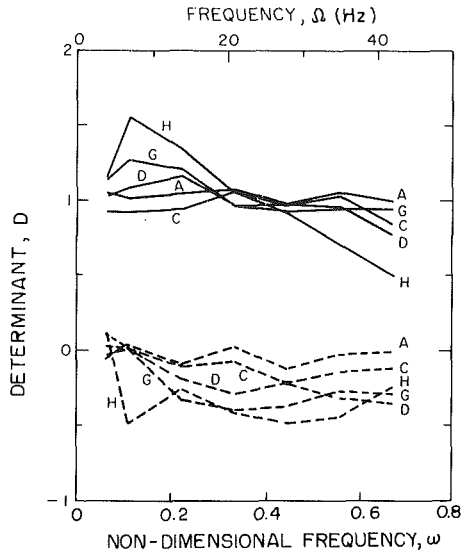

Fig. 7 The determinant, D, for the transfer matrices of Fig. 4. Real and imaginary parts are represented by the solid and dashed lines, respectively.

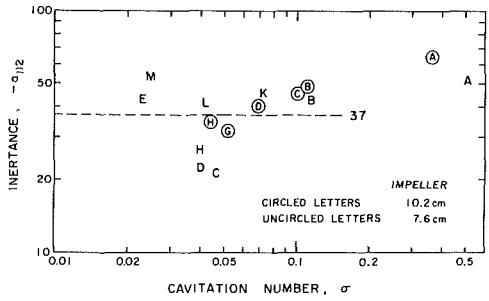

Fig. 8 Comparison of the low frequency inertances, $-a_{112}$, for the two impellers and equaton (9)

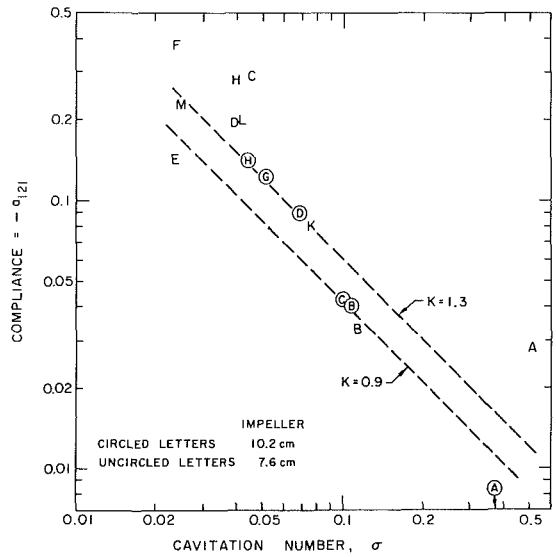

Fig. 9 Comparison of the low frequency compliances, $-a_{121}$, for the two impellers and equation (10) with K = 1.3 and 0.9

agreement between the two impellers insofar as the pressure gain term (ZP_{11}) and its variation with cavitation number are concerned. The imaginary part of ZP_{21} which is generally termed the compliance increases with σ in the expected manner in both cases. However, the larger impeller yielded negative real parts for ZP_{21} which did not occur for the smaller impeller. Finally, the general character of the incremental changes with cavitation number in the mass flow gain term (ZP_{22}) are similar in both cases.

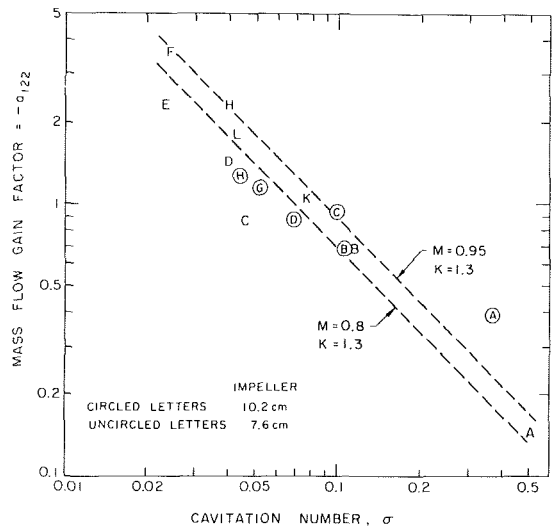

Fig. 10 Comparison of the low frequency mass flow gain factors, $-a_{122}$, for the two impellers and equation (11) with $K = 1.3, M = 0.8$, and 0.95

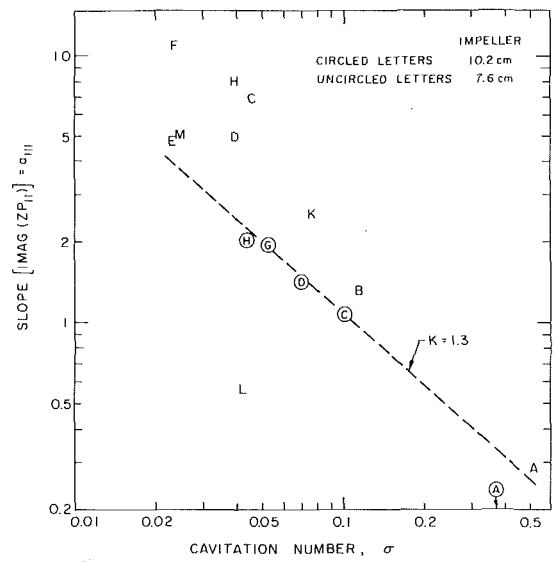

Fig. 11 Comparison of the low frequency slope of the imaginary part of ZP_{11}, (a_{111}) for the two impellers and equation (7) with $K = 1.3, F = 0$

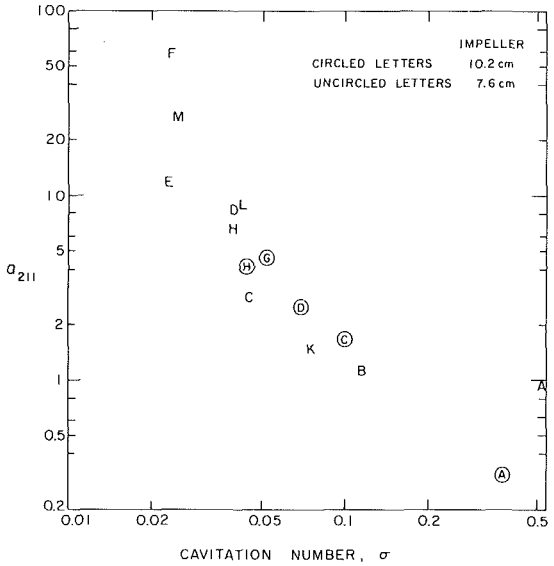

Fig. 12 Comparison of the terms of order $(j\omega)^2$ in ZP_{11}, (a_{211}) for the two impellers

The significance of the determinant, D, of $[ZP] + [I]$ has been discussed previously ([1], [2], [6]); the deviation from a value of unity presents some measure of the extent to which the dynamics of the pump have become potentially active. The determinants of the 10.2 cm impeller transfer matrices of Fig. 4 are plotted in Fig. 7. This exhibits the same features discussed previously for the 7.2 cm impeller [1]. Without cavitation the determinant is indeed unity; increasing the amount of cavitation results in progressive departure from passive dynamics. It has recently been demonstrated that serious system instabilities can result from this trend of increasingly active dynamics at lower cavitation numbers [6].

All of the above results were obtained close to the design flow coefficient, $\phi = 0.07$ and at an ambient temperature of 21°C. Some transfer functions were obtained at other flow coefficients (up to 0.076) and temperatures (up to 74°C) to investigate both off-design and thermodynamic effects. Only minor variations in the transfer functions were observed.

5 Comparison with the Bubbly Flow Model

The bubbly flow model yields theoretical transfer matrices given by equations (35) through (38) of reference [2]. They are functions of geometrical parameters, the flow coefficient, a blade-passage friction parameter, the mean length of the cavitating region (a surrogate cavitation number parameter) and, of course, the reduced frequency, ω. In addition, it is necessary to assume values for the two parameters K and M described in the Introduction. The purpose of this section will be to compare the model with experimental results described above. To begin with, however, it is instructive to confine attention to a comparison at the lower frequencies. The complicated expressions for the theoretical transfer matrices reduce at low frequencies to the following approximate relations:

$$ZP_{11} \simeq K\phi F\epsilon + j\omega K\tau\epsilon\{\cot\gamma + (1-\epsilon/2)F + \phi/\sin^2\gamma\} \quad (2)$$

$$ZP_{12} \simeq -2j\omega\tau/\sin^2\gamma - 2\cot\gamma - 2F \quad (3)$$

$$ZP_{21} \simeq -j\omega\epsilon\tau K/2 \quad (4)$$

$$ZP_{22} \simeq -j\omega\epsilon\tau\{M/\phi - K\phi/\sin^2\gamma\} \quad (5)$$

These expressions include only the terms of order $(j\omega)^0$ and $(j\omega)^1$ resulting from an expansion for small ω (the third order terms are long and involved and will not be repeated here). Correlation with the polynomial form (1) used to fit the data yields the following relations which must presumably hold if the model has value:

$$a_{011} = K\phi F\epsilon \quad (6)$$

$$a_{111} = K\tau\epsilon\{\cot\gamma + (1-\epsilon/2)F + \phi/\sin^2\gamma\} \quad (7)$$

$$a_{012} = -2\cot\gamma - 2F \quad (8)$$

$$a_{112} = -2\tau/\sin^2\gamma \quad (9)$$

$$a_{121} = K\tau\epsilon/2 \quad (10)$$

$$a_{122} = -\tau\epsilon\{M/\phi - K\phi/\sin^2\gamma\} \quad (11)$$

With these expressions, a three-way comparison will be made between the values for the a_{NIJ} coefficients derived from the experiments on 7.6 cm and 10.2 cm impellers and the values calculated from the expressions (7)–(11). For this purpose note that the impellers have a blade angle at the tip of $\gamma = 9°$ and a geometric value of τ of 0.45.

The simplest component to start with is the inertance, $-a_{112}$, which is plotted against cavitation number in Fig. 8. From equation (9) the theoretical first order term with $\tau = 0.45$ yields a value of 37. It can be seen from the experimental data that the actual inertance first decreases somewhat as the cavitation number is lowered and then increases at lower

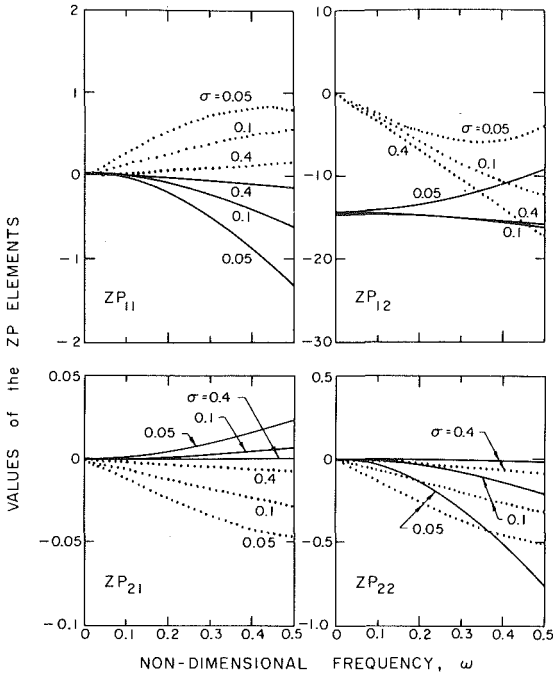

Fig. 13 Transfer functions calculated from the complete bubbly flow model with $\phi = 0.07$, $\gamma = 9$ deg, $\tau = 0.45$, $F = 1.0$, $K = 1.3$, and $M = 0.8$. Various cavitation numbers according to $\epsilon = 0.02/\sigma$ are shown.

cavitation numbers. Although the first order term in the theory is a simple constant, the complete expressions indicate similar theoretical trends with cavitation number (see reference [2] and Fig. 13). Note that the two impellers yield similar results. However, the value of 37 is probably low due to the neglect of the fact that the cross-sectional area of the flow is decreasing through the impeller as the hub radius increases; this would yield higher values for the inertance or a higher equivalent value of τ of about 0.6.

The observed experimental relation [2] between σ and $\epsilon = 0.02/\sigma$, permits comparison of the compliance, $-a_{121}$, and mass flow gain factor, $-a_{122}$, which are presented in Figs. 9 and 10. Both figures indicate consistency between the two sets of experimental results even though the older data for the 7.6 cm impeller is more scattered. They are also consistent with the trend exhibited by the theoretical expressions (10) and (11); it would appear that K and M values of about 1.3 and 0.8, respectively, best fit the data.

The slope of the imaginary part of ZP_{11}, (a_{111}) is presented in Fig. 11; the term involving F in the relation (7) has been omitted for this purpose and, not unexpectedly, the resulting theoretical line in Fig. 11 is on the lower side of the experiments. The magnitude of the zeroth order real part of ZP_{11}, (a_{011}) is small, positive, and increases with decreasing σ in both theory and experiment. In practice, however, the real part of ZP_{11} is dominated by terms of order $(j\omega)^2$ and higher as can be seen in Figs. 5 and 6. It is therefore more useful to present plots of the experimental values of a_{211} as has been done in Fig. 12. Here again the results of the experiments for the two impellers are similar.

Finally, the complete bubbly flow model has been used with $\gamma = 9$ deg, $\tau = 0.45$, $\phi = 0.07$, $F = 1$, $K = 1.3$, and $M = 0.8$, to produce the complete transfer function depicted in Fig. 13 for purposes of direct comparison with Figs. 5 and 6.

The value of F is unimportant and could just as well be set equal to zero; resulting changes in the transfer matrices are minor, the most obvious being an increase in the $\omega \to 0$ intercept of $\mathrm{Re}(ZP_{11})$ as F is increased.

Comparison with Figs. 5 and 6 reveals quite similar qualitative trends in virtually all of the elements of the transfer matrices. The most notable exception is the $\mathrm{Re}(ZP_{21})$; this component, however, is usually rather unimportant in determining the stability of a hydraulic system (reference [6]).

6 Conclusions

Dynamic transfer functions for two geometrically similar impellers, 7.6 and 10.2 cm, have been obtained compared, and analyzed. Within the data scatter there is little evidence of any effect of size or speed apart from that implicit in the nondimensionalization of total pressures, mass flow rate, and frequencies. The quality of the 10.2 cm impeller data is better than the previous data for the 7.6 cm impeller because of improved flow rate measurements using the EM meters.

The data for both impellers has also been compared with the predictions of the bubbly flow model (reference [2]). This comparison documents values of 1.3 and 0.8 for the two unknown constants (K and M) implicit in the model. It then appears that the bubbly flow model has considerable merit and yields theoretical transfer matrices within the experimental uncertainty.

Acknowledgments

The authors are grateful for the help of A. J. Acosta, D. Braisted, G. Hendrikson, and C. Park. The support of the NASA George Marshall Space Flight Center, Huntsville, Alabama, under Contract No. NAS 8-29313 and the National Science Foundation under Grant Eng. 76-11225 is also gratefully acknowledged.

Statement of Uncertainties Not Given in Figure Captions

Uncertainties in the measured transfer functions presented in Fig. 4 were evaluated using methods described in reference [1]. Ordinate error bars based on both (i) the influence of individual measurement scatter, and (ii) the influence of individual excitation modes on the resulting transfer functions, were evaluated for each point plotted in the figure. The results were similar to those presented in reference [1]. The uncertainty in the polynomial fitted transfer functions of Figs. 5 and 6 is evident from the comparison with data from which they were derived. The possible scatter in Fig. 7 is a direct result of the possible error in Fig. 4, and is $\pm$ 0.05 at most. The ordinate scatter in Figs. 8, 9, 10, 11, and 12 is self evident.

References

1 Ng, S. L., and Brennen, C., "Experiments on the Dynamic Behavior of Cavitating Pumps," ASME JOURNAL OF FLUIDS ENGINEERING, Vol. 100, 1978, pp. 166–176.

2 Brennen, C., "Bubbly Flow Model for the Dynamic Characteristics of Cavitating Pumps," *Journal of Fluid Mechanics*, Vol. 89, Part 2, 1978, pp. 223–240.

3 Shercliff, J. A., *The Theory of Electromagnetic Flow Measurement*, Cambridge University Press, 1962.

4 Rocketdyne Report, "Test Results of SSME Low Pressure Oxidizer Turbopump Model Inducer," Internal Letter No. R/H 4194-3074, 1974.

5 Brennen, C., "On Noncavitating Axial Inducer Performance," A brief unpublished note, 1977.

6 Braisted, D., "Cavitation Induced Instabilities Associated with Turbomachines," Ph.D. thesis, California Institute of Technology, Pasadena, Calif., 1979.

7 Ghahremani, F. G., "Turbopump Cavitation Compliance," Report No. TOR-0059 (6531-01)-2, Aerospace Corp., El Segundo, Calif., 1970.

8 Vaage, R. D., Fidler, L. E., and Zehnle, R. A., "Investigaton of Characteristics of Feed System Instabilities," Final Report MCR-72-107, Martin Marietta Corp., Denver, Col., 1972.

9 Brennen, C. and Acosta, A. J., "The Dynamic Transfer Function for a Cavitating Inducer," ASME JOURNAL OF FLUIDS ENGINEERING, Vol. 98, 1976, pp. 182–191.

10 Brennen, C., "The Dynamic Behavior and Compliance of a Stream of Cavitating Bubbles," ASME JOURNAL OF FLUIDS ENGINEERING, Vol. 95, 1973, pp. 553–542.

11 Brennen, C. E., Meissner, C., Lo, E. Y., and Hoffman, G. S., "Scale Effects in the Dynamic Transfer Functions for Cavitating Inducers," ASME Paper 80-WA/HT-51, Nov. 1980.

New Method for Monitoring and Correlating Cavitation Noise to Erosion Capability

M. K. De[1]
Nuclear Engineering Department.

F. G. Hammitt
Mechanical Engineering and
Applied Mechanics Department.

University of Michigan,
Ann Arbor, Mich. 48109

For the purpose of obtaining a correlation between cavitation noise and damage, the source of damage, and its variance with flow parameters, was investigated. The individual cavitation pressure pulses were monitored by measuring the peak pulse amplitudes in a cavitating venturi. A pressure-bar probe and an acquisition system has been designed, constructed and used along with a commercial Kistler 601A probe for this purpose. The acoustic power derived from the pulse height spectra (PHS) was found to vary with the nth power of venturi throat velocity, where 6.8 < n < 10.5. The major component in this variation was the number of bubbles collapsing. This is a key factor in cavitation noise intensity variation, in this and other cavitating geometries. The acoustic power has been found to correlate linearly, with a small threshold, with the cavitation damage rate (MDPR) of 1100-0 aluminum. The feasibility of using cavitation erosion efficiency (ratio between erosion power and acoustic power) in predicting eventual cavitaion erosion rates in various geometries has been investigated.

I Introduction

In present state of art it is difficult or impossible to predict the conditions in fluid machinery for which cavitation damage will occur, or the eventual rate of such damage. Thus it is desirable to have an easily measurable quantity which will indicate the damaging capability of a given flow regime. Cavitation bubble collapse emits high intensity shock waves and/or liquid microjets. A measure of these pulses should enable one to predict damage [1–3, e.g.].

Due to geometrical difficulties and lack of sophisticated instrumentation, none of the previous studies [1-3 e.g.] have measured the physical quantity derived from the amplitudes of the individual acoustic waves emitted by single bubble collapses and rebounds in a flowing system as in the present study. Some have measured the mean intensity (root mean square pressure) as a function of frequency with a spectrum analyzer. Lush and Hutton [1] found the pitting rate and mean intensity to vary as V^4 in a venturi. Ramamurthy and Bhaskaran [3] found a linear relationship between the mean intensity at 8.0 KHz and damage measured as weight loss. The use of acoustic intensity alone prevents identifying the key factors of this complex process. Pulse amplitude and rate, are important quantities varying with flow parameters, as here shown.

II Experimental Apparatus and Instrumentation

The present work studies the acoustic waves emitted by single bubble collapses and/or rebounds. Bubbles, incepted at the throat, collapse in the diffuser of a plexiglass venturi, part of the U-M high-speed water tunnel facility [4].

Figure 1 is a schematic of the plexiglass venturi. Damage specimens and transducers are mounted flush to the wall of the venturi in the same axial plane. The venturi throat velocity and the axial extent of the cavitation cloud is controlled by pump speed and downstream pressure. The cavitation cloud is composed of travelling bubbles which randomly nucleate in the liquid from microbubbles.

A commercial probe (Kistler 601A), and a pressure-bar probe developed by the authors were used to record acoustic wave amplitudes. Criteria for the pressure-bar were minimum overshoot, rise-time, and sensitive head area. The Kistler 601A was used to acquire the bubble collapse pulse height spectra (PHS) for this study, because of the relative fragility

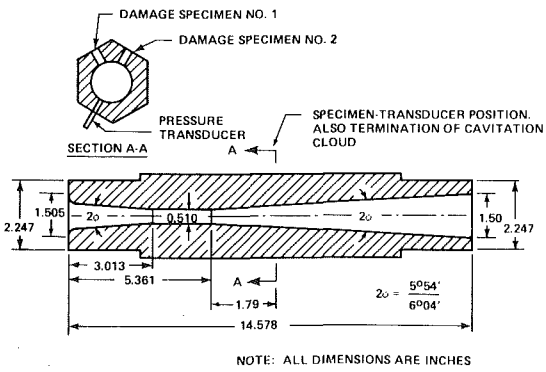

Fig. 1 Venturi flow path

[1] Presently at Westinghouse Electric Corp., Nuclear Energy Systems, Pittsburgh, Pa.

Contributed by the Fluids Engineering Division for publication in the JOURNAL OF FLUIDS ENGINEERING. Manuscript received by the Fluids Engineering Division, June 4, 1981.

of the pressure-bar design. The pressure-bar probe was used for comparisons with the Kistler to yield more realistic peak amplitudes of the pressure waves. The detailed design and results of the pressure-bar probe study may be found in reference [5].

A microprocessor-based data acquisition system was designed and constructed to record and process pulse amplitudes to a pulse height spectrum, PHS. This allows measurement of absolute PHS in real time, data which is physically and statistically meaningful.

Figure 2 is a block diagram of the data acquisition system. The Kistler probe signal is first amplified in a charge amplifier. The cavitation pulses are in general much larger than background flow noise, which has frequency components up to ~ 10 KHz. A multifunction filter in high-pass mode attenuates the flow noise when venturi flow parameters produce a reduced cavitation noise compared to general flow noise.

The pulse amplitude is detected by a peak detector designed here. It is digitized by an analog-to-digital converter with timing logic signals generated by a programmable clock and timing circuitry. The original signal may also be digitized directly. The pulse amplitudes are processed to PHS during acquisition with a suitable microprocessor. The data is then stored on a floppy-disk system, and can also be displayed on an oscilloscope or copied on a hard copy terminal. The details of the circuits designed here, system logic and software are found elsewhere [5, 9].

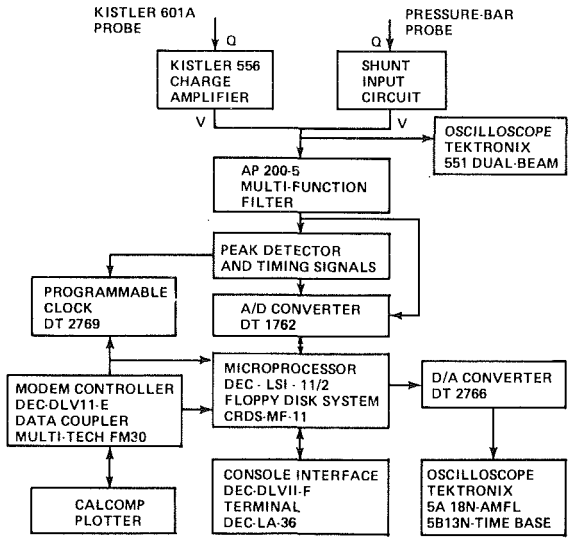

Fig. 2 Components block diagram

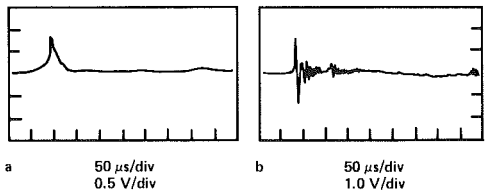

Fig. 3 Responses of Kistler (601-A) probe to cavitation bubbles in venturi

III Experimental Observations

A. Cavitation Pressure Pulses. Figure 3 shows responses of the Kistler probe to bubble collapses and/or rebounds in the venturi. The rise-times of the pulses no doubt depend on their origin and intensity. They range (Fig. 3) from 3 μs to 10 μs. Presumably, large amplitude shock fronts would steepen at a faster rate. The slower rise (10 μs) in Fig. 3 may be due to a liquid jet impact as observed by Kling [6] in a similar venturi, rather than shock waves. The Kistler probe responds accurately to waves with rise-times greater than 3 μs as is seen in Fig. 3, but oscillates at its fundamental longitudinal mode (~ 130 KHz) for pulses with rise-time < 3 μs, as is seen in Fig. 3(b). The second pulse in Fig. 3(b) 80 μs after the first, may be due to a rebound of the same bubble.

Reflected waves from the opposite wall would arrive ~ 30 μs after the initial, and would be attenuated in the water by a factor R_0/R. R_0 is the maximum bubble radius, i.e., ~ 1.5 mm [7]. The reflection coefficient of water to plexiglass is 0.2. Thus reflected wave amplitude will be only ~ 1 percent of the original wave amplitude.

Figure 3 shows typical pulse traces, indicating that they are generally discrete in time. An a-d converter was used to digitize the original wave form to study pressure pulses over a longer period (250 ms, limited by available memory). Since the sampling rate was limited to 70 KHz, a low-pass filter set at 50 KHz was used to attenuate the 130 KHz resonant frequency of the transducer, resulting in the attenuation of the

Nomenclature

a = amplitude of pressure pulse
a_c = cutoff amplitude
A/D = analog to digital converter
BHN = Brinell hardness number
C = sonic velocity
CL = cavitation length
Calcomp = California computation
c_p/c_v = specific heat ratio
CRDS = Charles River Data System
D/A = digital to analog converter
DEC = Digital Equipment Corporation
DT = Data Translation
E = energy per unit area of the acoustic wave
E = elastic modulus
f = bubble surface oscillation frequency
MDPR = mean depth penetration rate-volume loss rate per exposed area
MTS = Michigan Terminal System
N = number of pressure pulses
n = velocity exponent
P_D = downstream pressure
P_v = vapor pressure
PHS = pulse height spectrum
PSD = power spectral density
R = radius of bubble
R_i = radius of microbubble
R_0 = radius of bubble prior to collapse
RT-11 = Digital Equipment Corporation real time operating system for the PDP-11
s = decay constant for PHS
T_s = sampling period for PHS
T = temperature
t = time
UR = ultimate resilience = $UTS^2/2E$
UTS = ultimate tensile strength
V_t = space time mean velocity of liquid in axial direction in venturi throat
σ = liquid surface tension
ρ = liquid density
σ_c = cavitation number $= \dfrac{P_D - P_v}{\rho V_t^2/2g}$

peak pressures of the cavitation pulses by 24db/octave from the cut-off point (50 KHz). Figure 4 shows a typical segment of the data, running from 0 to 4.2 ms, showing that pulse amplitudes are indeed much larger than background flow noise. Figure 4 also shows that the pulses are in fact discrete. The repeated signal at about 10 KHz confirms that some of the bubbles do oscillate. This phenomenon has been photographically observed here in similar venturis. The oscillation frequencies (5.0 to 20.0 KHz, Figs. 3(*b*) and 4) correspond to the natural frequencies of bubbles here observed [6, 7]. These ranged in diameter from 0.25 to 1.3 mm. The resonant frequency of a bubble in an infinite medium can be calculated [8] using the following expression,

$$f = \frac{1}{2\pi R}\left[\frac{3Cp/C_v\,(P_L + 2\sigma/R)^{1/2}}{\rho}\right]$$

where C_p/C_v = specific heat ratio
R = radius of bubble

Neglecting surface tension, this expression results in resonant frequencies of 4.7 KHz and 23.6 KHz for air bubbles in water at 1 bar, and the above size.

Further work is planned to obtain better statistics concerning collapse, rebound, oscillation, liquid jet impact, the spatial origin of the bubbles, and correspondence between the measured acoustic energy and the calculated potential energy for the collapsing bubbles. This could be achieved using two transducers at 180 deg separation. Another useful, but difficult measurement, would be pressure pulse rise-time spectrum, i.e., the relation between the risetimes and the number of the pressure pulses which is believed to be a major factor in cavitation erosion.

B. Venturi Pulse Height Spectra. Measured spectra are discussed next. Unless otherwise stated, all were acquired with water at 80°F (26°C) and containing 0.8 percent volume of air (47 percent of saturation at STP). The cavitation cloud, determined visually, ended at the axial probe position (Fig. 1). Figure 5 is a typical spectrum. Repetitive measurements at the same flow conditions yielded similar spectra (magnitude and shape). The vertical lines drawn in Fig. 5 indicate the variation in the threshold setting used to discriminate against background flow noise. Figure 6 shows pulse height spectra taken at flow conditions with varying throat velocity.

An attempt was made [9] to derive the pulse height spectrum shape that should be observed by a probe flush with the venturi wall at the bubble collapse axial position. A brief outline illustrates the overall complexity of the problem.

Due to pressure reduction at the venturi throat, randomly distributed gas and/or vapor "nuclei" of various sizes become unstable. They then grow to various maximum sizes, and collapse in the diffuser section, emitting pressure pulses of differing amplitudes. The nuclei radius probability density function, $W(R_i)$ has been calculated [10] and experimentally verified here [11] and elsewhere [12] to be approximately,

$$\begin{aligned} W(R_i) &= A\,R_i^{-3} \\ A\int_{R_{\min}}^{R_{\max}} R_i^{-3} &= 1 \end{aligned} \qquad (1)$$

The pressure in the venturi is assumed to be deterministic and steady even though it is in reality stochastic due to the turbulent nature of the flow. The microbubble "nucleus" growth can be calculated, using the well-known Rayleigh equation [13], i.e.,

$$\frac{-Rd^2R}{dt^2} - \frac{3}{2}\left(\frac{dR}{dt}\right)^2 = \frac{P_L(t) - P_B(t)}{\rho} \qquad (2)$$

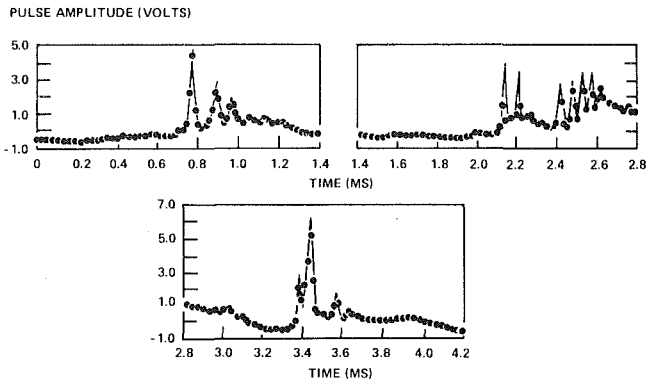

Fig. 4 Typical digitized cavitation pressure pulses, Kistler 601A probe, V_t = 47.0 m/s, CL = up to probe = 9.8 cm

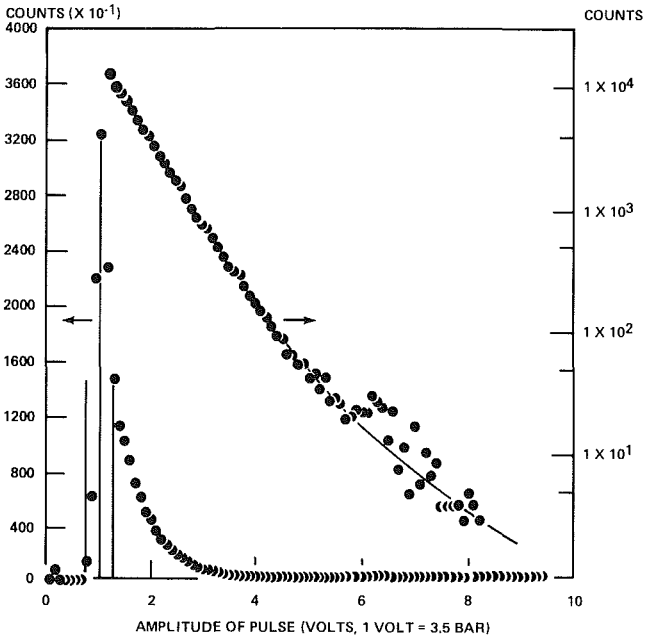

Fig. 5 Typical pressure pulse height spectrum, Kistler 601A probe, V_t = 47.0 m/s, CL = up to probe = 9.8 cm, sampling time = 30 min, σ_c = 0.025

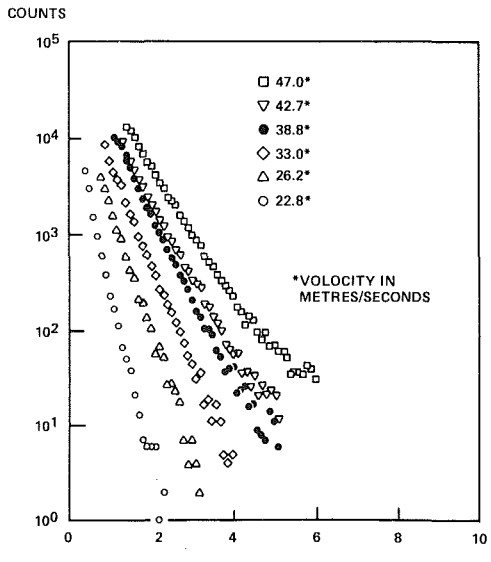

Fig. 6 Pressure pulse height spectra, Kistler 601A probe, CL = up to probe = 9.8 cm, sampling time = 30 min, σ_c = 0.025

where: R = radius of bubble
P_L = liquid pressure in the throat
P_B = liquid pressure at the bubble wall
ρ = liquid density

Pressure is assumed uniform in the cylindrical throat region. The growth period is determined by the liquid velocity, and length of the cavitation region. Equation (2) was solved numerically to yield maximum bubble radius, (R_{max}) for various size nuclei. The energy emitted from a collapsing bubble can be assumed roughly proportional to the potential energy of the bubble at its maximum radius times the liquid pressure above vapor pressure ("suppression pressure") at the point of collapse. It might then be further assumed that pressure pulse amplitude would also vary, as assumed for the present analysis. The fully realistic problem is extremely complex [7, 14, e.g.] so that a more exact analysis was impractical for the present study. Thus, for pulse amplitudes, a:

$$a \propto V_{max}(P_L - P_v)$$
$$a \propto \frac{4\pi R_{max}^3}{3}(P_L - P_v) \tag{3}$$

Assuming all bubbles to collapse in the same axial plane where they are uniformly distributed, the distribution function $W(a)$ of the amplitudes sensed at the venturi wall can be estimated from the distribution function $W(R_i)$ of the equilibrium microbubbles in the liquid by evaluating:

$$W(a) \propto W(R_i)\frac{dR_i}{da} \tag{4}$$

Figures 7 and 8 show these results, using venturi conditions. The function $W(a)$, Fig. 8, passes through an inflexion point for intermediate values of "a," and then decreases for smaller values due to decrease of dRi/da. The calculated distribution function $W(a)$ is similar in shape to that measured (Figs. 5 and 6). An absolute comparison can only be made if the acoustic energy from a bubble is measured by two probes at the same axial position at 180 deg separation.

However, the parameters significant for such a calculation are the growth period, the minimum throat pressure and the liquid pressure at point of collapse. The minimum throat pressure cannot be easily measured because of turbulence effects. Present lack of knowledge of the space-time correlation function of the turbulent fluctuations does not allow such a calculation. Although approximate, the theory outlined above does clarify somewhat the physical basis of the measured pulse height spectra.

It seems evident, however, (Figs. 5 and 6) that the Kistler probe (best commercial state-of-art) fails to record the correct absolute pulse amplitudes. The peak pulse amplitudes are believed, due to work elsewhere [15, 16], to be in the range 10^4 -10^5 bar. The pressure-bar probe, discussed earlier, was designed specifically to measure such peak pulses. Approximate results [9] indicate that the pressure pulse amplitudes in the venturi are also in the range 10^4–10^5 bar.

C. Variation of Acoustic Power With Velocity. The acoustic energy emitted by cavitation bubble collapse was calculated using linear acoustic theory [17] in which the energy flux, E radiated by a pressure is:

$$E = \frac{1}{\rho C}\int_0^\infty p^2(t)\,dt \tag{5}$$

Equation (5) was used to estimate the wave energy flux incident on the probe or damage specimen. This may not be a very good assumption since most damaging collapses are necessarily close to the wall, and effects due to asymmetries, large pressures, and steep shock fronts will be important. However, a more exact model is beyond the scope of this paper. The wave energy is then proportional to pressure

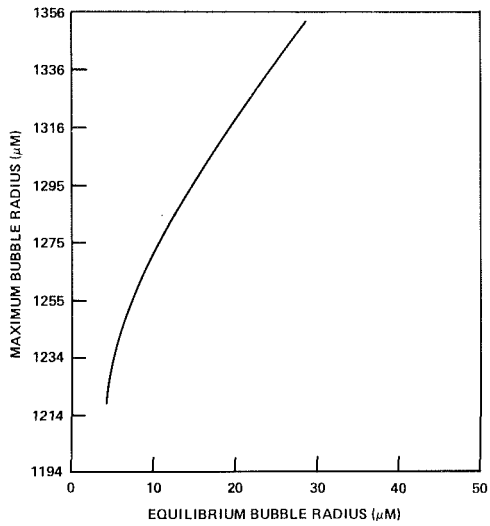

Fig. 7 Calculated maximum bubble versus "nuclei" radii

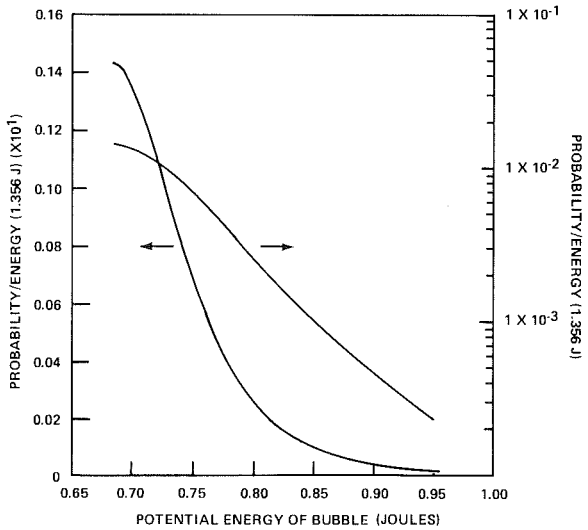

Fig. 8 Calculated distribution function of pressure wave amplitudes

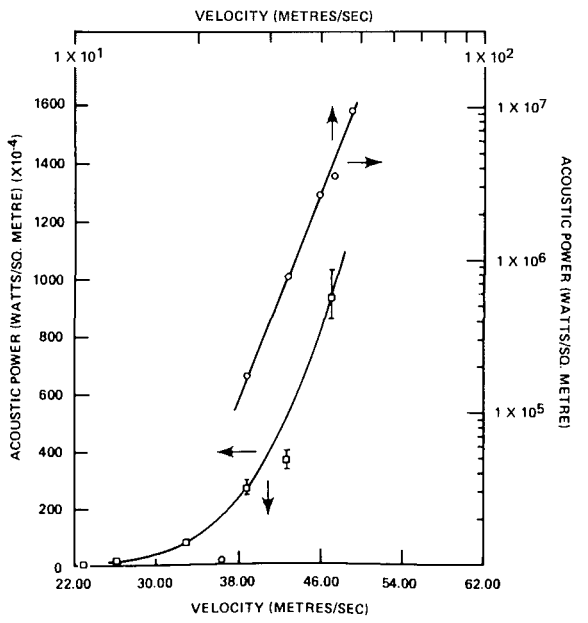

Fig. 9 Acoustic power versus velocity

squared (equation (5)) as would be expected, assuming liquid and specimen to be elastic materials. Integration time interval of 2 μs [16] was used. The cavitation acoustic power flux, $P_{acc.}$ is then:

$$P_{acc.} = \frac{1}{T_s} \sum_{E_c}^{E_m} E \frac{dN(E)}{dE} \tag{6}$$

E_c is the cutoff energy for the calculation, and E_m the maximum energy recorded. $dN(E)/dE$ is the number of pulses of energy, E_m per unit energy interval, calculated from the pulse height spectrum (PHS). T_s is the acquisition time for the pulse height spectrum.

Figure 9 is a typical plot of acoustic power (equation (6)) versus velocity. The minimum cutoff amplitude for equation (6) was determined by background flow noise, which would otherwise trigger detectable pulses, thus registering flow noise peaks, rather than bubble pulses. The Kistler amplitudes were corrected ($\times 500$) to obtain approximate amplitudes which would have been sensed if the pressure-bar probe were in place. The two probes were compared to obtain this factor in a spark bubble chamber [9].

Figure 10 shows variation of acoustic power with cavitation termination location. In general, it increases when the cloud termination is closer to the probe, either upstream or downstream. There is also the effect on wave attenuation of increasing bubble number and size as downstream pressure decreases.

Acoustic power at fixed flow condition is measured with ± 9 percent uncertainty (Fig. 11). These observations were made by changing and then resetting pump speed and system pressure.

The acoustic power may be correlated (Fig. 9) to velocity by a power law,

$$P_{acc.} \alpha V^n \tag{7}$$

Number of counts and mean peak pressure versus velocity are shown (Fig. 12). These may also be correlated by a power law of the form of equation (7). Table 1 lists exponents for such correlations, and variation of mean amplitude with velocity is shown in Table 2.

Table 1 indicates that the velocity exponent for acoustic power increases as cutoff amplitude, a_c is increased, i.e., there is decreasing spectrum slope with increasing velocity (Fig. 6). The slopes are listed in Table 2. Various researchers have found that the velocity exponent for cavitation damage rate measured by the number of craters or weight loss, in various flow geometries, ranges from negative values to about 10 [18, e.g.]. A velocity exponent of 4.5 was here observed for soft (1100-0) aluminum. Wood et al. [19] found the damage velocity exponent in a rotating disk facility attained values up to 10, and increased with material hardness. This is consistent with the acoustic power exponents summarized in Table 1, which shows that velocity exponent increases for increasing cutoff amplitudes.

The velocity exponent for acoustic power is mainly due in our tests to an increase of pulse count rate with velocity. This may be partially due to increased turbulence effects on inception. Various researchers [20, 21, 22] have investigated the variation of bubble inception rate due to turbulent fluctuations. In the light of the above investigations and our results, we conclude that bubble inception rate is a major factor in cavitation noise intensity varition with velocity, and is surely affected by turbulence.

D. Correlation of Acoustic Power With Erosion. Cavitation damage rate (MDPR) for soft aluminum (1100-0) was found to be linearly proportional to cavitation acoustic power calculated from pulse height spectra (PHS) according to the present method (Fig. 13).

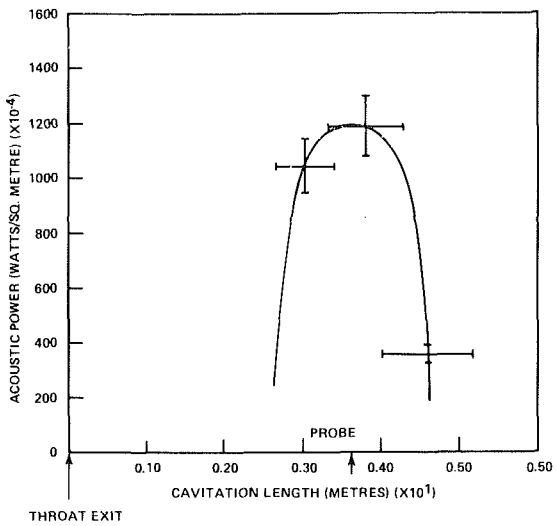

Fig. 10 Acoustic power versus cavitation region length, V_t = 47.0 m/s

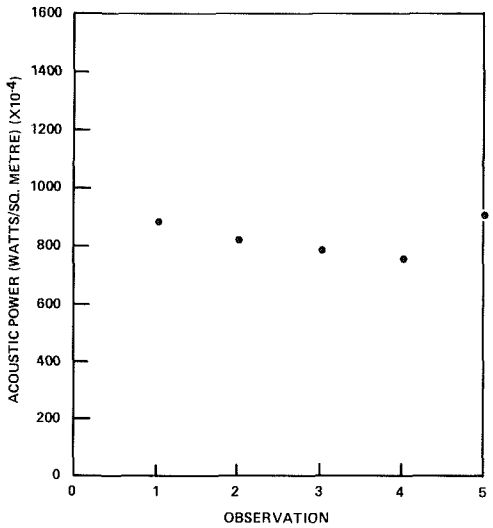

Fig. 11 Acoustic power at constant flow parameters, V_t = 47.0 m/s CL = 9.8 cm = up to probe, σ_c = 0.025

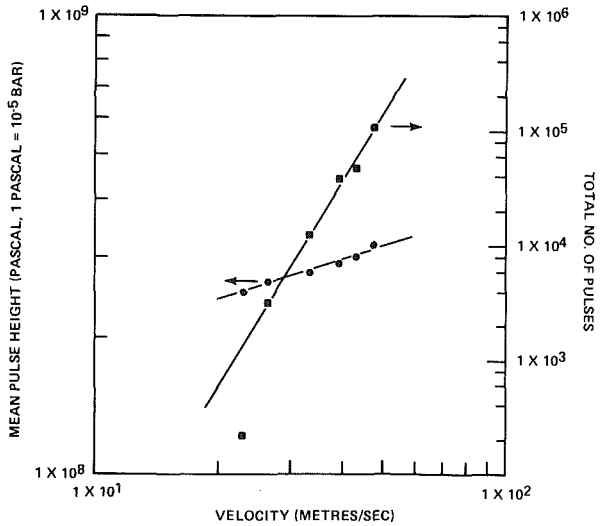

Fig. 12 Mean peak pressure and total number of pulses versus velocity, CL = 9.8 cm = up to probe

Table 1 Deductions from pulse height spectra

Cutoff amplitude	Velocity exponent, (equation (9))			
	Acoustic power	Pulse count	Pulse mean	Amplitude meansquare
a = 1.3 volts	6.8	6.1	0.1	0.8
a = 2.0 volts	7.8	7.5	0.3	0.6
a = 2.7 volts	10.5	10.3	0.2	0.4

Table 2 Characteristics of pulse height spectra

Velocity (V) (m/s)	Decay constant (s) (1/volt)	Mean $<a>$ (volts) (from PHS)	Mean $<a>$ (volts) (from (s))
22.8	4.6	1.46	1.52
26.2	3.0	1.54	1.63
33.0	2.6	1.61	1.69
38.8	2.1	1.69	1.78
42.7	1.9	1.75	1.83
47.0	1.6	1.84	1.93

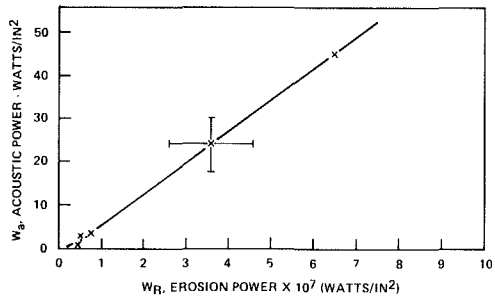

Fig. 13 Acoustic power versus erosion power for 1100-0 aluminum

We have defined "cavitation erosion efficiency," η_c to be the ratio or erosion (or pitting-volume) power to PHS acoustic power. As computed from the linear relationship for 1100-0 aluminum (Fig. 13) $\eta_c = 6.8 \times 10^{-11}$. Ideally, η_c should reflect only the ratio between the pressure pulse energy in the liquid adjacent to the damaged material and that portion of the energy absorbed in the material which results in damage. Thus, the ratio of reflected to absorbed energy, primarily a function of the acoustic impedance ratio between liquid and sample material, is involved. However, a still larger factor is due to the fact that the highly loaded probe or specimen area (pit) is much smaller than the active face of the probe. Bubble collapse photographs obtained here earlier [6] indicate that the impinging microjet diameter is $\sim$ 10 μm diameter for a similar geometry. The geometrical factor included in η_c is then $\sim 0.5 \times 10^{-6}$. Its precise value is uncertain, as is the actual ratio of reflected to absorbed energy. However, for the prediction of eventual cavitation damage rates from PHS acoustic power measurements, it is not necessary to compute these factors accurately, but merely to calibrate the device, assuming η_c is roughly independent of the detailed flow conditions.

The erosion power (or "pitting volume power") can be related to erosion rate, MDPR through volumetric failure energy of the test material, or energy required per volume to form such a pit can be determined experimentally. It should be emphasized that MDPR calculated from pit count and MDPR based on weight loss are not identical parameters. However, the values of MDPR measured in the weight loss tests for 1100-0 aluminum ($\sim$ 4 μm/h^{-1}) and MDPR obtained from pit volume calculations ($\sim$ 6 μm/h^{-1}) did not differ sufficiently for this factor to have an important effect on the magnitudes of η_c.

1100-0 aluminum, 2024-T4 aluminum, cast iron (three percent carbon), 1018 carbon steel, and 316 stainless steel were exposed to given cavitation conditions to determine correlations between MDPR and pertinent material mechanical properties (Table 3). MDPR is calculated from the slope of a best-fit straight line through the data points.

MDPR appears to be best correlated (using only one mechanical property) as inversely proportional to ultimate resilience, UR. The relation (equation (8)) is dimensionally consistent for $n = 1$, which is thus expected to be the case.

$$(\text{MDPR})^{-1} \propto \text{UR}^n \tag{8}$$

where $\text{UR} = \text{UTS}^2/2\text{E}$ = volumetric failure energy for brittle fracture failure, as often occurs in cavitation.

Since UTS $\widetilde{\propto}$ BHN for most materials of the same E, one expects for such materials:

$$(\text{MDPR})^{-1} \propto \text{BHN}^2 \tag{9}$$

More comprehensive data fits by Heymann [23], using both cavitation and impact data, show the best fit to be with $\text{BHN}^{1.85}$. However, the difference between $n = 2$ and $n = 1.85$ for erosion data is relatively unimportant, considering that the factorial standard deviation for such fits is $\gtrsim 3$.

As reported elsewhere [9] the expected linear correlation with UR was realized here only for the ferrous alloys, whereas the BHN correlation is approximated for the aluminum alloys and cast iron together.

Table 4 lists values of cavitation erosion efficiencies η_c, for the various metals tested. The erosion power per unit area is assumed proportional to the product of UR and MDPR. The efficiencies for the ferrous metals (Table 4) are similar, while those for the aluminum alloys are larger ($\sim \times 10$).

It is not surprising that the efficiencies are similar for the ferrous alloys, since their acoustic impedances are about equal. The aluminum alloys (smaller acoustic impedance) reflect less of the acoustic energy to the liquid. The feasibility of predicting cavitation damage in field machinery, by calibrating such a device and measuring η_c for a specific flow condition in a laboratory device, is thus indicated. Data sets such as Table 4 can be used to determine relative cavitation damage to various metals, since flow conditions and geometries should not grossly affect η_c for different metals. Further work to determine the change in PHS acoustic power detected at various positions in geometrically different field machinery is necessary. Such knowledge would eliminate the need for further calibration and enable prediction of cavitation damage with a single measurement.

3. Bandwidth of Cavitation Noise. Variation of pressure pulse band width with velocity was also measured. (Fig. 14). Pressure pulses from the Kistler probe were filtered in a low-pass mode at various cutoff frequencies. The multifunction filter (Fig. 2) has a bandwidth of 20 Hz - 2 MHz. The bandwidth of the Kistler probe is $\sim$ 500 KHz. Therefore, acoustic power does not further increase for higher filter settings. A low pass cutoff frequency of 100 KHz attenuated the 130 KHz ringing frequency of the Kistler. Figure 14 shows that a low pass cutoff at 240 KHz attenuates the signal relatively more at a higher velocity. Thus the higher velocity cavitation pressure

Table 3 Material mechanical properties

Alloy	U.T.S. bar $\times 10^{-3}$	E bar $\times 10^{-6}$	ρ g/cc	*UR* bar	BHN
Aluminum −1100-0	0.76	0.69	2.71	0.42	41
Aluminum −2024-T-4	4.14	0.73	2.77	11.72	78
Cast Iron (3 %C)	2.24	1.07	7.29	2.35	184
Carbon Steel-1018	4.83	2.07	7.85	5.63	120* 110.5**
Stainless Steel-316	5.60	2.00	7.91	7.86	134

* U.S. Not annealed.
** Japanese. Annealed (both US and Japanese specimens have been used in our tests).

Aluminum properties from *Alcoa Structural Handbook*, 1960.
Cast iron and carbon steel properties from *Kent's Mechanical Engr's Handbook*, 12th ed., Design and Production, 1952.
Stainless steel-316 properties measured for ASTM G-2 Cavitation Round Robin, *Materials Research and Standards*, Oct. 1970, p. 19, F. G. Hammitt, et al. ASTM.

Table 4 Cavitation erosion efficiencies for various metals

Material	*UR* bar	*MDPR* μm/hr	Erosion power, watts/m^2 $\times 10^{-6}$	Cavitation erosion efficiency $\times 10^{-12}$
Stainless steel −316	7.86	0.34	73.2	7.7
Carbon steel −1018 ...	5.63	0.46	71.8	7.6
Aluminum −1100-0...	0.42	55.88	646.8	68.1
Aluminum −2024-T4	11.72	4.90	1582.7	166.6
Cast iron ...	2.35	1.42	92.0	9.7

Note: Acoustic Power = 9.5×10^6 watts/m^2 and $V = 47.0$ m/s.

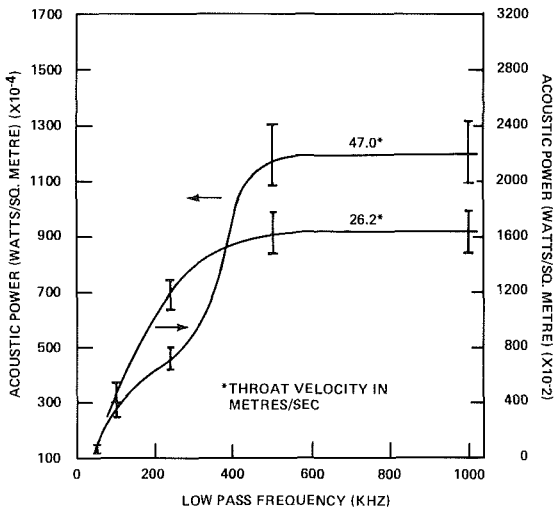

Fig. 14 Bandwidth of cavitation noise, Kistler 601A probe, CL = up to probe = 9.8 cm

pulses have greater high frequency content than those for lower velocity. One of course expects bubble collapse to be more violent at higher velocities, resulting in the emission of stronger shock waves with shorter rise-times, as here verified. Thus acoustic signature power spectrum moves toward higher frequencies at higher velocities.

Presumably, it will be more difficult than in the present venturi to detect individual pressure pulses in rotating machinery due to the problem of placing a probe close enough to the cavitation. If such direct measurement is not possible, the pulses, submerged in the background noise, can still be analyzed in terms of the power spectrum of the acoustic signature. The frequency shift here observed in the power spectral density (PSD) could possibly then be used as an indicator of the acoustic power. Tests covering the frequency spectrum in sufficient detail could be used to correlate frequency shift with velocity and damage. Such a correlation would be independent of geometry, if the frequency response of the configuration were known. Such information could presumably be made available more easily than transmission loss coefficients in a cavitating region of unknown void fraction.

IV Conclusions

A data acquisition system has been designed, constructed and successfully used, along with a commercial transducer (probe), to measure the characteristics of acoustic waves from hydrodynamic cavitation in a venturi. Acoustic power derived from pulse height spectra, PHS was found to vary with the nth power of velocity, for constant cavitation termination point,[2] n varying from 6.8 to 10.5. The major component of this variation was found to be the number of cavitation bubbles incepted and collapsing. Thus, the number of pressure pulses, and not their peak amplitudes, is the major factor in the variation with velocity of acoustic power as here defined, in this, and perhaps other geometries.

The PHS acoustic power correlated linearly with erosion rate for soft (1100-0) aluminum with only a small threshold value. The "cavitation erosion efficiency," η_c for 316 SS,

[2] Cavitation sigma (downstream pressure) was found to decrease with velocity.

1018 C/S, and cast iron (3 percent carbon) was $\sim 10^{-11}$. η_c for 1100-0 and 2024-T4 aluminum was larger by $\sim \times 10$. The feasibility of using η_c to predict eventual cavitation erosion rates from PHS acoustic power data has thus been demonstrated.

For predicting cavitation damage rates more precisely, further PHS measurements to obtain detailed information on amplitude and frequency characteristics of the pressure pulses at various flow conditions are required. Cavitation erosion efficiencies can be determined by exposing different metals to cavitation in the same device. These efficiencies can be defined in terms of PHS acoustic power integrated over the frequency spectrum, or possibly by using the frequency shift in power spectral density, PSD, or both.

Acknowledgments

Financial support was provided by Office of Naval Research Contract No. N00014-76-C-0697, as well as Work Study and SEP internal University of Michigan funds. Also, National Science Foundation Equipment Grant No. ENG-78-07997 provided the necessary instrumentation package. We also wish to thank Mr. William Kittle for his advice and help in the design of the data acquisition system, and also numerous undergraduate and graduate students who assisted in the research.

References

1 Lush, P. A., and Hutton, S. P., "The Relation between Cavitation Intensity and Noise in a Venturi-type Section," *Proceeding International Conference on Pump and Turbine Design*, Glasgow, Sept. 1976, I. Mech. Eng., London.

2 Numachi, F., Chida, I., and Hongo, M., "Ultrasonic Shock Wave Emitted by Cavitation at Perforation on Plate," *Rep. Inst. High Speed Mech.*, Vol. 32, 1975, No. 283.

3 Ramamurthy, A. S., and Bhaskaran, P., "Velocity Exponent for Erosion and Noise Due to Cavitation," *Proceedings, ASME/CSME Applied Mechanics, Fluids Engineering and Bioengineering Conference*, Niagara Falls, N.Y. June, 1979.

4 Robinson, M. J., "On the Detailed Flow Structure and the Corresponding Damage to Test Specimens in a Cavitating Venturi," PHD thesis, Nuclear Engr. Dept., Univ. Mich., Aug. 1965; see also M. J. Robinson, and F. G. Hammitt, "Detailed Damage Characteristics in a Cavitating Venturi," ASME *Journal of Basic Engineering*, Vol. 89, No. 1, Mar. 1967, pp. 161–173.

5 De, M. K., and Hammitt, F. G., "Instrument System for Monitoring Cavitation Noise," *Journal of Physics E: Scientific Instruments* Vol. 15, No. 7, July 1982, pp. 741–745.

6 Kling, C. L., "A High-Speed Photographic Study of Cavitation Bubble Collapse," PHD thesis, Nuclear Engr. Dept., Univ. Mich., 1969; see also C. L. Kling and F. G. Hammitt, "A Photographic Study of Spark-Induced Cavitation Bubble Collapse," ASME *Journal of Basic Engineering*, Vol. 94, No. 4, Dec. 1972, pp. 825–833.

7 Ivany, R. D., "Collapse of a Cavitation Bubble in Viscous, Compressible Liquid - Numerical and Experimental Analyses," PHD thesis, Nuclear Engr. Dept., Univ. Mich., 1965; see also R. D. Ivany and F. G. Hammitt, "Cavitation Bubble Collapse in Viscous, Compressible Liquids - Numerical Analyses," ASME *Journal of Basic Engineering*, Vol. 87, No. 4, 1965, pp. 977–985.

8 Shima, A., and Tsujino, T., "The Natural Frequency of a Spherical Bubble in a Finite Volume of a Liquid," *Rep. Inst. High Speed Mech.*, Vol. 33, 1976, No. 292.

9 De, M. K., "Acoustic Waves from Hydrodynamic Cavitation," PHD thesis, Nuclear Engr. Dept., Univ. of Michigan, 1980, Ann Arbor, Mich.

10 Dobrokhotov, S. N., Kapustina, O. A., and Statnikov, Yu. G., "On The Size Distribution of Stable Bubbles in a Liquid," *Soviet Physics-Acoustics*, Vol. 15, No. 4, Apr.-June, 1970.

11 Ahmed, O., "A New Technique for the Measurement of Cavitation Nuclei Spectra," PHD thesis, Nuclear Engr. Dept., 1965; see also F. G. Hammitt, A. Keller, O. Ahmed, J. Pyun, E. Yilmaz, "Cavitation Threshold and Superheat in Various Fluids," *Proc. Conf. Cavitation*, I. Mech. E., Herriot-Watt Univ., Edinburgh, U.K., Sept. 1974, pp. 341–354.

12 Levkovskii, Yu. L., and Chalov, A. V., "Statistical Analysis of the Cavitation Strength of a Liquid," *Soviet Physics-Acoustics*, Vol. 22, No. 3, May-June, 1976.

13 Lord Rayleigh, "On The Pressure Developed in a Liquid During The Collapse of a Spherical Cavity," *Phil. Mag.*, Vol. 34, 1917, pp. 94–98.

14 Hickling, R., and Plesset, M. S., "Collapse and Rebound of a Spherical Bubble in Water," *Physics of Fluids*, Vol. 7, 1964, pp. 7–14,

15 Fujikawa, S., and Akamatsu, T., "Experimental Investigations of Cavitation Bubble Collapse by a Water Shock Tube," *Bulletin of the JASME*, Vol. 21, No. 152, Feb. 1978.

16 Sutton, G. W., "A Photoelastic Study of Strain Waves Caused by Cavitation," *Calif. Inst. of Tech. Hydrodyn. Lab. Rep.* 21-21, 1955.

17 Cole, R. H., *Underwater Explosions*, Dover, 1965.

18 Hammitt, R. G., *Cavitation and Multiphase Flow Phenomena*, Advanced Book Series, McGraw-Hill, 1980, New York.

19 Wood, G. M., Knudson, L. K., and Hammitt, F. G., "Cavitation Damage Studies with Rotating Disk in Water," ASME *Journal of Basic Engineering*, Vol. 89, No. 1, 1967, pp. 98–110.

20 Levkovskii, Yu. L., and Chalov, A. V., "Influence of Flow Turbulence on the Inception and Growth of Cavitation," *Soviet Physics-Acoustic*, Vol. 24 No. 2, Mar.-Apr. 1978.

21 Daily, J. W., and Johnson, V., "Turbulence and Boundary Layer Effects on Cavitation Inception from Gas Nuclei," in: *Cavitation in Hydrodynamics, Teddington Conf.*, London (1956); see also Trans. ASME Vol. 78, 1956, p 1695.

22 Il'ichev, V. I., "The Frequency of Cavity Formation in Turbulent Boundary Layers and Wakes," *Soviet Physics Doklady*, Vol. 6, No. 2, Aug. 1961.

23 Hammitt, F. G., and Heymann, F. J., "Liquid Erosion Failures," in *Metals Handbook, 10, edit. 8*, Am. Soc. Metals, Metals Park, Ohio, 1975, pp. 160–167.

1018 C/S, and cast iron (3 percent carbon) was $\sim 10^{-11}$. η_c for 1100-0 and 2024-T4 aluminum was larger by $\sim \times 10$. The feasibility of using η_c to predict eventual cavitation erosion rates from PHS acoustic power data has thus been demonstrated.

For predicting cavitation damage rates more precisely, further PHS measurements to obtain detailed information on amplitude and frequency characteristics of the pressure pulses at various flow conditions are required. Cavitation erosion efficiencies can be determined by exposing different metals to cavitation in the same device. These efficiencies can be defined in terms of PHS acoustic power integrated over the frequency spectrum, or possibly by using the frequency shift in power spectral density, PSD, or both.

Acknowledgments

Financial support was provided by Office of Naval Research Contract No. N00014-76-C-0697, as well as Work Study and SEP internal University of Michigan funds. Also, National Science Foundation Equipment Grant No. ENG-78-07997 provided the necessary instrumentation package. We also wish to thank Mr. William Kittle for his advice and help in the design of the data acquisition system, and also numerous undergraduate and graduate students who assisted in the research.

References

1 Lush, P. A., and Hutton, S. P., "The Relation between Cavitation Intensity and Noise in a Venturi-type Section," *Proceeding International Conference on Pump and Turbine Design*, Glasgow, Sept. 1976, I. Mech. Eng., London.

2 Numachi, F., Chida, I., and Hongo, M., "Ultrasonic Shock Wave Emitted by Cavitation at Perforation on Plate," *Rep. Inst. High Speed Mech.*, Vol. 32, 1975, No. 283.

3 Ramamurthy, A. S., and Bhaskaran, P., "Velocity Exponent for Erosion and Noise Due to Cavitation," *Proceedings, ASME/CSME Applied Mechanics, Fluids Engineering and Bioengineering Conference*, Niagara Falls, N.Y. June, 1979.

4 Robinson, M. J., "On the Detailed Flow Structure and the Corresponding Damage to Test Specimens in a Cavitating Venturi," PHD thesis, Nuclear Engr. Dept., Univ. Mich., Aug. 1965; see also M. J. Robinson, and F. G. Hammitt, "Detailed Damage Characteristics in a Cavitating Venturi," ASME *Journal of Basic Engineering*, Vol. 89, No. 1, Mar. 1967, pp. 161–173.

5 De, M. K., and Hammitt, F. G., "Instrument System for Monitoring Cavitation Noise," *Journal of Physics E: Scientific Instruments* Vol. 15, No. 7, July 1982, pp. 741–745.

6 Kling, C. L., "A High-Speed Photographic Study of Cavitation Bubble Collapse," PHD thesis, Nuclear Engr. Dept., Univ. Mich., 1969; see also C. L. Kling and F. G. Hammitt, "A Photographic Study of Spark-Induced Cavitation Bubble Collapse," ASME *Journal of Basic Engineering*, Vol. 94, No. 4, Dec. 1972, pp. 825–833.

7 Ivany, R. D., "Collapse of a Cavitation Bubble in Viscous, Compressible Liquid - Numerical and Experimental Analyses," PHD thesis, Nuclear Engr. Dept., Univ. Mich., 1965; see also R. D. Ivany and F. G. Hammitt, "Cavitation Bubble Collapse in Viscous, Compressible Liquids - Numerical Analyses," ASME *Journal of Basic Engineering*, Vol. 87, No. 4, 1965, pp. 977–985.

8 Shima, A., and Tsujino, T., "The Natural Frequency of a Spherical Bubble in a Finite Volume of a Liquid," *Rep. Inst. High Speed Mech.*, Vol. 33, 1976, No. 292.

9 De, M. K., "Acoustic Waves from Hydrodynamic Cavitation," PHD thesis, Nuclear Engr. Dept., Univ. of Michigan, 1980, Ann Arbor, Mich.

10 Dobrokhotov, S. N., Kapustina, O. A., and Statnikov, Yu. G., "On The Size Distribution of Stable Bubbles in a Liquid," *Soviet Physics-Acoustics*, Vol. 15, No. 4, Apr.-June, 1970.

11 Ahmed, O., "A New Technique for the Measurement of Cavitation Nuclei Spectra," PHD thesis, Nuclear Engr. Dept., 1965; see also F. G. Hammitt, A. Keller, O. Ahmed, J. Pyun, E. Yilmaz, "Cavitation Threshold and Superheat in Various Fluids," *Proc. Conf. Cavitation*, I. Mech. E., Herriot-Watt Univ., Edinburgh, U.K., Sept. 1974, pp. 341–354.

12 Levkovskii, Yu. L., and Chalov, A. V., "Statistical Analysis of the Cavitation Strength of a Liquid," *Soviet Physics-Acoustics*, Vol. 22, No. 3, May-June, 1976.

13 Lord Rayleigh, "On The Pressure Developed in a Liquid During The Collapse of a Spherical Cavity," *Phil. Mag.*, Vol. 34, 1917, pp. 94–98.

14 Hickling, R., and Plesset, M. S., "Collapse and Rebound of a Spherical Bubble in Water," *Physics of Fluids*, Vol. 7, 1964, pp. 7–14,

15 Fujikawa, S., and Akamatsu, T., "Experimental Investigations of Cavitation Bubble Collapse by a Water Shock Tube," *Bulletin of the JASME*, Vol. 21, No. 152, Feb. 1978.

16 Sutton, G. W., "A Photoelastic Study of Strain Waves Caused by Cavitation," *Calif. Inst. of Tech. Hydrodyn. Lab. Rep.* 21-21, 1955.

17 Cole, R. H., *Underwater Explosions*, Dover, 1965.

18 Hammitt, R. G., *Cavitation and Multiphase Flow Phenomena*, Advanced Book Series, McGraw-Hill, 1980, New York.

19 Wood, G. M., Knudson, L. K., and Hammitt, F. G., "Cavitation Damage Studies with Rotating Disk in Water," ASME *Journal of Basic Engineering*, Vol. 89, No. 1, 1967, pp. 98–110.

20 Levkovskii, Yu. L., and Chalov, A. V., "Influence of Flow Turbulence on the Inception and Growth of Cavitation," *Soviet Physics-Acoustic*, Vol. 24 No. 2, Mar.-Apr. 1978.

21 Daily, J. W., and Johnson, V., "Turbulence and Boundary Layer Effects on Cavitation Inception from Gas Nuclei," in: *Cavitation in Hydrodynamics, Teddington Conf.*, London (1956); see also Trans. ASME Vol. 78, 1956, p 1695.

22 Il'ichev, V. I., "The Frequency of Cavity Formation in Turbulent Boundary Layers and Wakes," *Soviet Physics Doklady*, Vol. 6, No. 2, Aug. 1961.

23 Hammitt, F. G., and Heymann, F. J., "Liquid Erosion Failures," in *Metals Handbook, 10, edit. 8*, Am. Soc. Metals, Metals Park, Ohio, 1975, pp. 160–167.

DISCUSSION

Juliusz Kirejczyk[1]

The subject of the paper has a great significance for cavitation damage prediction in fluid machinery. Interesting results in this field were obtained recently by energy measurement methods.

The energy flux density (or, following the authors, the acoustic power) delivered from the cavitation cloud to the walls limiting the flow region seems to be the best method of the damage threat evaluation. Obviously for estimating the material volume losses one should know not only the energy and its spectrum but also the material properties under the specific load which appears during cavitating flow. These two elements are equally important.

The measurement of the energy delivered from collapsing cavitation bubbles to the flow region walls is limited by response of contemporary pressure transducers, especially to strong pulses of short duration. The authors recognized that but used the Kistler transducer with exceptional linearity but with relatively long rise-time and low, strongly marked resonance frequency. Results published by other authors show that in many cases the rise-time is lower than 3 μs. The Fourier transform of a pulse of few microseconds duration gives frequencies up to 10^6 Hz. Thus frequency range in discussed experiments seems to be low, as well as sampling frequency of the A/D conversion. One may expect that some pulse energy was not taken into account in acoustic power calculation.

With regard to the obtained mean value of acoustic power, it should be noted that its value is very high, but during a very small time period of pulse duration, on a very small area. For estimation of acoustic power in such conditions nonlinear effects should be taken into consideration. However the mean value of the acoustic power delivered to the wall limiting cavitating flow is much smaller. I cannot agree with the authors that it reaches 10^7 W/m^2 which is the energy flux density expected in thermonuclear reactors. The probable discrepancy is the correction factor of the Kistler amplitude. In real conditions the measured pulse value is averaged over the whole transducer membrane area and the energy of the electric signal in the transducer output is proportional to the pulse energy. A correction factor would be superfluous. In this situation η_c increases significantly. Perhaps better estimation of a geometrical factor would increase η_c few orders of magnitude.

[1] Institute of Fluid Flow Machinery, Polish Academy of Sciences, Gdańsk, Poland.

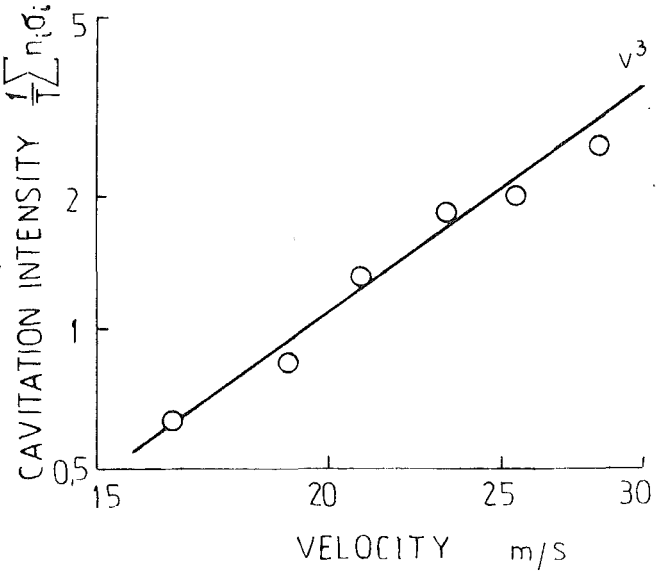

Fig. 1

A transducer can represent an element of the wall in contact with the cavitation cloud. In this situation stress waves in solid material rather than in liquid should be considered. This simple change of assumptions has relatively great consequences. Qualitatively the obtained signal is the same but quantitatively it contains fewer components. This method may permit estimation of the cavitation intensity at some distance from the place of cavitation influence on the wall. Presumably the estimation of stress waves propagation in solids would not be more difficult than calculation of the absorbed energy by pressure pulse measurement.

As an example, Fig. 1 presents cavitation intensity vs. free stream velocity in a cavitation tunnel with a circular cylinder as a cavitator. The experiments were carried out for constant sigma. The cavitation intensity was measured by an ultrasonic device (with high pass filter at 0.5 MHz) on the outside wall of the tunnel which counted ultrasonic pulses of various amplitudes.

Authors' Closure

The authors wish to thank Juliusz Kirejczyk for his comments on the paper and agree that it is extremely difficult to accurately measure the transient characteristic of of each cavitation pressure pulse, and that such information is essential for accurately measuring the acoustic power delivered from the cavitation cloud. Admittedly, the method used here for estimating the acoustic power from cavitation is approximate due to the difficulty of accurately measuring and processing the transient characteristics of each detected pressure pulse. The authors have, however, attempted[2] to investigate the rise time of pressure pulses emitted from bubbles in a spark chamber and venturi with a pressure-bar probe designed by the authors. The pressure-bar probe is too fragile for use in lengthy experiments presented in this paper. Also, it is difficult to measure and process the short rise times of the pressure pulse on line to obtain good statistics.

The authors feel that Juliusz Kirejczyk has failed to recognize the major significance of the results presented in this paper, i.e., that the number of pulses emitted per unit time is the major factor in the increase of acoustic power with velocity. These results indicate that the increase in cavitation damage with throat velocity measured here is mainly due to increased cavitation bubble inception rate. This suggests that fracture of the metal may be due to cyclic stresses causing fatigue to the metal; the number of stress cycles per unit time increases dramatically with throat velocity causing increased metal weight loss.

The subject discussed in the paper is extremely complex and the authors hope that the experimental results presented shed some light on the matter. Further theoretical investigations and similar measurements in various geometries are necessary before cavitation damage is fully understood, and a suitable damage prediction method can then be developed.

De, M. K., and Hammitt, F. G., "Instrument System for Monitoring Cavitation Noise," *J. of Physics E: Scientific Instruments*, Vol. 15, No. 7, July 1982; pp. 741–745.

A Set of Instruments Useful for Liquid Quality Control During Cavitation Research

D. M. Oldenziel
Research Scientist,
Pumps and Industrial Circulations Branch,
Delft Hydraulics Laboratory,
Delft, The Netherlands

It is well-accepted by investigators of cavitation phenomena that undissolved and dissolved gas content in the liquid used affect the onset and type of cavitation in many cases. That is why not only cavitation studies have been carried out to understand the hydrodynamic properties and interactions but also to get insight into the relations between cavitation and liquid quality. The liquid quality is a criterion which gives information about the dissolved gas content and about the undissolved gas content in terms of size distribution and concentration of bubbles and gas pockets dispersed in the liquid. Although not every detail of the interaction between cavitation (inception) and liquid quality is known, it is at least necessary to control and to know the liquid quality. In this way experiments become repeatable and the investigator is allowed to focus his attention to hydrodynamical questions only. In this paper some new and modified instruments and control systems in respect to liquid quality are described. They are an automatic dissolved air (gas) content meter, an acoustic doppler system for bubble detection and a bubble filter for injection of a known bubble mixture.

Introduction

Cavitation studies are mainly carried out in cavitation tunnels and sometimes in towing tanks [1]. In cavitation tunnels liquid is recycled and passes a pump or propellor, bends and the test section with a device under test. The test section has been constructed in such a way that hydraulic parameters as pressure, velocity, and turbulence intensity can be chosen in a wide range. But also the liquid quality at the upstream side of the test device should be known and be kept constant during any test procedure. This is not always as simple as it looks like.

As stated in the abstract, the liquid quality is a criterion for the dissolved gas content and for the undissolved gas content in terms of size distribution and concentration of bubbles and gas pockets dispersed in the liquid used. A gas pocket is defined here as an amount of gas molecules, embedded in liquid, large enough to yield the universal gas laws; it is often adsorbed (attached) at (to) a solid particle. From a basic point of view it should be mentioned that the dissolved gas content and the gas pocket size distribution are dependent on each other. By transport of gas across the interface between gas/vapor mixture and liquid by diffusion, often enforced by convection, the amount of gas inside the gas pocket changes. It is generally assumed that clean gas bubbles disappear totally after a while but gas pockets adsorbed at solid particles can be stabilized. The geometry of the particle, surface tension and contact angle between gas, liquid and solid wall are the important parameters here. The time lapse to reach the state of equilibrium is the important quantity in respect to liquid quality control.

The length of a cavitation tunnel is finite. That means the time for stabilization is limited. If the cavitation tunnel is too short then the free gas content mainly produced in the test section by the cavitating device has not reached his state of equilibrium that belongs to the present dissolved gas content. The consequence is that the liquid quality in terms of size distribution and concentration of bubbles and gas pockets depends on the cavitation properties of the device under test. The liquid quality at both sides of the device under test can be uncoupled by construction of a cavitation tunnel in which under normal test conditions the cycling time is long enough to achieve plenty of time for stabilization. The presence of bubbles in a liquid flow is an unstable situation: small bubbles go into solution due to surface tension and large bubbles will be transported to any free surface or stagnate somewhere. That means there are no free bubbles left in the liquid at the upstream side of the test section. Only gas pockets are left. If bubbles are wanted here they should be injected.

The control of dissolved gas content is more easy because the concentration is uniform in space. Also if plenty of gas bubbles are generated at a certain place by diffusion this is true. This can be made clear in the following way. If water is saturated with air at atmospheric pressure about 18 ml l^{-1} is dissolved. This value depends on temperature but nevertheless it is about 2 percent by volume. In the other case if the free gas content is about 0.1 percent by volume and consists of air bubbles with a radius let's say 100 μm, the mixture looks like milk. This never happens in practice so the concentration of dissolved gas is orders of magnitude higher than the con-

Contributed by the Fluids Engineering Division for publication in the JOURNAL OF FLUIDS ENGINEERING. Manuscript received by the Lubrication Division, February 11, 1980; revised manuscript received June 8, 1981.

centration of undissolved gas: the local dissolved gas content is not affected by local bubble production.

Control and Determination of Dissolved Gas Content

Determination of Dissolved Gas Content. The measurement of dissolved gas content is carried out mechanically in general. The principle is based on enforced gas transport across liquid/gas interfaces in a known volume. Gas transport across any surface is described by Fick's law [2]:

$$\frac{dj}{dt} = D \operatorname{grad} C \tag{1}$$

in which j denotes the flux of dissolved gas, transported across a surface per unit area, D is the coefficient of diffusion, and C denotes the dissolved gas content. Integration over a surface A and assuming that the gradient of C at the surface is given by a linear drop of the concentration from C_1 to C_2 over a distance l the transport of gas is given by:

$$\frac{dm}{dt} = DA\frac{C_1 - C_2}{l} \tag{2}$$

It is obvious that the coefficient A/l should be made as large as possible. Practically this is realized by e.g., stirring or spraying; the area of the interface is increased by geometrical means and the gradient is increased by convection. The "driving force" of gas transport $C_1 - C_2$ is given by the concentration of gas in the bulk liquid and the pressure in the gas phase. There is a linear relation between pressure and saturated concentration given by Henry's law [3]:

$$C_s = kp \tag{3}$$

Equation (2) can slightly be changed into:

$$\frac{dm}{dt} = D\left(\frac{A}{l}\right)(kp - C_0) \tag{4}$$

If $kp > C_0$ the liquid is unsaturated in respect to pressure p and gas is transported into the liquid. In the other case the liquid is supersaturated and transport of gas is out of the liquid. This principle is applied in instruments to determine the value of C_0. A known volume of liquid is separated from the bulk liquid under vapor pressure: $p = 0$. If the liquid is agitated during a certain time $dm/dt \to 0$ and if $p \sim 0$, $C_0 \sim 0$ and determination of the amount of gas, which came free gives the concentration C_0.

Van Slyke and Neill [4] constructed an apparatus to measure the concentration of gases in blood by shaking a sample of 2 ml in vacuum. Many laboratories use a modified version of this principle, which is described by Williams [5]. Here, the sample volume has been increased from 2 ml to 10 ml and the water sample is sprayed in vacuum. Gast [6] and Kümmel [7] describe also instruments to measure the dissolved gas content mechanically. Linnenbom et al. [8] used the gas chromatography method to determine the dissolved gas content. In a sample of liquid, many small helium bubbles are injected, which strip the solution of its dissolved gas quickly and effectively. After drying, the gas mixture goes to the partitioner and the amount of gas is determined. Borden [9] describes a method in which a water sample comes in a hydrogen atmosphere at constant pressure. The amount of dissolved gas is determined by measuring the partial pressure of hydrogen by conduction of heat. The physical properties of dissolved gases are thus known.

The amount of gas dissolved in water can also be measured chemically. These methods will only be mentioned here for the sake of completeness. Only the oxygen is measured then, as described by Eckenfelder and Barris [10]. This method is the so-called polarographic method and is based on an electric current between gold and silver electrodes in a solution of potassium chloride. The electric current is a yard stick for the dissolved oxygen content. Another method is based on a titration procedure with the help of manganese hydroxide and is referred to the Winkler method [11].

An automatic dissolved gas content meter, which is based on the principle of Van Slyke and Neill [4], will be described now. It has a bigger sample volume than the apparatus of Williams [5] and it works automatically. It is called the total gas content meter because dissolved gas content and gas inside the bubbles suspended are measured. However, as mentioned before, the amount of gas in the bubbles can be neglected. The scheme of the instrument is drawn in Fig. 1. The apparatus consists of an hydraulic unit and an electronic control unit. An electronic clock controls the sampling time and an electronic program opens or closes the electromagnetic valves when the mercury sensors give electric signals. The mercury in the glass spheres serves to move the water and to measure the pressure. The mercury level can be varied by changing the

Nomenclature

A = area of interface between water and air, m^2
A_h = area of mercury level, m^2
a = algebraic power of R
a_d = amplitude of acoustic doppler signal, V
C_0, C_1, C_2 = dissolved air (gas) content, mol m^{-3}
C_s = saturated dissolved air content, mol m^{-3}
c = sound velocity in water, m s^{-1}
D = diffusion coefficient of air in water, m^2 s^{-1}
d_f = diameter of bubble filter pipe, m
d_h = diameter of reading tube, m
d_l = optical path length in water, m
F = concentration calibration factor, $m^{-1.2}$ V^{-2}
$F_c(T)$ = calibration factor of total gas content meter, m^{-2}
f = transmitted frequency of acoustic doppler, s^{-1}
f' = received frequency of acoustic doppler, s^{-1}
f_d = acoustic doppler frequency, s^{-1}
g = acceleration of gravity field, m s^{-2}
h = depth in water column of bubble filter, m
h_f = height of water column in bubble filter, m
h_g = mercury level reading at vapor and gas pressure, m
h_v = mercury level reading at vapor pressure, m
h_w = water level at gas and vapor pressure in sampling sphere, m
h'_w = water level at vapor pressure in sampling sphere, m
j = flux of dissolved gas, mol m^{-2}
I_0 = transmitted light intensity, lx
I_t = undisturbed light source intensity, lx
K_1 = electronic amplification factor
K_2 = proportionality constant, m^2V^2
k = gas absorption coefficient, mol $m^{-2}kg^{-1}s^2$
k_f = wave number, m^{-1}
l = distance, m
l_a = distance between transducer and scattering volume, m
l'_a = part of l_a lying within the flow pipe, m

pressure in the reference sphere. If the mercury level reaches the upper sensor a, the valves A, B, and C open and a water sample can be taken into sphere I. The pressure above the water sample is decreased by lowering the mercury level as far as sensor c when valves A and B are closed and valve C is open; the water sample is then gathered in sphere II. By raising the mercury level while valve C is closed now, the water sample returns to sphere I through spray nozzles, allowing the dissolved gas to escape from the water. This spraying cycle is repeated by changing the mercury level between the two sensors b and c under and above sphere II. The amount of gas is determined by measuring the level of the mercury surface h_g with the atmospheric pressure as a reference after several sprayings. When the escaped gas is driven out by pushing the mercury level up to the upper sensor when valve A is open, the vapor pressure can be defined from h_v, too. The value of the vapor pressure is a direct indication of the temperature as well.

It is possible to use a control valve to take continuously samples from a system with high pressure. The sample discharge must be adjusted in such a way that the pressure in sphere I will not become too high. The control valve may cavitate, provided the gas bubbles do not stagnate.

The gas content of a water sample is given by the expression:

$$V_d = \frac{\pi d_h^2 h_g}{4} \frac{T_0}{p_a V_0 T} g\left[\left\{\rho_h\left(1+\frac{\pi d_h^2}{4A_h}\right)-\rho\right\}(h_g-h_v) + \rho(h_w-h_w')\right] \approx F_c(T)\,h_g(h_g-h_v) \quad (5)$$

and is obtained by comparing the hydrostatic pressure in the mercury column with the atmospheric pressure p_a and by use of the law of Boyle-Gay Lussac. In this equation the amount of gas V_d is expressed in volume of gas at atmospheric pressure and at reference temperature T_0 per unit of water volume. The dissolved gas content can be expressed in different ways. A useful unit is ml gas per liter water (1 ml l^{-1} at $p_a = 10^5$ Pa and $T_0 = 273°K$ corresponds with 45×10^{-3} mol m^{-3}). Alternatively the dissolved gas content can be expressed in ppm (by mol).

In practical circumstances the factor $F_c(T)$ in the last expression is obtained from calibration; the gas concentration of a saturated water sample at known temperature and pressure is measured and compared with table values (see for example Handbook of Chemistry and Physics [12]).

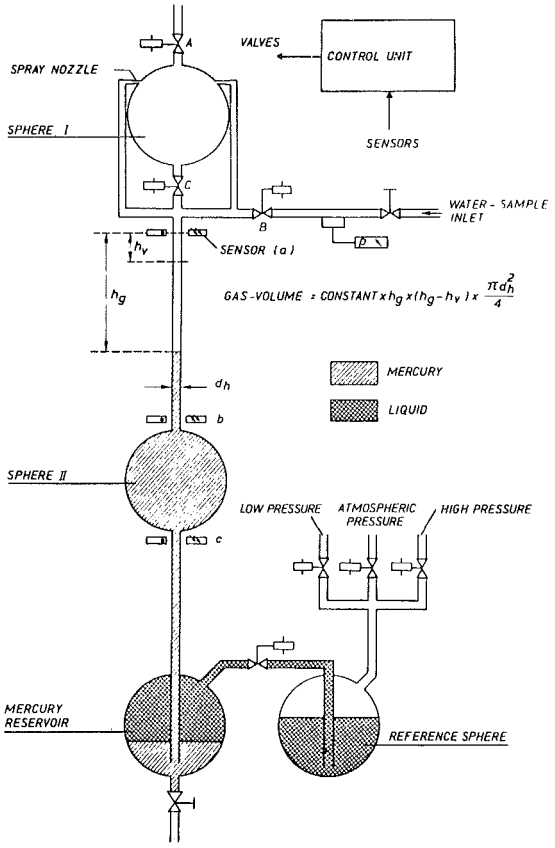

Fig. 1 The hydraulic unit of the total gas content meter

This instrument has a much lower ratio of vapor-gas volume and water sample volume than the conventional type of Van Slyke apparatus, in which the water volume is about 10 ml and the vapor-gas volume during the sprayings is about 100 ml (Williams [5]). In the present modified automatic instrument the water volume is about 130 ml and the mean volume of the vapor/gas phase is about 60 ml. That means the gas pressure increases considerably and the dissolved gas

Nomenclature (cont.)

m = amount of gas substance in bubble, mol
$N(R)$ = bubble size distribution, m^{-4}
n = bubble concentration, m^{-3}
p = pressure, kg $m^{-1}s^{-2}$
p_0 = reference pressure, kg $m^{-1}s^{-2}$
p_a = standard atmospheric pressure, kg $m^{-1}s^{-2}$
q = discharge, m^3s^{-1}
q_1 = discharge in injection pipe, m^3s^{-1}
q_2 = discharge in calibration pipe, m^3s^{-1}
R = bubble radius, m
R_0 = reference bubble radius in logarithmic normal bubble size distribution, m
R_m = mean bubble radius based on theoretical bubble size distribution, m
R_{ms} = measured mean bubble radius, m
S = concentration signal, V^2
s = standard deviation
T = temperature, K
T_0 = reference temperature, K
t = time, s
t_f = stabilization time of bubble filter, s
u = water velocity, m s^{-1}
V_a = effective scattering volume, m^3
V_d = dissolved gas content in water
V_0 = sample volume in total-air content meter, m^3
α = beam divergence angle, rad
β = effective optical scattering fraction
ξ = dummy variable
ν = kinematic viscosity of water, m^2s^{-1}
ρ = density of water, kg m^{-3}
ρ_h = density of mercury, kg m^{-3}
τ = differential acoustic scattering cross-section of bubble, m^2
τ_0 = optical scattering cross-section of bubble, m^2
τ_a = acoustical absorption cross-section of bubble, m^2
τ_e = acoustical extinction cross-section of bubble, m^2
τ_s = total acoustical scattering cross-section of bubble, m^2
ϕ = angle between the axis of transmitter and receiver, rad

cannot come out of solution completely. That is why a second series of sprayings is carried out. The gas pressure can be neglected then. In Fig. 2 the amount of extracted gas from the sample volume is shown as a function of the number of sprayings. After the ninth spraying the amount of gas is measured and is pushed out of the measuring volume. A second series of sprayings is started afterwards.

Control of Dissolved Gas Content. For the control of dissolved gas content the same principle is applied in general. A dissolved gas control device can be shunted to the main test loop. The shunted circuit contains a tank in which the interface between liquid and gas is made very large. Furthermore the boundary layer is made very thin by agitating the liquid. The gas pressure in the tank is controllable and so the "driving force" $(kp-C)$. If $kp>C$ the dissolved gas content increases, otherwise it decreases. An example of such a device is described by Oldenziel [13].

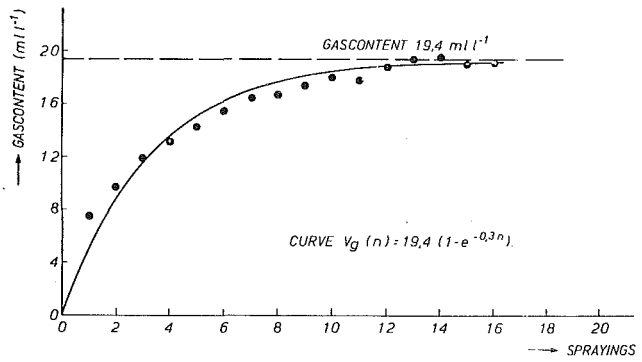

Fig. 2 De-aeration of a water sample in the total gas content meter as function of the number of sprayings. The black dots are the measured values, which are based on at least five measurements. The standard deviation is 0.5 ml l^{-1} for the first 10 sprayings and is about 0.2 ml l^{-1} for the last 6 sprayings.

Control and Determination of Free Gas Content

Determination of Free Gas Content. It is known that undissolved gas content consists of gas bubbles suspended in the liquid flow and gas pockets adsorbed at solid particles also embedded in the liquid. It is obvious that the concentration of gas bubbles and gas pockets and their size distribution should be measured.

In accordance to the present state of knowledge the free gas content is only of interest in cavitation research to determine the concentration of impurities which act as cavitation nuclei. Cavitation nuclei generate bubble explosions in regions of low pressure (tensile stresses). Depending on the nature of those nuclei (gas bubble, gas pocket, and its geometry) and size the nuclei explode at a certain pressure. The radius of gas bubbles, at a certain pressure, gives information about the critical pressure at which bubbles explode. So the concentration and size distribution of gas bubbles give adequate information about potential cavitation nuclei. The explosion criteria of gas pockets stabilized on solid particles are very complicated and cannot be simply derived from the size of the solid particle.

Several optical systems are available to determine the concentration and size distribution of bubbles in water. See for instance Peterson et al. [14] or Godefroy et al. [15]. It is also possible to detect bubbles acoustically. The very sharp resonance frequency of radial volume oscillations of an air bubble is used. Schiebe and Killen [16] used the acoustic tone burst attenuation technique and tried to measure the bubble size distribution in water. Their findings reveal that the usefulness of the technique is limited to the bubble volume concentration range between 0.03 and 1.0 parts per million. A slightly different method is reverberation time measurements at the machine structure or in the fluid, which may show the presence of gas bubbles and even provide an indication of their size distribution. For the principle of this method see, for instance, Lawly and Reed [17], which will be referred to as the reverberation method.

Very small concentrations of bubbles cannot be measured with these techniques. Since it is desired to measure small bubbles, the problem is compounded by further division of the number of nuclei among several resonant frequencies. See the discussion of Silberman and Killen [18] on the paper of Hammitt et al. [19]. These principles are normally associated with complications such as reflection and complex behavior of bubbles in acoustic fields. A review of acoustic detection methods has been written by Scarton and McDonald [20].

A new acoustic method is the application of an acoustic doppler system. A simplified scheme of this system is shown in Fig. 3. A perspex pipe segment with the same inner diameter (in this case 20.7 mm) as the test section contains the

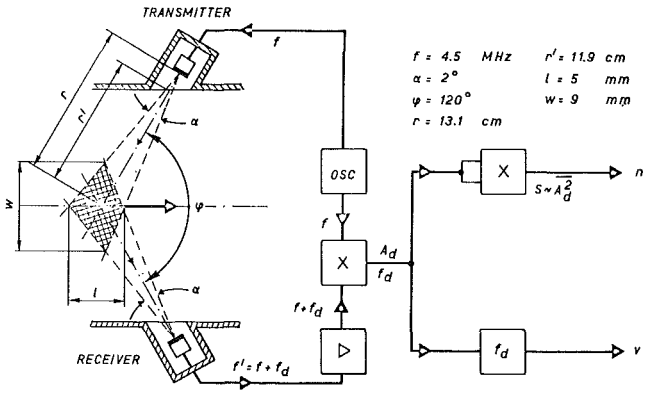

Fig. 3 Scheme of the principle of the acoustic doppler system

transmitting transducer and the receiving transducer. These transducers (frequency 4.5 MHz; diameter 10 mm) are mounted in two opposite water-filled housings, separated from the water flow in the test section by thin windows of plexiglass, forming part of the inner pipe wall. The intersection of the narrow transmitting and receiving beams forms the scattering volume located on the axis of the test section in this case 66 mm upstream of the transducer plane. The -3 dB top angle of the beams is 2 deg and the intersection angle of the beam axes is 120 deg, defining a biconical scattering volume of 0.1 cm^3 with length 5 mm and width 9 mm.

Synchronous detection of the sound scattered by the bubbles passing the scattering volume yields a doppler signal with amplitude envelope a_d and frequency f_d. The mean square value $a_d{}^2$ is proportional to the scattered sound intensity which in turn is proportional to the bubble concentration n. The doppler frequency is given by:

$$f_d = f - f' = \frac{2f\,u\cos\left(\frac{\phi}{2}\right)}{c} \tag{6}$$

The general relation between the concentration signal S and n is given by:

$$S = K_1\overline{a_d{}^2} = K_1 K_2 \frac{n\,V_a\,\tau}{l_a{}^4} e^{-2n\,\tau_e\,l_a'} \tag{7}$$

where V_a is the effective scattering volume, τ the differential scattering cross-section of the bubbles, l_a the distance between scattering volume and transducers, l_a' the part of l_a lying within the test section and τ_e the extinction cross-section of the bubbles, K_1 is the electronical amplification factor and K_2 is a constant depending on the properties of the transducers

and the water. The extinction cross-section is the sum of the total scattering cross-section and the absorption cross-section of the bubbles, $\tau_e = \tau_s + \tau_a$. For $k_f R > 1$, τ_a is negligible, so that $\tau_e = \tau_s$. According to Nishi [21] and Medwin [22] $\tau_s \approx 3\pi R^2$ for $k_f R \approx 1$, which corresponds to $R \approx 50$ μm at $f = 4.5$ MHz. For $R \approx 50$ μm and $n < 17$ cm^{-3} equation (7) is practically linear and reduces to:

$$S \sim n\tau \tag{8}$$

For $k_f R \approx 1$ the normalized differential cross-section $\tau/\pi R^2$ depends weakly on R. From Nishi [21] and Medwin [22] it was found that:

$$\tau = (k_f R)^{-0.2} \pi R^2; \; 0.5 < k_f R < 2 \tag{9}$$

Introducing the calibration factor F and combining equations (8) and (9) finally the practical form is arrived

$$n = F R^{-1.8} S \tag{10}$$

The calibration factor F has been determined experimentally by means of the calibration setup schematically shown in Fig. 4. This setup consists of two coupled circuits, a flow circuit containing the acoustic doppler system, and a bubble injection circuit containing a bubble generating device, an optical transmissometer, and a bubble photography cell. In a vertical tube of plexiglass partially filled with water, a water jet in air penetrates the liquid surface and creates a cloud of small air bubbles. The bubble concentration was measured at the bottom of the water column by means of the optical transmissometer which consists of a laser and a photodiode mounted opposite on the tube wall. The bubble concentration was varied by injection of a dilute soap solution in the water entering the filter. Calibration of the bubble generation device was performed by using the bubble photography cell (15 × 24 × 81 mm) made of plexiglass and mounted vertically in a flexible bypass of the bubble injection conduit. After adjusting the filter parameters the water is allowed to flow through the bypass for some time. When the transmissometer indicates an equilibrium situation the valves of the cell are closed quickly and simultaneously. Next, the cell is turned over in a horizontal position, so that the bubbles rise to the upper window and can be photographed (effective surface 14 mm^2).

Analysis of the pictures with bubbles showed that the bubble size distribution is nearly logarithmic-normal:

$$N(R) = N(R_0) e^{-\frac{1}{2s^2} \ln^2 \left(\frac{R}{R_0} \right)} \tag{11}$$

where R_0 is a reference bubble radius and s is the standard deviation. R_0 was varied in the interval 40–70 μm. It has been found that s was approximately 0.4. The reading of the transmissometer was analyzed using the light transmission formula:

$$I_t = I_0 e^{-\frac{n d_1 \int_0^\infty N(R) \tau_0(R) dR}{\int_0^\infty N(R) dR}} \tag{12}$$

where I_t is the transmitted light intensity, I_0 the intensity at $n = 0$, $\tau_0(R)$ the optical scattering cross-section of the bubbles and d_1 the optical path length in the water. The cross-section τ_0 is proportional to the geometric cross-section

$$\tau_0 = \beta \, \pi R^2 \tag{13}$$

where β is an effective fraction for laser light scattering by air bubbles in water. Combining equations (11), (12), and (13) and using the general integral solution

$$\frac{\int_0^\infty \xi^a \exp\left(-\frac{1}{2s^2} \ln^2 \xi \right) d\xi}{\int_0^\infty \exp\left(-\frac{1}{2s^2} \ln^2 \xi \right) d\xi} = \exp\left\{ \frac{1}{2} a(a+2) s^2 \right\} \tag{14}$$

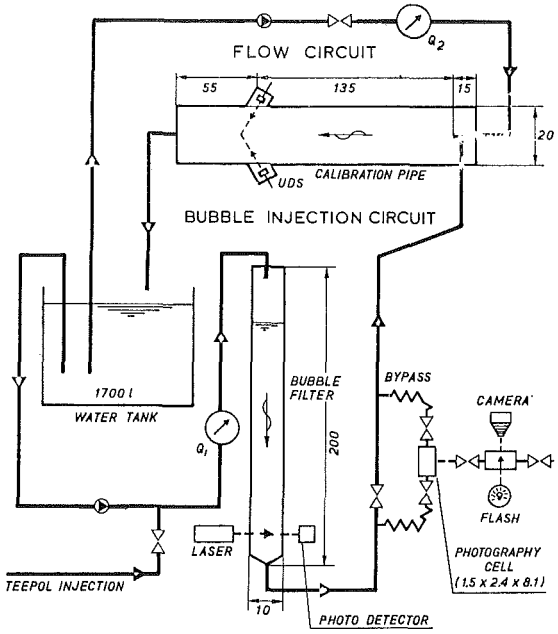

Fig. 4 Calibration set-up for the acoustic doppler system

one finds for the bubble concentration:

$$n = \{ \pi d_1 \beta R_0^2 \exp(4s^2) \}^{-1} \ln\left(\frac{I_0}{I_t} \right) \tag{15}$$

From this equation the unknown β was calculated by substituting n, R_0, and s obtained from the bubble pictures and I_t obtained from the corresponding transmissometer readings.

Repeating the derivation of equations (7) through (10), but now using the logarithmic-normal distribution of equation (11) instead of the uniform radius R, the following expression for the calibration factor is found:

$$F = \left[\frac{\int_0^\infty R^{1.8} N(R) dR}{\int_0^\infty N(R) dR} \right] \frac{n}{S} \tag{16}$$

which is, with the aid of equation (14), further evaluated to

$$F = R_0^{1.8} \frac{n}{S} e^{3.42 s^2} \tag{17}$$

Substitution of equation (15) into equation (17) and taking into account the difference in flow rate between the injection pipe q_1 and the flow pipe q_2 the calibration factor is expressed in terms of the variables measured

$$F = \frac{q_1}{q_2} \left[\frac{\ln \frac{I_0}{I_t} e^{-0.58 s^2}}{\pi d_1 \beta {R_0}^{0.2} S} \right] \tag{18}$$

The calibration of the acoustic doppler system was done by measuring simultaneously the output signal S and the transmissometer signal I_t. The value of F was calculated from equation (18), for several values of R_0 and n by averaging.

In principle, also small solid particles can be detected with this acoustic doppler system. However, the size of a solid particle does not give any information about the amount of free gas adsorbed at this particle as described by Jansen [23]. Furthermore the pressure at which a gas pocket, often stabilized in a crevice of a solid particle, explodes does not only depend on the amount of gas inside the gas pocket but also its shape is an important parameter. Besides this, there is a possibility that solid particles without any free gas can act as

cavitation nuclei. So it is clear that this part of free gas is not important for cavitation phenomena directly. The investigator should be aware however of the existence of those "weak" nuclei. Instruments are available now, that measure the critical pressure of solid particles. The principle of such an instrument is based on the local generation of a pressure well in which nuclei explode when the pressure exceeds a certain level. This instrument is called the cavitation susceptibility meter and is described by Oldenziel [24] and Godefroy et al. [15].

Control of Free Gas Content. Control of free gas content at the upstream side of the test section in cavitation tunnels is rather complicated. As mentioned previously the cycle time of water in cavitation tunnels should be long to achieve the decoupling between the free gas content at the downstream and at the upstream side of the test section. In that case the free gas content at the upstream side of the test section is in equilibrium with the present pressure distribution and dissolved gas content.

A long cycle time can be introduced by constructing a cavitation tunnel with a large capacity. Examples of those tunnels can be found at the California Institute of Technology [1] and at the Delft Hydraulics Laboratory [13]. Often a tank with a large capacity is included and in which the liquid velocity is extremely low; this is called a resorber.

Especially small bubbles must be allowed to have ample time to dissolve. Big bubbles rise to the top of the circuit and coalescence. After some time also these bubbles go into solution, when the liquid is not (super)saturated. The time scale for dissolution of bubbles, suspended in the liquid is difficult to predict. The transport of gas across the bubble surface depends on dissolved gas content, pressure and flow field around the bubble. If surface active materials are present on the bubble surface, coating effects play an important role and the rate of gas transport is reduced. Analytical expressions for gas diffusion rates across clean bubbles are given by Levich [25]. Experiments show that a cycle time of 200 s would be safe [26].

In cavitation tunnels with a long cycle time and with unsaturated water the concentration of cavitation nuclei can be controlled by injection of small bubbles. The radius of those bubbles is normally between 10 and 100 μm. Different systems are applicable for bubble injection.

The generation of electrolysis-bubbles is very attractive for bubble injection. Especially hydrogen bubbles are very small. Very thin wires of platinum or tungsten are placed at the upstream side of the test section. If these wires are connected to the negative output of a power supply small hydrogen bubbles are generated here. The amount of free gas produced per unit of time can be derived from tunnel pressure and electric current. A typical bubble size distribution is shown in Fig. 5. If the bubble size distribution is known and is constant in time the bubble concentration can be determined.

Also small bubbles can be generated by the so-called expansion method. The principle of this method is described as follows. A tank is almost filled with water. The pressure in the tank is kept at a high value at least at a much higher value than the pressure in the system in which bubbles should be injected. By agitating, the volume of water is saturated at the pressure in the tank. May be the dissolved gas content is ten times higher than the gas content in water saturated at atmospheric pressure. If bubbles are wanted, water is injected from the tank into the water tunnel through very small holes. At the exit of these holes cavitation occurs; exploding and imploding bubbles. During the violent bubble dynamics enforced gas transport takes place across the bubble surfaces. The "driving force" $(kp-C)$ is extremely large and many bubbles can be generated in this way. During their implosion, the bubbles are splitted in smaller ones, so only small bubbles

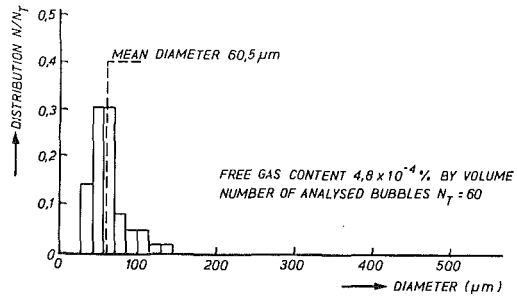

Fig. 5 Size distribution of hydrogen bubbles measured by means of holography. This analysis has been carried out once. The error is in the range of $\sqrt{N}/N_T$.

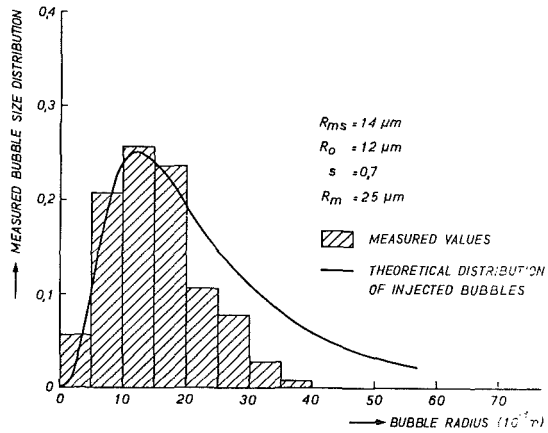

Fig. 6 Measured bubble size distribution in the bubble filter. The histogram is based on five independent measurements of the bubble size distribution. The error in the distribution is about 0.03 (vertical scale) of each column.

are generated. Both bubble injection devices, previous described, have some disadvantages. Electrolysis applied for bubble injection in large systems produces a large quantity of hydrogen gas, partly dissolved in water and partly present in gas mixtures above free surfaces (for instance in pressure control vessels). This may be is a dangerous situation. Bubble generation with the expansion method is limited in time by the volume of the high pressure reservoir.

Recently another system for bubble injection has been introduced. This system is the so-called bubble filter and consists of a vertical tube, partly filled with water. The diameter of this tube is about 0.1 m. Water jets in air penetrate the liquid surface and generate several small gas bubbles. This bubble formation process is very complicated and is a process of splitting and coalescence. Surface active materials at the bubble wall strongly affect these processes. The injection of a small amount of soap increases the number of bubbles.

Directly below the water surface a mixing zone exists. Size distribution measurements as described for the calibration of the acoustic doppler system show that the bubble size distribution in the mixing zone is logarithmic normal. In Fig. 6 a histogram of the bubble size distribution is shown, measured just below the mixing zone. The curve is the logarithmic normal distribution calculated from experimental results.

The liquid column in the vertical pipe has a slow velocity in downwards direction, say about 10^{-3}m s^{-1}. The relative motion of the injected bubbles due to gravity obviously depends on the bubble size. Large bubbles have a relative velocity which is higher than the downward water velocity in the vertical pipe: they are rising in respect to the laboratory frame. Small bubbles, however, have a velocity downwards in respect to the laboratory frame. Figure 7 illustrates the situation.

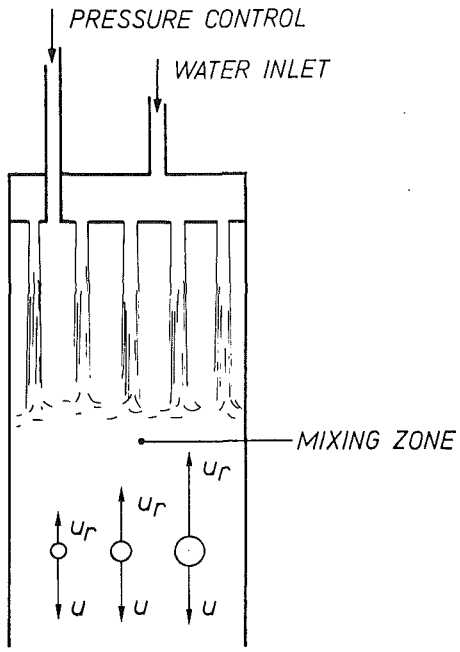

Fig. 7 Principle of bubble filter

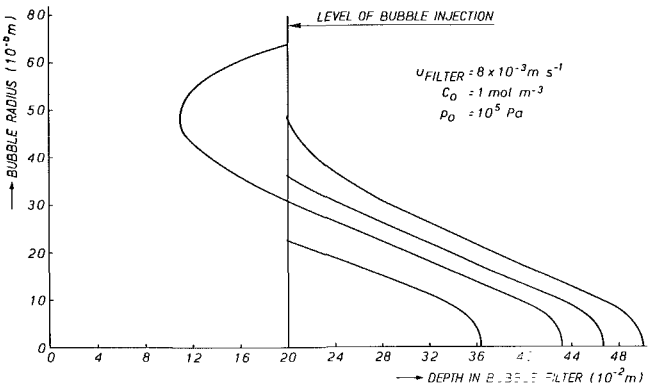

Fig. 8 Bubble radius as a function of the depth for different initial bubble sizes, C_0, p_0, and q are constant

During the motion of bubbles in the vertical pipe their radius changes by diffusion of gas across the bubble surface. If the dissolved gas content in the liquid, the pressure and the velocity of the water column are known, the bubble size distribution and the bubble concentration can be calculated as function of depth h. This depth is expressed by

$$\frac{dh}{dt} = \frac{4q}{\pi d_f^2} - \frac{1}{3}\frac{1}{\nu\rho}\frac{dp}{dh}R^2 \qquad (19)$$

in which dp/dh is the hydrostatic pressure gradient due to gravity, q is the discharge in the vertical pipe, and d_f the diameter of the pipe. The velocity distribution is considered uniform. The Reynolds number in respect to the bubble diameter is smaller than unity so the relative bubble velocity as derived by Hadamard - Rybczynski [25] has been used.

In Fig. 8 the bubble radius is shown as function of depth, with the initial bubble radius as parameter. The absolute pressure p_0, the gas content C_0 and the discharge q are fixed. These curves are found by solving the equation for transport across the bubble surface [25] simultaneously with equation (19).

Although the initial bubble size distribution is assumed to be logarithmic normal, the distribution at a certain depth is different. The concentration is thus a function of the relative bubble velocity and is given by

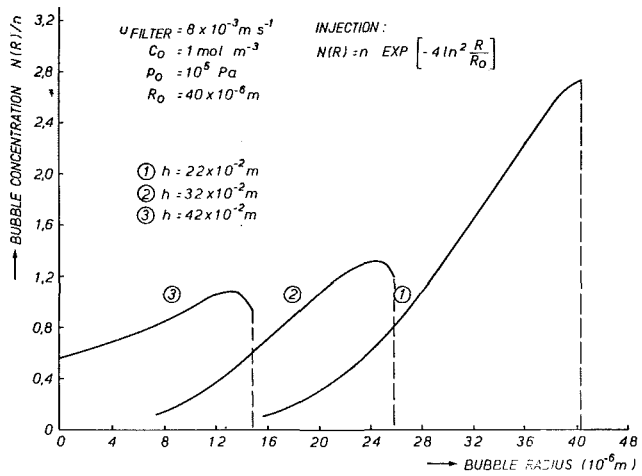

Fig. 9 Bubble size distribution with the depth as a parameter

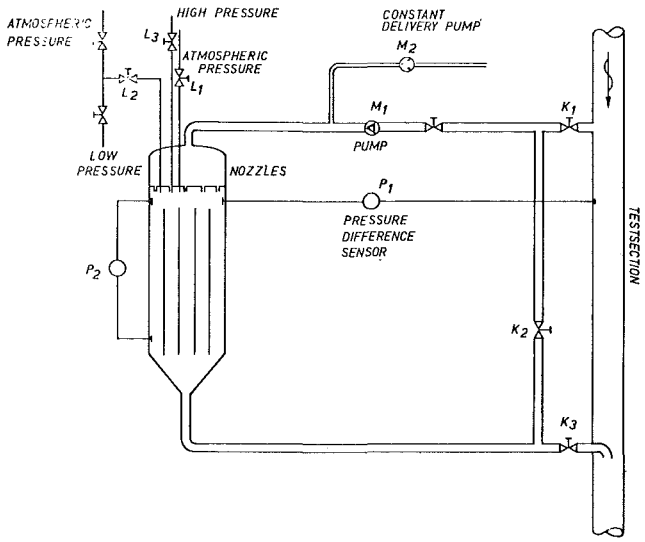

Fig. 10 Scheme of bubble injection system

$$N(h,R;R_0) = \frac{4q}{4q - \frac{\pi d_f^2}{3\nu\rho}\frac{dp}{dh}R^2}\,\frac{n\,e^{-\frac{1}{2}s^2}}{\sqrt{2\pi}s\,R_0}\exp\left[-\frac{1}{2s^2}\ln^2\frac{R}{R_0}\right] \qquad (20)$$

Applying the curves drawn in Fig. 8 the bubble size distribution can be computed at different depths in the vertical pipe. In Fig. 9 some distributions are given with h as a parameter and with fixed values of C_0, p_0, and q. The assumption has been made that the bubbles don't interact below the mixing zone, so there is no coalescence.

The bubble size distribution, given in this way, is valid only for stationary conditions. The physical process described is very slow and the time for stabilizing the system is rather long. Approximately this time t_f is given by:

$$t_f \sim \frac{\pi h_f d_f^2}{4q} \qquad (21)$$

where h_f denotes the total height of the water column.

In Fig. 10 the bubble injection system, as used at the Delft Hydraulics Laboratory is shown. The tank in the left-hand side of the drawing has a diameter of 0.5 m and contains several vertical pipes with a diameter of 0.1 m. Above each pipe a nozzle is located. The pump M_1 feeds the tank with water from the test rig and a bubble mixture is injected

passing valve K_3. If necessary the constant delivery pump feeds the water line with a small amount of soap. The pressure in the tank in respect to the pressure in the test section and the water level in the tank is controlled automatically. Signals from the pressure sensors P_1 and P_2 can activate the valves L_2, L_3, and L_4.

The operation of the system is as follows. In stage 1 the tank is pressurized in the same range as the pressure in the test section. In stage 2 the tank is filled with water and the water level is adjusted. Stage 3 is the stand-by mode: pump M_1 runs, valve K_1 and K_3 are closed and valve K_2 is opened. In this way the bubble formation process is running. If bubbles are needed in the test section valves K_1 and K_3 are opened and valve K_2 is closed.

Discussion

With a set of control and measuring devices previously discussed the investigator in cavitation phenomena has the opportunity to carry out measurements with known and steady liquid quality. However, some critical remarks should be mentioned.

The instrumental equipment shows to full advantage with a tunnel having a long cycle time. A tunnel with a short cycle time can have extremely good hydraulic qualifications, but it is not possible to control the liquid quality for a long time. Only in the period when the liquid has not completed one cycle yet the liquid quality is fixed. This period is quite short and good trigger conditions are necessary for optimum cavitation analyses. Cavitation measurements which need long test runs, for instance cavitation erosion measurements, cannot be carried out with controlled free gas content. In those circumstances the tensile strength equals the vapor pressure and it does not make sense to measure the cavitation susceptibility.

It is not always necessary to apply a set of advanced instruments for liquid quality aspects. In fact only in the case of cavitation inception measurements the liquid quality should be measured and controlled. In the situation of developed cavitation especially the free gas content should be considered. However if the device under test is heavy cavitating the free gas content does not seem to affect the cavitation performances significantly and under very heavy circumstances (choking flow past a valve or head drop in a pump) also the dissolved gas content does not matter.

If acoustic analyses are associated with cavitation (inception) measurements the investigator should be aware of complicated situations. In the case that free stream bubbles are wanted, bubble injection should be carried out very carefully. The free gas content heavily affects the noise measurement because bubbles absorb and reflect acoustic energy. The investigators have to decide for the most important detail: cavitation inception number, type of cavitation or radiation of pressure waves.

In the case of bubble injection, the injection device should be located far upstream of the device under test to ensure a homogeneous spatial bubble distribution. The relatively long traveling time of bubbles from injection to test location has consequences for the bubble size distribution due to diffusion of gas across the bubble wall.

Acknowledgment

The author appreciates the suggestions of and discussions with Dr. R. H. J. Jansen, who developed the acoustic doppler system for measurement of sand transport and made some calculations for the applications to detect air bubbles. In addition, Dr. Jansen conducted the calibration measurements for this system; this is gratefully acknowledged.

References

1 Knapp, R. T., Daily, J. W., and Hammitt, F. G., *Cavitation*, McGraw-Hill, New York, 1970.

2 Bird, R. B., Stewart, W. E., and Lightfoot, E. N., *Transport Phenomena*, Wiley, 1960.

3 Epstein, P. S., *Textbook of Thermodynamics*, Wiley, 1933.

4 Slyke, D. D. van, and Neill, J. M., "The Determination of Gases in Blood and Other Solutions by Vacuum Extraction and Manometric Measurements," *J. of Biological Chemistry*, Vol. 61, No. 2, Sept. 1924, pp. 523-573.

5 Williams, E. E., "The Determination of Dissolved Air in Water," *Laboratory Practice*, Vol. 3, No. 7, July 1954, pp. 275-278.

6 Gast, P., "Experimentelle Untersuchungen über den Beginn der Kavitation an umströmter Körper," Ph.D. thesis, Tech. Univ. of Darmstadt, Germany, 1971.

7 Kümmel, K., "Theoretische und Experimentelle Untersuchungen über die Rolle der Strömungskeime bei der Entstehung von Flüssigkeitskavitation," Ph.D. thesis, Tech. Univ. Darmstadt, Germany, November 1977.

8 Linnenbom, V. J., Swinnerton, J. W., and Cheek, C. H., "Evaluation of Gas Chromatography for the Determination of Dissolved Gases in Sea Water," *Ocean Science and Ocean Engineering, Trans. of Joint Conf. of Marine Techn. Soc. and Am. Soc. of Limnology and Oceanography*, Washington, D.C., June 1965, pp. 1009-1032.

9 Borden, A., "Design, Operation and Maintenance of a Meter for Recording the Air Content of Water in the David Taylor Model Basin Water Tunnels," David Taylor Model Basin, Washington, D.C., Report 549, Dec. 1946.

10 Eckenfelder, W. W., and Barris, C. T., "Polarographic Measurement of Dissolved Oxygen," Am. Society of Testing and Materials, Special Tech. Publ. No. 219, 1957.

11 Winkler, L. W., "Die Bestimmung des im Wasser aufgelösten Sauerstoff," *Berichte der Deutscher Chem. Gesellschaft*, Vol. 21, 1888, pp. 2843-2854.

12 *Handbook of Chemistry and Physics*, 57th Edition CRC Press, Cleveland, Ohio, 1977.

13 Oldenziel, D. M., "Bubble Cavitation in Relation to Liquid Quality," Ph.D. thesis, Tech. Univ. Twente, Delft Hydraulics Laboratory, Publication No. 211, May 1979.

14 Peterson, F. B., Danel, F., Keller, A. P., Lecoffre, Y., "Comparative Measurements of Bubble and Particulate Spectra by Three Optical Methods," *Proc. 14th Int. Towing Tank Conference*, Rep. of Cavitation Committee, 1975.

15 Godefroy, H. W. H. J., Jansen, R. H. J., Keller, A. P., Lecoffre, Y., Oldenziel, D. M., and Renesse, R. L. van, "Comparison of Measuring and Control Methods of the Water Quality With Respect to Cavitation Behaviour," Delft Hydraulics Laboratory, Jan. 1981.

16 Schiebe, F. R., and Killen, J. M., "An Evaluation of Techniques for Measuring Gas Bubble Size Distribution in Cavitation Research," St. Anthony Falls Hydraulic Lab., Univ. of Minn., Minneapolis, Project Report 120, 1971.

17 Lawley, L. E., and Reed, R. D. C., "A Reverberation Method for the Measurement of the Absorption of Ultrasonic in Liquids," *Acoustica*, Vol. 5, 1955, pp. 316-322.

18 Silberman, E., and Killen, J. M., *Discussions at the conference, Conference of Cavitation*, Edinburgh, Scotland, Mech. Eng. Publication Ed., London and New York, 1975, p. 476.

19 Hammitt, F. G., Keller, A., and Ahmed, O. S. M., "Cavitation Threshold and Superheat in Various Fluids," *Conference on Cavitation*, Edinburgh, Scotland, Ed. Inst. Mech. Eng., London, Sept. 1974, pp. 341-354.

20 Scarton, H. A., and McDonald, J. F., "A Review of the Acoustic Detection of Boiling in Nuclear Reactors," *Proc. of Noise and Fluids Engineering Symposium*, Atlanta, Dec. 1977.

21 Nishi, R. Y., "The Scattering and Absorption of Sound Waves by a Gas Bubble in a Viscous Liquid," *Acoustica*, Vol. 33, 1975, pp. 65-74.

22 Medwin, H., "Acoustical Determination of Bubble Size Spectra," *J. Acoust. Soc. Am.*, Vol. 62, 1977, pp. 1041-1044.

23 Jansen, R. H. J., "The In-Situ Measurement of Sediment Transport by Means of Ultrasound Scattering," Delft Hydraulics Laboratory, Publication No. 203, July 1978.

24 Oldenziel, D. M., "A New Instrument in Cavitation Research: The Cavitation Susceptibility Meter," to be published in ASME JOURNAL OF FLUIDS ENGINEERING.

25 Levich, V. G., *Physico-Chemical Hydrodynamics*, Prentice Hall, Englewood Cliffs, New Jersey, 1962 (Trans. from Russian).

26 Brown, F. B., "Air Resorption in Water Tunnels," Calif. Inst. of Tech., Hydrodyn. Lab. Report N-62, 1949.

C. K. Krishnakumar
Research Engineer.

S. F. Fields
Manager,
Mechanics Research.

Gard, Inc.,
Niles, Ill. 60648

Criteria for Filling of Liquid-Carrying Pipes

Flow rate versus pressure drop relations for liquid flow in pipes are well established for the case of pipes running full. However, these relations are not applicable for pipes that run partially filled. This article summarizes an experimental study to determine criteria for establishing full-pipe flow in horizontal, open-ended pipes and submerged, downward-flow vertical pipes.

Introduction

When liquid is conveyed from one reservoir into another by a pipe line, the volume rate for a given pressure difference between the ends of the line depends upon whether it is a pure liquid-phase flow or a two-phase flow (gas and liquid phases). If both phases are present, calculations of filling or emptying time, mass flow rate, etc., using conventional hydraulic formulas (which are good for single-phase flow only) can be significantly in error. The present study was undertaken to define criteria for initial filling of horizontal and vertical (downward-flow) pipes in terms of flow and liquid parameters, so that equations established for single-phase flows become applicable. Although performance characteristics of boiling two-phase flow systems (including cavitating flows) have been studied extensively in the past [references 1, 2, 3, 4, 5], the problem at hand (namely, criteria for initial filling) has not been addressed by any of them.

The present study was done in three different phases.

Phase 1. Criterion for filling of a horizontal, open-ended pipe in turbulent flow.

Phase 2. Criterion for filling of a horizontal, open-ended pipe in laminar flow.

Phase 3. Criterion for filling of a downward-flow vertical pipe.

Phase 1. Criterion for Filling of a Horizontal, Open-Ended Pipe in Turbulent Flow

As the rate of flow of a liquid through a horizontal, open-ended pipe is gradually reduced, at some point the pipe ceases to remain filled and a free surface is formed within the pipe. This surface moves closer to the pipe entrance as the flow is reduced, until finally the entire pipe runs partially filled. A similar phenomenon occurs when liquid flow starts to build up in an empty pipe (see Figure 1 for typical flow configurations).

1.1 Dimensional Analysis. Primary geometric and fluid property variables relevant in this study are:[1]

D = pipe diameter
L = pipe length
V = average fluid velocity

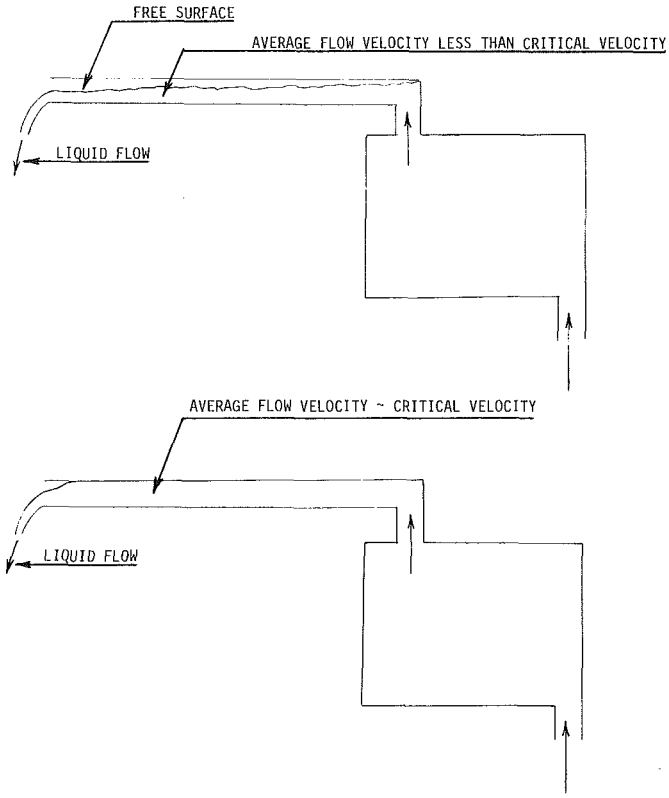

Fig. 1 Typical flow configurations

ν = kinematic viscosity
g = acceleration due to gravity

Application of the Buckingham's π – Theorem gives the following as the dimensionless groups which possibly have an influence on the phenomenon of interest:

(*a*) $\dfrac{V}{\sqrt{gD}}$, Froude number

(*b*) $\dfrac{VD}{\nu}$, Reynolds number

(*c*) $\dfrac{L}{D}$, Length/diameter ratio

[1] The effect of varying interfacial tension was not considered in this study.

Contributed by the Fluids Engineering Division for publication in the JOURNAL OF FLUIDS ENGINEERING. Manuscript received by the Fluids Engineering Division, December 5, 1980.

1.2 Experiments Carried Out in Phase 1. Figure 2 shows the layout of the experimental setup. Water was pumped through a flow meter and a vertical reservoir into the test pipe which was maintained horizontal. At relatively low flows, the flow rate was read on the rotameter for greater accuracy and at higher flow rates the rate was determined using the water meter and a stop watch.

A range of clear plastic pipes with inside diameters varying from one inch to two inches (25.4 mm to 50.8 mm) and with different length-to-diameter ratios (16 to 72) was used. Flow rate was gradually increased by adjusting the valves. When the free surface within the pipe was only half a pipe diameter away from the downstream end, the rate of flow was noted. This was considered to be the flow rate at which the pipe became full. Reynolds numbers in this study ranged from 7,000 to 25,000.

1.3 Results. These are tabulated in Table 1. (The critical velocity V_C appearing in this and the following tables refers to the minimum value of the flow velocity V at which the pipe flow becomes pure liquid phase flow.) The following empirical formula was obtained as the criterion for horizontal, open-ended pipes to fill up, in the turbulent regime of flow:

$$\mathrm{Fr}^2 \times \mathrm{Re}^{-.3} = 0.020 \quad (1)$$

Within the range tested, the length-to-diameter ratio was found to have no significant effect on the results. Therefore, this ratio was not considered as a variable for the remainder of Phase 1 and Phase 2 studies.

Phase 2. Criterion for Filling of a Horizontal, Open-Ended Pipe in Laminar Regime

An experimental setup similar to that of Phase 1 was utilized in conjunction with glycerol-water solutions with kinematic viscosities of 11×10^{-6} to 24×10^{-6} m^2/s. Pipe inside diameters of 3/4-in. (19.1 mm), 1-in. (25.4 mm), 1-1/2-in. (38.1 mm) and 2-in. (50.8 mm) were used. Reynolds numbers ranged from 155 to 2200.

Results of the Phase 2 study are tabulated in Table 2. The criterion for a horizontal, open-ended pipe to fill up in the laminar regime was determined to be:

$$\mathrm{Fr}^2 \times \mathrm{Re}^{-.3} = 0.046 \quad (2)$$

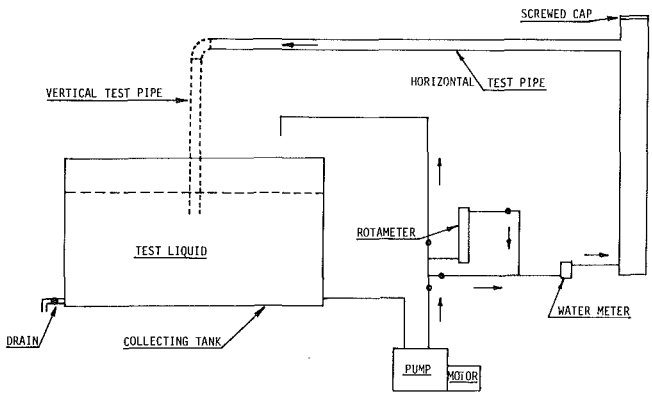

Fig. 2 Experimental setup – flow through horizontal, open-ended pipe (broken lines indicate the system modification for Phase 3 tests)

Phase 3. Criterion for Filling of Downward-Flow Vertical Pipes

Filling of a pipe containing downward flow is a complex phenomenon involving gas entrainment into the flowing liquid, bubble formation, and eventual expulsion of the bubbles from the pipe with the liquid flow. The rate of entrainment of the bubbles, their size, and forces acting on them are functions of several variables. Most important of these are flow velocity, pipe diameter, inlet configuration, density difference between gas and liquid, interfacial tension, liquid viscosity, and whether the bottom end of the pipe is submerged or not. The balance of forces on the bubbles is further complicated by bubble coalescence and break-up. In view of the complexity of the problem, the scope of the present investigation was limited to obtaining reasonably accurate empirical correlations. Further discussion of the phenomena involved is contained in the Appendix.

In this series of tests, the vertical test pipes were connected to horizontal lead pipes using cemented elbow joints (as indicated by the broken lines in Fig. 2). Diameters of the lead pipes and the elbows were the same as those of the vertical test pipes in each case. The test pipes were all made fifteen diameters long. This value of the length-to-diameter ratio was considered sufficient to minimize the influence of the flow pattern in the entrance region leading into the test pipes on the value of the critical velocity V_C.

Experimental Procedure

The system was filled with liquid by pumping liquid through it at a large enough flow rate. Air collected at the top of the vertical supply column was released by unscrewing the cap temporarily. The pump was shut off and the system inspected to ensure that it was leakproof. The syphon was then broken by removing liquid from the downstream collecting tank and uncovering the lower end of the vertical test pipe. Once the horizontal lead pipe and the test pipe were filled with air, the liquid level in the collecting tank was raised to submerge the test pipe by approximately two in. (50 mm). The pump was started again and flow admitted to the test pipe at a low rate. If no significant level rise was observed in the test pipe for a period of about 5 minutes, the liquid level in the collecting tank was lowered and the liquid in the pipes drained. The pump discharge rate was increased to a slightly higher value, the level in the collecting tank was again raised, and the sequence of operations was repeated until the flow rate was large enough to cause filling of the test pipe in a relatively short period (less than a minute). This value of the flow rate was taken as the critical flow rate.

Results

Results are tabulated in Tables 3A, 3B, and 3C. Critical

Table 1 Criterion for filling of a horizontal, open-ended pipe in turbulent flow

Pipe dia mm	Critical velocity, V_C m/s	$\mathrm{Fr} = \frac{V_C}{\sqrt{gD}}$	$\mathrm{Re} = \frac{V_C \times D}{\nu}$	$\mathrm{Fr}^2 \times \mathrm{Re}^{-.3}$
50.8 ± 1.6	0.457 ± 0.031	0.647 ± 0.045	24,880 ± 1,736	0.0201 ± 0.0028
41.3 ± 1.6	0.393 ± 0.032	0.617 ± 0.052	17,400 ± 1,464	0.0203 ± 0.0035
38.1 ± 1.6	0.363 ± 0.032	0.594 ± 0.054	14,875 ± 1,350	0.0197 ± 0.0036
38.1 ± 1.6	0.378 ± 0.033	0.618 ± 0.056	15,500 ± 1,395	0.0211 ± 0.0039
34.9 ± 1.6	0.329 ± 0.031	0.562 ± 0.055	12,375 ± 1,203	0.0186 ± 0.0037
25.4 ± 1.6	0.268 ± 0.034	0.537 ± 0.070	7,335 ± 964	0.0198 ± 0.0053
25.4 ± 1.6	0.274 ± 0.035	0.549 ± 0.072	7,500 ± 991	0.0207 ± 0.0055

NOTE: The pipes are considered to run full when they are filled to within half a pipe diameter of the downstream end. Test liquid: water ($\nu = 1 \times 10^{-6}$ m^2/s).

Table 2 Criterion for filling of a horizontal, open-ended pipe in laminar regime

Pipe dia mm	Critical velocity, V_C m/s	$\mathrm{Fr} = \frac{V_C}{\sqrt{gD}}$	Kinematic viscosity[a] $\nu \times 10^{+6}$ m^2/s	$\mathrm{Re} = \frac{V_C \times D}{\nu}$	$\mathrm{Fr}^2 \times \mathrm{Re}^{-.3}$
50.8 ± 1.6	0.500 ± 0.034	.709 ± 0.049	11.1 ± 0.07	2,280 ± 172	0.0494 ± 0.0069
38.1 ± 1.6	0.366 ± 0.032	.599 ± 0.054	13.8 ± 0.07	1,010 ± 98	0.0451 ± 0.0082
25.4 ± 1.6	0.280 ± 0.036	.561 ± 0.074	18.7 ± 0.09	385 ± 54	0.0528 ± 0.0141
19.1 ± 1.6	0.198 ± 0.035	.457 ± 0.083	24.4 ± 0.10	155 ± 30	0.0460 ± 0.0169
	0.210 ± 0.037	.485 ± 0.088	11.1 ± 0.07	360 ± 71	0.0402 ± 0.0148

[a] Test liquid: mixtures of glycerol and water.

Table 3 Criterion for filling of a downward-flow vertical pipe with submerged end

3A. Low Viscosity Liquids

Pipe dia mm	Kinematic viscosity[a] $\nu \times 10^{+6}$ m^2/s	Critical velocity, V_C m/s	$\mathrm{Re} = \frac{V_C \times D}{\nu}$ dimensionless	$\mathrm{Fr} = \frac{V_C}{\sqrt{gD}}$ dimensionless
50.8 ± 1.6	1	0.203 ± 0.015	11,115 ± 828	0.288 ± 0.021
38.1 ± 1.6	1	0.300 ± 0.026	12,310 ± 1,101	0.491 ± 0.044
25.4 ± 1.6	1	0.208 ± 0.027	5,690 ± 762	0.417 ± 0.056
19.1 ± 1.6	1	0.128 ± 0.024	2,625 ± 502	0.296 ± 0.057

[a] Test liquid: water.

3B. Medium Viscosity Liquids

Pipe dia mm	Kinematic viscosity[a] $\nu \times 10^{+6}$ m^2/s	Critical velocity, V_C m/s	$\mathrm{Re} = \frac{V_C \times D}{\nu}$ dimensionless	$\mathrm{Fr} = \frac{V_C}{\sqrt{gD}}$ dimensionless	$\frac{V_C}{D^{.2} \times \nu^{.6}}$ D in m, ν in m^2/s
50.8 ± 1.6	10.5 ± 0.06	0.259 ± 0.018	1,350 ± 96	0.367 ± 0.026	455 ± 32
	18.5 ± 0.09	0.373 ± 0.025	1,100 ± 76	0.528 ± 0.036	468 ± 32
38.1 ± 1.6	10 ± 0.07	0.321 ± 0.028	1,000 ± 91	0.525 ± 0.047	527 ± 46
	19 ± 0.09	0.373 ± 0.033	800 ± 73	0.610 ± 0.055	488 ± 43
25.4 ± 1.6	12 ± 0.07	0.249 ± 0.032	570 ± 75	0.499 ± 0.066	465 ± 60
	18.5 ± 0.09	0.404 ± 0.052	500 ± 80	0.809 ± 0.107	580 ± 75
19.1 ± 1.6	8.5 ± 0.06	0.216 ± 0.038	520 ± 95	0.499 ± 0.090	527 ± 93

[a] Test liquid: mixtures of glycerol and water.

Table 3 (Continued)

3C. High Viscosity Liquids in Small Diameter Tubes

Pipe dia mm	Kinematic viscosity[a] $\nu \times 10^{+6}$ m^2/s	Critical velocity, V_C m/s	$\mathrm{Re} = \frac{V_C \times D}{\nu}$ dimensionless	$\mathrm{Fr} = \frac{V_C}{\sqrt{gD}}$ dimensionless	$\frac{V_C}{D^{.2} \times \nu^{.6}}$ D in m, ν in m^2/s
25.4 ± 1.6	28.5 ± 0.12	0.701 ± 0.090	670 ± 89	1.404 ± 0.186	779 ± 101
19.1 ± 1.6	23.0 ± 0.10	0.469 ± 0.079	420 ± 73	1.084 ± 0.188	628 ± 106

[a] Test liquid: mixtures of glycerol and water.

values of the pipe filling parameter (for flow with the discharge end submerged) were obtained as follows:

For low viscosity liquids, Table 3A,

$$\mathrm{Fr} = 0.30 \text{ to } 0.50 \tag{3}$$

This result agrees well with those of reference [2]. However significant deviations were noted with liquid kinematic viscosities greater than roughly 10×10^{-6} m^2/s. In this regime of flow, a fully satisfactory correlation of the test results could not be obtained in terms of non-dimensional parameters. This is believed to be due to the complex effects of liquid viscosity on bubble size and shape, and possibly the role of surface tension on the balance of forces. (A more detailed discussion of the phenomenon is given in the Appendix.) Within the limited range of the test variables, a dimensional correlation was obtained as given in equation (4).

For liquids of kinematic viscosity above 10×10^{-6} m^2/s, Table 3B,

$$\frac{V_C}{D^{.2} \times \nu^{.6}} = 455 \text{ to } 580 \tag{4}$$

V_C is the critical velocity in m/s.

D is pipe diameter in m.

ν is kinematic viscosity in m^2/s.

Critical velocities measured in these experiments correspond to pipe filling in a relatively short time (less than a minute) after adjustment of flow. Since entrainment and expulsion of air bubbles could go on at exceedingly slow rates over long periods of time, pipe filling could be established at considerably lower rates of flow, given considerably more time.

Equation (4) is applicable only when the pipe diameter is not small enough and viscosity is not large enough to prevent bubbling at the liquid surface in the vertical pipe. In those cases, the air column in the vertical pipe would remain as a single long bubble until a high flow velocity is reached (see Table 3C). At this point the air column will be flushed out instantaneously by the jet coming down as a piston from the top.

Uncertainty in the Output Results

Uncertainties in the output results were computed by the method of Kline and McClintock [6]. If $F(x_1, x_2, \ldots, x_n)$ is an output result and Δx_i is the uncertainty in a measured variable x_i, then the uncertainty ΔF is given by

$$\Delta F = \left[\sum_{i=1}^{n} \left(\frac{\partial F}{\partial x_i} \Delta x_i \right)^2 \right]^{1/2}.$$

Odds in the measured variables were estimated as 20:1.

Concluding Remarks

The phenomenon of filling of liquid-carrying pipes is controlled by the nonlinear interaction of several variables. A simple criterion to demarcate the filled and unfilled regimes of flow is not to be expected. However, in many industrial pipe flow problems, an approximate evaluation of the critical flow rate would lead to problem solution. The relatively simple criteria developed in this limited experimental study enable one to predict minimum flow rates required to fill horizontal and vertical downward-flow pipes. For a more complete understanding of the phenomenon of pipe filling, the experimental range of the variables should be extended and the effect of varying surface tension included.

Acknowledgement

This work was performed for the General American Transportation Corporation of GATX Corp. as part of the flow calculations required for its proprietary system of interconnected tank cars known as the TankTrain® system.

References

1 Simpson, L. L., "Sizing Piping for Process Plants," *Chemical Engineering*, June 17, 1968, pp. 203-205.

2 Kelly, A. G., "Hydraulic Design of Syphons," *Proceedings of the Institute of Mechanical Engineers*, Vol. 180, No. 42, 1965, pp. 981-1011.

3 Baker, O., "Multiphase Flow in Pipe Lines," *The Oil and Gas Journal*, Nov. 10, 1958, pp. 156-167.

4 Hahne, E., and Grigull, U., eds., *Heat Transfer in Boiling*, Academic Press, New York, 1977.

5 Collier, J. G., *Convective Boiling and Condensation*, McGraw-Hill, New York, 1972.

6 Kline, S. J., and McClintock, F. A., "The Description of Uncertainties in Single Sample Experiments," *Mechanical Engineering*, Jan. 1953, p. 3.

7 *Chemical Engineers Handbook*, Perry, R. H. and Chilton, C. H., eds., 5th ed., McGraw-Hill, New York, 1973, pp. 18.68-18.71.

8 Davidson, L., and Amick, E. H., "Formation of Gas Bubbles at Horizontal Orifices," *AIChE Journal*, Vol. 2, No. 3, 1956, pp. 337-42.

9 Clift, R., Grace, J. R., and Weber, M. E., *Bubbles, Drops and Particles*, Academic Press, N.Y., 1978.

APPENDIX

Discussion of Phenomena Involved in the Filling of a Downward-Flow Vertical Pipe (Submerged)

Consider liquid flow commencing in the pipe system shown. When flow rate increases, air entrainment by the liquid stream falling down the vertical pipe becomes significant as can be seen by the bubbling at the liquid surface in the vertical pipe. The bubbles are acted on by mainly three forces – buoyant, inertial, and drag forces. These forces depend on liquid properties, flow velocity, and the size

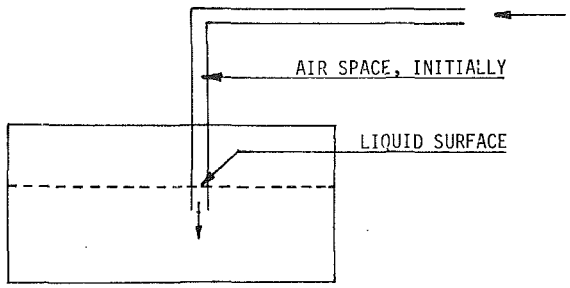

(radius) and shape of the bubbles. The size of the bubbles and their rate of formation depend on the flow rate, pipe diameter, interfacial tension, and liquid viscosity [7, 8, 9]. Very small bubbles tend to be spherical while larger ones are ellipsoidal or helmet-shaped. The typical bubble size is further modified by the phenomena of coalescence and break-up [7, 8]. Whether a bubble rises upward, maintains a mean equilibrium position, or moves downward with the stream depends on a balance of the relevant forces.

When the bubble size is very small (say less than 2 mm (3/32 in.)), the bubble Reynolds number (based on bubble diameter) is in the Stoke's Regime [7]. The dominant opposing forces are the forces of inertia and skin friction. With bubbles in the size range of 4-5 mm (3/16-1/4 in.) as in our experiments with water, buoyant forces become important and the role of drag forces diminishes. For a given liquid-gas phase, the forces to be balanced are inertial and gravity forces. This is shown to be true by the excellent correlation of the results with water for different diameter pipes on the basis of Froude number. However, when the liquid viscosity is increased, the bubbles become larger and the shape is more typically that of a helmet. The upward forces on the bubble increase and the relative magnitudes of buoyant and drag forces change.

One therefore expects larger flow rates to flush out the gas phase from the vertical pipe with increase of viscosity in this regime. A simple correlation in this regime is not possible because of the complex effects of viscosity on bubble size and shape and the varying importance of drag force in relation to buoyant force. When the pipe diameter is not very large compared to the bubble size (not more than about 10 times), the problem is further complicated by wall effects.

With liquid kinematic viscosities in the range of 10×10^{-6} to 19×10^{-6} m^2/s, and pipes of 3/4-in. (19.1 mm), 1-in. (25.4 mm), 1-1/2-in. (38.1 mm) and 2-in. (50.8 mm) inside diameter, a dimensional correlation parameter was obtained (equation (4)). Analysis of this parameter reveals the following:

1) For the same viscosity, the increase in the value of the critical velocity with increasing pipe diameter is smaller than for the low viscosity regime.

2) For a given pipe, increasing the liquid viscosity leads to a significant increase in the critical velocity.

With small-diameter pipes at large enough viscosities, an interesting phenomenon can be observed (19.1 mm and 25.4 mm pipes with kinematic viscosities of about 28×10^{-6} m^2/s in the present study). The liquid begins to flow down the surface of the vertical pipe as a falling film with no bubbling at the bottom liquid surface. As flow is increased, the liquid forms an envelope around the air column in the pipe, creating a single long cylindrical bubble. At a velocity considerably higher than the critical velocity predicted by the correlations in the other two regimes, the long bubble is suddenly swept away by the stream. This phenomenon may not be seen in large pipes in which the falling liquid is likely to break up and form a jet before forming an envelope inside the vertical pipe. However, this phenomenon needs further investigation.

O. C. Iloeje[1]
Lecturer,
University of Nigeria,
Nsukka,
Anambra State, Nigeria

J. A. Kervinen
Engineer.

J. Ireland
Engineer.

B. S. Shiralkar
Manager.

ECCS Methods,
General Electric
Nuclear Energy Division,
San Jose, Calif.

Flow Split Relationships in Two-Phase Parallel Channel Flows

The observed flow combinations through the channels were: cocurrent upflow in both channels, cocurrent upflow in one and countercurrent flow in the other channel, and cocurrent upflow in one and single phase liquid downflow in the other channel. The flow regimes in each channel varied from churn-turbulent, through anular flow, to chugging counter-current flow, as the flow conditions were varied. It was observed that the flow combination obtained was history dependent. However, for given flow combinations, certain flow split relationships were established. With both channels in cocurrent upflow, the flow quality into each channel was approximately the same as the flow quality in the lower plenum at the flow split elevation. For the other flow combinations, a simple relationship between the void fractions at the bottom of the channels which had two phase fluid, and the average void fraction and vapour flux in the lower plenum at the flow split elevation, was established.

Introduction

In the analysis of the thermal-hydraulic response of a Nuclear Reactor (BWR or PWR), during loss of coolant accidents, it is necessary to know the phase flow rates through each bundle so that an accurate fuel cladding heat-up transient can be calculated. A similar need is encountered in process industries when a two-phase mixture flows from a common inlet header (plenum) through multiple parallel channels, to a common exit header. The flow rates through each channel will depend on the homogeneity of the inlet flows, the pressure drop characteristics of the channels, and the conditions of energy and mass transfers inside the channels. If the inlet flow is homogeneous and the channel conditions are identical, then the phase flows may be assumed equally split among the channels. Generally, this is not the case, and an involved model is required to calculate the different flows.

Figure 1 shows a possible flow configuration for a set of vertical, parallel dissimilar channels. The configuration shows some channels in cocurrent upflow, and others in countercurrent flow or single phase flow at the bottom entry. There is an equally mixed flow mode at the top exit of the channels. Obviously an equal flow split among the channels cannot be assumed. If the channels and plena are assumed to be one dimensional flow paths in which pressure variations across a given elevation are negligible, then it may be assumed that the pressure drop across each channel is the same. This gives a set of equations for determining the phase flows into the channels. Additional equations are obtained from the conservation of mass and energy.

It can be shown that a total of $(5N+1)$ equations will be obtained from the above relationships, in terms of W_{g0}, W_{f0}, P, Q_i, W^b_{gi}, W^b_{fi}, W^t_{gi}, W^t_{fi}, ΔP_i, and θ_i. N is the total number of channels. With W_{g0}, W_{f0}, P, and Q_i as the known quantities, there are $6N$ unknowns. The additional $N-1$

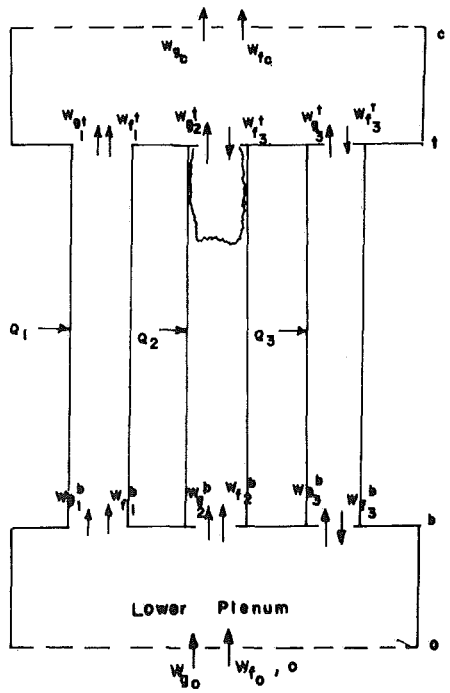

Fig. 1 Parallel channels with mixed mode flow

[1] Formerly Senior Engineer, General Electric Nuclear Energy Division, San Jose, Calif.

Contributed by the Fluids Engineering Division for publication in the JOURNAL OF FLUIDS ENGINEERING. Manuscript received by the Fluids Engineering Division, November 14, 1980.

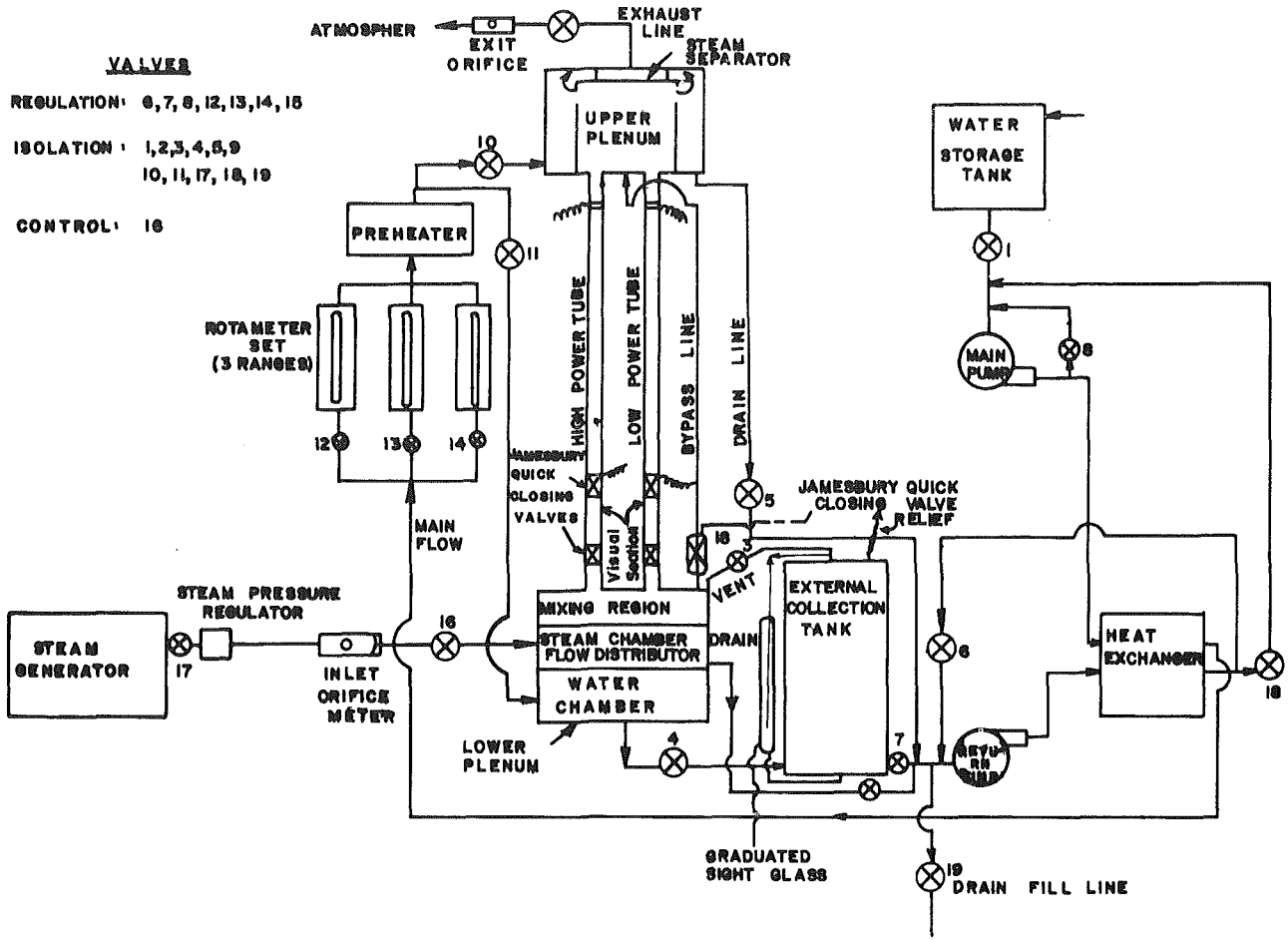

Fig. 2 Sketch of test loop

equations required can be supplied by specifying relationships between the liquid and vapor flows at the entries or exists to $(N-1)$ channels. Since these relationships are usually not known in the general case, and there's a high degree of uncertainty as to their assumption, an experimental programme was therefore set up to determine them.

Some Relevant Previous Work

Eselgroth and Griffith [1] studied the steady state flow configurations for five parallel tubes, using freon and blocked plena inlets. The authors, as in this paper, observed cocurrent up flow and countercurrent flow in the tubes. They concluded that cocurrent downflow was not possible. This conclusion may not hold in all cases. Countercurrent flow limitation (CCFL) at the upper orifices of some high power channels, or the introduction of subcooled liquid into some vapor filled channels, during a reflood transient, may cause most of the reflood liquid to flow down a few channels. The resulting high liquid velocities may cause transient cocurrent downflows. The effects of liquid subcool on parallel channel behaviour was studied in reference [2].

Reference [3] demonstrated that single tube data could be used to predict burnout, flow reversal points, and single phase liquid flow rates into a five channel array, with blocked inlets. There was no need for phase split relationships. Reference [4] presented a model for calculating two phase flow split transients (including flow reversals) for parallel channels. Single tube pressure drop correlations, as well as history dependent phase split relationships, were used.

The Experiment

The objectives of the test were therefore,

(*a*) to determine the relationship(s), if any, between the two phase flow in the lower plenum and the phase flows at the bottom entry into the channels.

Nomenclature

P = pressure bar
W = flow rate kg/s
θ = vapor generation rate kg/s
Q = heat addition rate kW
X, x = quality
ϕ, α = void fraction
$h; h_{fg}$ = enthalpy; enthalpy of evaporation KJ/kg
A, a = flow area m^2
C_0 = void distribution parameter
g = vapor phase
f = liquid phase
$f0$ = total inlet liquid
$g0$ = total inlet vapor
hpt, HPT = high power tube – with 9.5mm inlet orifice
lpt, LPT = low power tube – with 6.4mm inlet orifice
ch = channel
lp = lower plenum
V_{gj} = slip velocity m/s
G = mass flux kg/s – m^2
Re = Reynolds number
$\rho; \sigma$ = density kg/m^3; surface tension N/m
Δ = finite change in given quantity

Subscripts and Superscripts

$i, 1, 2$ = channel identifier
$b; t$ = bottom; and top of channel, respectively

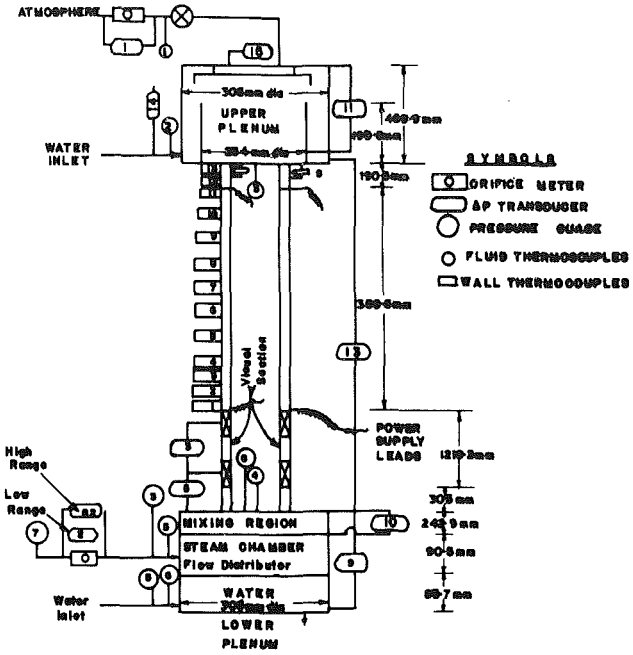

Fig. 3 Test section instrumentation (not to scale)

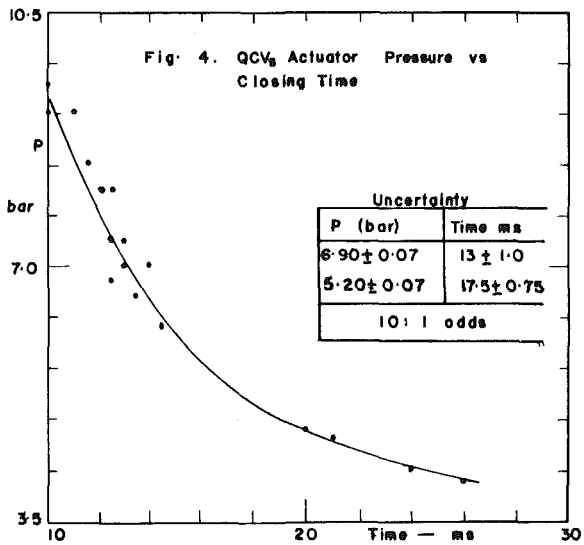

Fig. 4

(*b*) to determine the effects of test section power levels and power ratios, and methods of establishing the flows, on the relationship(s).

Test Loop. The test loop is sketched in Fig. 2. The loop includes a low pressure steam generator rated at 8.3 bar and 0.0378 kg/s. The steam passes through a pressure regulator, which maintains the downstream pressure at a preset value of 1.38 – 1.41 bar. It then flows into the steam side of the lower plenum flow distributor. The steam mixes with water in the upper region of the lower plenum, above the distributor, and the two phase mixture splits into the parallel tubes at phase ratios which depend on the flow conditions. In the upper plenum, the vapor flows around and over an inverted cup, which prevents liquid carry-over, before being exhausted into the atmosphere. The water returns through the drain line.

The water loop is a quasi-closed circuit, with make up water from the storage tank. The 33½ kW capacity preheater is used to bring the water to saturation before it flows into the upper or lower plenum, as required. Water, introduced into

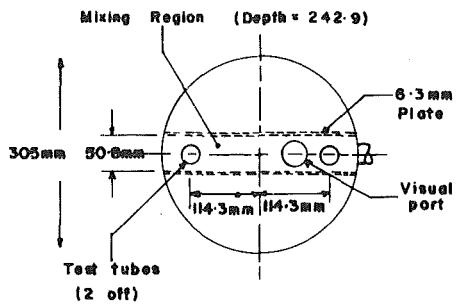

Fig. 5 Plan of lower plenum showing mixing region

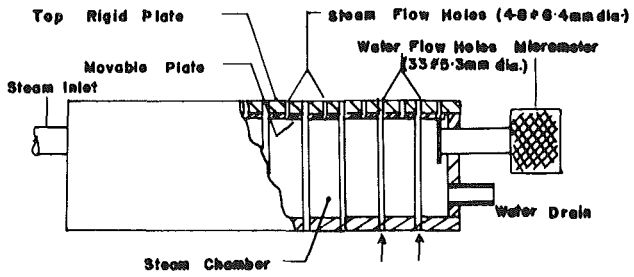

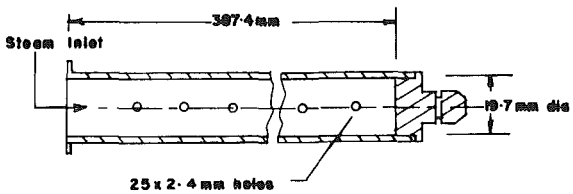

Fig. 6

the lower plenum, passes from the water side of the lower plenum flow distributor into the mixing region. The return flow from the upper plenum passes from the return pump back to the preheater. There is also a 0.283m^3 external collection tank, used in some experiments to measure the net amount of water draining from the channels into the lower plenum.

The test sections are two 5220mm long × 25.4 mm od × 23.6 mm id stainless steel tubes, instrumented as shown in Fig. 3. They can be electrical-resistance heated over approximately 3505mm of their lengths. Each tube has a 1219mm long visual section made of 23.6mm id pyrex tube, between the QCV's. The restriction at the bottom entry of the HPT is a 9.5mm square-edge orifice, and that for the LPT is a 6.4mm orifice of similar design. At the top exit of each tube is a 4-hole × 7.6mm orifice.

The four 25.4mm Jamesbury ball valves, which form part of the Quick Closing Valve system, are designed to close or open simultaneously. The closing time for the test was 13-14 milliseconds (actuator air pressure of 7 bar). A plot of air-pressure vs closing time is shown in Fig. 4. When actuated, the valves trap the fluid between them. After stratification the volume of liquid trapped between the QCV's, and hence the average void fraction between the valves, can be measured.

The outputs of the measuring instruments, in millivolts (except for the rotameters and pressure gauges) were recorded on a Dymec data acquisition system, and appropriately converted to actual units using the instruments caliberation curves.

The Mixing Region. The plan of the lower plenum, sketched in Fig. 5, shows the mixing region. It is a 50.8mm wide × 242.9mm deep section, running diametrically across

Table 2 Results for tests of Table 1

Run Number		38	39	40	3000	3024	1001	1004
W_g*10^3	HPT	5.71	4.95	5.66	1.17	5.30	4.94	4.81
kg/s	LPT	0.0	0.81	0.0	0.08	0.84	0.69	0.0
W_f*10^3	HPT	247.6	27.6	232.1	272.2	32.3	29.5	18.7
kg/s	LPT	−247.6	−27.6	−232.1	28.0	14.9	−29.5	−52.4
α between	HPT	.8055	.956	.8049	.6545	.9499	.9552	.9597
QCV's	LPT	0.0	.780	0.0	.6545	.9123	.7605	0.0
Inlet	HPT	.023	.152	.024	.0043	.141	.1436	.2048
Quality	LPT	0.0	–	0.0	.003	.0535	–	0.0
Lower Plenum	α	.4301	.4574	.4217	.185	.505	.4452	.4162
(top)	X	–	–	–	.004	.115	–	–
$\frac{1}{\alpha_{lp}} - \frac{1}{\alpha_{ch}}$	HPT	1.08	1.13	1.13	3.50	0.92	1.19	1.35
(α_{ch} at inlet)	LPT	–	1.19	–	3.22	0.86	1.25	–
$(\rho_g V_{gj}/G_g)_{lp}$		0.85	0.74	0.89	3.62	0.60	0.79	0.94

Table 1 Sample test matrix

Run number			W_{g0} $*10^3$kg/s	W_{f0} $*10^3$kg/s (net)	Test procedure	T Atm °C	P_{lp} bar	P test section bar
	HPT	LPT						
38	0.0	0.0	5.71	0.0	Gradual introduction of vapor	26	1.72	0.38
39	0.0	0.0	5.76	0.0	Sudden introduction of vapor	26	1.48	0.096
40	1.878	1.0	5.66	0.0	Gradual introduction of vapor	26	1.79	0.34
3000	3.612	2.025	1.25	300.26	Gradual introduction of liq. and vap. in LP	23.9	1.97	0.35
3024	3.60	1.975	6.14	47.14	Same as for 3000	23.9	1.67	0.24
1001	1.806	1.0	5.56	0.0	Gradual introduction of vapor	23.9	1.53	0.08
1004	1.758	1.0	4.82	−33.73	Same as for 1001 with net liquid downflow	23.9	1.57	0.165

the lower plenum. Liquid and vapor are introduced, through uniform distribution holes, into the bottom of the mixing region, and they flow out through the channels at the top of the region.

Flow Distributor. The two types of flow distributors used are shown in Fig. 6. The vapor hole size for type 1 (Runs 10 to 1012, and 3000 to 5026R) can be altered, using the movable plate. Type-2 (for Runs 1013 to 2017 and 9015) is a simple tube with holes drilled on its upper side.

Further details of the test section may be found in reference [5].

Experimental Procedure. In the tests, saturated vapor was always supplied to the lower plenum. Saturated liquid was supplied either to the lower plenum or to the upper plenum. In the former case, net cocurrent flow through the channels, were established. In the latter, net countercurrent flow or net zero liquid flow (liquid downflow in one channel = liquid upflow in the other channel) was established. For liquid supply to the upper plenum, the external collection tank was used to measure the net liquid downflow.

With the net liquid down flow as zero, the method of introducing the vapor was varied. In some of such runs, the vapor flow rate was gradually increased to the desired value. In others, the QCV's were closed while the vapor was introduced into the lower plenum. The lower plenum was thus pressurised. The QCV's were then opened, so that vapor was suddenly introduced into the channels. The flow rates were allowed to stabilize before data were taken.

At steady state, the transducer outputs were recorded on channels 1-62 of the Dymec over many cycles. The average values over the cycles were used. Pressure gauge and rotameter readings were manually taken. From these data, total liquid and vapor flow rates, test section powers, inlet void fractions, qualities, pressures, and pressure drops were calculated.

The tube/QCV system was calibrated for void/quality

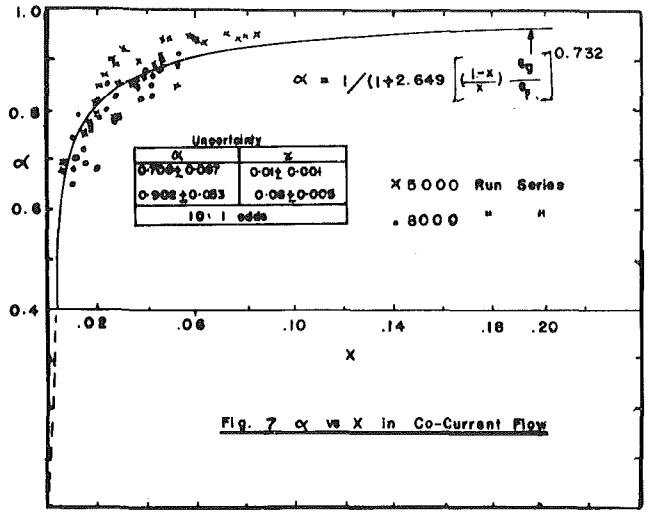

Fig. 7 α versus X in cocurrent flow

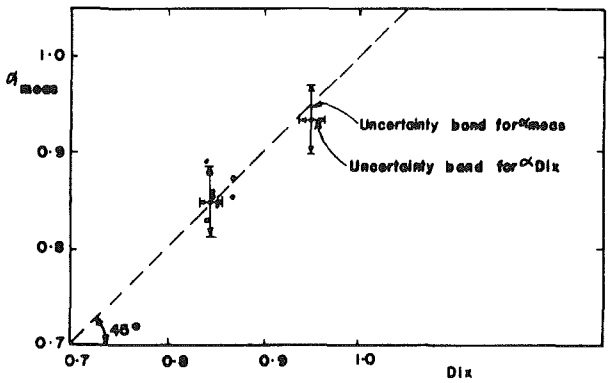

Fig. 8 α_{meas} versus α_{DIX} in chugging countercurrent flow

relations in cocurrent and counter-current flows, with one tube operating at a time.

Test Matrix. The flows and heat inputs varied within the following ranges:

W_{g0}: $1.26 - 129.8 * 10^{-3}$ kg/s; W_{f0}: (downflow) $0 - 472.5 * 10^{-3}$ kg/s

Q_{hpt}: $0 - 20.7$ KW; W_{f0}: (upflow) $0 - 504.9 * 10^{-3}$ kg/s

Q_{lpt}: $0 - 5.2$ KW; Q_{hpt}/Q_{lpt}: $1 - 1.8$

The test matrix for some representative tests is shown in Table 1, with the corresponding results shown in Table 2.

Data Reduction

Void Fraction and Flow Quality. The average void fraction between the QCV's is given by

$$\alpha = \frac{\text{Volume between QCV's} - \text{Volume of liquid trapped}}{\text{Volume between QCV's}} \quad (1)$$

If the flow is fully developed and there is negligible flashing or condensation of vapor between the QCV's, then the value of α given by equation (1) is also the value of the constant α between the QCV's.

Using Latzko's [6] expression for onset of fully developed turbulent velocity profile in single phase flow, (equation (2)), but with a two phase flow viscosity given by equation (3),

$$Z/D = 0.693\ \mathrm{Re}^{1/4} \quad (2)$$

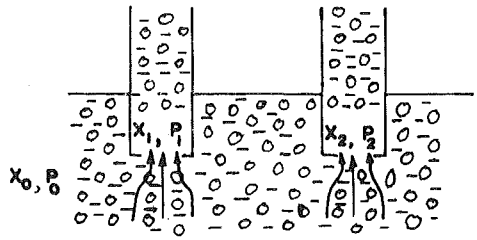

Fig. 9(*a*) All channel inlets and lower plenum in cocurrent up flow

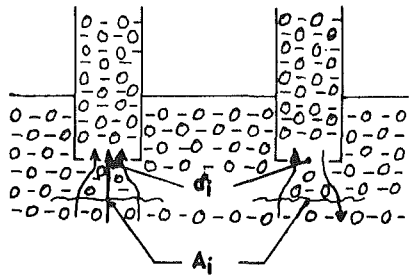

Fig. 9(*b*) Mixed flow modes at channel entries. All channel inlets submerged in two phase mixture in lower plenum

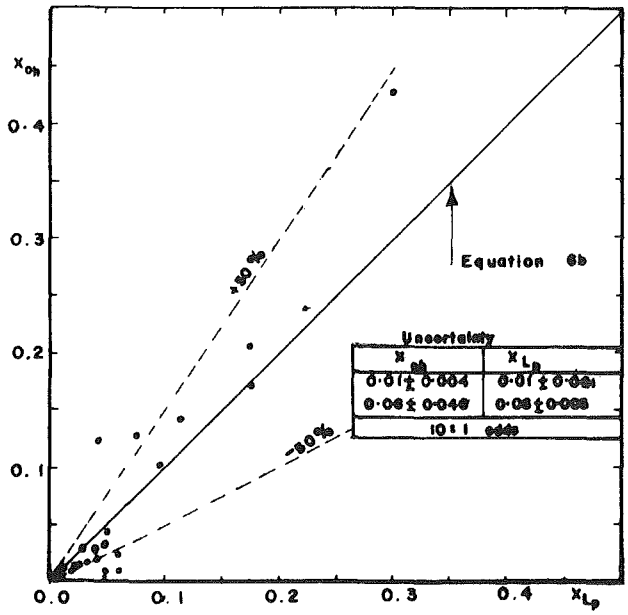

Fig. 10 X_{ch} versus X_{lp} for HPT

$$\mu = \chi\mu_g + (1-x)\mu_f \quad (3)$$

the largest Z/D for fully developed flow in the experiments was approximately 10. Allowing for an underestimate of 50 percent by equation (2), the value becomes 20. This gives a developing length of 472 mm. The length of tube between the lower plenum and the lowest QCV was 305 mm, or 13 diameters. Thus at highest flow rate, length of developing flow extending into the pyrex tube was 167 mm, or only 14 percent of the length of the pyrex tube. The flow was therefore assumed fully developed, or nearly so, at entry to the pyrex section.

The measured α corresponded to the actual α somewhere between the QCV's. Changes in vapor flow rate between the QCV's, though small, arose predominantly from gravity pressure changes. For a given test, this was approximately linear with height. For small changes in x and α, α would also vary approximately linearly with height. The measured average void fraction was therefore assumed to correspond to the actual α at the midpoint of the pyrex tube. Errors from

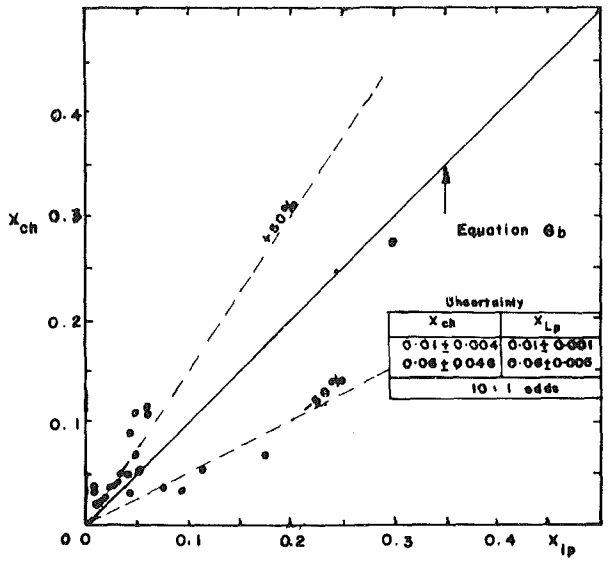

Fig. 11 X_{ch} versus X_{lp} for LPT

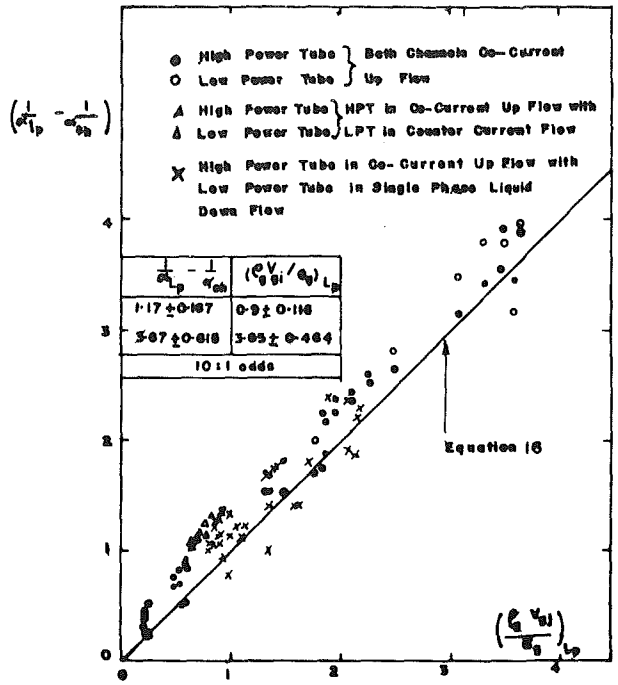

Fig. 12 Comparison of flow split data with equation (34) $(1/\alpha_{lp} - 1/\alpha_{ch})$ versus $(\rho_g V_{gj}/G_g)_{Lp}$

this assumption on the corresponding values of x were calculated and found negligible.

Flow quality, $W_g/(W_g + W_f)$, at entry to the channels differed from those within the pyrex tube, principally as a result of throttling at the inlet orifices. An energy equation between lower plenum and the midpoint of the pyrex tube was written to correct for the effects of pressure change, potential and kinetic energy changes and heat losses. The effects of the last three factors were very small.

Flow Split With Both Channels in Cocurrent Flow at Inlet. The phase flow rates, W_g and W_f at entry to each channel were determined using the mass conservation equations for liquid and vapor at lower plenum/channel boundary, void-quality relationship given in equation (4) and obtained from caliberation data, and the energy equation between the lower plenum and the midpoint of the pyrex tube for each channel.

$$x = 1/\left(1 + \frac{\rho_f}{\rho_g}\left(\frac{1-\alpha}{2.649\alpha}\right)1.366\right) \tag{4}$$

Equation (4) is shown in Fig. 7.

Flow Split With One Channel in Cocurrent, and the Other in Countercurrent, Flow. The equations were the same as those for both channels in cocurrent flow, except that for the counter-current channel, the drift flux void fraction equation, with the parameters C_0 and V_{gj} given by the Dix correlation, equation (5) and reference [7], replaced equation (4)

$$C_0 = 1.0 + f_1(\delta)^* f_3(\alpha)/(1 + \mathrm{Re}/4.11^*10^5)^{1/2} \tag{5a}$$

$$V_{gi} = 2.5 f_0(\rho) \text{ ------ for } 0 < \alpha < \alpha_2 \tag{5b}$$

$$V_{gj} = (2.5 + f_4(\mathrm{Re})(\alpha - \alpha_2)/0.1)^* f_0(\rho) \quad \text{for } \alpha_2 < \alpha < \alpha_2 + 0.1 \tag{5c}$$

$$V_{gj} = K_g(1-\alpha)^* f_0(\rho) \text{ --- for } \alpha_2 + 0.1 < \alpha < 1.0 \tag{5d}$$

where

$$\delta = \rho_g/\rho_f \tag{5e}$$

$$f_0(\rho) = (g\sigma(\rho_f - \rho_g)/\rho_f^2)^{1/4} \tag{5f}$$

$$\alpha_2 = 0.625 + 0.15\exp(-\mathrm{Re}/1.12^*10^5) \tag{5g}$$

$$f_1(\delta) = 0.5 \text{ for } \delta << 1.0 \tag{5h}$$

$$K_g = (2.5 + f_4(\mathrm{Re}))\delta^{1/2}/(0.9 - \alpha_2) \tag{5i}$$

$$f_3(\alpha) = 1.0 \text{ for } \alpha \le \alpha_1 \tag{5j}$$

$$= (1.0-\alpha)/(1.0-\alpha_1) \text{ for } \alpha > \alpha_1 \tag{5k}$$

$$\alpha_1 = (5/6)^* f_1(\delta)/(1 + \mathrm{Re}/4.11^*10^5)^{1/2}) \tag{5l}$$

$$f_4(\mathrm{Re}) = 0.9(1 - (\mathrm{Re}/2.01^*10^5)) \quad \mathrm{Re} \le 2.01^*10^5 \tag{5m}$$

$$= 0.0 \quad \mathrm{Re} > 2.01^*10^5 \tag{5n}$$

The above correlation was developed for cocurrent flow. However, by using the absolute value of the Reynolds number, the equation was found to correlate data for chugging counter-current flow well, as shown in Fig. 8. The countercurrent flow regime in the tests were of the chugging type.

Flow Split With One Channel in Cocurrent Flow, and the Other in Single Phase Liquid Downflow. The equations were the same as for the previous flow split cases, except that for the channel with single phase liquid, $W_g = 0$.

Analysis

A simple flow split relationship can be developed for the case in which both the lower plenum and all the channels are in cocurrent upflow. Figure 9(*a*) illustrates such a case. The flow is assumed homogeneous in the lower plenum. If X_0 and P_0 are the quality and pressure in the lower plenum at the flow split elevation, and X_1, P_1, X_2, P_2 are the qualities and pressures at entries to the respective channels, then at steady state,

$$x_0 h_{fg0} + h_{f0} + \frac{V_0^2}{2J} = x_1 h_{fg1} + h_{f1} + \frac{V_1^2}{2J} = x_2 h_{fg2} + h_{f2} + \frac{V_2^2}{2J} \tag{6}$$

If $P_1 \doteq P_2 \doteq P_0$ and kinetic energy changes are negligible, then

$$x_1 = x_2 = x_0 \tag{6a}$$

The flow split relationship for this flow situation becomes

$$x_{ch} = x_{lp} \tag{6b}$$

Figure 9(*b*) illustrates the more complicated case in which one channel is in cocurrent upflow while the other is in countercurrent flow, at their inlets. The inlets of both channels are submerged in the two phase fluid in the lower plenum.

Let W_{gi}, W_{fi} be the vapor and liquid flows through a channel entry.

a_i = Channel flow area at entry
A_i = Cross sectional area of the stream tube, in the lower plenum at the flow split elevation, through which the flows W_{gi} and W_{fi} pass.
α_i, ϕ_i = average void fractions over a_i and A_i, respectively

From the drift flux equations:

$$\alpha_i \equiv W_{gi} / \left(C_{0i} \left(W_{gi} \pm W_{fi} \frac{\rho_{gi}}{\rho_{fi}} \right) + a_i \rho_{gi} V_{gji} \right) \tag{7}$$

$$\phi_i = W_{gi} / \left(C'_{0i} \left(W_{gi} \pm W_{fi} \frac{\rho'_{gi}}{\rho'_{fi}} \right) + A_i \rho'_{gi} V'_{gji} \right) \tag{8}$$

(the primed quantities refer to values at A_i)

and making the following assumptions:

(*a*) Dynamic pressure heads are negligible, i.e., $P_i = P'_i$

(*b*) $C_0 = C'_0$ (*c*) $V_{gji} = V'_{gji}$

Then

$$\frac{1}{\alpha_i} = C'_{0i} \left(1 \pm \frac{W_{fi}}{W_{gi}} \frac{\rho_{gi}}{\rho'_{fi}} \right) + a_i \left(\rho'_{gi} \frac{V'_{gji}}{W_{gi}} \right) \tag{9}$$

$$\frac{1}{\phi_i} = C'_{0i} \left(1 \pm \frac{W_{fi}}{W_{gi}} \frac{\rho'_{gi}}{\rho'_{fi}} + A_i \left(\rho'_{gi} \frac{V'_{gji}}{W_{gi}} \right) \right) \tag{10}$$

$$\frac{1}{\phi_i} - \frac{1}{\alpha_i} = \frac{\rho'_{gi} V'_{gji}}{W_{gi}/A_i} \left(1 - \frac{a_i}{A_i} \right) \tag{11}$$

If, as in many cases of practical application, $a_i << A_i$, then equation (11) becomes

$$\frac{1}{\phi_i} - \frac{1}{\alpha_i} = \frac{\rho'_{gi} V'_{gji}}{W_{gi}/A_i} \tag{12}$$

Equation (11) has the correct limit as a_i approaches A_i. If we assume that both the void fraction and the vapor flux are uniform across a given elevation in the lower plenum, then

$$\phi_i = \alpha_{lp} \text{ at the flow split elevation} \tag{13}$$

$$W_{gi}/A_i = (W_g/A)_{lp} \quad " \quad " \quad " \tag{14}$$

When the void distribution over a lower plenum elevation is uniform, equations (13) and (14) are compatible. Such a situation is approximated during bulk vaporization in the lower plenum of a nuclear reactor which is undergoing a depressurization transient, or when all the channels and the lower plenum are in cocurrent flow or countercurrent flow. If some channels are in cocurrent flow while others are in countercurrent flow at their inlets, the two equations are not compatible. However, for computational reasons, we may assume the two equations to hold. Equations (11) and (12) then become

$$\frac{1}{\alpha_{lp}} - \frac{1}{\alpha_{ch}} = \left(\frac{\rho_g V_{gj}}{G} \right)_{lp} \left(1 - \frac{a_i}{A_i} \right) \tag{15}$$

$$\frac{1}{\alpha_{lp}} - \frac{1}{\alpha_{ch}} = \left(\frac{\rho_g V_{gi}}{G} \right)_{lp} \tag{16}$$

where lower plenum values are calculated at flow split elevation. When $a_i << A_i$, as will be the case if the channel inlet area is a significant proportion of the total lower plenum cross-sectional area at the flow split elevation, then equation 15 will be used, and the ratio a_i/A_i must be estimated. An estimate for the ratio is obtained by assuming that

$$A_i/A_{lp} = a_i / \sum_i a_i \tag{17}$$

$$\therefore a_i/A_i = \left(\sum_i a_i \right) / A_{lp} \tag{18}$$

Results

Test results for the matrix of Table 1 are shown in Table 2. The flow split data for both the channels and the lower plenum in cocurrent upflow are plotted in Fig. 10 and 11, for the HPT and LPT. Equation (6*b*) is seen to represent the data well, within experimental errors.

Figure 12 shows a plot of $(1/\alpha_{lp} - 1/\alpha_{ch})$ versus $(\rho_g V_{gj}/G_g)_{lp}$ for all the flow split combinations observed. Within the channels themselves, the observed flow regimes were churn-turbulent or slug or anular for cocurrent flow, chugging countercurrent flow, or single phase liquid downflow. Channel inlet void fractions when in countercurrent flow, V_{gj} and lower plenum void fractions were calculated using the Dix correlation (equation (5)). The figure also shows a comparison of the data with equation (16). The data are biased to one side of the equation, but nevertheless, the comparison is quite good.

The data in figure 12 appears to follow the equation

$$1/\alpha_{lp} - 1/\alpha_{ch} = \Phi + (\rho_g V_{gj}/G_g)_{lp} \tag{19}$$

Φ is non zero if the first two terms on the right-hand side of equations (9) and (10), or V_{gj} and V'_{gj} and V'_{gj}, are not equal. It is therefore a measure of how accurate assumptions (*a*), (*b*), and (*c*), on which the equations were based, are.

For the tests reported here, the maximum dynamic pressure head at channel entry was estimated as 4 percent of lower plenum pressure. This would introduce less than a 5 percent difference in vapor density, and negligible difference in liquid density. At rated flows, the dynamic pressure head at the channel entry nose piece of a BWR is 0.2 percent to 0.27 percent of system pressure (69 bar). Thus assumption (*a*) is fairly good.

Using the Dix correlation (equation (5)), the ratios C_0/C'_0 and V_{gj}/V'_{gj} were determined for $0.01 < \phi < 0.7$; $10^3 \le R'_e \le 10^5$; $1.01 \le P \le 69$ bar and $0.0 < a_i/A_i \le 1$. It was found that within these ranges of parameters, $0.8 \le C_0/C'_0 \le 1.0$. The V_{gj}-ratio was less well behaved. However, for $a_i/A_i > 0.5$ and $Re = 10^5$, then $0.8 < V_{gi}/V'_{gj} < 1.1$. For $a_i/A_i > 0.2$ and $Re = 10^3$, then $0.8 < V_{gj}/V'_{gj} < 1.3$. Assumption (*b*) is therefore acceptable within the range of parameters given above. Assumption (*c*) is admissible for $\phi < 0.7$, $a_i/A_i > 0.3$ and $10^3 \le R'_e \le 10^5$.

The data plotted in Figs. 10, 11, 12 were obtained with various test-section power levels, within the range given in the test matrix. No definite effect of channel power level or power ratio was observed in the figures.

For the tests with zero net liquid flow rate, the method of introducing the vapor into the channels was varied between a gradual and a sudden introduction of vapor. With gradual increase in vapor flow rate, the LPT remained in single phase liquid downflow until a total vapor flow rate of 0.0114 kg/s was reached. Chugging countercurrent flow was then established in this channel. On reduction of total vapor flow

rate, single phase liquid downflow was not re-established in this channel until the vapor flow rate was reduced to 0.0058 kg/s. There was thus a hysteresis effect on the flow configuration obtained as the total vapor flow rate was varied. It was also found that with sudden addition of vapor, chugging countercurrent flow was established in the LPT provided the total vapor flow rate was greater than 0.0058 kg/s. In all these flow configuration tests with zero net liquid flow, the HPT was in cocurrent upflow.

Figure 12 includes data obtained from the above flow configuration tests. Thus, though the method of introducing the flows affected the resulting flow configuration, the stable flow split relationship was not affected.

Conclusions

1. Simple flow split relationships for channels communicating between the same upper and lower plena have been developed and are given by equations (6*b*) and (15) or (16).

2. Equation (6*b*) is applicable when the lower plenum and all the channel inlets are in cocurrent upflow, and the lower plenum void distribution is uniform at a given elevation.

3. Equation (15) or (16) is applicable when the channel entries are submerged in a two-phase flow in the lower plenum, and the channel in question is in two phase flow at its lower plenum entry. The following conditions also need to be satisfied.

(*a*) Uniform void distribution in the lower plenum at the flow split evaluation.
(*b*) Low void fractions in the lower plenum (<0.7)
(*c*) Moderate-to-high ratio of total channel inlet areas to lower plenum cross-sectional area at flow split elevation.
(*d*) $10^3 \leq (\mathrm{Re})_{lp} \leq 10^5$. (The validity of the assumption on which the relationship was developed was not tested for $\mathrm{Re}_{lp} > 10^5$)

4. Experimental data from a vertical two channel system at near atmospheric pressure, have been compared with the relationships, with encouragingly good results.

5. Within the range of channel power levels and power ratios tested, no effect of these parameters was found to influence the validity of the flow split correlations.

6. Though the method of introducing the flows, and the flow levels, may influence the modes of flows at the channel entries, once a flow configuration is known to exit, equation (6*b*) or (15) or (16) will apply, irrespective of how the flows were established.

References

1 Eselgroth, P. W., and Griffith, P., "Natural Convection Flows in Parallel Connected Vertical Channels With Boiling," M.I.T. Report No. 70318-49, July 1967.

2 Iloeje, O. C., "Effects of Parallel Channel Interactions, Steam Flow, Liquid Subcool, and Channel Heat Addition on Nuclear Reactor Reflood Transient." (to be published) *Nigerian J. of Tech.*, NIJOTECH, Sept. 1982.

3 Eselgroth, P. W., and Griffith, P., "The Prediction of Multiple Heated Channel Patterns From Single Channel Pressure Drop Data," M.I.T. Report No. 70318-57, Oct. 1968.

4 Iloeje, O. C., and Avila, J., "Two Phase Flow Split Model For Parallel Channels," *Nig. J. of Tech.* (NIJOTECH), Mar. 1979.

5 Iloeje, O. C., Kervinen, J., Ireland, J., and Shiralrar, B. S., "Two Phase Flow Configurations and Flow Splits in Parallet Channels," General Electric Nuclear Energy Division, San Jose, NEDE, 1977.

6 Latzko, H., Z. angew Math. U. Mech., Vol. 1, p. 227, 1921; and as in *Turbulence*, by Hinze, J. O., p. 514, McGraw-Hill Book Co., 1959.

7 Dix, G. E., Sursock, J. P., and Wing, K. D., "New BWR Void Fraction Correlation," BWR Systems Department, Gen. Elec. Nuclear Energy Div., San Jose, Calif., Aug. 1975.

Discharge Coefficient for Venturi Flowmeter With Short Laying Length

Masahiro Inoue
Associate Professor,
Department of Mechanical Engineering,
Power Division,
Kyushu University,
Fukuoka, Japan.
Mem. ASME

This paper presents a method for predicting the discharge coeffcient for a venturi flowmeter with a short laying length where the static pressure is not uniform at the throat due to streamline curvature. The discharge coefficient is determined by combining potential flow calculations and one-dimensional viscous flow considerations. For the potential flow, an accurate computational technique proposed by the author is used to calculate the pressure at the throat tap by assuming that the total pressure is equal to the average one at the throat. The average total pressure is related to the inlet pressure by use of a generalized empirical equation based on one-dimensional considerations. Validity of the method is verified by comparison with published experimental data for short venturi flowmeters.

1 Introduction

From the viewpoint of energy conservation, the use of a venturi flowmeter is desirable for large flow rate measurement applications, since the pressure loss is much smaller than that for nozzle or orifice plate flowmeters. However, for applications involving large diameter pipes, the standard venturi flowmeter design [1, 2] becomes too long to be practical. Therefore, for such large applications, there is considerable interest at present in developing practical venturi tube designs that have a short laying length. However, before installation, these short venturi tubes need accurate calibration which becomes virtually impossible for large sizes. Hence, a reliable analytical method for obtaining the discharge coefficients for such short venturi flowmeters has been developed and is presented here.

For nozzle flowmeters, the discharge coefficient can be predicted using coupled potential flow and boundary layer flow calculations [3, 4]. An analogous method is adopted in this study where a potential flow calculation [5] is used with a one-dimensional viscous flow calculation [6]. Validity of this method is investigated by comparing results with Halmi's experiments [7] on short venturi flowmeters with low pressure loss.

2 Analysis

2.1 Discharge Coefficient For a Short Venturi Flowmeter. The discharge coeffcient C_D, of a venturi flowmeter is defined as

$$C_D = Q/\{(\pi/4)d^2\sqrt{2(p_i - p_t/\rho}/\sqrt{1-\beta^4}\} \quad (1)$$

Ignoring fluid compressibility the energy relation is

$$\bar{p}_i + \tfrac{1}{2}\rho\alpha_i\bar{v}_i^2 = \bar{p}_t + \tfrac{1}{2}\rho\alpha_t\bar{v}_t^2 + \bar{p}_l \quad (2)$$

In the one-dimensional case, where the static pressures are assumed to be uniform at the inlet and throat section, the respective wall pressures are

$$p_i = \bar{p}_i \text{ and } p_t = \bar{p}_t \quad (3)$$

Substitution of equation (3) into (2) leads to

$$C_D = \sqrt{(1-\beta^4)/(\alpha_t - \alpha_i\beta^4 + \zeta)} \quad (4)$$

where $\zeta = \bar{p}_l/\tfrac{1}{2}\rho\bar{v}_t^2$.

To date, the discharge coefficient has been studied on the basis of equation (4). For example, Ferron investigated the effects of velocity profile on C_D [8], and Benedict and Wyler [6] proposed a generalized equation for C_D which was applicable not only to venturi tubes but also to other differential pressure type flowmeters. In general, an inlet tap can be located at a point where $p_i = \bar{p}_i$ holds. In the case of a short venturi tube however the wall pressure p_t is lower than the average value $\bar{p}_t$ owing to the effect of streamline curvature. Therefore, the one-dimensional relation of equation (4) is not applicable.

Here, a new expression for the discharge coefficient is proposed to take into account the non-uniformity in the throat static pressure profile. This expression includes a

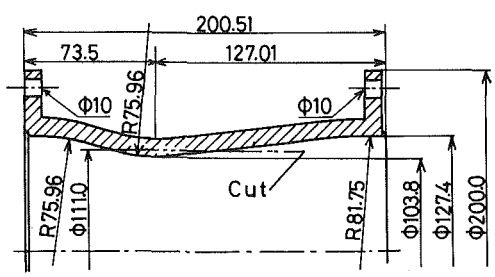

Fig. 1 Configuration of venturi tube used

Contributed by the Fluids Engineering Division for publication in the JOURNAL OF FLUIDS ENGINEERING. Manuscript received by the Fluids Engineering Division, September 1979.

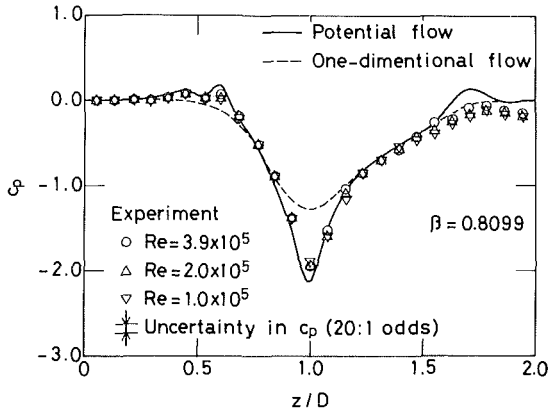

Fig. 2(*a*) Without cylindrical throat section

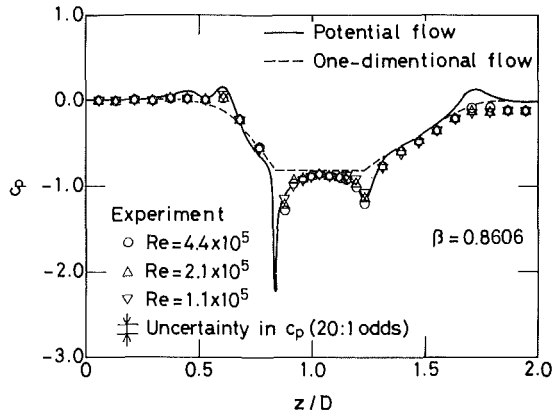

Fig. 2(*b*) With cylindrical throat section

Fig. 2 Distribution of surface static pressure for the venturi tube

rational approximation supported by experimental data. Namely, the pressure distribution is determined from the potential flow case where the stagnation pressure is the same as the average one at the throat section in the actual viscous flow. That is,

$$p_t + \tfrac{1}{2}\rho v_t^{*2} = \bar{p}_t + \tfrac{1}{2}\rho\alpha_t \bar{v}_t^2 \tag{5}$$

where v_t^* denotes the surface velocity at throat section in the potential flow. Substituting equation (5) and $p_i = \bar{p}_i$ into equation (2) gives the following relation:

$$C_D = \sqrt{(1-\beta^4)/(\gamma_t^2\beta^4 - \alpha_i\beta^4 + \zeta)} \tag{6}$$

where $\gamma_t = v_t^*/v_i$

Now, this relation is rewritten in a more convenient form by using a discharge coefficient C_I for the potential flow and a conventional discharge coefficient C_V for the one-dimensional viscous flow. Where,

$$C_I = \sqrt{(1-\beta^4)/(\gamma_t^2\beta^4 - \beta^4)} \tag{7}$$

using,

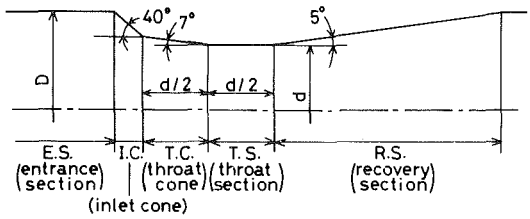

Fig. 3 Typical configuration of universal venturi tube [7]

$$p_i + \tfrac{1}{2}\rho v_i^2 = p_t + \tfrac{1}{2}\rho v_t^{*2},$$

and

$$C_V \equiv [C_D \text{ in equation (4)}]. \tag{4'}$$

From equations (6), (7), and (4'), it follows that

$$\frac{1}{C_D^2} = \frac{1}{C_I^2} + \frac{1}{C_V^2} - \frac{\alpha_t - \beta^4}{1-\beta^4} \tag{8}$$

An empirical relation is adopted for C_V, and hence, α_t is arbitrarily set equal to unity since the effect of α_t will be included in ζ [6]. Therefore, the discharge coefficient for the short venturi flowmeter becomes

$$C_D = C_V C_I / \sqrt{1-(1-C_V^2)\,(1-C_I^2)} \tag{9}$$

2.2 Potential Flow Study. The standard deviations on the discharge coefficients of the classical venturi tubes [2] range from 0.35 to 0.75%. Therefore, comparable or better accuracy is required in the potential flow calculation to determine C_I. This requirement can be satisfied by the method of singularity with spline fit distribution proposed by the author [5]. The application of the method to the venturi tube is summarized in the Appendix.

2.3 Empirical Relation for C_V. In general, for well designed venturi flowmeters as the Reynolds number increases C_V and hence its contribution to C_D decreases. Therefore, for the high Reynolds numbers encountered in large sized pipes and ducts where direct calibration is impractical, the small errors in the prediction of C_V will have a negligible effect on the prediction of C_D.

The value of C_V may hence be derived by extrapolation of the C_V versus R_e curve obtained from model tests, provided, of course, that the model tests are at high enough Reynolds number where an asymptotic behavior of C_V versus R_e is obtained. In the model tests, the values of C_V can be derived from the normal value of C_D by use of equation (9).

For a far simpler prediction of C_V without resorting to model tests, the generalized empirical equation by Benedict and Wyler [6] may be used:

$$C_V = [(1-\beta^4)/(1-\beta^4 + 9.7156\beta^{1/2}R_e^{-1/2} - 0.4505\beta^4 R_e^{-1/5})]^{1/2}$$

for "laminar" region ($Re \le 1\times10^5$) (10)

$$C_V = [(1-\beta^4)/\{1-\beta^4 + (0.17\beta^{1/5} - 0.4505\beta^4)R_e^{-1/5}\}]^{1/2}$$

for "turbulent" region ($Re > 1\times10^5$)

Nomenclature

C_D = discharge coefficient
C_I = discharge coefficient for potential flow
C_V = discharge coefficient for one-dimensional viscous flow
c_p = wall pressure coefficient $(=(p-p_i)/1/2\rho\bar{v}_i^2)$
D = diameter at inlet
d = diameter at throat
p = static pressure
$\tilde{p}_l$ = pressure loss
Q = flow rate
Re = Reynolds number referring to inlet condition
v = flow velocity
α = kinetic energy correction factor
β = diameter ratio $(=d/D)$
ζ = loss coefficient $(=\tilde{p}_l/1/2\rho\bar{v}_t^2)$
ρ = density of fluid

Suffix

i = inlet
t = throat
$-$ = average value
$*$ = potential flow

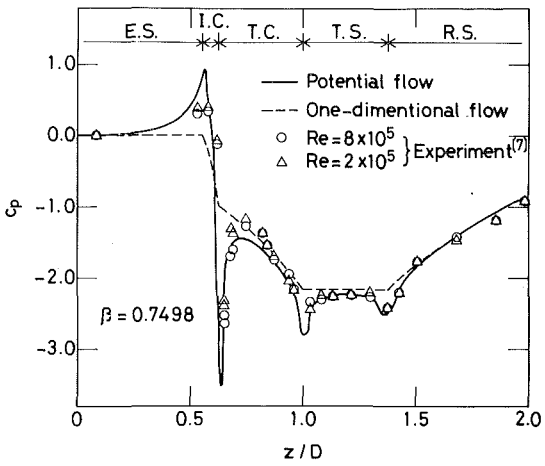

Fig. 4(*a*) β = 0.7498, inlet cone angle of 50 deg

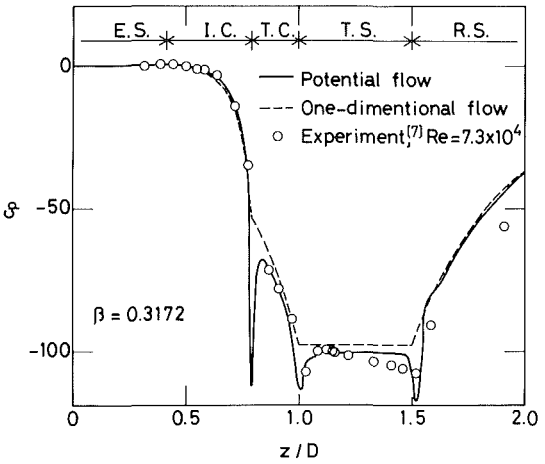

Fig. 4(*b*) β = 0.3172, throat section length of *D*/2

Fig. 4 Distribution of surface pressure for U.V.T.

3 Comparisons With Experiments

The proposed method uses potential flow theory. Hence, a question remains whether it can be applied to the fully developed viscous flow through the venturi tube installed in a long pipe line. Preliminary experiments were carried out to address this question. A converging-diverging tube as shown in Fig. 1 was installed downstream of long straight pipe. An inlet survey was performed to verify that a fully developed turbulent velocity profile occurred at the venturi tube inlet. Static pressures were measured along the wall surface, and are plotted in Fig. 2(*a*) in nondimensional form. In the figure, solid and broken lines indicate the calculated results from the potential flow theory and the one-dimensional theory, respectively. It is seen that the potential flow theory calculations show a good agreement, with the measured data. Whereas, a large discrepancy is observed between the experiment and the one-dimensional theory in the throat region.

Field designs of venturi flowmeters generally consist of a converging portion followed by a constant diameter throat section. Thus, the throat section was cut as shown in Fig. 1 and the pressure distribution was again measured and is shown in Fig. 2(*b*). Note that this geometry is suitable for field applications since the throat pressure measurement is relatively insensitive to the location of the throat tap due to the flat pressure distribution in the throat region. From Fig. 2(*b*) it is seen that for this geometry also, the potential flow theory predicts the experimental data quite well. This implies

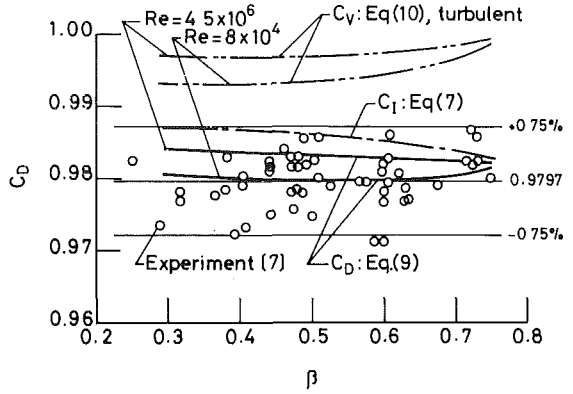

Fig. 5 Discharge coefficients for U.V.T.'s

that the discharge coefficients can be evaluated using potential flow theory with the viscous correction as described in the previous section. In fact, the measured discharge coefficient $C_D = 0.9696 \rightarrow 0.9729$ (for $R_e = 1.1 \rightarrow 4.4 \times 10^5$) agrees well with the calculated values of $C_D = 0.9658 \rightarrow 0.9678$ (Deviation: $0.0038 \rightarrow 0.0051$).

Next, comparisons are made with the numerous experimental data by Halmi [7], who developed the "universal venturi tube (U.V.T.)" with short laying length and low head loss.

Figure 3 shows a typical U.V.T. geometry which consists of a transition section with a 40°-inlet and 7°-throat cone followed by a constant diameter throat section, and a 5°-diverging recovery section. Figures 4(*a*) and (*b*) show the wall pressure distributions from Halmi's experiments, potential flow theory and one dimensional theory. Halmi observed some local separations and vena contractae at the entrance as well as at the exit of the cylindrical throat [7]. Nonetheless, the measured pressure distribution closely resembles that from potential flow theory in the case of $\beta = 0.7498$ (Fig. 4(*a*)). The drops in pressure at the intersection of the inlet and throat cone and of the throat cone and the throat section are therefore not solely due to the flow separations and the vena contractae, but also due to the effect of streamline curvature. In the case of low diameter ratio (Fig. 4(*b*)), there is some deviation between the data and the potential flow calculations in the downstream half of the throat section, but still the overall agreement between data and predictions is quite good.

Figure 5 shows the measured discharge coefficients from the calibrations of 51 standard U.V.T.s ranging in diameter from 7.62 to 106.68mm, and with $\beta = 0.2$ to 0.75, and $R_e = 8 \times 10^4$ to 4.5×10^6. Most of the data fall within a $\pm 0.75\%$ tolerance band around a mean value—"universal value"—of $C_D = 0.9797$, independent of β. In the figure, the predicted values for C_I, C_V, and C_D are also shown. A comparison between the predicted and the experimental results reveals that:

(i) The discharge coefficient cannot be predicted only by the one-dimensional viscous consideration (C_V) and the streamline curvature effects must be accounted for.

(ii) The predicted discharge coefficients are satisfactory for the wide range of β considered. The predictions are slightly higher than the "universal value" probably due to the local separations at the intersections, not accounted for in the prediction method.

(iii) The predicted values of C_D are nearly independent of β, since C_V tends to increase with β while C_I decreases.

In Figs. 6(*a*) to (*c*), the calculated results are compared with the experimental data in the ranges of low, medium and high Reynolds number case for which the data were obtained on U.V.T.s with $D = 38.1 \rightarrow 457.2$mm and $\beta = 0.31 \rightarrow 0.75$. Close

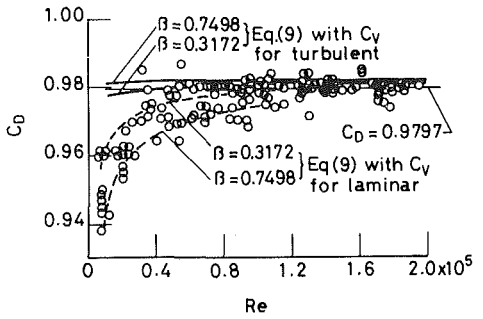

Fig. 6(*a*) Low Reynolds number

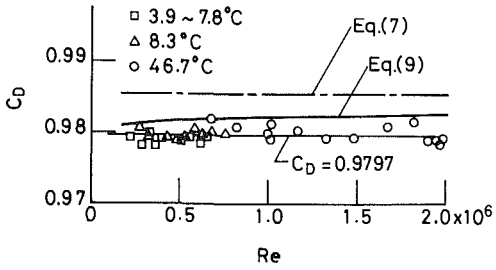

Fig. 6(*b*) Medium Reynolds number

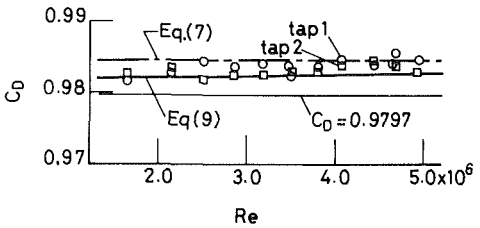

Fig. 6(*c*) High Reynolds number

Fig. 6 Effect of Reynolds number on discharge coefficient

agreement between the calculated and the experimental values are shown both in the laminar region (R_e below about 1.0×10^5) and the turbulent region (R_e over about 1.0×10^5). (Some experimental data from $R_e=0.4\times10^5$ to 1.2×10^5 probably belong to the transition region.)

In the case of medium Reynolds number (Fig. 6(*b*)) also, where data were obtained on a 152.4 diameter U.V.T. at various water temperatures, the prediction is satisfactory although the predicted values are a little higher than the experimental ones (about 0.2 percent higher).

In the case of high Reynolds numbers (Fig. 6(*c*)), for which a 344.5mm diameter-U.V.T. with $\beta=0.6628$ was calibrated on two independent tap sets located 180 deg apart, the predicted and experimental values agree precisely, while the "universal value" is considerably lower than the experimental values. From this figure, it is seen that the relation

$$C_D \approx C_I \tag{11}$$

can be used at high Reynolds numbers (where calibration becomes impractical), since the contribution of C_V on C_D beomes small as stated earlier.

4 Conclusion

A method for predicting the discharge coefficients for venturi flowmeters with short laying lengths has been developed. The method uses a potential flow calculation to account for streamline curvature at the venturi throat, coupled with a generalized empirical correlation to account for viscous effects. The validity of the use of potential flow calculations has been verified by comparisons against experimental data.

The discharge coefficients predicted by this method are compared against those measured for venturi flowmeters with short laying lengths. The predicted values agree closely with the measured values over low, medium and high Reynolds number ranges. The accuracy of the predicted discharge coefficients is especially good in the high Reynolds number range where calibration of venturi flowmeters is impractical. Therefore, the method presented here provides a useful and accurate tool for determining the discharge coefficients for venturi flowmeters with short laying lengths used for the measurement of flow rates in large sized pipes and ducts.

Finally, it should be noted that the method proposed is applicable to well designed venturi flowmeters only where flow separation and vena contractae effects are small.

5 Acknowledgments

In concluding this paper, the author wishes to express his appreciation to Mr. Hiroshi Kawashima for his considerable assistance in the computational work, and to Mr. Hidenobu Yano, who contributed his sustained effort to the preliminary experimental works.

References

1 "Fluid Meters—Their Theory and Application," *Report of ASME Research Committee on Fluid Meters*, 6th Edition, 1971, Bean, H. S., ed.

2 "Meaurement of Fluid Flow by Means of Venturi Tubes," *ISO Recommendation* R781, 1st Edition, 1968.

3 Rivas, M. A., Jr., and Shapiro, A. H., "On the Theory of Discharge Coefficients for Rounded-Entrance Flowmeters and Venturi," *Trans. ASME*, Vol. 78, Apr. 1956, p. 489.

4 Benedict, R. P., and Wyler, J. S., "Analytical and Experimental Studies of ASME Flow Nozzles," ASME JOURNAL OF FLUID ENGINEERING, Vol. 100, No. 3, Sept. 1978, p. 265.

5 Inoue, M., Kuroumaru, M., and Yamaguchi, S., "A Solution of Fredholm Integral Equation by Meanas of the Spline Fit Approximation," *Computer and Fluids*, Vol. 7, Jan. 1979, p. 33.

6 Benedict, R. P., and Wyler, J. S., "A Generalized Discharge Coefficient for Differential Pressure Type Fluid Meters," *ASME Journal of Engineering for Power*, Vol. 96, No. 4, Oct. 1974, p. 440.

7 Halmi, D., "Metering Performance Investigation and Substantiation of the Universal Venturi Tube (U.V.T.), Part 1-Hydraulic Shape and Discharge Coefficient," ASME JOURNAL OF FLUID ENGINEERING, Vol. 96, No. 2, June 1974, p. 125.

8 Ferron, A. G., "Velocity Profile Effects on the Discharge Coefficient of Pressure Differential Meters," ASME *Journal of Basic Engineering*, Vol. 85, No. 3, Sept. 1963, p. 338.

9 Walsh, J. L., Ahlberg, J. H., and Nilson, E. N., "Best Approximation Properties of the Spline Fit," *J. Math. and Mech.*, Vol. 11, 1962, p. 225.

APPENDIX

Method of Singularity with Spline Fit Distribution for Potential Flow Analysis [5]

In the method of singularities, ring vortices are distributed over the wall surface of the venturi tube. The strengths of these vortices is obtained from the solution of the Fredholm integral equation. In order to get the precise solution, the vortices are distributed continuously by means of a cubic spline fit approximation [9]. When the meridional line of the venturi is divided into N intervals s_j ($j=0,1,2,\ldots,N$), and the strengths of the vortex γ_j and the second derivatives $\delta_j=(d^2\gamma/ds^2)_j$ at the junction points are taken as unknowns, the vortex density in each interval is represented by

$$\gamma(s)=(1-f_j)\gamma_j+f_j\gamma_{j+1}-\frac{1}{6}(2f_j-3f_j^2+f_j^3)l_j^2\delta_j$$

$$-\frac{1}{6}(f_j-f_j^3)l_j^2\delta_{j+1}\quad(s_j\leqq s\leqq s_{j+1}) \tag{A1}$$

where s: coordinate along the meridional line

$$l_j = s_{j+1} - s_j$$

$$f_j = (s - s_j)/l_j$$

The $2N+2$ unknowns γ_j and δ_j ($j=0,1,\ldots,N$) can be obtained by solving a set of $2N+2$ linear simultaneous equations as follows: The boundary condition which prescribes the normal component of the velocity to vanish at a control point in each interval yields N linear equations, the condition of the first derivative to be continuous at the junction point and the two end conditions (namely, the conditions of the spline fit approximation) give $N+1$ equations, and the condition which prescribes the flow rate through the venturi tube gives the last equation. Then, the surface velocity at any point is calculated by equation (A1).

The accuracy of the calculation can be determined by examining whether the velocity at the wall surface induced by all the ring vortices coincides with equation (A1). If the required accuracy is not obtained, the number of intervals N in increased. In this study, the calculation was performed so that the difference between the induced velocity and the vortex density (equation (A1)) is smaller than 0.1 percent at the throat tap.

$$l_j = s_{j+1} - s_j$$

$$f_j = (s - s_j)/l_j$$

The $2N+2$ unknowns γ_j and $\delta_j (j=0,1, \ldots, N)$ can be obtained by solving a set of $2N+2$ linear simultaneous equations as follows: The boundary condition which prescribes the normal component of the velocity to vanish at a control point in each interval yields N linear equations, the condition of the first derivative to be continuous at the junction point and the two end conditions (namely, the conditions of the spline fit approximation) give $N+1$ equations, and the condition which prescribes the flow rate through the venturi tube gives the last equation. Then, the surface velocity at any point is calculated by equation (A1).

The accuracy of the calculation can be determined by examining whether the velocity at the wall surface induced by all the ring vortices coincides with equation (A1). If the required accuracy is not obtained, the number of intervals N in increased. In this study, the calculation was performed so that the difference between the induced velocity and the vortex density (equation (A1)) is smaller than 0.1 percent at the throat tap.

DISCUSSION

D. Halmi[1]

In view of the restricted space allowed for this discussion, subjects dealt with here are narrowed to points deemed most important for those who wish to use information from the paper or wish to refine its proposed discharge coefficient calculation method.

The paper presents a method by which C can be calculated accurately for "well designed" short Venturi Tubes. To gage how well this goal is achieved, we ought to realize that due to the nature of the concept of C, and due to the way Cs are used (also because of the means by which knowledge is obtained about them), we should consider their values, shapes, and the inevitable uncertainties of gathering knowledge about them.

The *value* of C is defined as:

$$C_t = \begin{matrix}\text{True}\\ C\\ \text{Value}\end{matrix} = \frac{\text{True Actual Rate of Flow}}{\text{True Idealized Rate of Flow Calculated by Flow Formula}} = \frac{\text{Actual Flow Mechanism}}{\text{Flow Mechanism Described by Flow Formula}}$$

The *true* shape of C describes the change in single C_t values in the function of some controlling parameters like

C_t versus Re; or

C_t versus Re versus β or

C_t versus Re versus β versus D, etc.

The *uncertainty* is a calculated $\pm$ C value band that should contain the errors with the specified confidence level included in a determined C value or shape due to the execution of the method by which they were determined.

Utilizing above clarification, the discusser puts forth some of his observations:

- The calculations – for UVT's indicate no size effect (D) but some β and Re sensitivity. The UVT experimental data – to the extent of its uncertainty band – verifies the size insensitivity but contradicts the β and Re sensitivity. Further work would be required either to disprove the indications of the experimental data or improve the mathematical image of C to make it agree with the results of the experiments.
- C values and shapes have been determined by the calc method but no attempt is presented in the paper to calculate the uncertainties that belong to the determined C values and shapes. To develop such knowledge is indispensable if the calc method is intended to be used for C determination without flow calibration.
- The mathematical "image" could be (should be) refined by recognizing in it the energy loss that occurs as the flow moves through the tube. By adding this refinement to the calc method would eliminate the disagreement illustrated by Fig. 4(*b*) in the UVT's throat section. The test points indicate a lowering of the static pressure as dictated by the laws of nature in contrast to the calculated shape that, apparently, disregards this energy loss.
- A further refinement could be achieved on the mathematical image of the physical phenomenon that takes place in the UVT if the fact was recognized that the UVT paper – from which the test data was taken – indicates wall pressures as sensed by piezometer holes with their centerline perpendicular to the axis of the tube. These pressures, consequently, indicate true static pressure only if the flow moves in a cylindrical section (like throat section) through a sufficiently long distance after a tube contour change. If this is not the case, the contour of the tube shall effect the magnitude in which the true local static pressure appears at the wall.
- The paper seems to consider a Venturi Tube "well designed" if in it flow separation and vena contractae effects are small. A more proper term here would be "suitably designed" meaning a design that lends itself for accurate and reliable C calculation.
- At last, a few points are mentioned for correction and/or clarification:
- P – Average static pressure. The paper should indicate how the average static pressure should be calculated to satisfy the requirements of the calc method.
- Quote from Paper: "In general, an inlet tap can be located at a point where $P_i = \bar{P}_i$." How can this be achieved?

  The physical meaning of surface velocity ought to be explained (v^*).
- The diverging recovery cone angle is 5 deg (Not 50,) See Pg. 6, Line 15.
- On Page 7 in lines 14 and 15, the terms laminar and turbulent regions are used without elaborating on what is meant by them here.

R. P. Benedict[2]

The author has contributed a useful paper on fluid flow meters which considers for the first time the effect of

[1] Director Flowmetering & New Product Development, B. I. F. Industries, W. Warwick, R. I. 02893

[2] Westinghouse Electric Corp., Lester, Pa., Fellow ASME

nonuniform static pressures at the venturi throat on the discharge coefficient.

Two questions are raised concerning Professor Inoue's analysis. The first concerns the author's equations (10). The Benedict-Wyler equations (6) show no β factor in the third terms of the denominators. Does the author have a basis for these additional terms? The second concerns the throat taps used in the experimental verification data. Were static tap corrections applied before comparing theoretical discharge coefficients with measured discharge coefficients? The effect of such corrections is on the order of 0.5 percent on the discharge coefficient (see for examples: [4, 10, and 11]).

Again, let me congratulate the author for his worthy contribution to the open literature.

Additional References

10 Benedict, R. P., "Generalized Fluid Meter Discharge Coefficient Based Solely on Boundary Layer Parameters," ASME *Journal of Engrg. for Power*, Vol. 101, Oct. 1979, p. 572.

11 Benedict, R. P., "The Plenum Inlet Discharge Coefficient for an ASME Nozzle," *Flow Its Measurement and Control in Science and Industry*, Vol. 2, 1981, p. 363.

Author's Closure

The author wishes to thank Mr. Benedict for his bringing up key questions and to thank Mr. Halmi for his much appreciated comments.

The first question of Mr. Benedict is linked to definition of Reynolds number which refers to inlet condition in this paper. Namely, the equation (10) is derived by substituting the relation of

$$R_{ed} = \frac{\bar{u}_t d}{\nu} = \frac{\bar{u}_i D}{\nu} \cdot \frac{\bar{u}_t}{\bar{u}_i} \cdot \frac{d}{D} = \frac{R_e}{\beta}$$

into the original equation.

The author agrees with Mr. Benedict that the tap size corrections are not negligible especially in the case of high Reynolds number if C_D is calculated by a theory with zero tap size. However, one should remember that the present method is based on a combination of a potential flow consideration and an empirical viscous flow consideration. As the empirical relation was obtained in the flowmeters with finite tap size, the tap size corrections are included to some extent in this method. Therefore the corrections were not applied.

The purpose of the paper is to consider the effect of nonuniform static pressure at the throat in the prediction of C_D, but not criticize the universal value of the UVT proposed by Mr. Halmi. The β insensitivity of the UVT has been verified in this paper (see the description iii in relation to Fig. 5). The R_e sensitivity may be caused by using the generalized empirical equation (10), in spite of the existence of the artificial vena contractae in the UVT. However, it should be noted that the differences between the predicted and the universal values are small in comparison with the uncertainty band. The availability of the universal value of the UVT is accepted.

The uncertainties can be estimated from the law of propagation of errors, equation (9) and equation (7).

$$\epsilon_D = \sqrt{\left(\frac{\partial C_D}{\partial C_I}\right)^2 \epsilon_I^2 + \left(\frac{\partial C_D}{\partial C_V}\right) \epsilon_V^2}$$

$$= \sqrt{\left(\frac{C_D}{C_I}\right)^3 \epsilon_I^2 + \left(\frac{C_D}{C_V}\right)^3 \epsilon_V^2}$$

where

ϵ_D: uncertainty of C_D
ϵ_V: uncertainty of C_V
ϵ_I: uncertainty of C_I

$$\epsilon_I = \left| \frac{\partial C_I}{\partial \gamma_t} \right| \epsilon_\gamma = C_I^3 \frac{\gamma_t \beta^4}{1-\beta^4} \epsilon_\gamma \approx \frac{\beta^2}{1-\beta^4} \epsilon_\gamma$$

ϵ_γ: uncertainty of γ_t

In this method ϵ_I becomes $0.00006 \sim 0.0008$ for $\beta = 0.25 \sim 0.75$ providing that $\epsilon_\gamma = 0.1$ percent (see Appendix). Therefore, the ϵ_D is mainly dependent upon ϵ_V which is obtained experimentally.

As to the other comments of Mr. Halmi, the author would like to emphasize again the basis of present method. One may use a more refined empirical or theoretical equation related to the energy loss as a viscous consideration.

For the last points for clarifications, the author's answers are as follows:

- it is not necessary to calculate $\bar{p}$,
- the term $p = \bar{p}_i$ means the uniform inlet pressure,
- the meaning of v^* should refer to reference [5],

and

- the terms laminar and turbulent regions are on the basis of the equation (10).

(• '50-diverging recovery cone angle' was a mistyping.)

Non-Newtonian Liquid Blade Coating Process

S. S. Hwang
Project Manager,
Xerox Corporation,
Rochester, N.Y. 14644
Mem. ASME

A blade coating process for non-Newtonian liquids is presented using different air pressure applied at the inlet and the exit of the coating gap. The system consists of a coating blade to form a gap and a vacuum box to create different air pressures to permit coating a thin liquid film on an advancing plastic web. The solution consists of matching the boundary conditions of each subregion of the coating process. The calculated liquid film thickness as a function of the coating gap and applied air pressure difference agrees closely with experimental data obtained on a laboratory coating device.

Introduction

Two problems are encountered in thin liquid film blade coating: (1) parts manufacture and assembly require very close tolerances to assure a correct gap setting distance between the coating blade and the web surface and (2) large dirt and lint particles can be trapped between the blade and the web (Fig. 1). These conditions will give rise to nonuniform liquid films. Also, large particles caught at the gap can cause the tearing of thin webs.

The most desirable way to overcome these two problems is to widen the coating gap and still obtain the same liquid film thickness. To achieve this, some forces have to be applied at the gap to support and thin the liquid in the widened gap. One way to supply a force to thin the liquid flow is to create a higher pressure at the exit of the gap and/or to create a lower pressure at the inlet of the gap. Since the web with the coated liquid film is moving, the baffle creating the pressure difference cannot completely be sealed. Thus, if a high positive air pressure is applied in the box, high speed air will leak from the exit baffle. The high speed air may generate waves on the surface of the coated liquid films. Therefore, it is an advantage to create a small vacuum at the inlet of the gap. When there is no pressure difference between inlet and outlet, the coated liquid film thickness is about one half of the coating gap for a shear dominated flow. When a vacuum is applied at the inlet side of the gap, it creates a force that pushes the liquid backward (Fig. 1). This action tends to thin the liquid coated on the web. On the other hand, if the exit pressure is less than the inlet pressure, the liquid will be pushed forward and a thicker film will be produced on the web.

The objective of this work is to develop techniques which enable prediction of the coated non-Newtonian liquid film thickness as a function of coating gap and air pressure difference and to compare the results with experimental data.

Theoretical and experimental work on entrainment of liquid films has been studied before and was reviewed by Tallmadge and Gutfinger [1]. Their work dealt with upward withdrawal of objects from liquid baths. Since then, some further work has been added. Tuntiblarphol and Tallmadge [2] studied length effects in short, flat withdrawal obstructions. They found that deviations from the long gap theory were relatively small. Lee and Tallmadge [3] measured meniscus shapes in withdrawal of flat sheets from liquid baths. Ruschak [4] studied the limiting flow in a pre-metered coating device theoretically in Newtonian flow.

Theory

The analysis discussed here is restricted to: laminar flow and wave free, homogeneous fluid; complete wetting and no slip at the wall; no shear at the liquid-air interface; constant temperature; and negligible inertial forces.

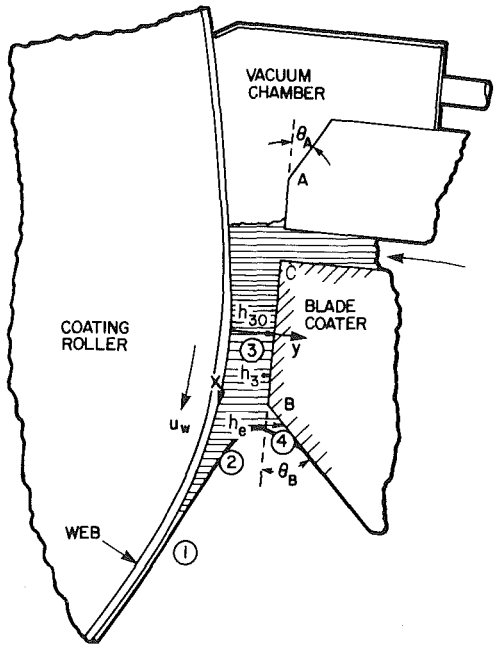

Fig. 1 Sketch of coating process divided into four regions

Contributed by the Fluids Engineering Division for publication in the JOURNAL OF FLUIDS ENGINEERING. Manuscript received by the Fluids Engineering Division, April 25, 1980.

From the assumptions made above, the coating process can be described conveniently by dividing it into four regions (Fig. 1). The circular coordinates are used. Since the liquid film thickness is small compared with the radius of the supporting roller and no variation in roller curvature occurs, the equations simplify to the same form as for regular cartesian coordinates [5].

1. The region well below the coater blade: In this region, the film thickness h_1 is constant on the web surface. The pressure gradient and the surface tension are negligible and the flow equation reduces to

$$\frac{\partial}{\partial y}\left(\mu \frac{\partial u}{\partial y}\right)+\rho g_x=0 \tag{1}$$

2. The region where the film is separating from the blade coater: This is a region of dynamic meniscus. The equation of motion is

$$\frac{\partial}{\partial y}\left(\mu \frac{\partial u}{\partial y}\right)+\rho g_x+\frac{\partial}{\partial x}\left(\frac{\sigma}{r}\right)=0 \tag{2}$$

The curvature of the meniscus is

$$\frac{1}{r}=\frac{d^2h/dx^2}{[1+(dh/dx)^2]^{3/2}} \tag{3}$$

3. The region inside the gap: The flow equation inside the coating gap is

$$\frac{\partial p}{\partial x}=\frac{\partial}{\partial y}\left(\mu \frac{\partial u}{\partial y}\right)+\rho g_x \tag{4}$$

While the surface tension term is not shown in the equation, it will appear in the inlet and exit boundary conditions.

4. The region near the coating walls: Here the flow effects are less pronounced, and the system can be described by the equation of capillary statics

$$\frac{d^2l/ds^2}{\left[1+\left(\frac{dl}{ds}\right)^2\right]^{3/2}}=\frac{-\rho g_s s}{\sigma} \tag{5}$$

A solution to this problem can be obtained by a proper matching of these four regions. It should be recognized that, because of the approximate nature of both the subdivision and the matching procedure, one does not expect to obtain the exact solution. However, it is sufficient for practical purposes.

The boundary conditions for the moving film in regions 1 and 2 are

$$u=u_w \quad \text{at} \quad y=0 \tag{6a}$$

$$\frac{\partial u}{\partial y}=0 \quad \text{at} \quad y=h \tag{6b}$$

The boundary conditions of the flow inside the gap, i.e., region 3, are

$$u=u_w \quad \text{at} \quad y=0 \tag{7}$$

$$u=0 \quad \text{at} \quad y=h_3 \tag{8}$$

The dynamic viscosities of the liquid were measured and can be generalized in a power law form for a non-Newtonian fluid

$$\mu=\mu_0\left|\frac{\partial u}{\partial y}\right|^{n-1} \tag{9}$$

When $n = 1$, it is a Newtonian flow. If n is not an integer, the sign of terms with negative argument and fractional exponent is determined from Newtonian flow.

Regions 1 and 2 can be matched together by using the steady state condition of equal flow rates in both regions.

$$Q_1=Q_2 \tag{10}$$

Integrating equation (1) with respect to y twice and satisfying the boundary conditions (6) yields

$$u_1=u_w+\left(\frac{\rho g_x}{\mu_0}\right)^{1/n}\left(\frac{n}{n+1}\right)\left[h_1^{\frac{n+1}{n}}-(h_1-y)^{\frac{n+1}{n}}\right] \tag{11}$$

which gives

$$Q_1=\int_0^{h_1} u_1\,dy$$

$$=h_1\left[u_w+\left(\frac{\rho g_x}{\mu_0}\right)^{1/n}\frac{n}{2n+1}h_1^{\frac{n+1}{n}}\right] \tag{12}$$

and,

$$Q=u_w h_0 \tag{13}$$

Equating equations (12) and (13), one finds h_0 to be

$$h_0=h_1\left[1+\left(\frac{\rho g_x}{\mu_0 u_w^n}\right)^{1/n}\frac{n}{2n+1}h_1^{\frac{n+1}{n}}\right] \tag{14}$$

From equation (2), one obtains the liquid velocity in region 2 as

$$u_2=u_w+\frac{n}{n+1}\left[\frac{\rho g_x}{\mu_0}+\frac{1}{\mu_0}\frac{\partial}{\partial x}\left(\frac{\sigma}{r}\right)^{1/n}\right]$$

$$\cdot\left[h_2^{\frac{n+1}{n}}-(h_2-y)^{\frac{n+1}{n}}\right] \tag{15}$$

and the flow rate as

$$Q_2=h_2\left\{u_w+\frac{n}{2n+1}\left[\frac{\rho g_x}{\mu_0}+\frac{1}{\mu_0}\frac{\partial}{\partial x}\left(\frac{\sigma}{r}\right)\right]^{1/n}h_2^{\frac{n+1}{n}}\right\} \tag{16}$$

Nomenclature

A = a variable, $(\partial p/\partial x - \rho g_x)/\mu_0$
C_1, C_2 = integration constants
e,i = subscripts, denote exit and inlet to the coating gap
G = dimensionless thickness, $h_1(\rho g_x/\mu_0 u_w^n)^{1/n+1}$
g_x = gravity constant in the direction of the x-coordinate
H = relative thickness, h_2/h_1
h = liquid film thickness
h_0 = coated liquid film thickness
h_{30} = the minimum spacing of coating gap
l = liquid film thickness in static meniscus
n = viscosity exponent
p = liquid pressure
Δp = applied pressure difference
Q = coating volume flow rate per unit width
R = coating roller radius
r = meniscus radius
S = dimensionless withdrawal speed, $\mu_0 u_w^n h_1^{1-n}/\sigma$
s = coordinate in static meniscus
u = component of velocity
u_w = web speed, or, coating speed
X = dimensionless coordinate
x,y = coordinates
1,2,3 = subscripts denote regions in 1, 2, 3
Θ_A = coater top angle
Θ_B = coater bottom angle
μ = liquid viscosity
μ_0 = liquid viscosity constant
ρ = liquid density
σ = liquid surface tension

The flow rates Q_1 and Q_2 are substituted into equation (10) to yield

$$h_1\left[u_w+\frac{n}{2n+1}\left(\frac{\rho g_x}{\mu_0}\right)^{1/n}h_1^{\frac{n+1}{n}}\right] = h_2\left\{u_w+\frac{n}{2n+1}\left[\frac{\rho g_x}{\mu_0}+\frac{\sigma}{\mu_0}\frac{\partial}{\partial x}\frac{d^2h_2/dx^2}{[1+(dh_2/dx)^2]^{3/2}}\right]^{1/n}h_2^{\frac{n+1}{n}}\right\} \tag{17}$$

with boundary conditions

$$h_2=h_1,\ \frac{dh_2}{dx}=\frac{d^2h_2}{dx^2}=0 \tag{18}$$

at the matching line of the two regions. Equation (17) is a third-order differential equation in h_2. Theoretically, it can be integrated numerically to express h_2 as a function of x, h_1, u_w, and liquid properties to satisfy the boundary conditions. Generally, h_1 is unknown unless it is measured. Therefore, an additional condition is necessary for matching regions 2 and 3 to express h_1, and hence h_0, as a function of the coating gap and air pressure difference.

Solving equation (4) with the boundary conditions (7) and (8), one obtains the liquid velocity in region 3 (see the Appendix for additional discussion).

$$u_3=u_w-\frac{y}{h_3}\left\{u_w+\frac{n}{n+1}[Ah_3^{n+1}]^{1/n}\right\}+\frac{n}{n+1}[Ay^{n+1}]^{1/n} \tag{19}$$

and the flow rate

$$Q_3=h_3\left\{\frac{u_w}{2}-\frac{n}{2(n+1)(2n+1)}[Ah_3^{n+1}]^{1/n}\right\} \tag{20}$$

From equations (13) and (20), the mean coated liquid film thickness can be expressed as

$$h_0=h_3\left\{\frac{1}{2}-\frac{n}{2(n+1)(2n+1)u_w}[Ah_3^{n+1}]^{1/n}\right\} \tag{21}$$

Equation (21) offers one way to estimate the coated liquid film thickness if the pressure gradient and the gap width are known.

Equation (21) can be rearranged into the form

$$\frac{\partial p}{\partial x}=\rho g_x+\left[\frac{(n+1)(2n+1)}{n}\right]^n\mu_0{u_w}^n\left[\frac{1}{h_3^{\frac{n+1}{n}}}-\frac{2h_0}{h_3^{\frac{2n+1}{n}}}\right]^n \tag{22}$$

Integration of equation (22) with respect to x yields

$$p_e-p_i=\rho g_x(x_e-x_i)+\left[\frac{(n+1)(2n+1)}{n}\right]^n\mu_0{u_w}^n\cdot\int_{x_i}^{x_e}\left[\frac{1}{h_3^{\frac{n+1}{n}}}-\frac{2h_0}{h_3^{\frac{2n+1}{n}}}\right]^n dx \tag{23}$$

From the meniscus equation, we also have,

$$p_e-p_i=\Delta p-\sigma\left(\frac{1}{r_e}-\frac{1}{r_i}\right) \tag{24}$$

The gap width h_3 is a function of x, which varies as follows:

for $x\le x_A$ (Fig. 1)

$$h_3=h_{30}+x^2/2R+(x_A-x)\tan\Theta_A \tag{25a}$$

for $x_A\le x\le x_B$

$$h_3=h_{30}+x^2/2R \tag{25b}$$

and for $x\ge x_B$

$$h_3=h_{30}+x^2/2R+(x-x_B)\tan\Theta_B \tag{25c}$$

The definition of h_3, h_{30}, and h_e are also shown in Fig. 1.

Equations (23)–(25) can then be used to estimate the exit meniscus curvature, $1/r_e$, which is the additional condition necessary for matching regions 2 and 3 to express the liquid film profiles as a function of the coating gap and air pressure difference.

In the static meniscus region 4, the liquid is independent of the viscous force because it is nearly motionless. In this static meniscus region, the film profile can be obtained by integrating equation (5) with the same initial conditions for curvature and slope as in region 2.

For certain liquids and web speeds, n, μ_0, ρ, σ, and u_w are all known values. The inlet and the exit positions, x_i and x_e, which can be measured or estimated as done by Hwang [6], are functions of liquid pumping rate, pressure gradient, liquid properties, and web withdrawal speed. The exit position x_e can be obtained from the exit gap width when the coater geometry is known. The exit gap width is a function of pressure gradient, withdrawal speed, and liquid properties.

One way to estimate the exit gap width is from the Prandtl-Hopkins exit conditions, i.e.,

$$u_3\Big)_e=\frac{\partial u_3}{\partial y}\Big)_e=0 \tag{26}$$

which gives

$$\frac{n}{n+1}A^{1/n}{h_e}^{n+1/n}-[(n+1)u_wA]^{1/n+1}h_e+u_w=0 \tag{27}$$

For plastic and pseudoplastic liquids, the viscosities decrease with the shear rate. Therefore, the power law exponent n is less than unity, and equation (27) is a fractional algebraic equation. Equation (27) usually cannot be solved readily in closed form and numerical iteration is used. Once h_e is known, the exit position x_e can be solved from equation (25).

Meniscus Profile. The complete liquid film profile is obtained by solving equations (5), (17), and (23) and matching their boundary conditions at interfaces.

It is convenient to solve equation (17) in dimensionless form, which can be done by using the following dimensionless groups as used by Gutfinger and Tallmadge [7]:

Dimensionless thickness:

$$G=h_1\left(\frac{\rho g_x}{\mu_0{u_w}^n}\right)^{\frac{1}{n+1}} \tag{28}$$

Dimensionless withdrawal speed, capillary number, or the ratio between viscous force and surface tension:

$$S=\mu_0u_w^nh_1^{1-n}/\sigma \tag{29}$$

The dependent variable - relative thickness:

$$H=h_2/h_1 \tag{30}$$

Independent variable - dimensionless coordinate:

$$X=\left[\left(\frac{2n+1}{n}\right)^nS\right]^{1/3}\frac{x}{h_1} \tag{31}$$

Substituting equations (28) to (31) into equation (17), one obtains

$$\frac{d}{dX}\frac{d^2H/dX^2}{\left\{1+\left[\left(\frac{2n+1}{n}\right)^nS\right]^{2/3}(dH/dX)^2\right\}^{3/2}}$$

$$= \left[1 - H + \frac{n}{2n+1} G^{\frac{n+1}{n}}\right]^n / H^{2n+1} - \left(\frac{n}{2n+1}\right)^n G^{n+1} \quad (32)$$

with the boundary conditions

$$H = 1, \; dH/dX = d^2H/dX^2 = 0 \quad (33)$$

at the interface of regions 1 and 2, X_{12}.

If the boundary conditions at the interface of regions 2 and 3, i.e., x_{23}, are known, equation (32) can be integrated from there down to the interface of regions 1 and 2. Since these boundary conditions are not known, it is necessary to use the boundary conditions (33) and integrate equation (32) from X_{12}, which can arbitrarily be chosen as $X_{12} = 0$ to X_{23} where the curvature is to be matched with the solution from region 3, i.e., the solution of equation (23) by assuming $r_i = 0.5h_i$. This matching region is in the range of thickness that is large compared with the coated liquid film thickness h_0.

Equation (32) was integrated by a four-point extrapolation-interpolation method which uses Falkner extrapolation formulas and Adams interpolation formulas.

Figure 2 shows examples of the liquid film profile with different applied pressure differences. Figure 2 shows the results for a 0.23 mm gap with different air pressure differences as indicated on the curves. At a low pressure difference, the shear force is the major force acting in the gap and, therefore, the web pulls more liquid with it to the exit side of the coater blade. When the applied pressure difference is increased, the pressure difference becomes more important and the liquid is pushed upward to inside the gap. If the pressure difference is too high, air will be pushed through the gap and the coated liquid film bursts and becomes nonuniform.

As equation (32) is integrated from $X = 0$ (where $H = 1$) upward to X_{23}, the film thickness H increases and the radius of curvature r_e decreases. When X is close to X_{23}, H increases rapidly and r_e reaches a limit for the examples given. The film thickness H cannot be greater than the exit gap H_e; therefore, the integration is stopped at the point before H becomes greater than H_e. The exit meniscus radius r_e decreases with increasing of pressure difference and coating gap width.

Liquid Film Thickness as Function of Pressure and Gap. The pressure gradient and gap width are the two most important factors to influence the coated liquid film thickness. In experiments, it is easy to measure the pressure difference but not the pressure gradient. Therefore, we express liquid film thickness as a function of pressure difference and gap width. For a certain coater at specified coating conditions, the coating length is a function of pumping and coating rates and time. To achieve continuous uniform films at the beginning of coating, the liquid is usually slightly overpumped. At steady state there is no over-pumping; the coating length $\Delta X = (X_e - X_i)$ is a function of pumping rate only and independent of time. The coating length at the lowest pumping rate to obtain a continuous film is a function of pressure difference and gap width. The results based on 89 mm/s web speed at steady state are shown in Fig. 3. These are obtained from equations (20) and (21) with known n, h_3. u_w and Q_3 which can be measured.

The results show that, for a certain gap width, the liquid film thickness decreases as the vacuum is increased. At moderate vacuum, film thickness stays constant for a certain range of vacuum. And as the vacuum is further increased, the liquid film thickness increases before it bursts.

As has been shown before, at low vacuum, the viscous force is the dominant force inside the gap. The shear force pulls the liquid down from the gap to the exit side and produces a thicker coated film on the web. As the pressure difference is increased, it gradually becomes important and pushes the liquid up into the gap. This action is similar to an air knife

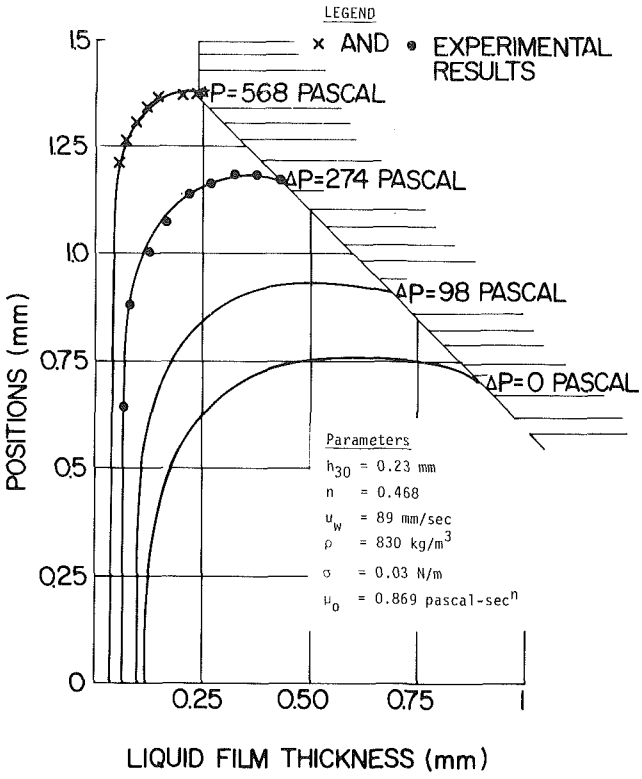

Fig. 2 Liquid film profiles with different vacuum for a 0.23 mm gap

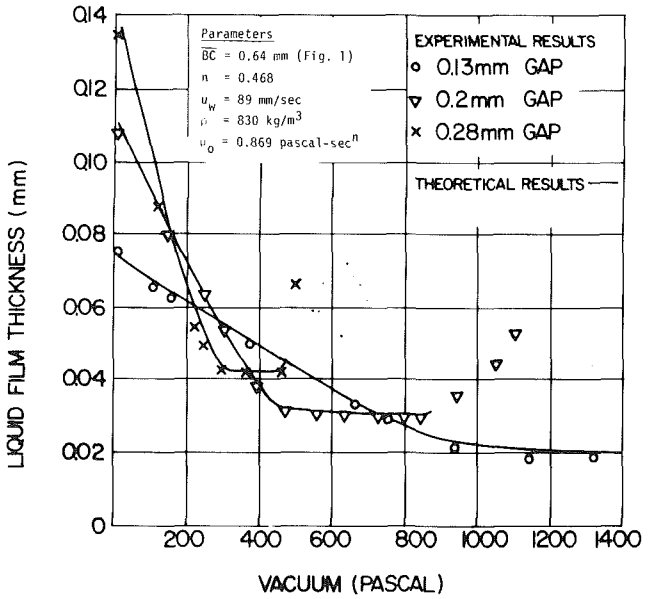

Fig. 3 Liquid film thickness based on the minimum pumping rates

thinning the liquid moving with the web. If the vacuum is further increased, the differential pressure will exceed the value which the liquid film can support and liquid will blow through the gap. Just prior to air blow through, the air stream tends to push through along the stationary coater surface; therefore, an increase in liquid thickness is observed. When the air leaks through the gap, a normal liquid film will not be formed. Instead, a pattern characteristic of such instabilities is formed in the liquid film.

Experiments

Liquid Viscosity. The viscosities of the mineral oil-based liquid that we used were measured with a Haake

Rotoviscometer. These liquid viscosities can be expressed in the form of equation (9). The viscosity constants are $\mu_0 = 0.869$ and $n = 0.468$, which give the liquid viscosities in units of pascal-second for shear rates from 10 to 400 s^{-1}. The difference between equation (9) and the experimental results is of the order of + 4 percent for shear rates between 10 and 200 s^{-1} and (−13 percent) for shear rates between 200 and 400 s^{-1}.

Meniscus Profiles and Coated Film Thickness. The cross section of the device for the experiments is similar to the one sketched in Fig. 1. The fixture consists of a liquid container, a delivery-metering fluid pump, a fluid distribution top plate, a coater blade, and a receiving web substrate with back-up roller. In addition to these components, a suction air blower is connected to the vacuum box to create a vacuum at the inlet side of the gap. The coating roller is a precise 49mm diameter steel roller. The coater blade has a smooth and straight edge with a 0.64mm thickness at the lip. Liquid is supplied by the pump to the coater blade and is coated on an advancing plastic web (0.025mm thick) which is wrapped over the coating roller. The width of the coated liquid film on the web for these experiments was 220mm and web speed was kept at 89 mm/s.

The profiles of the exit menisci were taken photographically by using a series of lenses and mirrors. The surfaces of the coater wall, web, and meniscus were obtained by a slit double-exposure technique. The surfaces of the bottom face of the coater and the web were photographed prior to coating. A second exposure was made at one to two seconds later while the coating was in progress for photographing the profiles of the exit menisci. The meniscal shapes were then traced from slides projected to approximately 90X of actual size. From the photographs the profiles of the exit menisci were obtained. Two typical results of enlarged meniscus profile are shown in Fig. 2. Comparison of the experimental and theoretical results at vacuums of 274 pascal and 568 pascal can be seen from the figure. They are very close.

The experimental results of liquid film thickness shown in Fig. 3 are based on the lowest pumping rates to obtain continuous films. The liquid film thickness is obtained from the volume of the liquid pumped and area of the coated liquid film. At a constant pressure difference, if the pumping rate is increased, the pressure gradient is decreased. The film thickness will then increase and the film has less tendency to become irregular. The uncertainty of experimental data is ±5 percent for both Figs. 2 and 3 as determined from averaging the data.

Conclusions

Theoretical aspects of the pressure differential blade coating system have been studied and compared with experimental results. Good agreement is observed. As the applied pressure difference is increased, the exit point of the coating process is pushed inside the coating gap, and the coated liquid film is thinned. The latitudes of applied pressure difference and coating gap width are highly encouraging. The coated liquid films are continuous and have straight leading and trailing edges.

The system is capable of achieving gap/film ratios ranging from about 2 to 7, while the gap/film ratio in blade coating shear dominated liquids without pressure difference is about 2 [6]. Hwang [6] showed that the coated liquid film thickness equals half of the coating gap plus a small term which increases with liquid surface tension and the gap and decreases with liquid viscosity and web speed. It is different to dip coating where the coated film thickness always increases with the speed. At large gap/film thickness ratios, it will significantly relax the part manufacturing tolerances and avoid the trapping of large particles at the gap. The system is quite insensitive to different formulations of liquid at normal operating conditions.

Acknowledgment

The author wishes to thank C. Abreu, D. Hoesly, and E. Jackson of Xerox Corporation for their assistance in making the experiments possible.

References

1 Tallmadge, J., and Gutfinger, C., "Entrainment of Liquid Films," *Ind. & Eng. Chemistry*, Vol. 59. No. 11, 1967, pp. 18-34.

2 Tuntiblarphol, M., and Tallmadge, J., "Length Effect in Short, Flat Withdrawal Obstructions," *Ind. Eng. Chem. Process Des. Develop.*, Vol. 10, No. 3, 1971, pp. 353-356.

3 Lee, C., and Tallmadge, J., "Meniscus Shapes in Withdrawal of Flat Sheets from Liquid Baths. Dynamic Profile Data at Low Capiliary Number," *Ind. Eng. Chem., Fundam.*, Vol. 13, No. 4, 1974, pp. 356-360.

4 Ruschak, K. J., "Limiting Flow in a Pre-metered Coating Device," *Chemical Engineering Science*, Vol. 31, 1976, pp. 1057-1060.

5 Schlichting, H., *Boundary Layer Theory*, McGraw-Hill, New York, 1960, p. 112.

6 Hwang, S. S., "Hydrodynamic Analyses of Blade Coater," *Chemical Engineering Science*, Vol. 34, No. 2, 1979, pp. 181-189.

7 Gutfinger, C., and Tallmadge, J., "Films of Non-Newtonian Fluids Adhering to Flat Plates," *A.I.Ch.E. Journal*, Vol. 11, No. 3, 1965, pp. 403-413.

APPENDIX

Integration of Equation (4)

The flow equation of the liquid around the gap is

$$\frac{\partial p}{\partial x} = \frac{\partial}{\partial y}\left(\mu \frac{\partial u_3}{\partial y}\right) + \rho g_x \tag{4}$$

Substituting equation (9) into equation (4) and integrating equation (4) with respect to y yields

$$\left(\frac{\partial u_3}{\partial y}\right)^n = \frac{1}{\mu_0}\left(\frac{\partial p}{\partial x} - \rho g_x\right) y + C_1 \tag{A1}$$

or

$$\frac{\partial u_3}{\partial y} = (Ay + C_1)^{1/n} \tag{A2}$$

Integration of equation (A2) with respect to y again yields

$$u_3 = \frac{n}{n+1}\frac{1}{A}(Ay + C_1)^{\frac{n+1}{n}} + C_2. \tag{A3}$$

Applying the boundary conditions (7) and (8) into equation (A3), one can solve for the integration constants C_1 and C_2 from

$$u_w = \frac{n}{n+1}\frac{1}{A} C_1^{\frac{n+1}{n}} + C_2 \tag{A4}$$

$$0 = \frac{n}{n+1}\frac{1}{A}(Ah_3 + C_1)^{\frac{n+1}{n}} + C_2 \tag{A5}$$

From equations (A4) and (A5), the equation to solve for C_1 is

$$C_1 \frac{n+1}{n} - (Ah_3 + C_1)^{\frac{n+1}{n}} = \frac{n+1}{n} A u_w. \tag{A6}$$

Obviously, C_1 cannot be solved analytically except when n equals unity, which is the case of Newtonian fluid.

The liquid velocity in the gap can be solved by an alternate approach. Instead of using equation (A2), if we approximate

$$\frac{\partial u_3}{\partial y} = (Ay)^{1/n} + C_1' \tag{A7}$$

then

$$u_3 = \frac{n}{n+1}\frac{1}{A}(Ay)^{\frac{n+1}{n}} + C_1' y + C_2'. \tag{A8}$$

Applying the boundary conditions (7) and (8) to solve for C_1' and C_2', one obtains

$$C_1' = -\frac{1}{h_3}\left[u_w + \frac{n}{n+1}(Ah_3{}^{n+1})^{1/n}\right] \tag{A9}$$

$$C_2' = u_w.$$

Substituting C_1' and C_2' into equation (A8) gives

$$u_3 = u_w - \frac{y}{h_3}\left[u_w + \frac{n}{n+1}(Ah_3{}^{n+1})^{1/n}\right] + \frac{n}{n+1}(Ay^{n+1})^{1/n}. \tag{A10}$$

When n equals one, the results of equations (A3) and (A10) are exactly the same. For $n = 0.5$, the difference in Q_3 based on these two methods of determining U_3 is about 18 percent.

A Controlled Buoyant Jet for Enhancing Stratification in a Liquid Storage Tank

H. N. Gari

R. I. Loehrke

Mechanical Engineering Department,
Colorado State University,
Fort Collins, Colo. 80523

An inlet manifold is described for introducing liquid of arbitrary temperature into a tank without destroying pre-existing stratification. This manifold may be described as a controlled, buoyant jet. A one-dimensional, analytical model of the manifold is developed. The predictions of this model are compared in a qualitative sense, with the results of flow visualization experiments. Quantitative comparisons are also made with the results of thermal tests of the major components of the manifold.

Introduction

Under certain circumstances it may be desirable to store liquids of unlike composition or unlike temperature in a single tank. Sharp and Loehrke [1], for example, predict a significant improvement in the performance of solar heating and cooling systems using sensible heat storage in water if thermal stratification can be maintained in the storage tank. One of the key components in a storage tank designed for stratification enhancement is an inlet which will introduce water into the tank with minimum mixing between fluids of unlike temperature.

A fixed inlet location is acceptable if the temperature of the water entering the tank is always at or beyond the storage temperature extremes. Warm water, for example, would be introduced near the top of a cool tank. This situation is illustrated in the photograph Fig. 1(*a*). Warm water, colored with dark dye, enters from the left into an inlet chamber consisting of a vertical segment of transparent pipe. The horizontal momentum of the incoming fluid is reacted by the pipe wall and *net* vertical momentum is imparted by buoyancy forces. The warm fluid rises and spreads out beneath the free surface at the top of the tank with little mixing.

It is not always the case, however, that the temperature of the incoming fluid is beyond the storage temperature extremes. Net energy collection may be realized in a solar system with a stratified storage tank even though the water returning to the tank from the collectors is cooler than the water stored at the top of the tank. Under such conditions, liquid introduced at the top of the tank will flow downward, mixing with the surrounding fluid, until some equilibrium level is reached. The turbulent mixing which can occur in this situation is illustrated in Fig. 1(*b*) by the expansion of the colored, negatively-buoyant jet issuing from the bottom of an inlet chamber positioned near the top of a tank. This mixing is, of course, detrimental to the pre-existing tank stratification.

A means to inhibit this mixing, and hence enhance

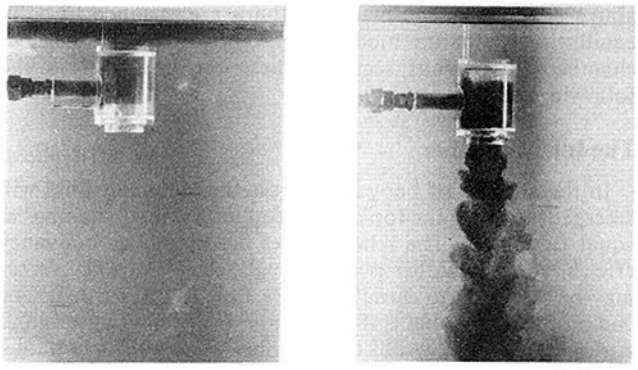

a) Warm water entering cool tank *b)* Cool water entering warm tank

Fig. 1 Water entering tank near upper surface through inlet chamber

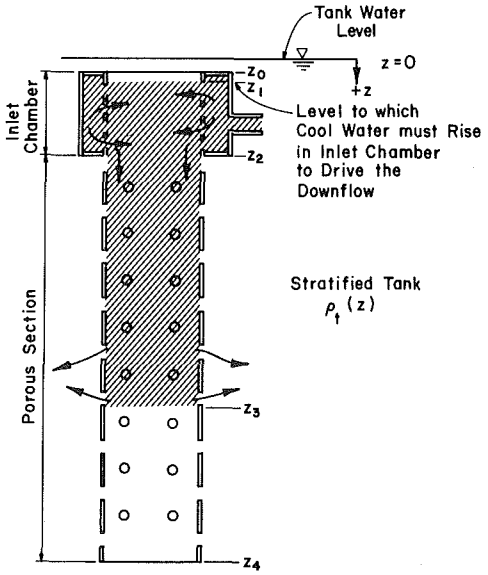

Fig. 2 Rigid, porous distribution manifold

Contributed by the Fluids Engineering Division for publication in the JOURNAL OF FLUIDS ENGINEERING. Manuscript received by the Fluids Engineering Division, September 14, 1981.

stratification, was demonstrated by Loehrke, et al. [2]. They showed that mixing could be significantly reduced by enclosing the vertical jet in a porous shroud. Their vertical distribution manifold produced, in effect, a controlled buoyant jet. The purpose of this paper is to present a simple model of the operation of that manifold which can be used to identify the design parameters. The major features of the model are corroborated by experiment.

The Distribution Manifold

A schematic drawing of a porous distribution manifold is shown in Fig. 2. It consists of two parts: an inlet chamber and a porous section. The inlet chamber may be located at any vertical position with porous sections both above and below, but for this discussion the orientation shown in Fig. 2 will be assumed. The horizontal momentum of the incoming fluid is reacted by the walls of the inlet chamber and vertical momentum is imparted to the fluid. If the incoming liquid is sufficiently warmer than the surrounding tank liquid it will rise to the top of the tank as in Fig. 1(*a*). If it is sufficiently cooler than the liquid at the top of the tank it will descend into the porous section. This is the condition shown in Fig. 2. The function of the porous section in this case is to inhibit mixing between the manifold and tank fluids until the level is reached at which the density of the two fluids match. The shaded areas in Fig. 2 represent incoming liquid flowing down the porous section and entering the tank just above z_3. Below z_3 and above z_1 the tank and manifold fluids are assumed to be in equilibrium. Separate models were constructed for the inlet chamber and porous section. These are described in the following sections.

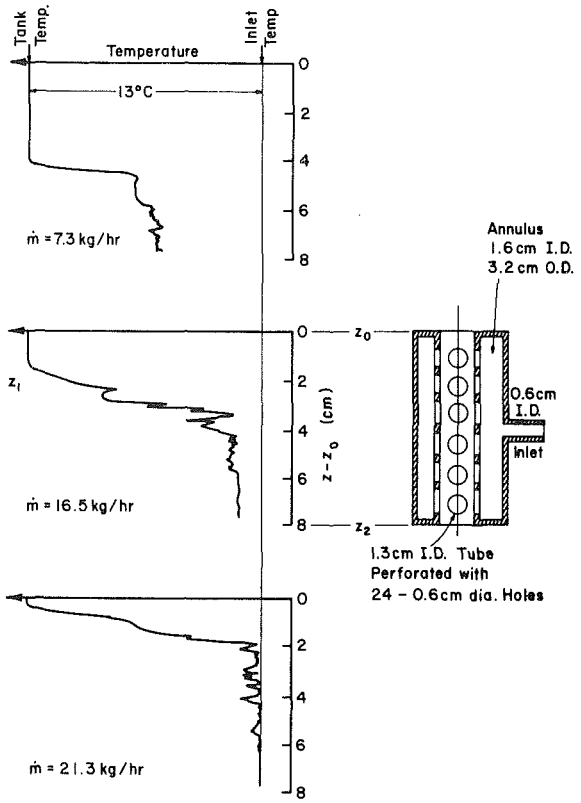

Fig. 3 Vertical temperature profiles down the center of an annular inlet chamber. Cool water entering warm tank. (Uncertainty in overall temperature difference = ± 0.2°C, in $z - z_0$ = ± 0.1 cm, in $\dot{m}$ = ± 0.50 kg/hr.)

The Inlet Chamber

In the absence of buoyancy forces the incoming fluid will emerge from both the top and bottom of the inlet chamber at equal flow rates. The relative rates are biased by buoyancy effects. If the chamber is tall enough, then buoyancy forces may be sufficient to cause all of the flow to exit through one end or the other. That is the situation shown in Figs. 1 and 2. An estimate for how tall the chamber must be for unidirectional flow can be obtained from momentum considerations. A simple, one-dimensional analysis of the inlet chamber, in which friction and entrainment across the density interface at z_1 are neglected, indicates that the height to which the cool incoming water must rise to drive the downflow when the pressures in the tank and in the manifold at level z_2 are equal is given by

$$h = z_2 - z_1 = \frac{1}{g}\left(\frac{\dot{m}_2}{\rho_2 A}\right)^2 + \frac{1}{\rho_2}\int_{z_1}^{z_2} \rho_t(z)\,dz. \qquad (1)$$

If $\rho_t(z) = \rho_t$ = constant between z_1 and z_2 this reduces to

Nomenclature

A = cross-sectional area of manifold
A_0 = open area of porous wall
A^* = dimensionless manifold area
A_s = dimensionless state parameter = $\rho_{\min}/\rho_2$
B_s = dimensionless state parameter = $\beta(T_{\max} - T_{\min})(\rho_{\min}/\rho_2)$
c_p = specific heat
C_D = discharge coefficient
C_f = dimensionless friction parameter = $\dfrac{2fL}{D}$
C_0 = dimensionless wall permeability parameter
$= \sqrt{2}\, C_D \dfrac{L}{A}\dfrac{dA_0}{dz}$
C_ρ = dimensionless density parameter = $\dfrac{gLA^2\rho_2^2}{\dot{m}_2^2}$
D = hydraulic diameter of manifold passage
f = friction factor
F = friction force per unit length of manifold
g = acceleration of gravity
h = $(z_2 - z_1)$ in Fig. 2
L = length of porous section, $(z_4 - z_2)$ in Fig. 2
$\dot{m}$ = mass flow rate through manifold
M = dimensionless mass flow rate
p = pressure
P = dimensionless pressure
T = temperature
$T_{\max}$ = maximum tank temperature
$T_{\min}$ = minimum tank temperature
z = vertical coordinate
z_0, z_1, z_2, z_3, z_4 = vertical positions in tank, Fig. 2
Z = dimensionless distance
β = state constant
θ = dimensionless temperature
ρ = density
$\rho_{\min}$ = water density at $T_{\min}$
$\bar{\rho}$ = dimensionless density

Subscripts

t = conditions in tank
1, 2, 3, 4 = evaluated at locations z_1, z_2, z_3, z_4

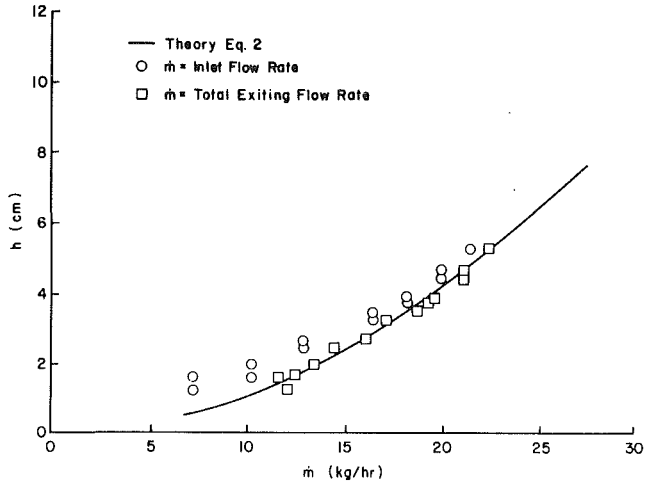

Fig. 4 Location of interface in annular inlet chamber. (Uncertainty in h = ± 0.5 cm, in $\dot{m}$ = ± 0.50 kg/hr.)

$$h = \frac{(\dot{m}_2/A)^2}{g\rho_2\Delta\rho} \tag{2}$$

where $\Delta\rho = |\rho_2 - \rho_t|$. Although the tank density profile and the manifold inlet conditions may change with time the rate of change is slow enough, in the applications described earlier, so that a steady state analysis is appropriate. The pressure in the manifold at z_2 is determined by the flow conditions in the porous section. A model for predicting this pressure and techniques for controlling it are described in the next section. At this point, however, the one-dimensional model of the inlet chamber can be evaluated by reviewing tests which were performed without a porous section attached so that the pressure in the inlet chamber at z_2 was known to be identical to that in the tank at this level.

A number of inlet chambers ranging in diameter from 2.5 cm to 10 cm have been built and tested. Vertical temperature profiles measured in one of these chambers are shown in Fig. 3. In this test cool water was introduced into a warm tank. The temperature in the upper section of the chamber is uniform and equal to the tank temperature. A relatively sharp interface between warm and cool water is detected with large temperature fluctuations at and below the interface. This interface rises as the flow rate of water into the chamber is increased. With a fixed flow rate the interface remains stationary indicating that there is a downflow of warm water from the tank through the inlet. The water issuing from the bottom of the chamber is noticeably warmer than the water being pumped into the chamber at the two lower flow rates shown in Fig. 3 because of this downflow.

An estimate for the distance h was obtained from a series of profiles such as those shown in Fig. 3 for a range of flow rates. The results are plotted in Fig. 4. The circle symbols represent data plotted against the flow rate of the incoming cool water. These points lie above the prediction of equation (2). This is because the actual mass flow being accelerated downward includes warm water entrained across the temperature interface. The magnitude of this entrainment flow rate was determined from mass and energy balances on the inlet chamber and the measured inlet and outlet temperatures. The square symbols represent the same measurement for h plotted against total flow rate leaving the bottom of the chamber. These points are in good agreement with theory.

The experiments indicate that the simple, one-dimensional model of the inlet chamber is adequate providing that entrainment across the density interface is accounted for. This entrainment is, however, difficult to predict. It depends on the construction details of the chamber and on the flow conditions. The best performance, i.e., minimum entrainment, was obtained from among several inlet chamber configurations tested, with the annular, radial inflow chamber shown in Figs. 1 through 3. The entrainment flow rate approaches zero for this chamber as the temperature interface approaches the top of the chamber. Thus, equation (2) can be viewed as a sizing relation which specifies the required inlet chamber diameter to ensure that cool water does not spill out the top of an inlet chamber of a given height. This sizing must be done for some specified flow rate and minimum density difference.

The Porous Section

The function of the porous section of the manifold is to prevent mixing between the downflowing cool water and the surrounding tank water until the level is reached at which the temperatures of the two fluids match. To accomplish this the wall perforations must be small enough to inhibit shear-induced turbulent mixing and the pressure difference across the perforations must be zero to prevent inflow or outflow until the equal density level is reached. The following analysis is directed at the second requirement.

The three basic assumptions of this analysis are that the flow down the porous section is steady and one-dimensional and that the temperature of the downflowing water is changed only if there is net inflow of tank water into the porous section due to a difference between the tank and manifold pressures. The one-dimensional differential momentum equation for the fluid within the manifold is

$$\frac{dp}{dz} = \rho g - \frac{F}{A} - \frac{1}{A}\frac{d}{dz}\left(\frac{\dot{m}^2}{\rho A}\right) \tag{3}$$

while in the tank

$$\frac{dp_t}{dz} = \rho_t(z)g. \tag{4}$$

To prevent inflow or outflow through the porous walls these pressure gradients must be matched for the specified $\rho_t(z)$. Equation (3) suggests that the pressure gradients may be matched for a specified tank density profile by either tailoring the frictional characteristics of the manifold $F(z)$ or the cross-sectional area $A(z)$. The former approach was adopted in the rigid, porous manifild (RPM) which will be discussed first while the latter approach was used for the flexible porous manifold (FPM) which will be discussed later.

Analysis of Rigid Porous Manifold

In the RPM the area of the porous section is constant and the frictional properties are selected for a particular set of conditions. In the following analysis the resistance will be modeled as a continuous function of vertical position although in practice the desired resistance function may be approximated by discrete resistance elements. Equations (3) and (4) are sufficient to specify the $F(z)$ required to prevent flow through the perforations provided $\rho > \rho_t$. This requirement is

$$F(z) = gA(\rho - \rho_t(z)) \tag{5}$$

Additional relationships are required if $\dot{m}$ is not constant, as in off-design operation, and when $\rho = \rho_t$ and outflow into the tank is desired.

Continuity dictates that the amount of increase or decrease in the flow rate inside the manifold be balanced by the amount of inflow or outflow of fluid through the perforations. The inflow or outflow in turn may be related to the pressure difference across the porous wall yielding

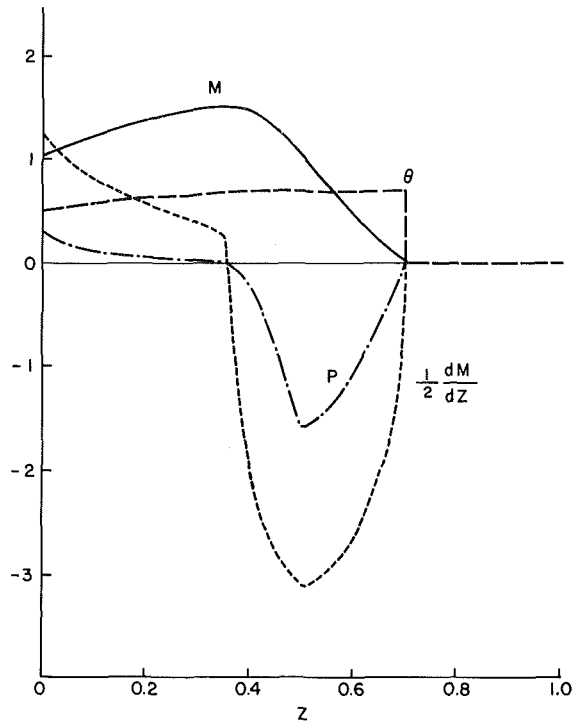

Fig. 5 Predicted RPM manifold performance. Intermediate temperature water entering a tank with stair-step stratification. $C_0 = 5$, $C_f = 2$ and $C_\rho = 3526$.

$$\frac{d\dot{m}}{dz} = \begin{cases} C_D\sqrt{2\rho_t}\sqrt{p_t - p}\dfrac{dA_0}{dz}, & \text{inflow} \\ -C_D\sqrt{2\rho}\sqrt{p - p_t}\dfrac{dA_0}{dz}, & \text{outflow} \end{cases} \tag{6}$$

The form chosen for the relationship between pressure difference and flow rate has been verified by experiment to be appropriate for the range of flow rates and geometries to which this analysis has so far been applied. The open area of the porous wall is treated as a continuous function of position in the analysis. In practice, this area has taken the form of circular holes uniformly distributed over the surface of the manifold and the derivative shown in equation (6) was assumed constant at an average value.

A combination of the energy and continuity equations for the manifold yields

$$\frac{d(\dot{m}T)}{dz} + T_t\frac{d\dot{m}}{dz} \tag{7}$$

where variation of heat capacity with temperature is neglected. Heat transfer through the manifold wall has been neglected to simplify the formulation of the problem. For some applications this simplification may not be justified and an additional parameter will arise.

For the outflow case T and ρ are constant. For the inflow case they may change and an equation of state is required to relate these variables. The linear relation

$$\rho = \rho_{\min}(1 - \beta(T - T_{\min})) \tag{8}$$

is adopted. If equation (3) is subtracted from equation (4) and F/A is replaced by the more conventional form for flow in a duct

$$\frac{2f}{DA^2}\frac{\dot{m}^2}{\rho}$$

the momentum equation becomes

$$\frac{d(p_t - p)}{dz} = \frac{2f}{DA^2}\frac{\dot{m}^2}{\rho} + \frac{1}{A^2}\frac{d(\dot{m}^2/\rho)}{dz} + g(\rho_t - \rho) \tag{9}$$

Equations (6) through (9) are the governing differential equations for the operation of the rigid, porous manifold which are to be solved subject to the following boundary conditions:

$$\text{at } z = z_2 \text{ (Top of RPM)} \begin{cases} T = T_2 \\ \dot{m} = \dot{m}_2 \\ \rho = \rho_2 \end{cases}$$

and at $z = z_3$

either $z_2 < z_3 \le z_4 \quad p = p_t, \dot{m} = 0$

or $z_3 = z_4$ (bottom of RPM) $\quad p = p_t, \dot{m} \neq 0$

The last boundary condition says that either all of the flow leaves the manifold through the perforated sidewall and an interface exists below which the flow rate is zero or else some of the flow exits through the bottom. These equations and boundary conditions were recast in dimensionless form by defining the following variables:

$$M = \dot{m}/\dot{m}_2, Z = \frac{z - z_2}{z_4 - z_2} = \frac{z - z_2}{L}$$

$$P = \frac{(p_t - p)}{\dot{m}_2^2/\rho_2 A^2}, \bar{\rho} = \rho/\rho_2, \theta = \frac{T - T_{\min}}{T_{\max} - T_{\min}}$$

The resulting dimensionless governing equations are:

$$\frac{dM}{dZ} = \begin{cases} +\sqrt{C_0{}^2\bar{\rho}_t P}, & P \ge 0 \\ -\sqrt{-C_0{}^2\bar{\rho}P}, & P < 0 \end{cases} \tag{10}$$

$$\frac{d\theta}{dZ} = \begin{cases} \dfrac{\theta_t - \theta}{M}\dfrac{dM}{dZ}, & \dfrac{dM}{dZ} > 0 \\ 0, & \dfrac{dM}{dZ} \le 0 \end{cases} \tag{11}$$

$$\bar{\rho} = A_s - B_s\theta \tag{12}$$

$$\frac{dP}{dZ} = C_f\left(\frac{M^2}{\bar{\rho}}\right) + 2\left(\frac{M}{\bar{\rho}}\right)\frac{dM}{dZ} + \left(\frac{M}{\bar{\rho}}\right)^2 B_s\frac{d\theta}{dZ} + C_\rho(\bar{\rho}_t - \bar{\rho}) \tag{13}$$

The boundary conditions become:

$$\text{at } Z = 0 \begin{cases} M = 1 \\ \theta = \theta_2 \\ \bar{\rho} = 1 \end{cases} \tag{14}$$

and either $0 < Z \le 1 \quad P = 0, \ M = 0$

or $\quad Z = 1 \quad P = 0, \ M \neq 0.$

The most important parameters in the model analysis are C_f and C_0. C_f is a measure of the flow resistance within the manifold, whereas C_0 is a measure of the permeability of the porous wall. These two parameters may be varied by the designer to tailor the operation of the manifold to a particular application. The area of the manifold and therefore the parameter C_ρ will be set by the design of the inlet chamber.

Numerical solutions to this nonlinear system of equations were obtained using a shooting technique and continuation

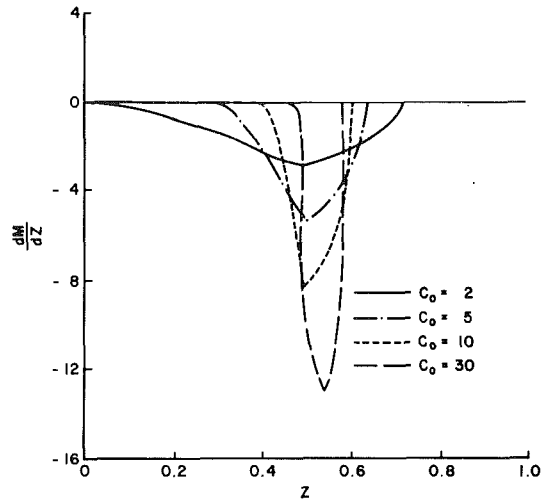

Fig. 6 Effect of wall permeability on the flow of intermediate temperature water into a tank with stair-step stratification. $C_f = 10$ and $C_\rho = 3526$.

procedure [3]. The mass flow rate, temperature and density at the top of the manifold are assumed known. A value for the pressure is guessed and the equations are integated in a downward direction until the last boundary condition is satisfied. If it is not satisfied anywhere along the length of the manifold a new pressure is guessed and the procedure is repeated.

Results of the Analysis

The results of a typical analysis are plotted in Fig. 5. In this situation the tank is stratified with warm water in the upper half and cool water in the lower half. Water enters the manifold at the average tank temperature. The constant values chosen for C_0 and C_f are lower than optimum. In the upper portion of the manifold the tank pressure exceeds the manifold pressure so that $P > 0$ and tank water is entrained into the manifold causing M and θ to increase. The pressure difference reverses about 1/3 of the way down the manifold and fluid is ejected from the manifold. The rate of change of the pressure difference is discontinuous at $Z = 0.5$, the location of the thermocline. The pressure difference P and manifold flow rate M both go to zero at $Z = 0.7$. Below this point the manifold contains stationary liquid at tank temperature. The variable dM/dZ is the entrainment flow rate per unit length of manifold. Beyond $Z = 1/3$ water is expelled from the manifold, dM/dZ is negative and θ remains constant. The entrainment of warm tank water into the upper portion of the manifold can be minimized by increasing C_f. In fact, since ρ_t is constant in the upper half of the tank equation (5) can be used to calculate that $C_f = 10$ will completely eliminate entrainment.

The effect of sidewall permeability variation on the manifold performance with this value of C_f is shown in Fig. 6. As the permeability is increased the water emerges from the manifold over a narrower band. Ideally, the intermediate temperature water would emerge in a horizontal sheet at $Z = 1/2$. For the manifold parameters modeled here, however, little improvement is obtained by increasing C_0 beyond 20.

Comparison With Experiment

Qualitative and quantitative confirmation of the analytical model was obtained with manifolds ranging in diameter from 1.25 cm to 10 cm in tanks ranging in capacity from 0.03 m^3 to 2.3 m^3 with flow rates ranging from 10 kg/hr to 2000 kg/hr. Flow visualization tests were performed in a 0.23 m^3 Plexiglas tank with a 3.8 cm diameter Plexiglas manifold. In the experiment shown in Fig. 7(*a*) cool water was introduced into a tank containing warm water. The cool water entered an inlet chamber and was accelerated downward through the porous section to the bottom of the tank. Contrast the appearance of this negatively buoyant, shrouded jet with that of the free jet shown in Fig. 1(*b*) under similar conditions. In the experiment pictured in Fig. 7(*b*) the tank was stratified with a step change in temperature at midheight. Water was introduced into the manifold at the average tank temperature. The conditions are similar to those used in the analysis presented in the previous section and so are the results. The interface between the dyed incoming fluid in the manifold and the clear cooler fluid in the bottom of the porous section is quite distinct. The incoming water entered the tank near the thermocline through the holes in the side of the porous section.

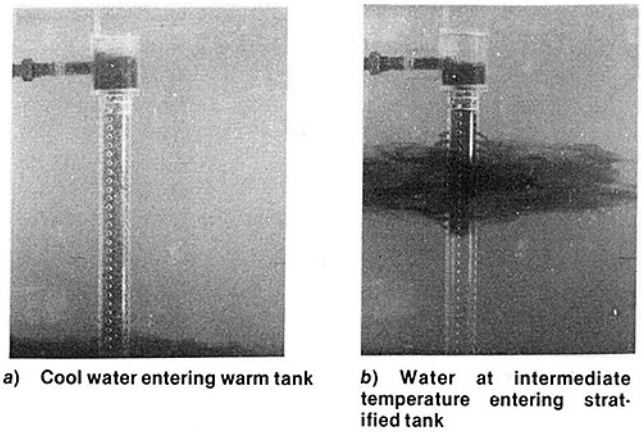

a) Cool water entering warm tank

b) Water at intermediate temperature entering stratified tank

Fig. 7 A rigid porous manifold

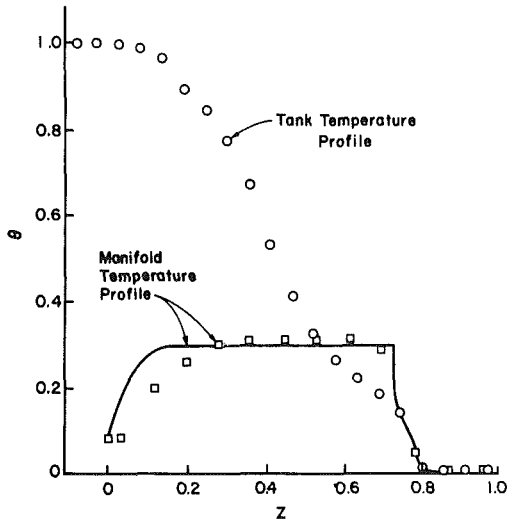

Fig. 8 Measured water temperatures in the tank and comparison between predicted (line) and measured (square symbols) water temperatues in the manifold. $\dot{m} = 1270$ kg/hr, $T_{max} - T_{min} = 17°C$, $C_0 = 4$, $C_f = 20$ and $C_\rho = 9190$. (Uncertainty in measured $\theta = \pm .015$, in $Z = \pm .003$.)

A quantitative check of the theory was obtained through experiments conducted in a 2.3 m^3 steel tank with a water depth of 2 m. The manifold for this tank was constructed from 10 cm dia. PVC pipe perforated with 2.5 cm dia. holes. A central rod running the entire 178 cm length of the porous section was used to support 22 equally spaced circular disks. These disks formed annular orifices which restricted the downflow and produced a suitably high C_f. The actual values of C_0 and C_f were determined from experimental measurements. The values obtained were close to those estimated using standard orifice equations. Full details of these experiments may be found in reference [4].

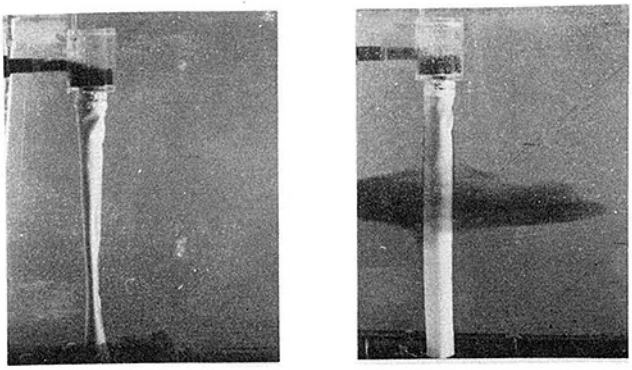

a) Cool water entering warm tank

b) Water at intermediate temperature entering stratified tank

Fig. 9 A flexible porous manifold

Vertical arrays of thermocouples were used to monitor the temperature of the water in the manifold and in the tank. The tank temperature variation was found to be essentially one-dimensional. For the experiments described here the top of the inlet chamber was blocked when cool water was introduced so that the flow rate of the water descending into the porous section was known to be equal to the measured inlet flow rate.

The results of one experiment run to check the theory are shown in Fig. 8. In this experiment that tank was partially charged with warm water creating a diffused, step-like stratification. After the thermocline reached the center of the tank the charging was terminated and cool water taken from the bottom of the tank was simply recirculated back to the tank through the manifold. The data shown in Fig. 8 represent the conditions twenty minutes after the beginning of recirculation. The inlet temperature was somewhat higher than the temperature at the bottom of the tank due to a slight heat addition in the external plumbing. The flow rate entering the manifold was 1270 kg/hr and the overall temperature difference from the bottom to the top of the tank was 17°C. These represent off-design conditions for this particular manifold. Specifically, C_f is too low to prevent inflow of warm water into the porous section near the top. This inflow raises the temperature of the water descending down the manifold. The theory predicts this rise in temperature. It also accurately predicts the lower extent of the outflow region as indicated by the temperature drop in the lower portion of the porous section.

Flexible Porous Section

In the discussion following equations (3) and (4) it was pointed out that the matching in pressures between the tank and manifold fluids could be accomplished by providing an appropriate manifold area distribution $A(z)$ for a specified tank density profile $\rho_t(z)$. In fact, if the walls of the porous section are constructed of a flexible material the appropriate $A(z)$ will be automatically formed for any $\rho_t(z)$. Inflow is not possible for an idealized, perfectly flexible porous manifold since a positive value for $p_t - p$ cannot be supported. Instead, the walls collapse to modify the cross-sectional area and force a pressure balance. Outflow can occur however after the flexible porous section has extended to its maximum diameter. Since inflow is not possible the temperature and density of the fluid within the manifold remain constant and the analysis is relatively straightforward. If $\rho > \rho_t$ then the criterion, analogous to equation (5) for the RPM, which must be satisfied for the FPM to prevent inflow is obtained by equating (3) and (4) with $\dot{m}$ and ρ set constant. This gives

$$\frac{dA}{dz} = \frac{F\rho A^2}{\dot{m}^2} - \frac{\rho g(\rho - \rho_t(z))}{\dot{m}^2} A^3 \tag{15}$$

In terms of dimensionless variable $Z = z - z_2/L$ and $A^* = A/A_2$, where $A_2 = A(z_2)$, this becomes

$$\frac{dA^*}{dZ} = \left[\frac{\rho FLA_2}{\dot{m}^2}\right] A^{*2} - \left[\rho g \frac{(\rho - \rho_t)A_2{}^2 L}{\dot{m}^2}\right] A^{*3} \tag{16}$$

In general ρ_t may be a function of Z and F may depend on both Z and A^*. In many applications the friction parameter $\rho FLA_2/\dot{m}^2 = C_{f2}$ will be small. For negligible friction and constant tank density equation (16) may be integrated to give

$$A^* = [1 + 2C_a Z]^{-1/2}$$

where

$$C_a = \frac{\rho g(\rho - \rho_t)A_2{}^2 L}{\dot{m}^2}.$$

This area variation would result if the entire tank contained fluid at a uniform density lower than that of the incoming fluid. The cross sectional area of the flexible porous sleeve should contract continuously to maintain conditions of zero inflow. This is the shape approximated by the flexible porous manifold shown in Fig. 9(*a*). This manifold was constructed by attaching a sleeve of limp nylon fabric to the bottom of an inlet chamber. The sleeve was also fixed at one point on the lower end to maintain the vertical orientation of the manifold and prevent any entrained air from lifting the flexible porous section to the water surface. The dramatic reduction in mixing inferred by the comparison between the flow illustrated here and that shown in Fig. 1(*b*) for similar conditions is confirmed by the enhancement of stratification reported in reference [2]. The expanded size of the flexible porous section is shown in Fig. 9(*b*) where intermediate temperature water is being introduced into a stratified tank through the porous sidewalls.

Concluding Remarks

The concepts outlined in this paper have provided the basis for the design of a number of manifolds for enhancing stratification in solar, thermal energy storage tanks. The performance of these manifolds in both design-point and off-design operation has exceeded that of conventional inlets. Quantitative comparisons in one application may be found in reference [2].

The one-dimensional model described here has been demonstrated to be qualitatively and quantitatively correct by comparison with experiments conducted over a wide range of conditions. Only a few of these comparisons could be included in this paper. The model has been used to identify important parameters which are valuable as design tools. There remain, however, several areas where more fundamental knowledge is required in order to provide complete design guidelines.

The effects of geometry on the entrainment across the density interface have not been explored in depth. A fundamental understanding of the mixing process would guide the way to a more efficient design and to a model for the entrainment flow rate. The effect of the porous wall on the turbulent mixing between two streams of different density is also not well documented.The model proposed in this paper can be used as a guide for selecting the porosity of the wall based on through flow requirements but it provides no limit on the maximum porosity nor does it specify the size of the pores. Guidelines based on limited experimental data suggest that the porosity should be maintained as low as possible consistent with acceptable through flow performance and that the hole size should be less than $D/4$ for the rigid porous section.

References

1 Sharp, M. K., and Loehrke, R. I., "Stratified Thermal Storage in Residential Solar Energy Applications," *J. of Energy*, Vol. 3, No. 2, 1979, p. 106.

2 Loehrke, R. I., Holzer, J. C., Gari, H. N., and Sharp, M. K., "Stratification Enhancement in Liquid Thermal Storage Tanks," *J. of Energy*, Vol. 3, No. 3, 1979, p. 129.

3 Roberts, S. M., and Shipman, J. S., *Two-point Boundary Value Problems: Shooting Methods*, American Elsevier, 1972.

4 Gari, H. N., Ph.D. thesis, Mechanical Engineering Department, Colorado State University, in preparation.

Additional References

D1 Lavan, Z., and Thompson, J., "Experimental Study of Thermally Stratified Hot Water Storage Tanks," *Solar Energy*, Vol. 19, 1977, pp. 519–524.

D2 Gross, R., "An Experimental Study of Single Medium Thermocline Thermal Energy Storage," AIAA/ASME Thermophysics, Fluids, Plasma, and Heat Transfer Conference, St. Louis, Mo., June 7–11, 1982.

D3 Torkelson, L., and Larson, D., "1980 Annual Report of the Collidge Solar Irrigation Project," Sandia National Laboratories, Report No. SAND80-2378, Feb. 1981.

References

1 Sharp, M. K., and Loehrke, R. I., "Stratified Thermal Storage in Residential Solar Energy Applications," *J. of Energy*, Vol. 3, No. 2, 1979, p. 106.

2 Loehrke, R. I., Holzer, J. C., Gari, H. N., and Sharp, M. K., "Stratification Enhancement in Liquid Thermal Storage Tanks," *J. of Energy*, Vol. 3, No. 3, 1979, p. 129.

3 Roberts, S. M., and Shipman, J. S., *Two-point Boundary Value Problems: Shooting Methods*, American Elsevier, 1972.

4 Gari, H. N., Ph.D. thesis, Mechanical Engineering Department, Colorado State University, in preparation.

Additional References

D1 Lavan, Z., and Thompson, J., "Experimental Study of Thermally Stratified Hot Water Storage Tanks," *Solar Energy*, Vol. 19, 1977, pp. 519–524.

D2 Gross, R., "An Experimental Study of Single Medium Thermocline Thermal Energy Storage," AIAA/ASME Thermophysics, Fluids, Plasma, and Heat Transfer Conference, St. Louis, Mo., June 7–11, 1982.

D3 Torkelson, L., and Larson, D., "1980 Annual Report of the Collidge Solar Irrigation Project," Sandia National Laboratories, Report No. SAND80-2378, Feb. 1981.

DISCUSSION

R. J. Gross[1]

This well-written paper, in conjunction with related work by the same authors, represents the only careful, well-planned study concerning the "diffusion" of the momentum of the initial jets entering a thermally stratified storage tank. The authors are correct in stating that a distributive manifold is one of the key components (if not the key component) in achieving the most efficient single-medium thermal storage system possible. Hopefully, this paper will create an interest in the minds of many workers in the thermal energy storage field who appear to be unaware of the importance of the distributive manifold. Lavan and Thompson [D1] and Gross [D2] as well as the authors have amply demonstrated this fact.

There are very few questions which this discussor could find concerning this work. It was mentioned that the size of the manifold's holes should be less than $D/4$, presumably to inhibit shear-induced turbulent mixing. Perhaps more could have been said on this. Also, in the experimental verification of the analysis of the rigid porous manifold, depicted in Fig. 8, it is apparent that the analysis diverges from reality in the top fifth or more of the tank. Is this the result of entrance effects of the incoming jet, some two-dimensionality of flow in the top section, or some other phenomena? Were the results of the analysis as accurate for higher flow rates?

Some other remarks are in order. The authors observed that the temperature variation in their 2.3 m^3 tank was essentially one-dimensional. This observation appears to hold true for stratified cylindrically-shaped storage tanks in general, if consideration is given to a momentum diffusion device. Substantiation is given by Torkelson and Larson [D3] for a 113.5 m^3 tank and by Gross [D2] for a 4.6 m^3 tank. Finally, the flexible porous device appears to be a simple and effective, certainly intriguing and ingenious, method of efficiently distributing the flow to the proper level without entrainment.

[1]Fluid Mechanics and Heat Transfer Division, Sandia National Laboratories, Albuquerque, N. Mex. 87185.

Authors' Closure

The authors appreciate Dr. Gross's generous comments and thoughtful questions. There seems to be a growing body of experimental evidence which indicates that the temperature distribution in a well-designed tank for diurnal storage is essentially one-dimensional. In addition to the citations of Dr. Gross the evidence includes the results of tests on a 2 m^3 cylindrical tank with horizontal axis which were conducted in our lab and analyzed in an unpublished report[2]. Localized exceptions to this generality may occur near a vertical distribution manifold. This is especially true under off-design conditions. If water leaves the manifold prematurely, before reaching the appropriate level in the tank, then the mixing region in the tank near the manifold takes on a multi-dimensional character. If the conditions are such that entrainment is realized then the mixing takes place within the manifold and so do the local temperature variations. We suspect that this is the primary cause for the disagreement between the single measured temperature at a given vertical location near the top of the manifold and the prediction of the one-dimensional (mixed flow) theory shown in Figure 8. The experimental results agreed better with theory at higher flow rates since these were closer to design point conditions and entrainment was neither predicted nor observed.

Identical experiments run with rigid manifolds with hole diameters ranging from D/4 to D/8 showed little influence of hole size on performance. These experiments form the only basis for the hole size limitation mentioned in the paper. We have found no guidance in the literature on the use of porous surfaces to inhibit shear-induced mixing.

[2]Kuhn, J. K., von Fuchs, G. F., and Zob, A. P., "Developing and Upgrading of Solar System Thermal Energy Storage Simulation Models," Technical Progress Report BCS-40311, Boeing Computer Services Company, Seattle, Washington 98124, May 1980.

Resonant Entrainment of a Confined Pulsed Jet

P. G. Parikh[1]

R. J. Moffat
Professor and Chairman.
Mem. ASME

Thermosciences Division,
Department of Mechanical Engineering,
Stanford University,
Stanford, Calif. 94305

This paper reports the discovery of a new resonant entrainment phenomenon associated with a confined, pulsed jet flow. It was found that a confined jet, when pulsed at an organ-pipe resonant frequency of the confinement tube, experiences greatly enhanced entrainment and mixing near the exit end of the confinement tube compared to a steady confined jet. The mixing and entrainment rates for the resonantly pulsed confined jet approach, and in some cases slightly exceed, those for an unconfined pulsed jet. Both visual and quantitative evidence of this phenomenon is presented. The new effect should be of considerable interest in ejector and combustor design, both of which benefit from any enhancement in mixing between a primary and a secondary flow.

Introduction

Rapid mixing of a primary jet flow with entrained or a coaxially flowing secondary flow is of great importance in many applications as diverse as ejectors, combustors, and chemical lasers. The importance of increasing the mixing rate between primary jet flow and entrained flow in a thrust-augmenting ejector was stressed by Quinn [1], who showed that the thrust augmentation was directly proportional to the degree of mixing attained at the ejector exit. In an industrial burner utilizing gaseous, liquid, or particulate fuel, rapid mixing in the reaction zone is of utmost importance for compactness, high combustion efficiency, and improved homogeneity which is beneficial for control of pollutant formation [2].

Several investigators have used deliberately introduced unsteadiness to improve the mixing rate of jets. In an investigation primarily aimed at study of large-scale orderly structures in a turbulent jet, Crow and Champagne [3] found that, even at amplitudes of excitation as low as 2 percent, the entrainment rate in the first six diameters from the jet exit plane increased by 20 percent over the unforced case. Binder and Favre-Marinet [4] used a spinning butterfly valve upstream of a nozzle to produce amplitudes of pulsations up to 40 percent of mean velocity. Both the decay of the centerline velocity and the spreading distance of the jet were strongly affected by pulsations. Their co-workers Curtet and Girard [5] conducted a visualization study of pulsed jets and provided smoke and Schlieren pictures of puff formation. Bremhorst and co-workers [6, 7] studied both fully pulsed and pulsed-core jets and attributed the increased entrainment of pulsed jets to their inherently larger entrainment interface structure. They also found lesser entrainment rates for pulsed-core jets as compared to a fully pulsed jet [7]. Viets [8] utilized a feedback fluidic loop to produce a flapping two-dimensional jet nozzle for V/STOL application and reported marked influence of this introduction of oscillating transverse velocity component on jet spreading rates.

During the course of their investigation of jet mixing rates, Hill and Greene [9] discovered the phenomenon of a "whistler nozzle," in which a step change in the area of an extended nozzle resulted in self-excited acoustic oscillations of the jet and led to significantly improved mixing rates, as evidenced by a rapid decay of the centerline velocity.

Recently, Habib and Whitelaw [10] reported measurements on velocity characteristics of a confined coaxial jet and found that confinement has beneficial effects on the mixing rate of coaxial jets.

The present paper describes a new phenomenon in which the mixing and entrainment rates of a confined jet increase dramatically downstream of the confinement tube exit plane when the jet is pulsed at the organ pipe resonant frequencies of the confinement tube. The entrainment and mixing rates downstream of the confinement tube exit plane for the

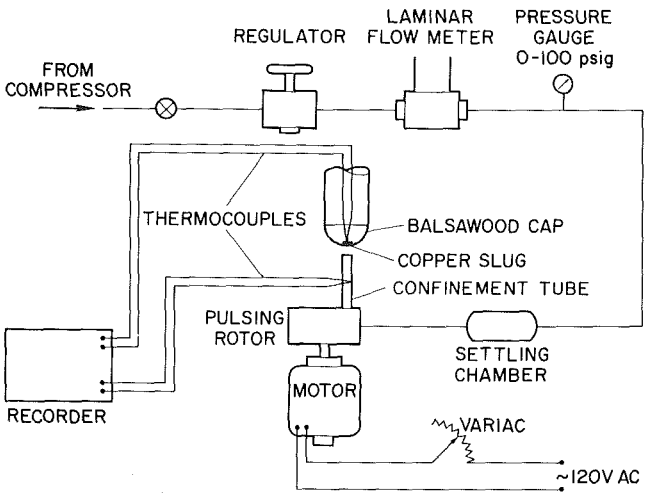

Fig. 1 Schematic of heat transfer experiment

[1] Present Address: Jet Propulsion Laboratory, California Institute of Technology, Pasadena, Calif. 91109.

Contributed by the Fluids Engineering Division for publication in the JOURNAL OF FLUIDS ENGINEERING. Manuscript received by the Fluids Engineering Division, January 6, 1981.

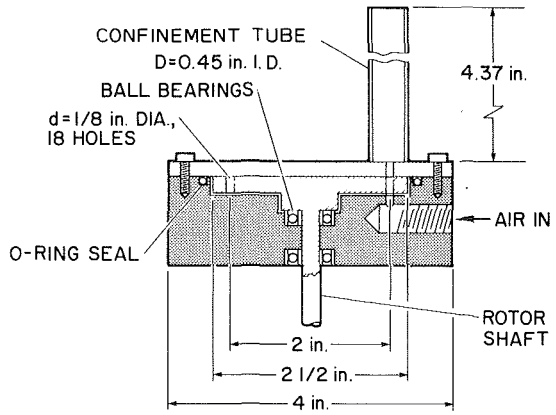

Fig. 2 Pulsing rotor

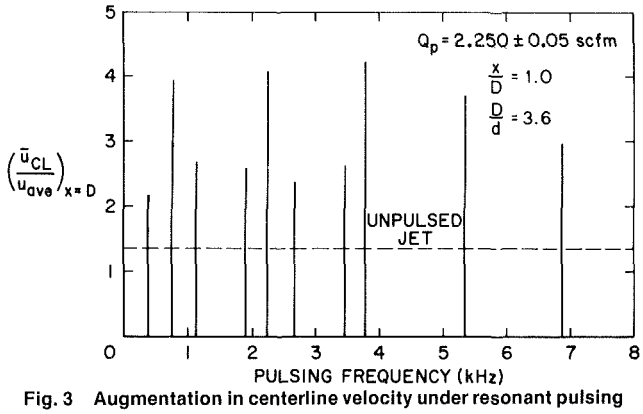

Fig. 3 Augmentation in centerline velocity under resonant pulsing

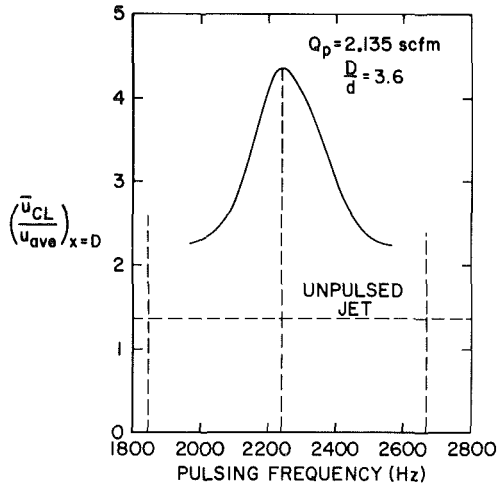

Fig. 4 Frequency dependence of centerline velocity around a resonance peak

reasonantly pulsed confined jet approach, and in some cases slightly exceed those for an unconfined pulsed jet.

Resonant Entrainment Phenomenon

The resonant entrainment phenomenon was observed during the course of an investigation to study effects of high-frequency pulsations on stagnation-point heat transfer. A schematic of the experiment is shown in Fig. 1. The supply air is filtered, metered by means of a laminar flow element, and delivered to a pulsing rotor device after passage through a settling chamber.

The details of the pulsing rotor device are shown in Fig. 2. The 0.318 cm (1/8 in.) diameter (d) opening at the base of the 1.143 cm (0.45 in.) diameter (D) confinement tube is opened and closed at high frequencies (up to 7.5 kHz) by means of a pulsing rotor. The rotor has eighteen 0.318 cm (1/8 in.) diameter holes and is driven by a Variac-controlled motor up to speeds of 25,000 rpm. The motor speed was measured directly by means of a photoelectric transducer.

The device thus produces a pulsed jet issuing from a 0.318 cm (1/8 in.) diameter orifice, whose pulsing frequency may be varied in the range 0 to 7.5 kHz.

The maximum jet velocity was attained, obviously, when the rotor was in fully open position and minimum when the rotor was in fully closed position. Due to the clearance between the rotor and the casing, the minimum jet velocity (or flow rate) was nonzero. For a fixed upstream pressure, the ratio of the flow rates for fully open position of the rotor to that at fully closed position (under stationary condition) was approximately 2.2. For the same upstream pressure, the flow rate under rotor spinning condition was approximately the average of the flow rates for fully open and fully closed stationary positions. From these stationary measurements, the amplitude of the velocity pulsations of the jet issuing from the orifice was estimated to be 37.5 percent of the mean velocity. This pulsed jet is confined by a confinement tube of diameter $D = 1.143$ cm (0.45 in.) and length $L = 11.1$ cm (4.37 in.) before issuing out into the ambient air. The region of interest is immediately downstream of the confinement tube exit plane.

Hot-wire measurements at the jet centerline, one diameter downstream of the confinement tube exit plane, showed that the mean velocity there increased sharply in the neighborhood of certain characteristic resonant pulsing frequencies. The peak velocities attained, together with corresponding resonant pulsing frequencies, are plotted in Fig. 3. The peak velocities are normalized with respect to U_{ave}, where

$$U_{ave} = \frac{\dot{m}}{\rho_e A_2} \tag{1}$$

Here $\dot{m}$ is the time-averaged mass flow rate as measured by

Nomenclature

A_1 = cross-sectional area of the jet orifice (see Fig. 6)
A_2 = cross-sectional area of the confinement tube
C = speed of sound
d = diameter of the jet orifice
D = diameter of the confinement tube
f = pulsing frequency
L = confinement tube length
$\dot{m}$ = time-averaged primary mass flow rate
p_1 = mean pressure at the confinement tube base under resonant pulsing
p_2 = mean pressure near the confinement tube exit under resonant pulsing
$p_{1,s}$ = pressure at the confinement tube base, steady flow
$p_{2,s}$ = pressure near the confinement tube exit, steady flow
p_a = ambient pressure
Q_p = primary volume flow rate
Q_{total} = primary + entrained volume flow rate
r = radial coordinate
r_0 = radius of the jet orifice
R = radius of the confinement tube
u_0 = jet velocity at orifice exit (see Fig. 6)
u_1 = uniform jet velocity at confinement tube exit (see Fig. 6)
ρ = density
ν_p = pulsing frequency
$\nu_{n,0-c}$ = resonant frequency of an organ pipe with one end open, the other closed

Table 1 $Q_p \approx 2.250$ scfm, $\nu_{1,0-c} = 751.6$ Hz

ν_p	$(\bar{u}_{CL}/u_{ave})x=D$	$\nu_p/\nu_{1,0-c}$
Hz	----	----
378	2.17	$0.503 \simeq 1/2$
747	3.93	$0.994 \simeq 1$
1132	2.67	$1.506 \simeq 3/2$
1896	2.58	$1.523 \simeq 5/2$
2241	4.08	$2.982 \simeq 3$
2667	2.37	$3.548 \simeq 7/2$
3448	2.61	$4.588 \simeq 9/2$
3772	4.23	$5.019 \simeq 5$
5336	3.71	$7.100 \simeq 7$
6860	2.97	$9.127 \simeq 9$

the laminar flow meter (Fig. 1), ρ_e is the exit plane density, and A_2 is the confinement tube cross-sectional area. $\dot{m}$ was maintained nearly constant during measurements at all frequencies. At the flow rates employed, U_{ave} was approximately 10 m/s (33 ft/s).

The horizontal dashed line in Fig. 3 shows the normalized centerline velocity value (1.37) for an unpulsed jet for the same flow rate. This value was determined experimentally with the rotor stationary and in the fully open position. It may be seen that the augmentation in the centerline velocity at some resonant frequencies over the stationary value is up to 200 percent.

To provide an estimate of the half-width of this resonant behavior, measurements of centerline mean velocity one diameter downstream from the confinement tube exit plane were taken in the vicinity of the $\nu_p = 2241$ Hz resonance (Fig. 4). The vertical dashed lines denote the location and the magnitude of the normalized peak mean velocity for adjacent resonances. The horizontal dashed line denotes the experimental $(\bar{u}_{CL}/u_{ave})_{x=D}$ value for the unpulsed jet at the same mean primary mass flow rate. Notice that the half-width is approximately 100 Hz and that the normalized mean velocity between resonances remains substantially higher than the unpulsed value of 1.37.

Significance of the Resonant Frequencies

The frequencies at which a local maximum in the centerline velocity was observed (Fig. 3) were compared with the resonant frequencies of an open/closed-ended organ pipe of the same length as the confinement tube. The resonant organ pipe frequencies are given from [11] as

$$\nu_{n,0-c} = (2n-1)\frac{C}{4L'}, \quad n = 1,2,3, \ldots, \tag{2}$$

Here L' is the corrected length given by

$$L' = L + 0.3D \tag{3}$$

where L is the actual length and D is the pipe diameter [11].

Using the discharge tube dimensions of $L = 11.1$ cm and $D = 1.143$ cm (0.45 in.), together with the speed of sound $C = 344$ m/s at 21°C,

$$\nu_{1,0-c} = \frac{C}{4L'} = 751.6 \text{ Hz}.$$

The measured resonant frequencies for the resonant entrainment phenomenon are tabulated in Table 1 and are normalized with the $\nu_{1,0-c}$ value determined above. Notice that strong resonances are observed when

$$(\nu_p/\nu_{1,0-c}) = 1, 3, 5, 7, 9,$$

while weak resonances are observed when

$$(\nu_p/\nu_{1,0-c}) = 1/2, 3/2, 5/2, \text{ etc.}$$

To ascertain that the "resonant" frequencies were indeed the organ-pipe resonant frequencies of the confinement tube, different tube lengths ranging from 6 to 24 cm were employed. In all cases the phenomenon was found to scale on the organ-pipe resonant frequency based on the tube length employed.

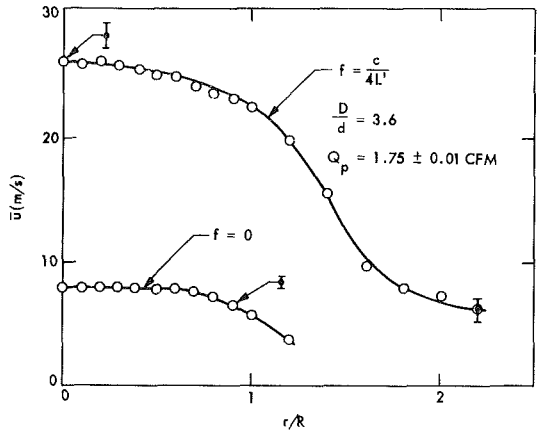

Fig. 5 Radial profiles of velocity at $x/D = 1.0$

Radial Profiles and Centerline Velocity Decay

Radial traverse of the jet one confinement tube diameter downstream from the exit plane with hot wire showed that high mean velocities persisted a considerable distance from the centerline. Figure 5 shows a comparison between the unpulsed confined jet and the confined jet pulsed at the resonant frequency, $f = C/4L'$ at the same primary mean flow rate. To minimize the radial velocity contribution in these measurements, the hot wire axis was aligned with the radial direction during the radial traverse. Effects of possible flow reversals during pulsations could not be accounted for in these measurements. Note that, under resonant pulsing, not only are the mean velocities substantially larger, but so is the spreading distance. As the primary flow rate is the same for the two cases, the substantially higher volume flow rate for the pulsed jet must result from increased entrainment. This increased entrainment occurs only in the vicinity of the organ-pipe resonant frequencies of the confinement tube, hence the phenomenon will be termed resonant entrainment.

The question now arises as to where the large increase in the momentum of the jet comes from during resonant pulsing. To answer this question, we consider the unpulsed confined jet, as shown in Fig. 6. In this case, the high momentum of the small jet (of diameter d) is reduced considerably as the jet attaches to the confinement tube wall and the mean velocity decreases to satisfy continuity. If we assume an incompressible, one-dimensional flow at inlet and exit and neglect wall friction, a control volume analysis shows that

$$u_0 = \frac{A_1}{A_2}u_1 = \left(\frac{d}{D}\right)^2 u_1 \tag{4}$$

$$\rho u_0^2 A_2 = \frac{A_1}{A_2}\rho u_1^2 A_1 = \left(\frac{d}{D}\right)^2 \rho u_1^2 A_1 \tag{5}$$

and

$$p_{2,s} - p_{1,2} = \rho u_1^2 \left(\frac{d}{D}\right)^2 \left[1 - \left(\frac{d}{D}\right)^2\right] \tag{6}$$

Also, for steady flow,

$$p_{2,s} = p_a \tag{7}$$

Thus, we see from equation (5) above that, under steady flow conditions, the momentum of the primary jet is larger than that of the jet issuing at the exit of the confinement tube by a factor of $(D/d)^2$. Furthermore, the decrease in the momentum is accompanied by an increase in the pressure from $p_{1,s}$ to $p_{2,s} = p_a$, as shown by equations (6) and (7) above.

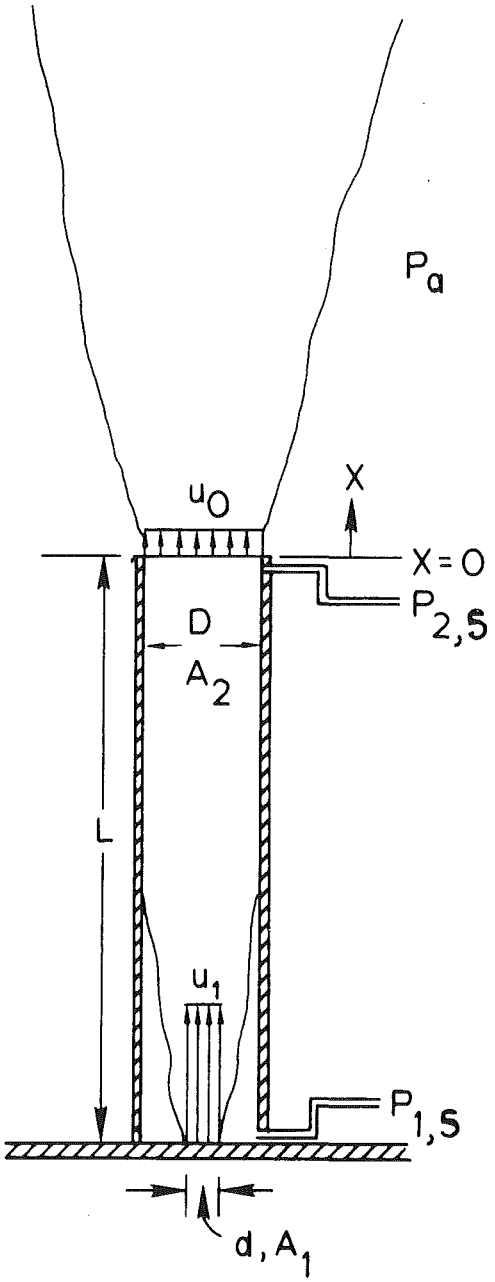

Fig. 6 Schematic of unpulsed confined jet

We shall next show that the momentum of the resonantly pulsed confined jet is comparable to that of an unconfined pulsed jet of diameter d at the same mean primary flow rate.

The confinement tube of diameter D was replaced by a tube of the same length L but of a diameter d, i.e., the same as that of the orifice. The latter configuration ($D/d = 1.0$) resulted in an unconfined jet discharged from a tube of diameter d, which could be either steady ($f = 0$) or pulsed at any frequency, including $f = C/4L'$. Radial profiles of velocity were measured at two axial locations $x/d = 24$ and 48, where x was measured from the exit plane of the tube. Results for the following three cases are compared in Figs. 7(a) and (b).

Case (i) $D/d = 1.0$, $f = 0$
Case (ii) $D/d = 1.0$, $f = C/4L'$
Case (iii) $D/d = 3.6$, $f = C/4L'$

The mean primary flow rate was maintained at the same value in all three cases.

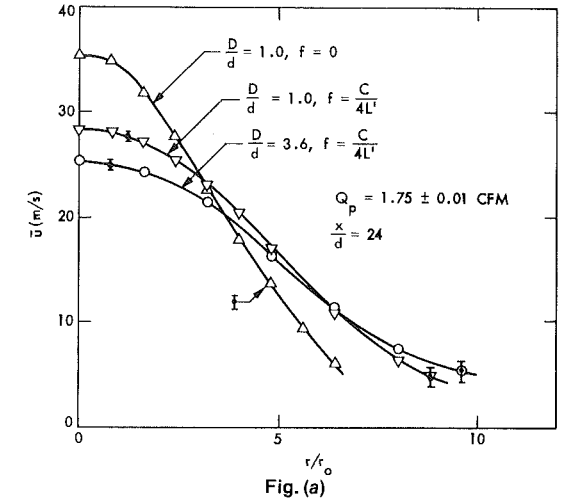

Fig. (a)

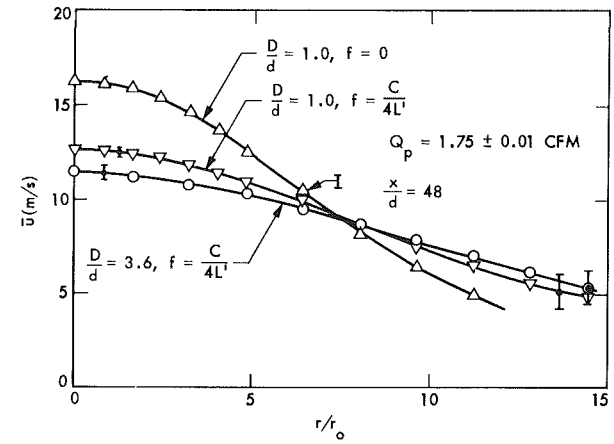

Fig. (b)

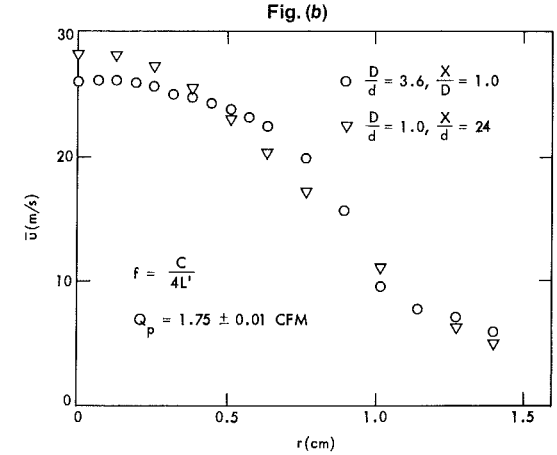

Fig. (c)

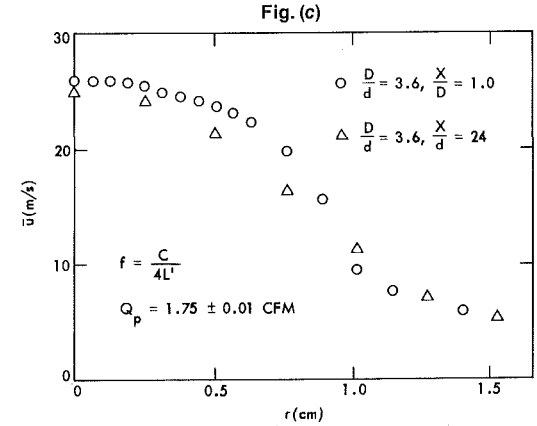

Fig. (d)

Fig. 7 Comparison of radial profiles of velocity

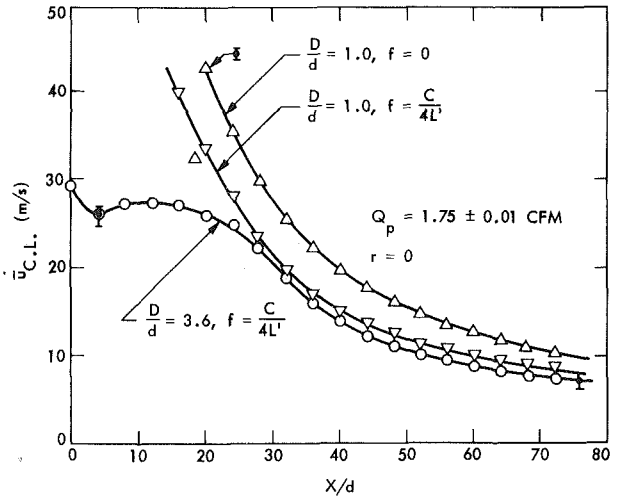

Fig. 8 Axial profiles of centerline velocity

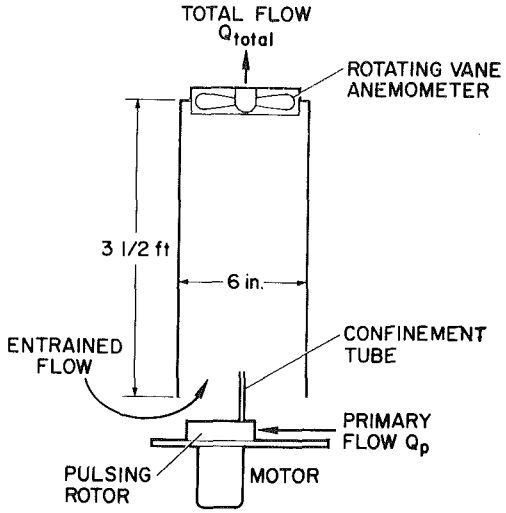

Fig. 9 Apparatus for direct measurement of total entrainment

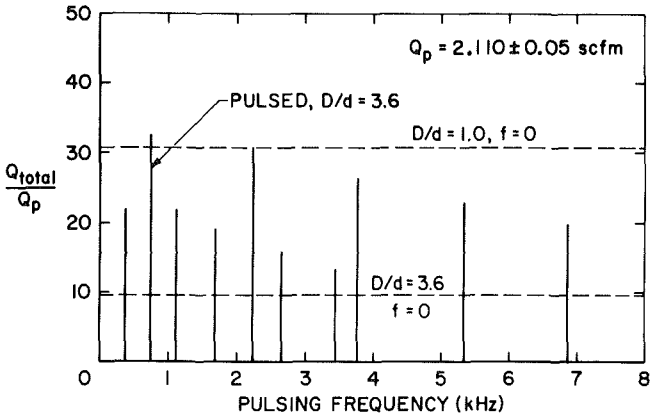

Fig. 10 Augmentation in total entrainment under resonant pulsing

A comparison of cases (i) and (ii) shows that an unconfined pulsed jet spreads faster than a steady one – an observation previously made by several investigators [3, 4, 8]. A comparison of cases (ii) and (iii) reveals that the spreading distance of the resonantly pulsed confined jet (case (iii)) is slightly larger than that of the unconfined pulsed jet (case (ii)). Furthermore, the closeness of the profiles for the latter two cases indicates that the momentum is comparable. Direct measurements of momentum were unfortunately not made during this investigation.

Next, we shall compare the volume flow rates of the resonantly pulsed confined jet with those for an unconfined pulsed jet.

A comparison of the radial profile of velocity for the resonantly pulsed confined jet at $X/D = 1.0$ (i.e., $x/d = 3.6$) with that for the unconfined pulsed jet at $x/d = 24$ is shown in Fig. 7(*c*) by combining the same profiles shown separately in Figs. 5 and 7(*a*). The closeness of these profiles indicates that the volume flow rates for the two profiles are comparable. Since the primary flow rates in the two cases are the same, this could mean that the resonantly pulsed confined jet ($D/d = 3.6$) entrains as much fluid in a distance $x/d = 3.6$ from the confinement tube exit plane as the $D/d = 1.0$ pulsed jet does in a distance $x/d = 24$ from its exit plane. It could also mean that the resonantly pulsed confined jet draws entraining fluid *into* the confinement tube and mixes with it before exiting the confinement tube, thereby requiring a reversal in the velocity profile at the exit plane. In the latter case there arises a question on how far the secondary flow penetrates into the confinement tube before being entrained by the primary jet. A preliminary flow visualization study by use of a transparent confinement tube in conjunction with a smoke-strobe technique revealed that the secondary flow penetrates only slightly below the confinement tube exit plane. More detailed measurements of the flow field in the vicinity of the confinement tube exit plane are needed, but from the preliminary results reported here it appears that this is the region where a strong mixing between the primary jet and the entrained flow takes place.

Despite an initially strong entrainment into the region in the immediate vicinity of the confinement tube exit plane during resonant pulsing, additional entrainment appears to be suppressed in the region $3.6 < x/d < 24$ as there is hardly any evolution of the radial profile between these two stations as seen from Fig. 7(*d*). A further evidence of this behavior may be seen from measurements of the centerline velocity along x, shown in Fig. 8. Notice that the centerline velocity for the resonantly pulsed confined jet starts out at the exit plane at a much lower value compared to the unconfined ($D/d = 1.0$) cases, but remains nearly unchanged up to $x/d = 24$. However, for x/d larger than about 24, the resonantly pulsed confined jet resumes its spreading and entrainment behavior as seen from Figs. 7(*b*) and 8 and eventually, over a large axial distance attains a total entrainment slightly larger than that for an unconfined pulsed jet as will be seen in the next section.

Direct Measurements of Total Entrainment

In an effort to estimate the augmentation in the total entrainment over a large axial distance of free jet development during resonances, the pulsed jet was used in an ejector configuration (Fig. 9). The confinement tube was placed at the entrance end of a 15.24 cm (6 in.) diameter duct of 1.067 m (3-1/2 ft) length. The sum of the primary and the entrained flow rates was measured at the exit end of the duct by means of a rotating vane anemometer. The latter was calibrated in a wind tunnel for a relationship between the rotational speed and the flow rate.

The total flow rate through the rotating vane anemometer, normalized with the time-averaged primary flow rate, is shown in Fig. 10 for the resonant frequencies. The lower dashed line shows experimentally measured (Q_{total}/Q_p) value for the unpulsed jet with $D/d = 3.6$, while the upper dashed line denotes the experimentally measured value for the unpulsed jet with $D/d = 1.0$. The primary flow rates in both cases are the same.

Comparing the two unpulsed cases, the Q_{total}/Q_p ratio for the $D/d = 1.0$ case is considerably higher due to its larger

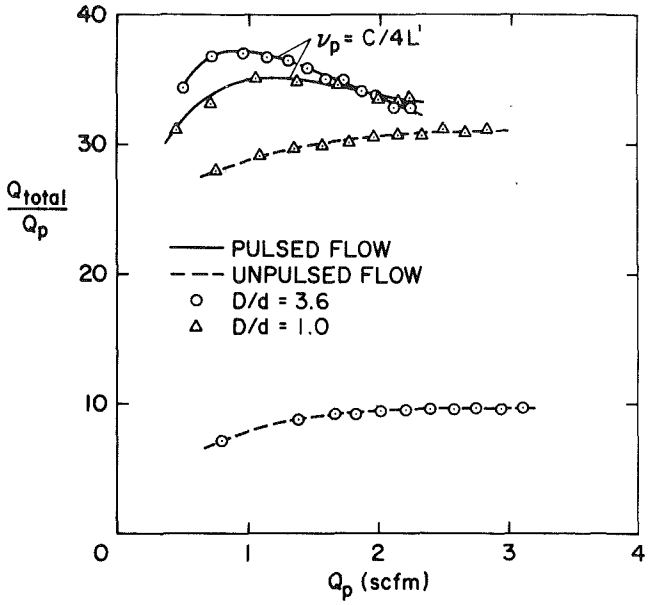

Fig. 11 Variation of total entrainment with primary flow rate

entrainment length-to-diameter ratio. For a steady jet, it may be shown that $(Q_{total}/Q_p + 1)$ increases linearly with the entrainment length-to-diameter ratio.

Notice that, under resonant pulsing conditions, the (Q_{total}/Q_p) ratio for the $D/d = 3.6$ configuration approaches and even exceeds the unpulsed jet with $D/d = 1.0$. For a fixed geometry, $D/d = 3.6$, the augmentation in (Q_{total}/Q_p) ratio at some pulsing frequencies is more than 200 percent over the unpulsed value.

The effect of varying Q_p on the (Q_{total}/Q_p) ratio is shown in Fig. 11. The data points represented by circles are for the $D/d = 3.6$ configuration, while those represented by triangles are for the $D/d = 1.0$ configuration. In both cases the upper curve represents flow pulsed at a resonant frequency $\nu_p = C/4L'$, while the lower curve represents unpulsed flow.

In both cases of unpulsed flow, the (Q_{total}/Q_p) ratio levels off as Q_p is increased, while both cases of pulsed flow attain a maximum in the (Q_{total}/Q_p) ratio.

The increase in total entrainment due to pulsing over the unpulsed value for the $D/d = 1.0$ case is about 20 percent at $Q_p = 1.0$ scfm. Such increased entrainment for unconfined pulsed jets has been observed by previous investigators [3, 4, 8]. However, for the $D/d = 3.6$ case, resonant pulsing augments the (Q_{total}/Q_p) ratio by 375 percent over the unpulsed value at $Q_p = 0.8$ scfm.

Finally, comparing the two pulsed cases, both with resonant pulsing at $f = C/4L'$, the case of $D/d = 3.6$ results in total entrainment slightly higher than those for the $D/d = 1.0$ case over most of the flow rate range. More significantly, as seen from Fig. 7(c), the initial entrainment rate of the resonantly pulsed confined jet immediately downstream of the confinement tube exit plane is greater for $D/d = 3.6$ configuration than that for the $D/d = 1.0$ configuration.

Flow-Visualization Experiments

The vane anemometer measurements showed that the *total* entrainment of the confined pulsed jet ($D/d = 3.6$) approaches and even exceeds that of the unconfined pulsed jet ($D/d = 1.0$). What is more important, however, is that the *local* entrainment and mixing rates in the immediate vicinity of the confinement tube exit are larger for the $D/d = 3.6$ case under resonant pulsing, as seen from a comparison of radial profiles in Fig. 7(c).

The dramatically enhanced entrainment and mixing rates

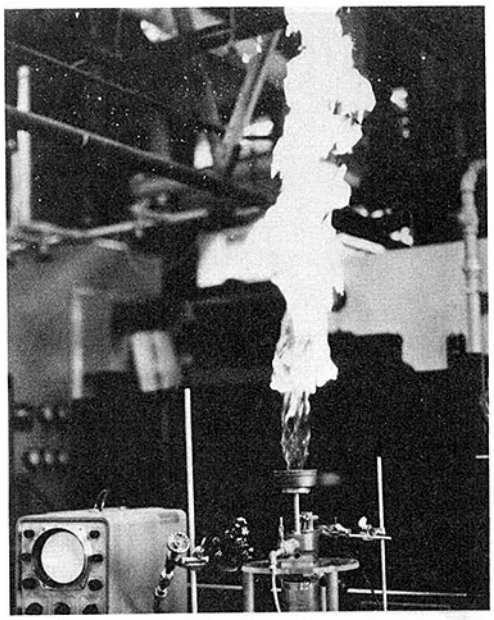

Fig. 12(a) Unpulsed burning methane jet ($D/d = 3.6$)

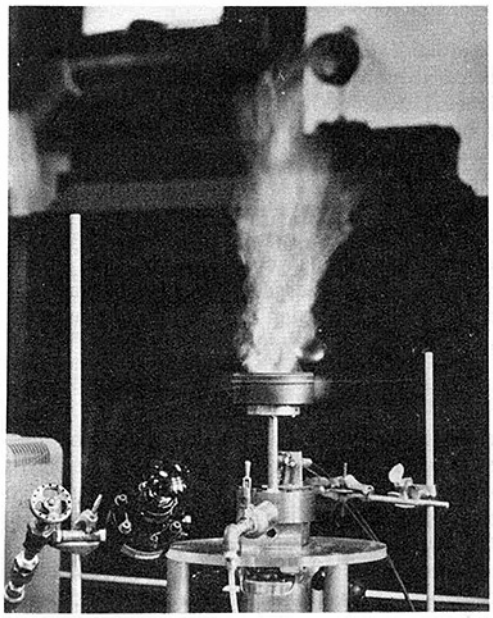

Fig. 12(b) Burning methane jet under resonant pulsing ($D/d = 3.6$)

that occur in the vicinity of the confinement tube exit when the confined jet ($D/d = 3.6$) is taken from no pulsing to resonantly pulsed condition were visualized by two methods: (i) methane flame and (ii) smoke injection.

(i) Methane Flame. Methane gas was introduced as the primary fluid and burned at the exit end of the confinement tube ($D/d = 3.6$). Under resonant pulsing, the entrainment of ambient air was too excessive to maintain the fuel/air ratio above the lean flammability limit, and it was necessary to curtail the entrainment by means of a shallow can mounted at the exit end of the confinement tube. Photographs of the flame under no pulsing and resonant pulsing conditions are shown in Fig. 12. Figure 12(*a*) shows unpulsed methane jet burning freely in air. Figure 12(*b*) shows the flame for the same mean flow rate of methane, but pulsed at the resonant frequency $\nu_{1,0-c}$. Notice the considerably shortened flame length and the absence of soot-particle radiation, both of which are demonstrative of enhanced mixing and lean combustion.

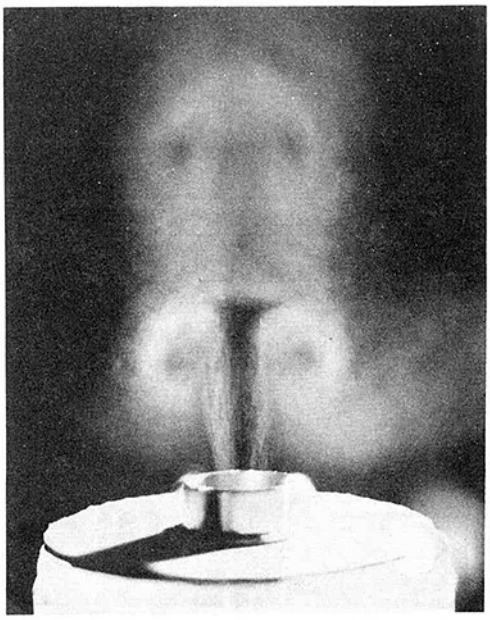

Fig. 13 Smoke-strobe visualization of confined pulsed jet at resonance

(ii) Smoke Injection. Smoke was introduced through a ring placed around the confinement tube, slightly below the exit plane. The objective was to trace the ambient air entrained by the jet issuing from the confinement tube. The smoke was made visible by a strobe light source, which was pulsed in synchronization with the pulsing rotor. Strong vortex interaction between the jet flow and the entrained flow was revealed under resonant pulsing. Figure 13 shows a photograph of the large vortices at the exit from the confinement tube. No such large-scale vortex interaction could be detected under no pulsing and off-resonant-pulsing conditions.

Mean Pressure Measurements

Recall that, under steady flow conditions, the pressure $p_{1,s}$ at the base of the confinement tube ($D/d = 3.6$) is lower than that ($p_{2,s}$) at the exit, as shown by equation (6). Furthermore, the pressure $p_{2,s}$ at the exit is the same as the ambient pressure p_a. A few preliminary measurements were made to determine how this mean pressure distribution is affected by resonant pulsing. These measurements showed that, as the fundamental resonant frequency was approached, the pressure distribution along the confinement tube was markedly affected.

Under resonant pulsing, the mean pressure p_2 at the confinement tube exit approached the value $p_{1,s}$, while the mean pressure p_1 at the confinement tube base approached p_a. This means that the mean pressure near the exit of the confinement tube drops significantly below the ambient pressure p_a, causing a large quantity of ambient air to be drawn into the confinement tube. Furthermore, the jet issuing from the orifice at the base does not seem to attach to the walls of the confinement tube and appears at the exit as a small-diameter jet. Vigorous mixing between the jet and the entrained ambient air takes place near the exit end of the confinement tube through a strong vortex interaction. These observations are supported by the smoke-strobe visualization of the flow field shown in Fig. 13.

Conclusions

The investigation reported here has revealed the existence of a resonant entrainment phenomenon associated with a confined pulsed jet. Downstream of the confinement tube exit plane, the entrainment and mixing rates of a confined jet are dramatically enhanced when pulsing is applied at the organpipe resonant frequency of the confinement tube. The resulting total entrainment over a large distance, in some cases, is slightly larger than that even for the unconfined pulsed jet. The phenomenon should be of considerable interest in ejector and burner design, both of which benefit from any enhancement in mixing between a primary and secondary flow.

From the foregoing presentation of measurements on the resonant entrainment phenomenon, it appears that the following two requirements need to be met for the phenomenon to occur.

(1) The primary flow must be pulsed at frequencies which are equal to (or one-half of) the organ-pipe natural frequencies $\nu_{n,0-c}$ of the confinement tube.

(2) The diameter D of the confinement tube must be larger than the diameter d of the primary jet orifice.

Evidently the augmentation in entrainment acheived under resonant pulsing will depend upon several parameters, namely, the D/d ratio, the discharge tube length L, and the primary jet flow rate Q_p. This opens up the possibility of optimizing the entrainment by proper selection of these parameters.

The mechanism responsible for the resonant entrainment phenomenon appears to be twofold:

(1) Under resonant pulsing, there appears a low mean pressure region near the exit end of the confinement tube, which causes a large quantity of ambient air to be drawn in.

(2) The resonantly pulsed confined jet does not attach to the wall of the confinement tube and mixes vigorously with the entrained flow through a strong vortex interaction.

Clearly, more detailed phase-averaged hot-wire and pressure measurements together with flow-visualization techniques, will be necessary to uncover the underlying mechanism. Such an understanding will then lead to quantitative estimation of augmentation in entrainment rates under the resonant pulsing condition.

The amplitude of pulsation in the present investigation was approximately 37.5 percent of the mean velocity, which results in the sound level approaching that of a siren. It would be of interest to explore the minimum pulsation amplitude necessary to achieve resonant entrainment.

References

1 Quinn, B., "A Simple Estimate of the Effect of Ejector Length on Thrust Autmentation," *Journal of Aircraft*, Vol. 10, No. 5, May 1973, pp. 313–314.

2 Parikh, P. G., Sawyer, R. F., and London, A. L., "Pollutants from Methane-Fueled Gas Turbine Combustion," ASME *Journal of Engineering for Power*, Vol. 95, Series A, No. 2, Apr. 1973.

3 Crow, S. C., and Champagne, F. H., "Orderly Structures in Jet Turbulence," *Journal of Fluid Mechanics*, Vol. 48, Part 3, 1971, pp. 547–591.

4 Binder, G., and M. Favre-Marinet, "Mixing Improvement in Pulsating Turbulent Jets," ASME Symposium on Fluid Mechanics of Mixing, June 1973.

5 Curtet, R. M., and Girard, J. P., "Visualization of a Pulsating Jet," ASME Symposium on Fluid Mechanics of Mixing, June 1973.

6 Bremhorst, K., and Harch, W. H., "Near-Field Velocity Measurements in a Fully Pulsed Subsonic Air Jet," *Turbulent Shear Flows-I*, (eds. F. Durst et al.), Springer-Verlag, 1979.

7 Bremhorst, K., and Watson, R. D., "Velocity Field and Entrainment of a Pulsed-Core Jet," ASME JOURNAL OF FLUIDS ENGINEERING, Vol. 103, December 1981.

8 Viets, H., "Oscillating Jet Nozzles for V/STOL Application," AIAA Paper No. 74-1189 presented at AIAA/SAE 10th Propulsion Conference, Oct. 1974.

9 Hill, W. G., and Greene, P. R., "Increased Turbulent Jet Mixing Rates Obtained by Self-Excited Acoustic Oscillations," ASME Paper No. 77-FE-18 presented at ASME Fluids Engineering Conference, June 1977.

10 Habib, M. A., and Whitelaw, J. H., "Velocity Characteristics of a Confined Coaxial Jet," ASME JOURNAL OF FLUIDS ENGINEERING, Vol. 101, Dec. 1979, p. 521.

11 Stephens, R. W., and Bate, A. E., *Acoustics and Vibrational Physics*, Edward Arnold Publishers, 1966, pp. 174–175.

K. M. Isaac
Graduate Assistant.

J. A. Schetz
Professor and Chairman.
Fellow ASME

Aerospace and Ocean Engineering Department, Virginia Polytechnic Institute and State University, Blacksburg, Va. 24061

Analysis of Multiple Jets in a Cross-Flow

Introduction

The growing awareness of environmental pollution and the attempts to curb it have made the study of jets exhausting into a cross-flow of great practical interest. Chimney stacks exhausting smoke into a wind, cooling tower plumes, discharges of warm water from pipes laid out on the ocean bed, and pollutant discharges into a river are a few such examples. Other examples of gaseous jets in a cross-flow are the lift jets of V/STOL aircraft taking off and landing in strong winds, the injection of fuel into combustion chambers, and the cooling jets on turbine blades. Campbell and Schetz [1], Keffer and Baines [2], Abramovich [3], and others have given results from experimental and theoretical studies of single jets in a cross-flow. They employed momentum integral methods to predict gross properties such as the jet trajectory, the growth of the jet cross-sectional area, mass entrainment, the mean temperature of the jet, etc. and then compared the results with experimental data. These theoretical studies model the jet as a cylinder in a cross-flow, taking into account the "drag" force due to the blockage of the external flow, mass entrainment, and buoyancy. Good agreement with data have been found. (cf. reference [1]). Chien and Schetz [4] obtained exact numerical solutions for a three-dimensional buoyant jet in a cross-flow, using the steady state Navier-Stokes equations written in terms of velocity, vorticity, and temperature with a Boussinesq approximation for eddy viscosity. Patankar, Basu, and Alpay [5] numerically solved the elliptic equations for a deflected turbulent jet with the three velocity components and the pressure as the dependent variables. They used a two-equation turbulence model for the Reynolds stresses.

In many situations, however, one encounters more than one jet in proximity to another. Ziegler and Wooler [6] have analyzed multiple jets in a cross-flow, the jet induced velocity being determined by a combination of sinks and doublets. They assumed that the leading jet is not influenced by the presence of the rear jet; the rear jet is modified by the reduced dynamic pressure behind the leading jet. The present paper extends the analysis of Campbell and Schetz [1] to the study of multiple jets in a cross-flow. The interaction of the two jets is taken into account by a modification of the drag coefficient sensed by each jet.

Analysis

The present analysis is similar to that of reference [1] and interested readers may find details reported there. The governing equations from reference [1] for a jet with average exit conditions are given below.

Mass continuity:

$$E = \frac{\partial}{\partial s}(\rho A v) \tag{1}$$

Entrainment function:

$$E = (A/C)\rho_\infty E^*(v - U_\infty) \tag{2}$$

The entrainment coefficient E^* is given by an empirical expression based on the experimental data for single jets (reference [1]).

$$E^* = 0.2(s/d)^{1.37}/(v/U_\infty)^{0.6} \tag{3}$$

It is realized that this expression may not truly represent the entrainment mechanism in the case of multiple jet cases such as the present; its use is nevertheless partially justified by the subsequent good agreement obtained between the theory and the available data.

s-Momentum:

$$\frac{\partial}{\partial s}(\rho A v^2) = -A\frac{\partial \bar{p}}{\partial s} - gA(\rho - \rho_\infty)\sin\alpha + EU_\infty\cos\alpha - \text{II}h\tau \tag{4}$$

This equation represents the balance of forces along the jet trajectory. The contributing terms are due to the rate of change of tangential momentum, the pressure gradient along the trajectory, the buoyancy, the mass entrainment and the shear stress. In order to evaluate the pressure gradient term, the assumption is made that the static pressure field around a solid cylinder imposes itself on the jet flow. This is a rather simplified model for the pressure field arising from the complicated process of turbulent jet injection into a cross-flow. However, the procedure has been found to be adequate for use in the present mathematical model. Differentiating the expression for freestream static pressure yields

Contributed by the Fluids Engineering Division of THE AMERICAN SOCIETY OF MECHANICAL ENGINEERS and presented at the Winter Annual Meeting, Phoenix, Ariz., November 14-19, 1982. Manuscript received by the Fluids Engineering Division, August 13, 1981. Paper No. 82-WA/FE-4.

$$\frac{\partial \bar{p}}{\partial s} = -q_\infty \sin\alpha\cos\alpha \frac{d\alpha}{ds} \tag{5}$$

The viscous shear stress in the s-direction is proportional to the velocity gradient in that direction and can be expressed by

$$\tau = \rho(\nu + \epsilon)\frac{\partial u}{\partial n} \tag{6}$$

The kinematic viscosity, ν, is neglected in the present study since, for turbulent mixing flows, it is small compared to the eddy viscosity, ϵ. The eddy viscosity is estimated using Prandtl's hypothesis (reference [7]) for free turbulent flows. The eddy viscosity is represented by

$$\epsilon = \beta b(u_{\max} - u_{\min}) \tag{7}$$

The maximum velocity in this expression is defined as the mean jet velocity in order to be compatible with the mean flow assumptions of the present study, and the minimum velocity is the freestream velocity component in the s-direction. Thus the expression for the shear stress becomes

$$\tau = \rho\beta(v - U_\infty\cos\alpha)^2 \tag{8}$$

The buoyancy term is significant only in cases where the jets are nonisothermal and/or the jets and the free stream consist of gases of different densities. Substituting for the pressure gradient term, equation (5), and the shear stress term, equation (8), into equation (4), the final s-momentum equation becomes

$$\frac{\partial}{\partial s}(\rho A v^2) = q_\infty A\sin\alpha\cos\alpha\frac{d\alpha}{ds}$$
$$-gA(\rho - \rho_\infty)\sin\alpha + EU_\infty\cos\alpha - \Pi h\rho\beta(v - U_\infty\cos\alpha)^2 \tag{9}$$

Similarly, the n-momentum equation may be written as

$$-\rho A v^2\frac{d\alpha}{ds} = C_D q_\infty h\sin^2\alpha + gA(\rho - \rho_\infty)\cos\alpha + EU_\infty\sin\alpha \tag{10}$$

The n-momentum equation represents the balance of forces acting perpendicular to the jet trajectory. The term on the left-hand side represents the centrifugal force resulting from the curvature of the jet trajectory. This centrifugal force is balanced by the components of the drag force, the buoyancy, and the mass entrainment. The drag term arises due to the blockage of the free stream; this is postulated to be the drag on an equivalent cylindrical shape inclined at an angle to the free stream flow.

Energy:

$$\frac{\partial}{\partial s}(\rho A v C_p T) = EC_p T_\infty + \bar{h}C(T_\infty - T) \tag{11}$$

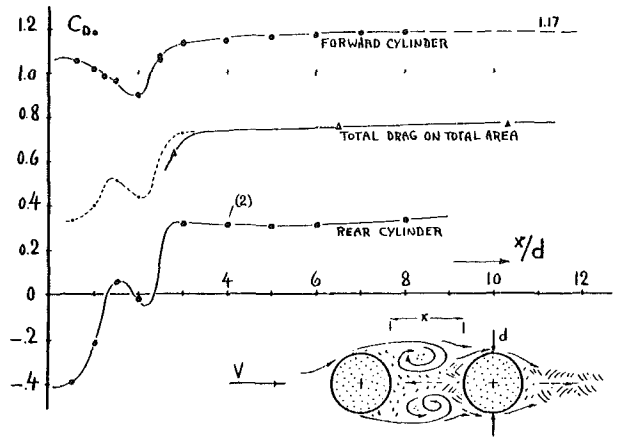

Fig. 1 Drag coefficient of two circular cylinders one placed behind the other. From reference [8].

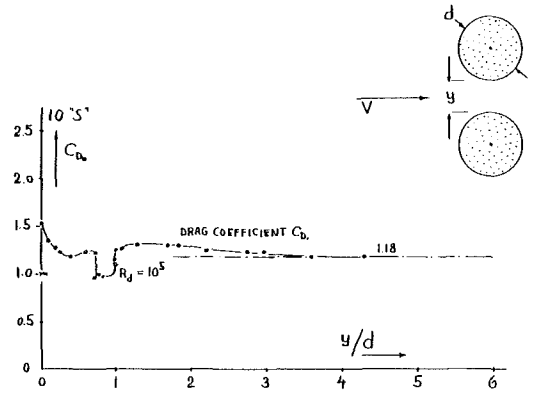

Fig. 2 Drag coefficient of a pair of circular cylinders placed side-by-side. From reference [8].

The energy equation represents the energy balance of the jet fluid due to temperature increase, mass entrainment, and convection at the jet boundary.

When there are two or more jets, their influence on each other may be represented through changes in the effective drag coefficient, C_D, sensed by each jet. Hoerner [8] gives drag coefficients of two circular cylinders when they are placed one behind the other and also side-by-side for Reynolds number of 10^5, as shown in Figs. 1 and 2. This value of Reynolds number is reasonable in many jet problems. In Fig. 1 the drag coefficient, C_D, tends to an asymptotic value

Nomenclature

A = cross-sectional area of the jet
C = effective jet circumference
C_D = drag coefficient
C_p = specific heat at constant pressure
D = jet exit diameter
d = effective jet diameter
ds = infinitesimal length of jet control volume
E = entrained mass per unit length of jet control volume
E^* = entrainment coefficient
g = gravity
h = width of jet
$\bar{h}$ = average film heat transfer coefficient
k = thermal conductivity of jet fluid
Nu_d = Nusselt number ($\bar{h}d/k$)
$\bar{p}$ = average static pressure of jet flow
Pr = Prandtl number
q_∞ = free stream dynamic pressure ($\frac{1}{2}\rho_\infty U_\infty^2$)
R = radius of curvature of jet trajectory
Re = Reynolds number based on d ($U_\infty d/\nu$)
s,n = natural coordinates along and normal to the trajectory
T = mean cross-sectional temperature of jet fluid
VR = effective velocity ratio $[(\rho v^2)/(\rho_\infty U_\infty^2)]^{1/2}$
u = general expression for velocity
v = mean cross-sectional velocity of jet fluid
U_∞ = free stream velocity
x,z = cartesian coordinates
α = inclination of the jet axis to the cross-flow direction
β = constant in expression for eddy viscosity
ρ = mean cross-sectional density of jet fluid
τ = shear stress in s-direction acting on jet control volume
ν = kinematic viscosity
ϵ = eddy viscosity

Subscripts

i = jet flow conditions at injection point
∞ = free stream conditions

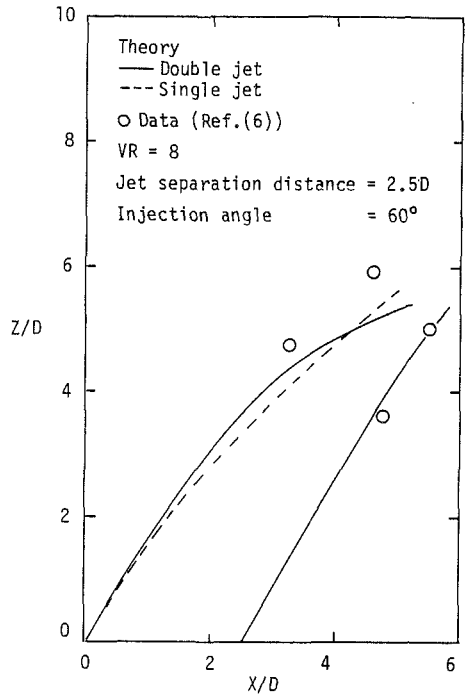

Fig. 3 Single and tandem jet trajectories

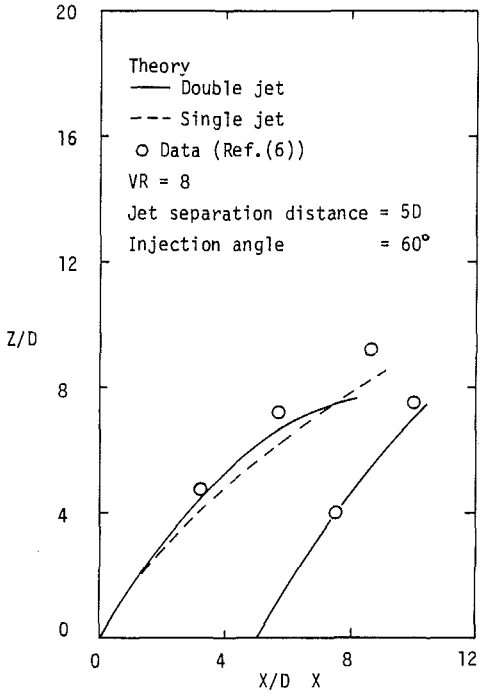

Fig. 4 Single and tandem jet trajectories

of 1.18 for large separation distances. Note that the drag on the rear cylinder (and, hence rear jet) can actually be counter to the main flow.

Equations (1), (9), (10), and (11) form a set of coupled, nonlinear ordinary differential equations which may be solved by using standard routines available. Haming's Predictor-Corrector Method with a fourth order Runge-Kutta starter, as given in reference [9], has been employed in the present case. The perpendicular distance between the two jets is calculated at each step in the integration and the drag coefficient C_D is computed from Figs. 1 and 2 using a cubic spline interpolating routine. The computations are terminated when the jet cross-sections grow and coalesce into each other.

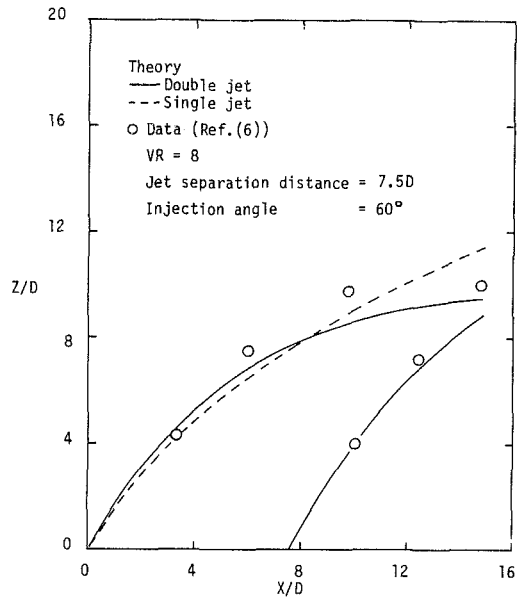

Fig. 5 Single and tandem jet trajectories

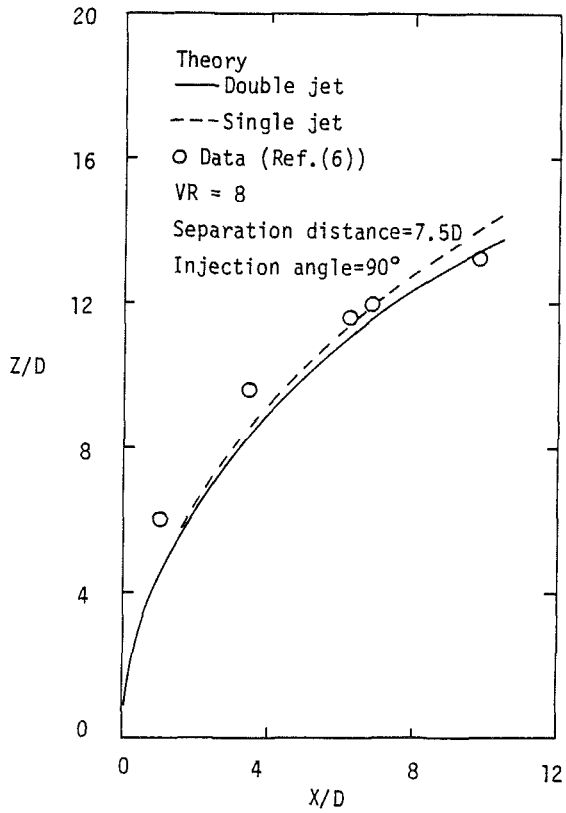

Fig. 6 Trajectories for single and side-by-side jets

Results

Figures 3 to 6 show data of reference [6] along with the present calculations for a 60 deg injection angle for tandem jets and a 90 deg injection angle for side-by-side jets. The single jet trajectory is also shown for reference. The sparseness of the data prevents any definitive conclusions from being drawn from the comparison of the data and the present analysis. The agreement is good in the case of the rear jet trajectory. The most important result of the present analysis is that the rear jet trajectory is significantly modified by the presence of the front one even when the jets are spaced far

apart. As expected, the jet in front is influenced less by the presence of the rear one than vice versa. For the case in Fig. 5, the trajectory of the front jet is significantly affected, and the analysis correctly predicts the observed influence.

The data of reference [6] indicate that, for the side-by-side case, the out of plane deflection of the jets is considerable for small separation distance (2.5D); hence no attempt is made to compare the data and the present analysis for this separation distance. However, for a separation distance of 7.5D, it is seen that the sideways deflection of jets is not signficant. It is, therefore, concluded that the analysis is valid when the jets are not too close to each other.

The main purpose of this study has been to show the significant results which could be obtained by a simple extension of the earlier approach, and the attempt seems to have been fruitful. A logical next step in the study would be to extend the analysis to the region of the merged jets, the initial conditions for which may be obtained by taking the mean properties of the two jets.

References

1 Campbell, J. F., and Schetz, J. A., "Flow Properties of Submerged Heated Effluents in a Waterway," *AIAA Journal*, Vol. 11, Feb. 1973, pp. 223-230.

2 Keffer, J. F., and Baines, W. D., "The Round Turbulent Jet in a Cross-Wind," *Journal of Fluid Mechanics*, Vol. 15, Part 4, 1963, pp. 481-496.

3 Abramovich, G. N., *The Theory of Turbulent Jets*, The MIT Press, Cambridge, Mass., 1963, pp. 541-553.

4 Chien, C. J., and Schetz, J. A., "Numerical Solution of the Three-Dimensional Navier-Stokes Equations with Application to Channel Flows and a Buoyant Jet in a Cross-Flow," ASME *Journal of Applied Mechanics*, Vol. 42, Sept. 1975, pp. 575-579.

5 Patankar, S. V., Basu, D. K., and Alpay, S. A., "Prediction of the Three-Dimensional Velocity Field of a Deflected Turbulent Jet," ASME JOURNAL OF FLUIDS ENGINEERING, Vol. 99, Dec. 1977, pp. 758-762.

6 Ziegler, H., and Wooler, P. T., "Analysis of Stratified and Closely Spaced Jets Exhausting into a Cross-Flow," NASA-CR-132297, 1973.

7 Schlichting, H., *Boundary-Layer Theory*, 6th Edition, McGraw-Hill, New York, 1968.

8 Hoerner, S. F., *Fluid Dynamic Drag*, Hoerner Fluid Dynamics, Brick Town, New Jersey, 1965, pp. 8-1-8-3.

9 Carnahan, B. L., Luther, H. A., and Wilkes, J. O., *Applied Numerical Methods*, Wiley, New York, 1969, pp. 381-406.

Measurements in a Jet-Pipe Flow Issuing Perpendicularly Into a Cross Stream

J. Andreopoulos
Sonderforschungsbereich 80,
Universität Karlsruhe,
Karlsruhe, West Germany

Measurements are presented of velocity fluctuation statistics in the jet-pipe of a jet in a cross-flow situation for various values of the jet-pipe to cross-flow velocity ratio. The nonuniformities of the velocity profiles inside the pipe extend as far as 3 pipe-diameters upstream of the exit plane for small velocity ratios and to 2.5 diameters for higher velocity ratios. Longitudinal flow acceleration and strong streamline curvature affect turbulence activities at the exit plane for small velocity ratios. The horseshoe vortex which is formed in front of the exit plane results in a streamline curvature with a stabilizing effect on turbulence in the nearby flow field while the streamlines are unstably curved everywhere else. At high velocity ratios the pipe flow is very weakly affected by the cross-flow.

Introduction

The problem of turbulent transport of momentum, heat, and mass is of great importance in engineering studies. If the problems related to turbulence modeling were solved, improved predictions for complex turbulent flows could be expected since the numerical aspects of prediction methods have been reasonably well developed. Additional experimental data are needed, however, to provide guidance and test cases for the development of better turbulence models.

The present experiment is part of an investigation of an incompressible jet in a cross-flow and deals with the upstream effect of the cross-flow on the flow inside the pipe from which the jet issues. Since the initial interaction between the jet fluid and cross-flow starts very early and depends heavily on the conditions inside the jet and on the oncoming boundary layer, some detailed information on the turbulence structure prior to merging is very important. In addition, experimental data are needed to verify various assumptions on boundary conditions made by most of the investigators who attempted to make three-dimensional calculations of jets or rows of jets into cross-flow. Patankar et al. [1], for instance, used uniform velocity profiles at the jet exit as boundary conditions to calculate a jet into a cross-flow. It is not known clearly how realistic such assumptions are which simplify the calculation procedure. It might be expected, however, that the external cross stream affects the flow inside the pipe and consequently the jet exit profiles. Some previous experimental results found in the thesis of Bergeles [3] and published in [13] are of very limited reliability because it is not possible to measure a flow with high turbulence intensity and two principal flow directions (U and V) by means of a single hot-wire sensor and without rotating the probe.

The aim of the present work was to investigate the flow structure at the jet-pipe exit plane and upstream inside the pipe and to provide data for testing calculation methods. The work covers cases from $R = 0.25$ to 3.0, where R is the ratio of the jet velocity to the cross-flow free stream velocity. The results include measurements of static pressures, first, second, and third order velocity correlations. At the early stages of the investigation and before the measurements started, a detailed flow observation study has been undertaken by Foss [4] which included flow visualization with dye injection in a water tunnel and surface streaking patterns techniques in the wind tunnel where the present measurements have been carried out. Foss found similar flow "models" applied for both, small R i.e., $0.1 \leqq R \leqq 0.4$ and for high R i.e., $0.6 \leqq R \leqq 3$. His classification is based on similarities of the flow outside the pipe.

The present measurements show that the lower the velocity ratio R the higher the distortion of the pipe flow by the cross-flow. Accordingly some changes in the structural characteristics of turbulence might be expected.

Experimental Arrangement and Techniques

The experiments were carried out in the closed-circuit wind tunnel of the Sonderforschungsbereich 80. A flat plate was installed in the octagonally shaped test section which has 6 m length and 1.5 m internal diameter with an adjustable ceiling to give zero longitudinal pressure gradient. The flat plate was 0.28 m above the tunnel floor and had a streamlined leading edge and a trailing edge flap to adjust for zero circulation around the plate (see Fig. 1), by trying to locate the stagnation point exactly on top of the leading edge nose. The free stream turbulence of the tunnel was about 0.06 percent at 14 m/s. For more details of the wind tunnel construction and performance see Ermshaus and Naudascher [5]. The pipe-jet flow was driven by a 2 stage-compressor through a plenum chamber and a heat exchanger, to control the air-flow tem-

Contributed by the Fluids Engineering Division and presented at the Winter Annual Meeting, Chicago, Ill., November 16-21, 1980 of The American Society of Mechanical Engineers. Manuscript received by the Fluids Engineering Division, December 30, 1980. Paper No. 80-WA/HT-24.

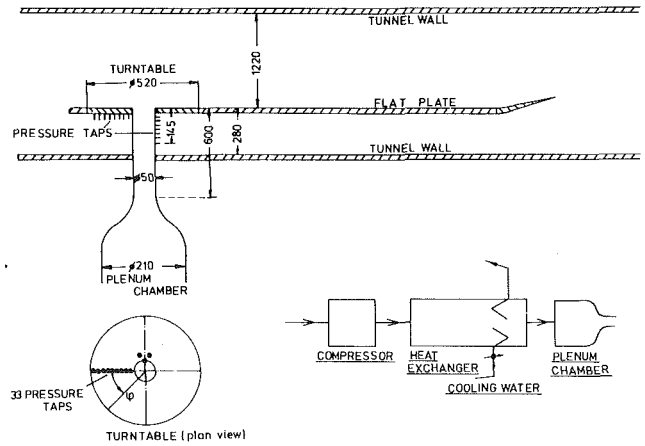

Fig. 1 Jet-pipe flow arrangement

perature, as is shown in Fig. 1. The brass pipe had a 50 mm internal diameter and its exit plane was 12 diameters downstream of the plenum chamber. It could be rotated and had a number of static-pressure taps located on a straight line parallel to its axis. For the pressure measurements a M.K.S. Baratron Type 144 Pressure Transducer was used. The pressure transducer output signal together with the signals of two potentiometers which indicated tap position and angle φ of rotation of the turntable, were fed into a Hewlett Packard Fourier Analyser 5451 C, digitized on line and evaluated to give pressure coefficients. Because most of the pressures were highly fluctuating, special care was taken to ensure convergence by adjusting, where it was necessary, the number of samples and the sampling rate.

Velocity and turbulence measurements were made with DISA type 55 MO1 constant temperature anemometers and DISA miniature slant-wire type PO2 and cross-wire type P51 probes with 5 μm plated wires. Special care has been taken in checking the upstream effect of the probe-holder interference with the flow since the probe entered the pipe from the exit plane. This effect was found to change the static pressure reading inside the pipe by only 0.5 percent. The jet in a cross-flow consists of two interacting vortical flows, namely the oncoming boundary layer and the pipe flow. In the boundary layer the longitudinal component of velocity is much greater than the vertical and spanwise respectively

$$U>>V,W \tag{1a}$$

The relation inside the pipe can be expressed in terms of the present system of coordinates as

$$V>>U,W \tag{1b}$$

Although simple superposition of these two flows is not realistic, it can be argued that because of (1*a*) and (1*b*) in the jet in a cross-flow case is:

$$U,V>>W \tag{2}$$

It was decided initially that the use of a single slant-wire which has the best spatial resolution should give a good indication of how the flow is behaving at the plane of symmetry XOY (see Fig. 1). There are various ways to extract mean velocities, turbulence intensities and shear stress from single wire measurements with different yaw, pitch, or rotation angles of the wire. Most of them try to expand the term U_{eff} in the expression of King's Law:

$$E^2 = A + BU_{\text{eff}}^n \tag{3}$$

An expansion of U_{eff}^n in a Taylor series requires one velocity component to be much larger than the other components, e.g., $U>>V$. In the present flow configuration close to the exit plane, V/U starts to have significant values because of (2) and consequently a Taylor expansion would not be valid. To solve this problem, another method was adopted: instead of measuring the mean voltage, E, the mean value of $[E^2 - A/B]^{2/n}$ was evaluated from the digitized signal E. Then the response equation becomes

$$(U\cos\psi - V\sin\psi)^2 + W^2 = [(E^2 - A)/B]^{2/n} = G^2(\psi) \tag{4}$$

In principle, with 6 different pitch angles the system of 6 unknowns can be solved. But since the coefficients of $\bar{W}^2$ and $\overline{w^2}$ which appear after averaging (4) remain unchanged at various values of ψ the corresponding matrix is zero and consequently is impossible to solve the system of equations. However, $\bar{W}$ is zero at the plane of symmetry, $z=0$ and because of (2), W can be omitted in equation (4).

Measurements with this technique were made at $X=0$. At a later stage, the use of an X-wire probe gave results which agreed very well with the slant-wire results provided that the X-wire probe was oriented properly to be parallel with the mean velocity vector. To obtain this position some trials were necessary. Then a data-analysis technique similar to that described by Andreopoulos and Bradshaw [6] was adopted and used. The agreement between the cross-wire results and those of the slant-wire indicated that the former were not affected by the instantaneous $\partial W/\partial z$ gradient. This means that the spatial resolution of the cross-wire is quite adequate and this is probably the only positive conclusion so far, because it was realized that the main source of error in the technique is the fact that the instantaneous velocity vector may lay at an angle too large for the cosine law approximations to be valid. For the case of velocity ratios $R=2$ and $R=1$ this is rather rare and the uncertainties are extremely small. For $R=0.5$ the turbulence intensities increase and this effect starts to cause errors which become significant for $R=0.25$. To overcome this problem the method of Friehe and Schwarz [9] has been applied in the way described by Andreopoulos [8]. This method is valid for a larger range of pitch angles (± 30 deg) and was found in [8] to compute the shear stress more accurately. In fact Andreopoulos's study indicated that the Friehe and Schwarz method computes the shear stress $\overline{uv}$ better than the modified cosine law by about 15

Nomenclature

c_f = skin friction coefficient
c_p = $(p-p_{\text{ref}})/0.5\rho U^2{}_j$
D = pipe diameter
E = hot wire voltage
p = static pressure
r = radius of curvature
R = U_j/U_e, pipe to cross-flow velocity ratio, values at infinity
S = stability parameter $\partial\bar{V}/\partial x/\partial\bar{U}/\partial y$
u,v,w = fluctuating velocity components
$\bar{U},\bar{V},\bar{W}$ = mean velocity components
U,V,W = instantaneous velocity components
u_τ = friction velocity
x,y,z = coordinates (see Fig. 1)
x_0 = upstream effect: distance from exit to point where cross-flow effects are negligible
α = angle of streamline deflection
δ^* = displacement thickness
ψ = angle of hot wire
φ = angle of pipe rotation
β = $\delta^* dp/dx\tau_w$ pressure gradient parameter
τ_w = wall shear stress

Subscripts

e = cross-flow at infinity
j = jet-pipe flow at infinity i.e., exit of the plenum chamber

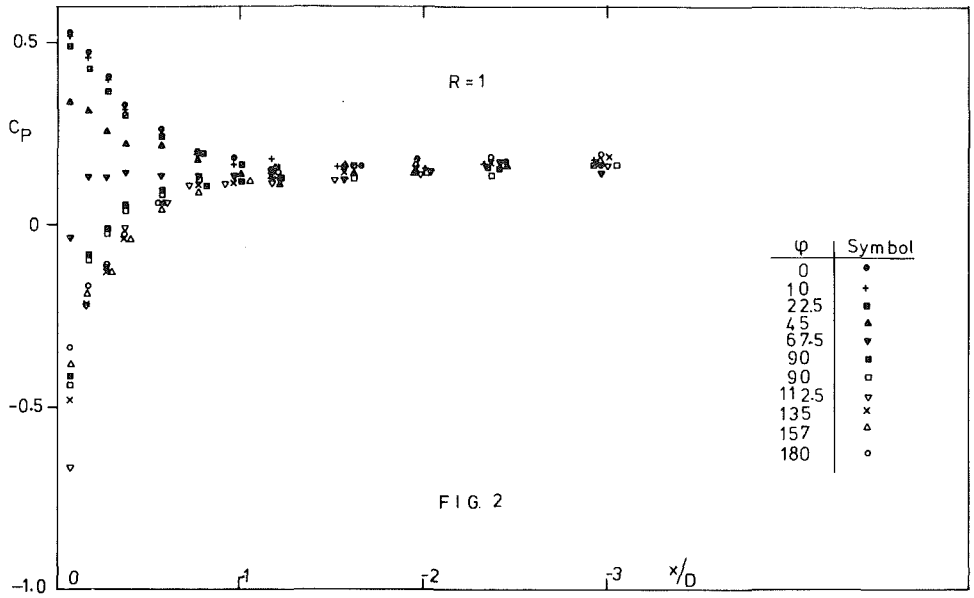

Fig. 2 Wall static pressure distribution

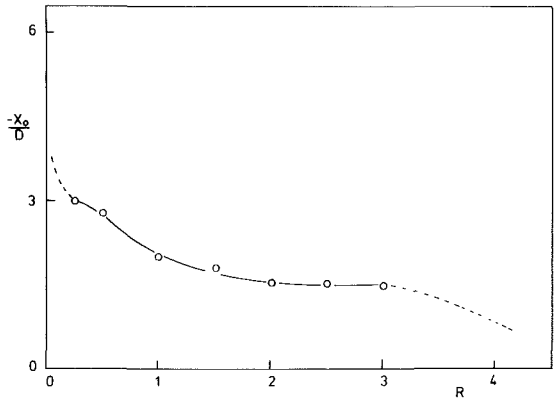

Fig. 3 Upstream effect versus *R*

percent. The improvement of the accuracy similarly is 6 percent on $\bar{U}$, 4 percent on $\overline{u^2}$, 12–15 percent on $\overline{v^2}$. Apart from the error due to high turbulence intensity because the hot-wire is not sensitive to the velocity direction, the present data analysis scheme does not take into account the effect of the W component on the effective cooling velocity. Tutu and Chevray [10] have estimated the error due to the combined effects of high turbulence intensity (i.e., rectification effects) and sensitivity to W component, as function of turbulence intensity. For 30 percent turbulence intensity they indicate that the errors can be 6.3 percent on $\bar{U}$, 5.2 percent on $\overline{u^2}$, 11.9 percent on $\overline{v^2}$ and 13.6 on $\overline{uv}$. The measurements presented here are intended to document terms of the transport equations for the turbulent kinetic energy and shear stress as fully as possible. Thus triple products that affect turbulent transport of shear and turbulent kinetic energy are also included. The error in measuring triple products is much higher than in the case of normal and shear stresses, and can reach values of the order of 20 percent.

All hot wire signals were digitized at 5 kHz per channel in real time and were recorded on digital magnetic tapes for later data analysis. The digitizing system and the data reduction program which evaluates all products of velocity fluctuations up to third order together with the flatness and skewness, are described by Andreopoulos [7].

Both interacting flow fields, i.e., the pipe flow and the cross-flow, were found to be developing turbulent flows for all the investigated velocity ratios. At $y=4D$, $x=0$, $z=0$, a position of negligible jet-pipe flow influence in the cross-flow, a friction coefficient $C_f=0.0037$ and boundary layer thickness = $0.278D$ at U_e = 13.932 m/s were measured. The results which are presented here are non-dimensionalized by D and $U_j = RU_e$. As was expected the results for various R do not collapse. Probably scales like local boundary layer thickness and the friction velocity u_τ (inside the pipe) with β as pressure gradient parameter could give a better collapse of the results at least for $x \neq 0$. However, measurements of δ^* and u_τ in 3-dimensional flows with pressure gradient are difficult to obtain and verify and in any case are not applicable to profiles a $x=0$ since strong curvature of streamlines in the leading edge boundary layer takes place for moderate and small R ($R \leqq 1$), resulting in a more complicated flow than a simple 3-D boundary layer under a pressure gradient.

Results and Discussion

Mean Velocities and Static Pressures. The initial interaction between the two vortical flow fields i.e., the developing pipe-flow and the cross-stream boundary layer, seems to take place under the existence of severe pressure gradients with streamline curvature and regions of flow separation. Therefore, the jet in a cross-flow case deserves to be called "complex" if not "extremely complex." One of the main objectives of the present study was to determine how far upstream, inside the pipe, effects of the cross-flow can be detected. This has been achieved by measuring the wall static pressures at various angles around the pipe. Pressure coefficient plots along the pipe for different angles of rotation are given in Fig. 2 for $R=1$. Figure 3 shows the pipe length x_0 affected by the cross-stream in terms of pipe diameters as a function of R. This length has been determined as the distance from the exit where the pipe-wall static pressure ceases to change with the angle of rotation φ. It is interesting to see that the upstream effect is larger at lower velocity ratio R, where the rate of changes with R is high too. For even smaller R and beyond the investigated range, x_0 might be expected to increase. For greater R, particularly in the range of $R=2$ to $R=3$, x_0 changes very slightly with, and seems to be almost independent of R. At values of R greater than 3, x_0 is expected to drop to zero with some, unknown as yet, rate.

The pressure coefficient plots of Fig. 2 are important in understanding this complex flow because they can provide information of the flow field *around* the circumference of the

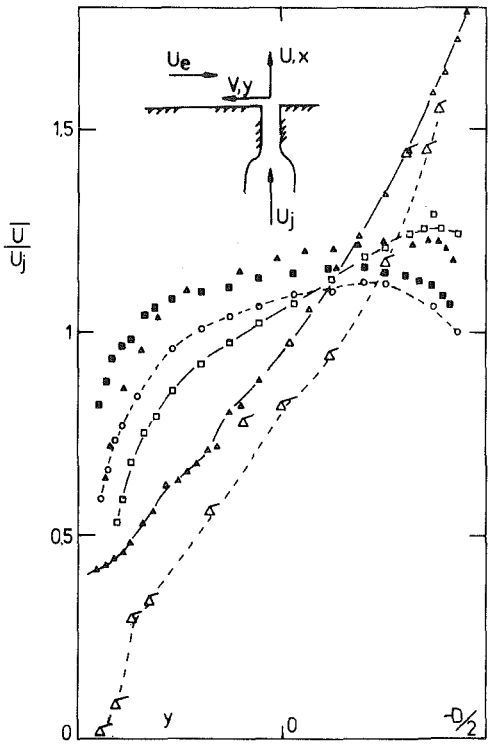

Fig. 4 Mean U-velocity profiles
symbols: x = $-D/2$ 0.0 1.5 mm R
2
1
0.5

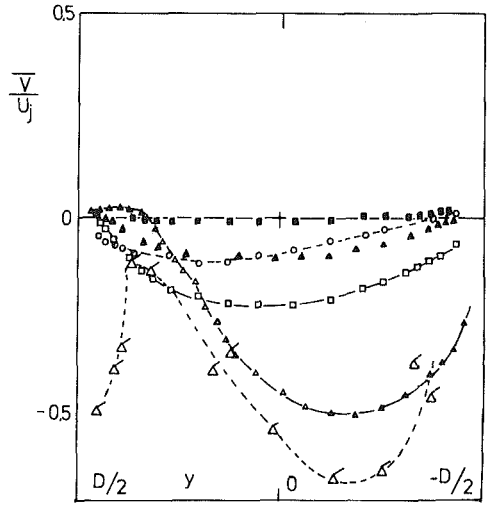

Fig. 5 Mean V-velocity profiles. Symbols as in Fig. 4.

pipe at various upstream positions as opposed to the hot-wire measurements which are limited on the plane of symmetry only. Far from the exit plane, the core inside the pipe is accelerated and it would have continued to do so, up to the exit plane if the cross-stream velocity U_e was zero. With the presence of the cross-flow, part of the pipe flow between φ = 0 deg and φ = 45 deg is decelerated and the other part is highly accelerated as the continuity equation demands. In fact this can be seen from the C_p contours where dC_p/dx changes sign at an angle between 45 deg and 67.5 deg. However, that feature of the flow is more obvious in the mean U-velocity profiles shown in Fig. 4, and will be discussed later.

In the absence of cross-flow the longitudinal velocity profiles inside the pipe should be symmetric with respect to the pipe axis. The imposition of a cross-stream at the pipe exit causes considerable asymmetries on the profiles which are more evident closer to the exit and less pronounced away from there, inside the pipe. This is demonstrated in Fig. 4. Even at $x=-D/2$ and for all investigated R, the $\bar{U}$ profiles are considerably skewed except that of $R=2$ which is only slightly skewed (to avoid crowding of Fig. 4, this profile is not shown).

The same characteristic is evident in Fig. 5 where the mean V-velocity profiles are plotted. With zero cross-flow, or far upstream inside the pipe for $U_e \neq 0$, the $\bar{V}$ profiles should be antisymmetric. In fact a slight antisymmetry is present for $R=1$ at $x=-D/2$ where $\bar{V}$ changes sign at about $x=-0.16D$. But most of the profiles are significantly distorted from their "antisymmetric" distributions, and it is better to examine their behavior in connection with the $\bar{U}$ velocity. At the leading edge ($Y=+D/2$) $\bar{U}$ is decreased from its "symmetric" profile while $\bar{V}$ starts to increase in the negative direction. Very close to the leading edge inside the pipe boundary layer $\bar{V}$ has to have small negative values (specially evident at $x=-D/2$) as the rapidly growing boundary layer demands. Close to the trailing edge ($y=-D/2$) $\bar{V}$ should be positive if the pressure gradient was zero. The fact that the pressure gradient there is favorable does not imply that $\bar{V}$ should be positive. It implies only that $\partial(-\bar{V})/\partial y$ is negative (as the plot indicates) although part of the $\partial\bar{U}/\partial x$ increase might have gone to the $\partial\bar{W}/\partial z$ which is not zero ($\bar{W}$ is zero).

Generally, the gradients around the exit plane are quite high as it is demonstrated from the $\bar{U}$ and $\bar{V}$ profiles at $x=+1.5$ mm for $R=0.5$ plotted in Figs. 4 and 5. In a sense the exit plane exhibits some characteristics of "discontinuity" of the pipe flow for small R and it might be expected that transport of any turbulence quantity is higher in that region.

If the flow inside the pipe was fully developed then the longitudinal gradients of the mean velocity should be zero, i.e., $\partial\bar{U}/\partial x=0$, which implies that $\partial\bar{V}/\partial y$ is also zero. It might be argued therefore, that in this case the velocity gradients around the exit might not be high as in the present case and probably transport of turbulent kinetic energy might be less. One of the key processes in the pipe flow, which can provide explanation for most of the present results is the development of the circular boundary layer inside the pipe. This turbulent pipe flow has to be partially developed within the rather short distance of 12 D only (i.e., the length between the pipe-entrance and pipe-exit) before it exhausts into the cross-stream. Apart of that, the variable pressure gradient imposed by the cross-flow, results in a non-uniform development of the boundary layer around the circumference of the pipe. Figure 6(a) shows a flow configuration picture along the plane of symmetry, according to the present results. For purposes of discussion only, we should distinguish the two shear layers of this figure although both belong to the same boundary layer: one shear layer at the leading edge of the pipe, which grows faster under the influence of the adverse pressure gradient which is present there and the second at the trailing edge, which develops under a favorable pressure gradient.

The skewed mean U-velocity profiles and the non zero V-profiles show clearly that the streamlines start to bend well inside the pipe and before the exit. In fact the lower the velocity ratio the sooner the curvature starts and almost in all investigated R ends somewhere outside the pipe. The curvature gives rise to a pressure gradient $\partial p/\partial y$ normal to the flow, in addition to the longitudinal pressure gradient $\partial p/\partial x$, and imposes an "extra" strain rate $e=\partial\bar{V}/\partial x$ on the flow over and above the "simple" shear $\partial\bar{U}/\partial y$.

So far the discussion has been focused on what are the effects of the cross-stream on the pipe flow. However, since both fields interact with each other, it can be expected that the jet flow affects the cross-flow as well. In fact the oncoming boundary layer rolls up into a horseshoe vortex, separates at a saddle point of the surface stress lines in front of the jet, like

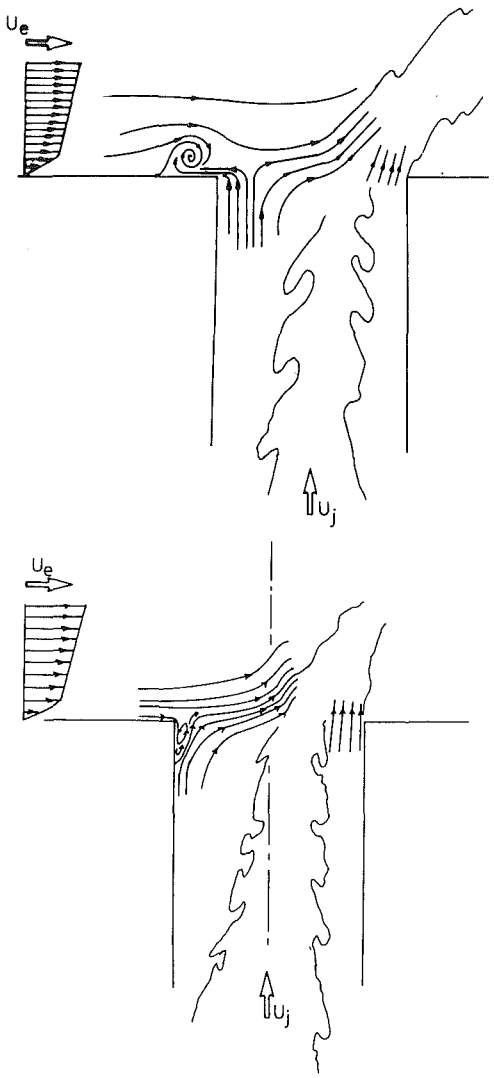

Fig. 6(*a*, *b*) Proposed flow configuration. Figure 6(*b*) mode is very short in duration.

the vortex generated by the atmospheric boundary layer in front of a tall building, but here moves backwards as the velocity ratio R increases. As a result of the vortex formation, jet fluid is sucked into the vortex and therefore mean-V-velocity component crosses the zero value at $y = 0.30\,D$ and $x = 0$ for $R = 0.5$ and starts taking on small but positive values.

One important feature of the present pipe flow is that the boundary layer at the leading edge of the pipe, for small values of R, can not overcome the high values of the adverse pressure gradient and separates from the pipe wall in a three-dimensional way (Fig. 6(*b*)) with a downstream release of the vortex, at the same time. This means that the flow has two stable modes. In both cases either the pipe flow or the cross-flow separates locally with a formation of a small region of a reverse flow. These transient effects were observed with diminishing occurrence up to $R = 0.5$. For $R = 0.5$ the mode of Fig. 6(*a*) is more predominant. Foss [4] also mentioned some dye reversals but not in connection with the formation of the horseshoe vortex. An attempt has been made to calculate the curvature of the streamlines since their inclinations and deflections at the measuring positions are known. If r is the curvature radius and ds is an infinite small increment in the streamline coordinate s i.e., along the streamline then the curvature can be expressed in terms of:

$$\frac{1}{r} = \frac{d\alpha}{ds} = \frac{\partial\alpha}{\partial x}\frac{\partial x}{\partial s} + \frac{\partial\alpha}{\partial y}\frac{\partial y}{\partial s}$$

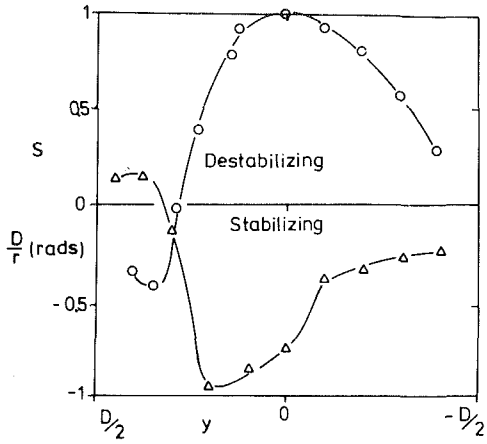

Fig. 7 △ Curvature 1/*r* and ○ Stability parameter *S* at $x = 0$ for $R = 0.5$

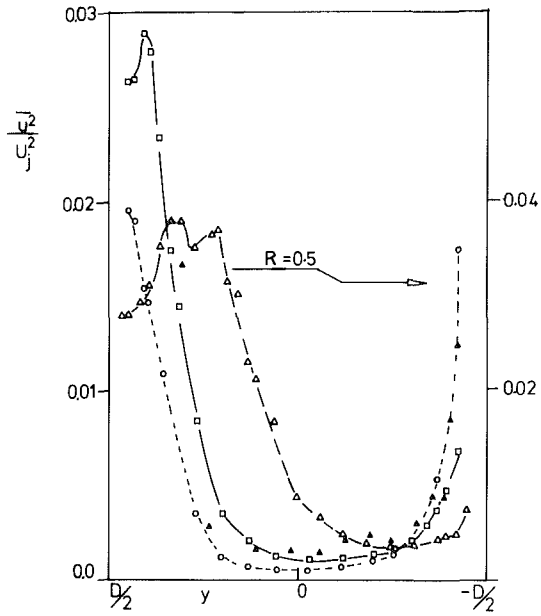

Fig. 8 $\overline{u^2}$ profiles. Symbols as in Fig. 4.

or

$$\frac{1}{r} = \cos\alpha\frac{\partial\alpha}{\partial x} + \sin\alpha\frac{\partial\alpha}{\partial y}$$

The results normalized with the pipe diameter D, are plotted in Fig. 7. The more interesting feature of them is that the curvature is not constant or even "fairly" constant having the same center of curvature. Near the upstream edge of the pipe, it varies very rapidly having an "impulse" like character and changes sign at $y \simeq 0.29\,D$. On the same Fig. 7 the stability parameter S defined as the ratio of the turbulent kinetic energy production by the extra strain rate $\overline{uv}\partial\bar{V}/\partial x$, to the "usual" production by the basic rate of shear strain. $\overline{uv}\partial\bar{U}/\partial y$, i.e., $S = \partial\bar{V}/\partial x / \partial\bar{U}/\partial y$. It is clear that when both gradients have the same sign, turbulence production is increased by curvature (destabilizing effect) and when are opposite turbulence production is significantly reduced (stabilizing effect). Values of this parameter are plotted typically for $R = 0.5$ and at the exit plane only. Curvature has a stabilizing effect on turbulence near the upstream edge of pipe and a destabilizing effect at $y \lesssim 0.29\,D$ where S changes sign.

The Turbulence Quantities. The interpretation of the results is based on the flow configuration of Fig. 6, which actually is the outcome of the investigation and therefore

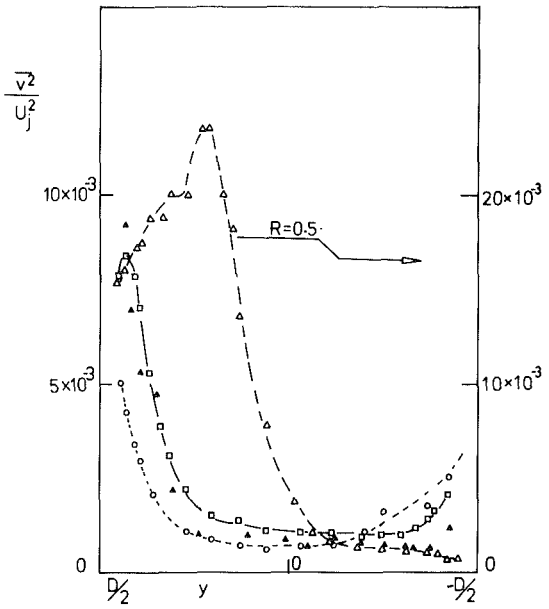

Fig. 9 $\overline{v^2}$ profiles. Symbols as in Fig. 4.

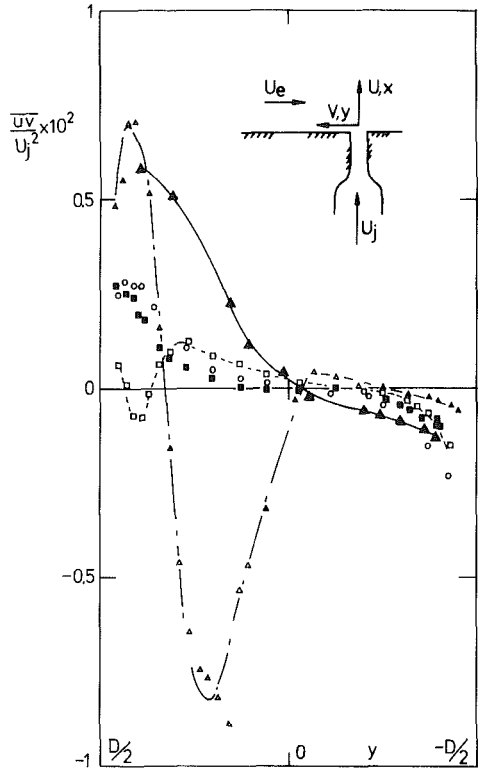

Fig. 10 $\overline{uv}$ profiles. Symbols as in Fig. 4.

should follow rather than precede them. However, it was thought that the analytic presentation of the flow features should be more comprehensive rather than the synthetic one.

The normal stresses $\overline{u^2}$, $\overline{v^2}$ and the shear stress uv are plotted in Figs. 8, 9, and 10, respectively. Very close to the walls all the above quantities exhibit local maxima or minima, with the effects of the adverse and favorable pressure gradient on the leading and trailing edge respectively being evident, especially for smaller R. As the velocity ratio R is decreased, the maxima of the turbulent intensities closer to the leading edge wall move away from the wall towards the center of the pipe. The opposite is happening at the trailing edge. The local maxima, due to the favorable pressure gradient, are formed closer to $y=-D/2$.

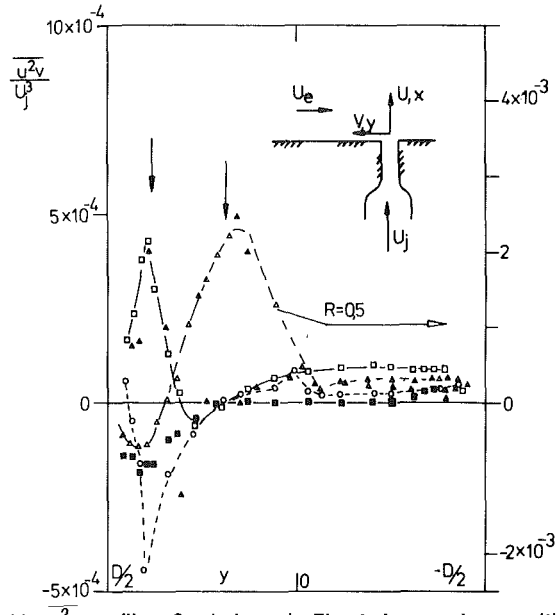

Fig. 11 $\overline{u^2v}$ profiles. Symbols as in Fig. 4. Arrows show position of maximum or minimum uv.

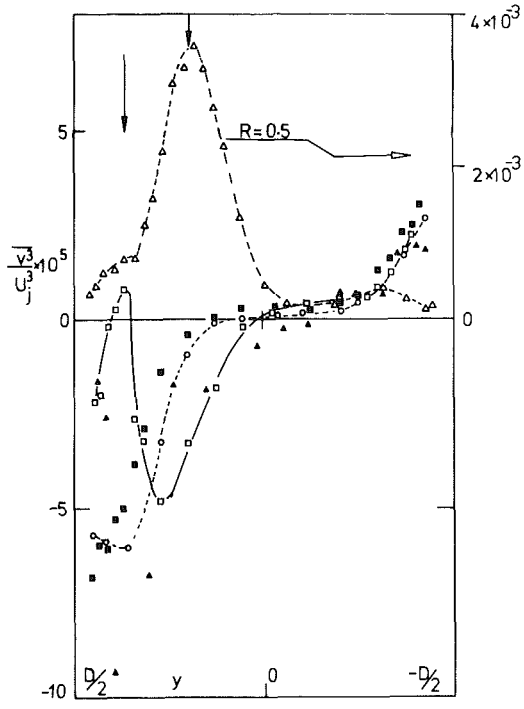

Fig. 12 $\overline{u^3}$ profiles. Symbols as in Fig. 4.

The profiles for $R=2$ show nothing unexpected while those for $R=0.5$ postulate quite different behavior particularly very close to the upstream side of the pipe at the exit plane. Therefore, most of the following discussion refers to the case of $R=0.5$ and can be partly applied to $R=1$ which is an intermediate case between $R=0.5$ and $R=2$. The $\overline{u^2}$ and $\overline{v^2}$ intensities exhibit two local maxima very close to each other; one of them, the closest to the upstream pipe edge, corresponds to the point where uv and $\bar{V}$ change sign, at $y\simeq0.30\ D$. The second maxima takes place at $y=0.24\ D$ exactly where uv reaches its minimum value.

From the three Reynolds stresses shown here $\overline{uv}$ changes more spectacularly than the normal stresses. At one upstream station inside the pipe i.e., at $x=-D/2$, it has one zero crossing only and an asymmetric distribution which is a result of the different longitudinal pressure gradient and at the exit

plane the profile has considerably changed, with two additional zero crossings. An explanation of that behavior as well as of the behavior of the other stresses too is possible by looking closer to the transport equations of each quantity, and particularly to the generation or production terms, which are basically controlled by the gradients of the mean velocity components. These gradients in consequence are affected through the mean momentum equation by pressure gradients. In the present case both pressure gradients are present: longitudinal one which is very strong near the exit plane and the normal one which is associated with streamline curvature. It was shown in Fig. 7 that at the exit plane curvature effects are expected to be high. Near the upstream edge $y=D/2$, where the curvature has a stabilizing effect on turbulence, turbulence production is damped, all stresses have small values. As soon as the stability parameter reaches higher values, $\overline{u^2}$ and $\overline{v^2}$ increase while $\overline{uv}$ decreases vary abruptly. In fact $\overline{uv}$ changes sign almost at the same point where S changes sign. All turbulent quantities start to relax at the point where S starts to decrease. Additionally to the curvature effects the extra rate of strain $\partial\bar{U}/\partial x$ due to acceleration or deceleration of the flow is expected also to be important, particularly near the upstream edge of the pipe. There the deceleration of the flow ($\partial\bar{U}/\partial x<0$) enhances turbulence activities as can be seen in the "complex production" term in the turbulent kinetic energy transport equation:

$$-[\overline{u^2}-\overline{v^2}]\frac{\partial\bar{U}}{\partial x}-\overline{uv}\left[\frac{\partial\bar{U}}{\partial y}+\frac{\partial\bar{V}}{\partial x}\right]-[\overline{w^2}-\overline{v^2}]\frac{\partial\bar{W}}{\partial z}$$

The first term represents production due to longitudinal acceleration or deceleration, the second term is the "usual" production combined with the extra rate of strain $\partial\bar{V}/\partial x$ because of streamline curvature and the last term is production by streamline lateral divergence or convergence which is expected to be small, inside the pipe, but certainly nonzero on the exit plane. In the close to the leading edge flow region the two strain rates $\partial\bar{U}/\partial x$ and $\partial\bar{V}/\partial x$ have quite opposite effect: the first increases turbulence production while the second damps turbulence production. In the unstable flow region i.e., at $y\leqq 0.20\,D$ both rate strains have the same sign and therefore enhance turbulence production. However near the downstream edge of the pipe i.e., at $y<-0.28\,D$ the flow is accelerating ($\partial\bar{U}/\partial x>0$) and turbulence production is reduced. In addition streamline curvature effects are diminished at that region and the flow has a boundary layer with favorable pressure gradient character.

In Figs. 11 and 12 $\overline{u^2v}$ and $\overline{v^3}$ are plotted. The basic feature of curvature effects are present and the profiles are compatible with the flow model of Fig. 6(*a*). Again here, high gradients in curvature result in high gradients in triple products i.e., high diffusion. Generally triple products seem to vary considerably around the exit. Whether the total term which also contains the pressure fluctuation part $\overline{p'v}$ has the same behavior with the velocity triple products is very difficult to speculate. Techniques to measure pressure fluctuations are not widely accepted because the ambiguities involved are extremely high. This is the reason why such measurements have not been attempted. It is dangerous to argue that pressure fluctuations are small in the present case because they were found to be negligible in the wake flow [6] or in the perturbed boundary layer flow of Andreopoulos and Wood [12]. It is also very dangerous to speculate that pressure fluctuations may counterbalance the triple products in a way that the total diffusion term will become smooth.

Conclusions

The present study has provided new measurements on the turbulence field inside a jet pipe flow with the presence of a cross-stream. It was found that the latter flow can affect largely the flow in the pipe i.e., up to 3 pipe-diameters upstream for small velocity ratios and up to shorter distances for high velocity ratios. The exit velocity profiles were found not uniform and the gradient $\partial\bar{U}/\partial y$ was monotonic throughout the measured region. Thus successful calculation methods for a jet or a plume could either take the measured velocity profile at the jet exit as boundary conditions or start the calculation far upstream inside the pipe at distance x_0 from the exit with uniform flow characteristics. In the light of the present experimental investigation Srivatsa and Rodi [2] have started using nonuniform exit velocity profiles as boundary condition in jets in cross-flow calculations, with encouraging preliminary results.

Streamline curvature and flow deceleration control turbulence activities on the exit plane at low velocity ratio. The most striking result of the present investigation is the existence of two flow regimes with stably and unstably curved streamlines respectively with well known effects on turbulence (see Smits et al. [13]). The "impulse like" change in streamline curvature causes rather spectacular changes in all turbulence quantities with the shear stress being the more typical one. The effects of both extra rate of strains seem to be more acute at low R and die out at higher R. In that respect only, the flow inside the pipe has similar features in all cases with $R\leqq 1$. The horseshoe vortex which is formed in front and/or above the exit plane affects the velocity profiles and causes a streamline curvature with a stabilizing effect on turbulence.

In all respects therefore the results are comparable with the postulate flow model of Fig. 6(*a*).

Acknowledgments

The financial support of the Deutsche Forschungsgemeinschaft is gratefully acknowledged. Special thanks are due to Mr. D. Bierwirth and Mr. P. Schaupp for helping with the test-rig construction. Stimulating discussion and comments provided by Prof. J. Foss are thankfully acknowledged.

References

1 Patankar, S. V., Basu, D. K., and Alpay, S. A., "Prediction of the Three Dimensional Velocity Field of a Deflected Turbulent Jet," ASME JOURNAL OF FLUID ENGINEERING, Vol. 99, 1977, pp. 758–762.

2 Srivatsa, S. K., and Rodi, W., Private Communication, Karlsruhe University, 1980.

3 Bergeles, G., "Three Dimensional Discrete Hole Cooling Processes An Experimental and Theoretical Study," Ph.D. thesis, London University, 1976.

4 Foss, J., "Flow Visualization Studies of Jets in a Cross Flow," SFB 80 Report/T/161, Karlsruhe University, 1980.

5 Ermshaus, R., and Naudascher, E., Der Niedergeschwindigkeitswindkanal des Institutes fur Hydromechanik an der Universität Karlsruhe. Z. Flugwiss. Weltraumforsch. 1, Heft 6, 1977, p. 419.

6 Andreopoulos, J., and Bradshaw, P., "Measurements of Interacting Turbulent Shear Layers in the Near Wake of a Flat Plate," *Journal of Fluid Mech.*, Vol. 100, 1980, p. 639.

7 Andreopoulos, J., "Digital Techniques and Computer Programs for Hot Wire Data Acquisition and Processing," Report SFB 80/ME/181, 1980.

8 Andreopoulos, J., "Comparison Test of Various Hot Wire Data Analysis Methods with Respect their Performance at Various Pitch Angles," Report SFB 80/E/82 and *Rev. Scient. Instr.*, Vol. 52, No. 9, 1981.

9 Friehe, C. A., and Schwarz, W. H., "Deviation from the Cosine Law for Yawed Cylindrical Anemometer Sensors," ASME *Journal of Appl. Mech.*, Vol. 35, 1968, p. 655.

10 Tutu, N. K., and Chevray, R., "Cross-wire Anemometry in High Intensity Turbulence," *Journal of Fluid Mechanics*, Vol. 71, 1975, p. 785.

11 Andreopoulos, J., and Wood, D. H., "The Response of Turbulent Boundary Layer to a Short Length of Surface Roughness," *Journal of Fluid Mechanics*, Vol. 118, 1982, pp. 143–164.

12 Smits, A. J., Young, S. T. B., and Bradshaw, P., "The Effect of Short Regions of High Surface Curvature on Turbulent Boundary Layers," *Journal of Fluid Mechanics*, Vol. 94, 1979, pp. 209–242.

13 Bergeles, G., Gosmann, A. D., and Launder, B. E., "The Near Field Character of a Jet Discharged Normal to a Main Stream," ASME *Journal of Heat Transfer*, Vol. 98, No. 3, 1976.

Viscous Flow in an Annulus With a Sector Cavity

V. O'Brien
Principal Staff Physicist,
Applied Physics Laboratory,
Johns Hopkins University,
Laurel, Md. 20707

The two-dimensional interaction of a circular shear flow and a sector cavity flow is predicted by finite-difference solution of the governing biharmonic equation for steady Stokes planar flow. The location of the dividing streamline is a function of geometry, lying perhaps wholly within the cavity or bulging up into the circular annulus. Also pressure-driven axial flow through the annular configuration is predicted by numerical solution of the governing Poisson equation. The results can be combined with the planar solution to describe a steady three-dimensional flow field which will enhance laminar mixing.

Introduction

Because the capacity and speed of digital computers have increased so dramatically in recent years, it is possible to anticipate realistic but expensive three-dimensional (3-D) inertial flow simulations in the near future. In the meantime we can continue to exploit limit situations which require considerably less actual computation but display some aspects of the real flow that are not intuitively obvious. The steady Stokes numerical simulations should be accepted in that light. Thus one result of the present two-dimensional (2-D) calculation is to reveal the geometry dependent *interaction* of a circular shear flow with a sector cavity flow, Fig. 1. This feature is totally missing in the usual cavity models [1]. The reciprocal influence is quite clear when the dividing streamline, which separates the shear flow from the cavity flow, is manifest in the flow field. (It is never in the location of the undisturbed wall, and the variation of vorticity along it is not the constant value of the undisturbed circular shear flow.) A beauty of the Stokes calculations is that we can superpose rectilinear flow parallel to the walls [2] onto the in-plane circular shear-cavity flow to visualize the resulting 3-D flow. Not only does this give insight into real measurable flow interactions, but the 3-D Stokes flows can provide convenient examples for the verification of 3-D primitive variable computer codes when they are implemented.

The planar 2-D finite-difference calculations are related to Cartesian flow simulations of infinite horizontal shear flows over rectangular cavities [3–5]. Our earlier computations [3] were done with a coarse mesh, but the qualitative features thus displayed are in accord with the present finer mesh calculations in the circular geometry. As stated in the earlier paper [3], a prototype cavity model which assumes an undisturbed dividing streamline [1] (and unrealistic constant velocity or vorticity values) is not an adequate representation of the cavity flow. The present interactive Stokes calculations show the cavity "lid" is not the unit arc and how the vorticity

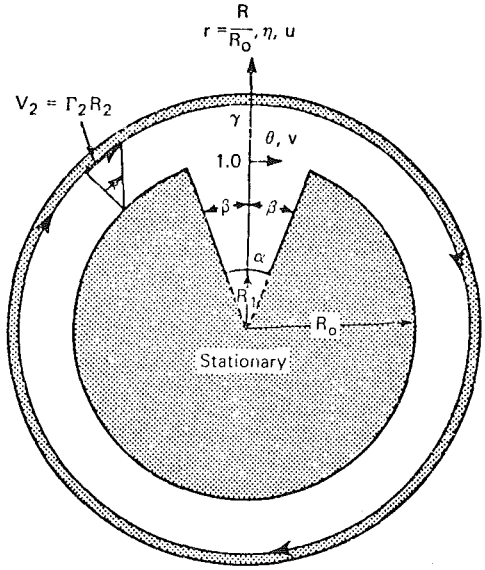

Fig. 1 Circular shear flow over a sector cavity (V_2 is azimuthal velocity of the outer cylinder rotating with angular velocity Γ_2)

varies along it. There are disturbances in the shear flow as well. As for planar Cartesian calculations at greater Reynolds numbers, the circular sector dividing streamline and the vorticity distribution along it will be slightly different with nonlinear inertial effects included, but the present discussion is confined to simple linear flow equations.

The appearance of apparent flow singularities due to unphysically sharp mathematical corners is discussed (see Appendix), but the problem is resolved by considering the corners to be slightly rounded in the numerical computations. This is consistent with the continuum approximation and more realistic regarding actual solid boundary geometries. The stagnation point regions are entirely regular and are always located within the cavity.

The pressure-driven axial flows are related to our earlier solutions for steady rectilinear flow through noncircular ducts [2]. The matrix capacitance method used here is carried out in coordinates appropriate to the present annular geometry.

Contributed by the Fluids Engineering Division of THE AMERICAN SOCIETY OF MECHANICAL ENGINEERS and presented at the Winter Annual Meeting, Phoenix, Ariz., November 14–19, 1982. Manuscript received by the Fluids Engineering Division, July 20, 1981. Paper No. 82-WA/FE-5.

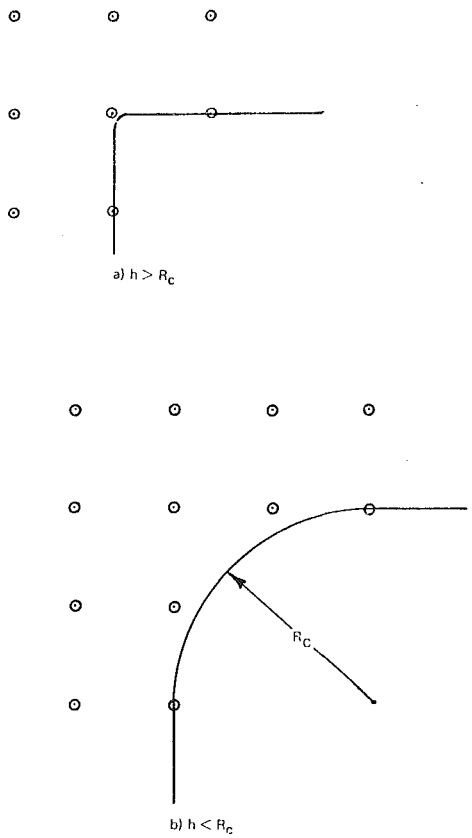

Fig. 2 The rounded corner in finite-difference approximation

Steady annular shear flow (Couette flow) and the rectilinear flow through the annulus are both viscometric flows and have been used for the measurement of shear viscosity for both Newtonian and non-Newtonian fluids. The addition of the sector cavity to the geometry makes the flows nonviscometric, but for a certain rheological constitutive model, namely a "second-order fluid," the Stokes velocity fields are the same as the flow fields calculated here for the Newtonian fluids [6]. Then we can use the planar wall shear results to predict the *first* normal stress difference along the flow boundaries for the second-order fluid [7]. From the rectilinear flow fields we can calculate the *second* normal stress difference distribution along the walls for the second order fluid [8, 9]. In each case the "pressure-error" of the pressure measured at the bottom of the cavity under the flowing non-Newtonian fluid can be predicted.

The combination of the two flow solutions in any proportion in a given geometry describes a swirling flow that has fluid parcels traveling on smooth helices in the annulus opposite the cavity, but it reveals a more complex 3-D flow in the vicinity of the cavity. While it is widely recognized that 3-D turbulence produces efficient mixing, it is not clear how much is due to the randomness of the usually high Reynolds number flows, and to what extent the 3-D shearing is an important agent. The present configuration offers the unique opportunity to study laminar mixing in a controllable situation, where the steady convective velocity fields can be predicted and measured.

Analysis

A Circular Shear Flow Over a Sector Cavity

1 Basic Equations. The normalized streamfunction equation for steady incompressible Newtonian 2-D Stokes flow is

$$\nabla^4\psi=\left[e^{-2\eta}\left(\frac{\partial^2}{\partial\eta^2}+\frac{\partial^2}{\partial\theta^2}\right)\right]^2\psi=0, \qquad (1)$$

in circular cylindrical coordinates [$\eta = \ln(R/R_0)$, θ]. The form of the Laplacian operator is only slightly different from the more familiar Cartesian form. The vorticity magnitude $\Omega = |\nabla \times \mathbf{q}|$. where $\mathbf{q}$ is the velocity normalized by V_2 = outer cylinder velocity, satisfies

$$\Omega=-\nabla^2\psi \quad \text{and} \quad \nabla^2\Omega=0. \qquad (2)$$

The normalized pressure field $P = pR_0/\mu V_2$ also satisfies a Laplace equation and there exists a complex potential $\phi = \Omega + iP$ where Ω and P are orthonormal conjugates (and thus coupled by Cauchy-Riemann relations).

2 Viscous Boundary Conditions. On a solid stationary surface viscous nonslip requires ψ = constant and $\partial\psi/\partial n = 0$ where $\mathbf{n}$ is the normal to the surface. The nondimensional tangential fluid velocity component (v) must be the same as the moving wall at outer arc; the normal velocity component (u) is zero. In the numerical solution of the coupled partial differential equations (2), corresponding vorticity boundary conditions are required (e.g., $\Omega = -\partial^2\psi/\partial n^2$ on the solid fixed surfaces).

If the viscous solution is known, or assumed known, at specified fluid boundaries and these close the flow domain, the elliptic viscous problem is usually well-posed mathematically. An exact solution then exists and is deterministic. The difficulty of realistically modeling a cavity flow is tied to the problems of locating the main dividing streamline that separates the given shear flow from the cavity and specifying conditions along it. These depend upon the shear flow and the geometry.

The corner regions require special consideration. For instance, if we try to substitute the moving solid wall for the fluid dividing streamline for small shear flow gaps ($R_2 \to R_0$), we invite trouble. At the corners the vorticity and pressure become infinite [10]. The singularities arise because the mathematical problem presupposes impossible sharp jumps in velocity from zero on the side walls to a finite one on the moving wall.

The assumption of a *sharp* square *convex* edge on the cavity under the shear flow is also unrealistic and introduces its own singularity complications to the problem. A mathematically sharp edge implies an infinitely small radius of curvature, which is inconsistent with incompressible continuum mechanics that can only describe phenomena on a length scale many times a mean molecular path length due to thermal agitation. Such a sharp corner implies a jump in normal derivative and induces locally infinite vorticity (as shown by asymptotic theory) [11]. Real corners are rounded and normals continuous along the surface. For valid finite-difference flow calculations the "corner point" must be a fluid point, not a wall point, if the local radius of curvature R_c is less than the mesh size, Fig. 2(*a*). For larger R_c more points may be involved, Fig. 2(*b*). If separation takes place near a "sharp" corner, the singularity situation is exacerbated (Appendix), but there is no difficulty with rounded corners.

Sharp or rounded *concave* square corners on the bottom of the cavity do not make much difference to the overall cavity flow solution because no singularities are involved. A rounded corner merely means a local finite 90 deg sector flow instead of the sharp angle solution, i.e., a finite number of separation eddies of diminishing size and intensity rather than an infinite number. (No more than one square corner eddy has ever been observed [12 and 13]).

Of course, it is possible to consider an analytical solution to the same physical problem. Much as in the fashion demonstrated recently for planar shear flow over rectangular cavities [5], appropriate infinite series solutions that satisfy the linear flow equation in the annular region and in a sector can be developed. Such solutions must satisfy nonslip boundary conditions on the solid isocoordinate walls and match normal

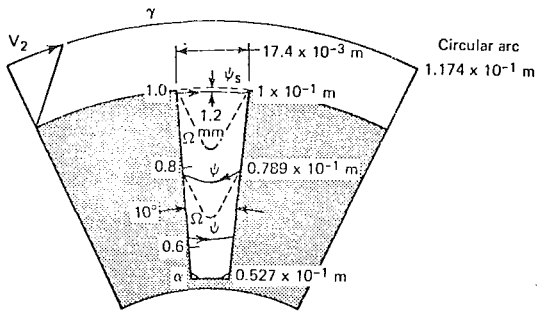

Fig. 3 Shear flow over a 10 deg sector ($\alpha = 0.527$, $\beta = 5$ deg, $\gamma = 1.1735$): null streamfunction and vorticity contours (ψ_s is the dividing streamline)

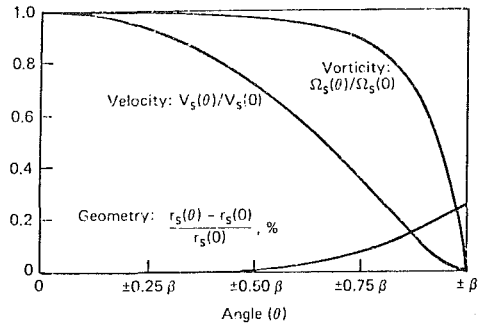

Fig. 4 Angular variation along the dividing streamline under incoming constant shear flow, for vorticity, velocity, and geometry (corresponding to Fig. 3)

and tangential stress over the common fluid boundaries (including the open arc at $\eta = 0$). However, such a *tour de force* still would not resolve the physical flow in the immediate corner region, for the matching arc must include the sharp corner point. The series' convergence fails at that singular point [14].

If the solid corners are realistically rounded for a continuum calculation, the series matching technique in separated coordinate solutions will not work. In principle, it should be feasible to conformally map the flow area to a smooth annulus and to solve the (still linear) flow equations in that transformation plane. Smoothing corners in a simpler context has been considered, for instance the removal of the Christoffel-Schwarz mapping singularity at a sharp corner between two flat plates [5]. Preserving the features of the relative geometry of the sector cavity and the circularity of the annulus would no doubt lead to a rather complicated mapping and correspondingly complex transformed partial differential flow equation. Closed analytic solutions may be possible, but they have not yet been demonstrated to the author's knowledge. In the meantime we can use the less sophisticated finite-difference approximations to visualize the flows.

3 Method of Numerical Approximation. Since a perturbation to a Stokes flow does not propagate very far up-or-downstream of the disturbance, undisturbed inlet and outlet circular shear flow was set at locations $\theta = \pm 3\beta$. In (η, θ) coordinates, $\psi(\eta) = C_1[\eta + \frac{1}{2}(1-e^{2\eta})]$ and $\Omega(\eta) = 2C_1$ with $C_1 = 2[2\eta_2 + (1-e^{2\eta_2})]^{-1}$. At mesh points on the solid boundaries viscous nonslip was satisfied to second-order, $0(h^2)$.

Successive over-relaxation of the finite-difference approximations of equations (2), alternating between ψ and Ω with different relaxation factors, was the numerical scheme used [16]. The relaxation factors were not optimized. The corners are slightly rounded according to Fig. 2(*a*).

B Pressure-Driven Axial Flow

1 Equations and Boundary Conditions. Using R_0 as the reference length, the viscosity coefficient μ and the pressure gradient magnitude $|dp/dz|$, a reference velocity W_0 can be defined: $W_0 \equiv (R_0^2/\mu)|dp/dz|$. Then the normalized axial velocity is $w = W/W_0$. The steady parallel flow equation is reduced to

$$\nabla^2 w = e^{-2\eta}\left(\frac{\partial^2}{\partial\eta^2} + \frac{\partial^2}{\partial\theta^2}\right) w(\eta, \theta) = -1 \qquad (3)$$

[Alternatively we could normalize by W_{max}, the maximum velocity in the undisturbed annulus. It would change the constant on the right-hand side of equation (3).] The viscous nonslip boundary condition is $w = 0$ on the stationary solid walls.

2 Method of Solution. The problem is laid out on a rectangular finite-difference mesh of (η, θ). A variant of the capacitance matrix method used for Cartesian problems [2] allows direct matrix inversion to the solution $w(\eta, \theta)$.

Results

A Circular Shear Flow Over a Cavity

1 10 deg Sector. The flow solution for a finite sector of total angle $2\beta = 10$ deg and $\alpha = R_1/R_0 = 0.527$ under a shear flow with $\gamma = R_2/R_0 = 1.1735$ was carried out by the finite-difference technique with $h_\eta = 0.010$, $h_\theta = 0.0055$. The shear flow gap is almost exactly the chord gap, Fig. 3. Results reveal the characteristic curves of the vortices shown in the figure. The main dividing streamline ψ_s that separates the shear flow from the cavity flow is nearly a circular arc; see Fig. 4. The internal dividing streamlines (and the vortex they enclose) are essentially the same shape as in a previous cavity sector model [17]. Bottom concave corner vortices are also seen, just barely.

The vorticity distribution along the dividing streamline has a maximum at the center and goes to zero at both walls Fig. 4, but the curve is fuller than the assigned vorticity function in the independent sector cavity model [17]. The approximate velocity distribution along the separating streamline is also shown. Qualitatively the velocity distribution resembles the vorticity distribution; neither is constant.

However, even though the main separating streamline is closely approximated by a circular arc, this arc is not located exactly at $r = 1$. The contour is located within the cavity a short distance below $r = 1$. If R_0 is 10^{-1} m, a reasonable size for a small laboratory experiment with a Couette apparatus after Fig. 1, various corresponding dimensions are shown on the right side of Fig. 3. A dip of the bottom streamline of the shear flow about 1 mm into the cavity is predicted, a measurement that would require fairly precise streamline location.

2 A Sector of 30 deg. Another example of the same circular shear flow over a wider sector of the same depth was carried out ($\alpha = 0.527$, $\beta = 15$ deg, $\gamma = 1.1735$). The meshes were $h_\eta = 0.010$ and $h_\theta = 0.0165$. The location of the main separation streamline is given in Fig. 5. The contour is not a circular arc; it arches up out of the cavity into the annular region as if lifted by a Magnus effect of the strong vortex in the cavity. Yet the stagnation points are slightly deeper into the cavity than for the narrow (10 deg) sector. The peak vorticity on this inversely curved dividing streamline of the wider sector is higher than for the narrow cavity. The relative central vorticities are 1.5 but both are smaller than the inlet vorticity, as expected, because the fluid opening has less frictional drag than a solid wall.

B Axial Flow

The pressure-driven flow through the circular annulus is well-known. In (η, θ) coordinates it is expressed as $w(\eta) =$

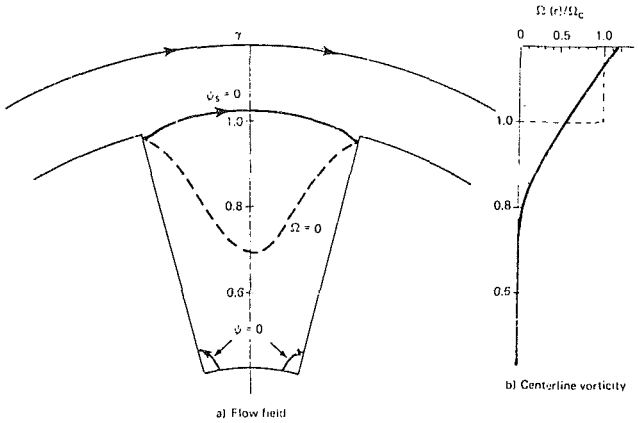

Fig. 5 Shear flow over a 30 deg sector (α = 0.527, β = 15 deg, γ = 1.1735). (The incoming circular shear flow vorticity is designated Ω_C.)

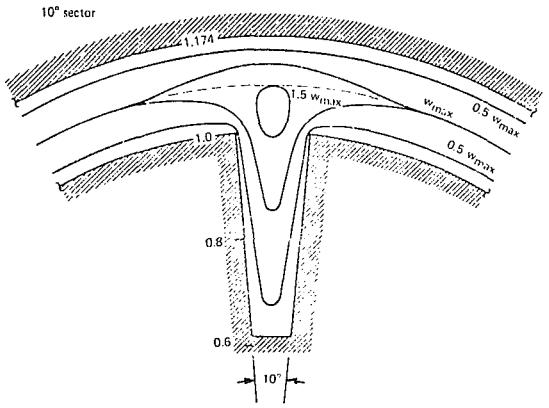

Fig. 6 Isovels for rectilinear flow in the noncircular annulus with a 10 deg sector (α = 0.619, β = 5 deg, γ = 1.1735)

(1/4) {1 − exp(2η) + (η/η_2)[exp(2η_2) − 1]}. It is easily verified that this satisfies $w = 0$ on $\eta = 0$ and $\eta_2 = \ln(R_2/R_0) = \ln \gamma$. The change in isovels when the flow area is enlarged by the slot cavity is seen in the figures showing the computed results.

1 10 deg Sector. Figure 6 shows the axial flow in the annulus sector configuration α = 0.619, β = 5 deg, γ = 1.1735. It nearly corresponds to Fig 3.[1] The interior curves are isovels and the corresponding undisturbed W_{max} circular arc is shown dashed for comparison.

2 30 deg Sector. Figure 7 shows the axial flow in the annulus-sector configuration α = 0.619, β = 15 deg, γ = 1.1735. The disturbance due to the wider sector is quite marked, and the peak velocity is greater than five times the undisturbed W_{max}.

Discussion

A Planar Shear-Cavity Flows

The present numerical results have established:

1 The stagnation points of the dividing streamline fall inside the cavity.

2 The total dividing streamline is not confined to the cavity, but may be located partially in the shear flow region.

3 Neither the velocity nor vorticity are constant along the dividing streamline but both go to zero at the cavity walls.

[1] The program was restricted in the number of meshes in the η direction. This limitation could be removed, but it was not felt necessary to rewrite the program since the results were intended for qualitative illustration rather than fidelity to an arbitrary domain.

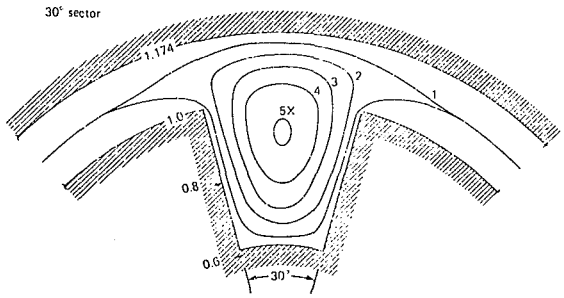

Fig. 7 Isovels for rectilinear flow in the noncircular annulus with a 30 deg sector (α = 0.619, β = 15 deg, γ = 1.1735). The numbers on the isovels represent multiples of undisturbed W_{max}

The variation of location of the dividing streamline with geometry qualitatively agrees with that shown earlier for the rectangular cavity flows [3], including the dividing streamline partially within the shear flow for wide cavities. (See previous Fig. 7.) Those coarse finite-difference simulations were direct solutions of the biharmonic streamfunction equation and the vorticity values were not calculated. The present (ψ, Ω) computations are finer mesh and quite accurate because the wall vorticity approximation is $0(h^2)$. The order of accuracy has been established by comparison to an exact analytic solution where only eight radial points in the upper cavity vortex gave velocity errors about two per cent [17]. The present wide sector cavity has 16 radial points in the same vortex so the velocity resolution should be four times better. The universal criteria for wall stagnation regions are satisfied [18]. The flow features revealed in the disturbed shear flow and the circulation within the cavity are capable of verification by accurate measurement, say by laser doppler velocimetry.

B Axial Flows

The interaction of the slot (sector) flow and the rectilinear annulus flow is most apparent near the symmetry centerplane. The numerical results have established:

1 The axial flow vectors are enhanced in the annulus by the presence of the slot, and increase as the size of the sector increases.

2 The peak velocity of the annulus-sector geometry may lie in the annulus or it may be in the cavity.

C Three-Dimensional Flows

An undisturbed Couette shear flow plus annular Poiseuille flow combination has steady helical pathlines on circular cylinders. Everywhere $U = 0$ while $V(r)$ and $W(r)$. The pitch of a particular streamline relative to the axis direction depends on the radius of the circular cylinder upon which it travels and the ratio W_{max}/V_2. The flow pattern is independent of Reynolds number formed either with longitudinal W_{max} or outer cylinder velocity V_2.

Now consider a combination of the Poiseuille flow through the annulus with cavity (with distorted noncircular W isovels) and the Stokes circular shear flow and cavity interaction. The in-plane shearing motion has $U(r, \theta)$ and $V(r, \theta)$ in and near the cavity. Steady pathlines 180 deg from the cavity centerplane will be essentially the same as the annular composite flow of the paragraph above, but near the cavity the deviations can be considerable. All three velocity components U, V, and W contribute to the 3-D motion, in a fashion too difficult to describe adequately in a brief paper. However, the individual contributions of the Stokes in-plane vectors and the longitudinal vectors can be combined to give the full three component vector velocity **V** of each fluid particle at every (R, θ) location. The superposition is strictly valid for Stokes flow

for we have neglected the nonlinear inertial term $\mathrm{Re}(\mathbf{V}\cdot\nabla\mathbf{V})$ in the analysis. That term in the Navier-Stokes momentum equation requires a much more involved simulation in primitive variables, velocity and pressure, instead of the linear equations we have used. (One could iterate from the present Stokes solutions.) The solution must depend on Reynolds number $\mathrm{Re} = (V_2 R_0/\nu)$ and the ratio $W_{\max}/V_2$ as well as geometry.

The effect of the 3-D shearing on the mixing of Newtonian fluids should be considerable. The steady helical motion in the simple annulus creates differential transport. The complex motion in the cavity region for the sector-annulus geometry will act as a periodic churning for the traveling fluid parcels. The laminar mixing should also be effective for non-Newtonian polymers [19], where turbulent mixing requires prohibitive power input. In a practical device more than one sector would improve efficiency, of course. But it is clear from the analyses that a large number of narrow sector cavities will not provide the same mixer as a small number of wide sector cavities for equal V_2 and $W_{\max}$.

Conclusion

Unsophisticated numerical simulations of circular shear flow-cavity interactions have been demonstrated for Stokes flows. More validly than previous independent 2-D cavity sector models [1, 17] they reveal the similarities and differences of various real viscous flows as they relate to the boundary geometry. In conjunction with rectilinear flow in the corresponding geometry we can predict features of 3-D flow which will be important in heat and mass transfer. The annulus-sector geometry (not previously studied in detail) lends itself to experimental investigation better than Cartesian simulations.

Acknowledgment

The computer programs to solve the linear flow equations by finite-difference approximation were written by Dr. L. W. Ehrlich, whose cheerful cooperation is gratefully acknowledged. The work was supported by the U. S. Navy under Contract N00024-81-C-5301.

References

1 Ghia, U., and Goyal, R. K., "Laminar Incompressible Recirculating Flow in a Driven Cavity of Polar Cross Section," ASME JOURNAL OF FLUIDS ENGINEERING, Vol. 99, 1977, pp. 774–777.

2 O'Brien, V., "Steady and Non-Steady Flow in Non-Circular Ducts," ASME *Journal of Applied Mechanics*, Vol. 99, 1977, pp. 1–6.

3 O'Brien, V., "Closed Streamlines Associated with Channel Flow Over a Cavity," Phys. Fl., Vol. 15, 1972, pp. 2089–2097.

4 Mir-Mohamad-Sadegh, A., and Rajagopal, K. R., "The Flow of a Non-Newtonian Fluid Past Projections and Depressions," ASME *Journal of Applied Mechanics*, Vol. 47, 1980, pp. 485–488.

5 Trogdon, S. A., and Joseph, D. D., "Matched Eigenfunction Expansions for Slow Flow Over a Slot," to appear in the *Journal of Fluid Mechanics*.

6 Tanner, R. I., "Plane Creeping Flows of Incompressible Second-Order Fluids," *Phys. Fl.*, Vol. 9, 1966, pp. 1246–1247.

7 Pritchard, W. G., "Measurements of the Viscometric Functions for a Fluid in Steady Shear Flows," *Phil. Trans. Roy. Soc.*, Vol. A270, 1971, pp. 507–555.

8 Rajagopal, K. R., and Mir-Mohamad-Sadegh, A., "A Boundary Integral Approach for Determining the Pressure Error," *Rheol. Acta*, Vol. 19, 1980, pp. 12–18.

9 O'Brien, V., "Bounds and Estimates of Second Normal Stress Difference in Rectilinear Flow," Numerical Simulation Workshop, 1981, to appear in *J. Rheol.*

10 Taylor, G. I., in *Aeronautics and Astronautics; Proceedings Durand Centennial Conference*, Stanford University, 1959, eds. N. J. Hoff and W. G. Vincente, Pergamon, New York, 1960, p. 12.

11 Weinsbaum, S., "On the Singular Points in the Laminar Two-Dimensional Near Wake Flow," *Journal of Fluid Mechanics*, Vol. 33, 1968, pp. 39–53.

12 Pan, F., and Acrivos, A., "Steady Flows in Rectangular Cavities," *J. Fl. Mech.*, Vol. 28, 1967, pp. 643–655.

13 Rotem, Z., Ratkowsky, D. A., and Neilson, J. E., "Viscous Flow in Angle Sectors," *Phys. Fl.*, Vol. 13, 1970, pp. 2650–2656.

14 Joseph, D. D., personal communication.

15 Henrici, P., *Applied and Computational Complex Analysis*, Vol. 1, Wiley, New York, 1974, pp. 422–432.

16 Ehrlich, L. W., "Solving the Biharmonic Equations as Coupled Finite-Difference Equations," *SIAM J. Num. Anal.*, Vol. 8, 1971, pp. 278–287.

17 Sanders, J., O'Brien, V., and Joseph, D. D., "Stokes Flow in a Driven Sector by two Different Methods," ASME *Journal of Applied Mechanics*, Vol. 102, 1980, pp. 482–484.

18 O'Brien, V., "Analytic Description of Steady Separation From Curved Surfaces," *Phys. Fl.*, Vol. 20, 1977, pp. 1045–1049.

19 Schrenk, W. J., Chisholm, D. S., and Alfrey, T., Jr., "Mixing of Viscous Fluids Flowing Through a Rotating Tube," *Mod. Plast.*, Jan. 1969, p. 152.

20 Batchelor, G. K., *An Introduction to Fluid Dynamics*, Cambridge Univ. Press, 1967, Chapter 5.

21 Michael, D. H., and O'Neill, M. E., "The Separation of Stokes Flows," *J. Fl. Mech.*, Vol. 80, 1977, pp. 785–794.

22 Dorrepaal, J. M., "Stokes Flow Past a Two-Dimensional Lens," *J. Appl. Math. Phys.* (ZAMP), Vol. 30, 1979, pp. 405–415.

23 Dorrepaal, J. M., "Stokes Flow Past a Smooth Cylinder," *J. Engr'g. Math.*, Vol. 12, 1978, pp. 177–185.

24 Roache, P. J., *Computational Fluid Dynamics*, Hermosa, Albuquerque, 1972; Chapter 3.

APPENDIX

Shear flow separation at convex corners and edges is a topic of concern to experimenters and theoreticians. In Batchelor's textbook [20] are the statements, ". . . the boundary layer always separates at the salient edge . . . ," and "It leaves the edge tangentially to the upstream face." The section is part of a chapter on flow at large Reynolds number and the "fixed" two-dimensional separation at an edge is the view of aerodynamicists in general. However, formal global theoretical analyses of Stokes flow shows separation is not necessarily fixed at a sharp edge [21, 22]. Likewise global Stokes analyses for uniform flow over smooth bodies with concavities indicate the stagnation points are located within the concavity [23], just as the present numerical results indicate stagnation points within the cavity.

A sharp corner (and the resulting discontinuity of slope) has presented a dilemma to numerical analysts who have handled it in various ways [24]. We had previously explored the different corner techniques with the final conclusion that the physical corner can never be mathematically sharp and that it always possesses a smoothly varying normal (in the continuum sense, not on a molecular scale). So locally the "corner point" is another fluid point, or if the mesh is sufficiently small to see the rounding of the corner (Fig. 2(*b*)), the wall approximation is achieved by "short-leg" calculations. Either way, on a smooth convex corner the separation line and null vorticity curve locally satisfy smooth wall criteria [18] and there is no singularity. This compares to the assumption that the corner is mathematically sharp and the vorticity (and pressure) goes to infinity as $r \to 0$ [11]. If there is separation in the vicinity, Weinbaum wrongly implies a constant angle of dividing streamline departure [11], neither tangent to the oncoming shear flow nor the angles shown by the present calculations.

Development of Secondary Flow and Vorticity in Curved Ducts, Cascades, and Rotors, Including Effects of Viscosity and Rotation

M. Pouagare
Graduate Assistant.

B. Lakshminarayana
Director of Computational Fluid Dynamics Studies and Professor of Aerospace Engineering.

Department of Aerospace Engineering, The Pennsylvania State University, University Park, Pa. 16802

This paper is concerned with the numerical solution of the secondary vorticity equations in curved ducts, cascades, and rotors. The classical approach of splitting the flow into primary and secondary flow fields is employed and extended to include effects of viscosity, rotation, and density stratification. All elliptical effects are neglected and the Crank-Nicolson method is used to solve the secondary vorticity equation. The secondary flow field is obtained by solving a Poisson equation using a successive over-relaxation method. The results are compared with theoretical and experimental data from stationary ducts, compressor and turbine cascades. The agreement is good for most of the cases.

Introduction

Secondary flow is produced when a streamwise component of vorticity is developed from the deflection of an initially sheared flow. Such secondary flows occur when a developed pipe flow enters a bend or cascade or a rotor, or when a boundary layer meets an obstacle normal to the surface over which it is flowing. One of the most important engineering aspects of secondary flow occurs in turbomachinery aerodynamics, where boundary layers growing on the casing and hub walls of the machine are deflected by rows of blades, stationary and rotating. At a sufficient distance from the walls, viscous effects are negligible and the normal pressure gradient is balanced by the centrifugal force due to the streamline curvature. However, the fluid within the boundary layers does not have sufficient momentum to balance the pressure gradients imposed by the inviscid outer flow. The result is a cross-flow component containing vorticity aligned in the streamwise direction. This results in flow losses, vorticity development, and flow deviation in the tangential and radial directions. The efficiency of the rotor is also affected by this secondary flow.

The primary assumption leading to the existing theoretical descriptions of secondary flows is that viscous effects produce a boundary layer on the wall upstream of the blade row, whereas within the blade row the imposed pressure gradients play the major role and viscosity has little effect on the resulting secondary flows. This assumption is characteristic of what is generally termed inviscid secondary flow analysis or "classical secondary flow theory" [1, 2, 3]. All these earlier analyses, reviewed in reference [3], are based on assumptions that the flow perturbations occur mainly in the cross section of the bend or cascade and that the perturbations due to secondary flow in the streamwise direction are small. This linearization approach uncouples the primary and secondary flow fields.

In general, these linearized theories provide accurate prediction of the spanwise exit-flow angle for the small turning angle in the inviscid regions. When features of the real flow are modelled, i.e., Bernoulli surface displacement, rotation, and viscous effects, the overturning near the end wall is reduced [4].

An exact approach would be to solve, numerically, the entire viscid or inviscid equations which do not uncouple the primary and secondary flow fields. Such attempts are presently being pursued by several groups [5–9]. However, these methods are quite complicated and time-consuming. The advantage of the classical approach lies in its simplicity. The objective of this paper is to extend the classical approach

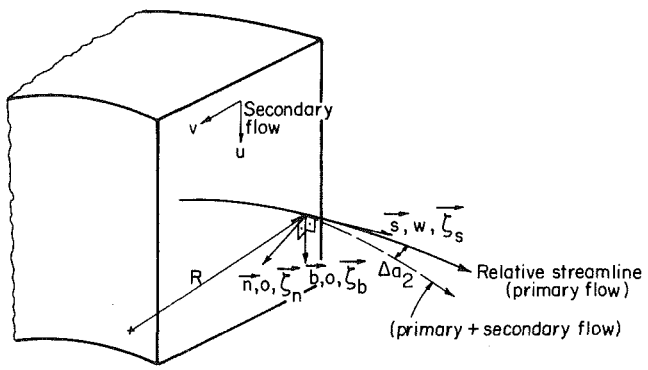

Fig. 1 Notations used and the coordinate system

Contributed by the Fluids Engineering Division and presented at the AIAA/ASME Joint Fluids, Plasma, Thermophysics and Heat Transfer Conference, St. Louis, Mo., June 7-11, 1982, of THE AMERICAN SOCIETY OF MECHANICAL ENGINEERS. Manuscript received by the Fluids Engineering Division, October 28, 1981.

by introducing the effects of viscosity, rotation, and inlet density gradients on the development of the secondary vorticity in curved duct and turbomachine blade passages. The agreement between the predictions from this analysis and several experimental data is shown to be good.

Analysis

The most generalized form of the equations for the secondary and normal vorticity in a rotating intrinsic coordinate system was developed by Lakshminarayana and Horlock in reference [10]. The coordinate system used is shown in Fig. 1. s is the relative streamline direction, n is the principle normal to the streamline direction, and b is the binormal direction. s, n, b form an orthogonal coordinate system.

The relative secondary vorticity ζ_s and the relative normal vorticity ζ_n along the relative streamline are given, respectively, by the following equations [10]

$$\frac{\partial}{\partial s}\left(\frac{\zeta_s}{\rho w}\right)=\frac{2\zeta_n}{\rho w R}+\frac{2\Omega_s}{\rho^2 w}\frac{\partial \rho}{\partial s}-\frac{1}{\rho^3 w^2}\left[\frac{\partial \rho}{\partial b}\frac{\partial P}{\partial n}-\frac{\partial \rho}{\partial n}\frac{\partial P}{\partial b}\right]+\frac{2\boldsymbol{\Omega}\cdot\nabla w}{\rho w^2}+\frac{\mu}{\rho^2 w^2}\mathbf{s}\cdot\nabla\,{}^2\boldsymbol{\zeta}-\frac{1}{\rho w^2}\mathbf{s}\cdot\nabla\left(\frac{\mu}{\rho}\right)\times\nabla\times\boldsymbol{\zeta}+\frac{4}{3}\frac{1}{\rho w^2}\mathbf{s}\cdot\nabla\left(\frac{\mu}{\rho}\right)\times\nabla(\nabla\cdot\mathbf{w}) \tag{1}$$

$$\frac{\partial}{\partial s}(\zeta_n w)=\frac{w}{\tau}\zeta_b-\frac{w}{a_b}\frac{\partial a_b}{\partial s}(\zeta_n+2\Omega_n)+\frac{2\Omega_s w}{R}-2\Omega_n\frac{\partial w}{\partial s}+\frac{1}{\rho^2}\left[\frac{\partial P}{\partial s}\frac{\partial \rho}{\partial b}-\frac{\partial P}{\partial b}\frac{\partial \rho}{\partial s}\right]+\mathbf{n}\cdot\frac{\mu}{\rho}\nabla\,{}^2\boldsymbol{\zeta}-\mathbf{n}\cdot\nabla\left(\frac{\mu}{\rho}\right)\times\nabla\times\boldsymbol{\zeta}+\frac{4}{3}\mathbf{n}\cdot\left(\nabla\left(\frac{\mu}{\rho}\right)\times\nabla(\nabla\cdot\mathbf{w})\right) \tag{2}$$

For an incompressible stratified fluid in b direction, the above equations simplify to

$$\frac{\partial}{\partial s}\left(\frac{\zeta_s}{w}\right)=\frac{2\zeta_n}{wR}-\frac{1}{\rho^2 w^2}\frac{\partial \rho}{\partial b}\frac{\partial P}{\partial n}+\frac{2\boldsymbol{\Omega}\cdot\nabla w}{w^2}+\frac{\mu}{\rho w^2}\mathbf{s}\cdot\nabla\,{}^2\boldsymbol{\zeta} \tag{3}$$

$$\frac{\partial}{\partial s}(\zeta_n w)=\frac{w}{\tau}\zeta_b-\frac{w}{a_b}\frac{\partial a_b}{\partial s}(\zeta_n+2\Omega_n)+\frac{2\Omega_s w}{R}-2\Omega_n\frac{\partial w}{\partial s}+\frac{1}{\rho^2}\frac{\partial P}{\partial s}\frac{\partial e}{\partial b}+\mathbf{n}\cdot\frac{\mu}{\rho}\nabla\,{}^2\boldsymbol{\zeta} \tag{4}$$

These equations will be solved in the region close to the wall where the inlet vorticity is present, i.e., in the boundary layer region.

Employing the usual boundary layer approximations, it is assumed that the pressure is imposed by the inviscid flow field and that the viscous effects are important only in the direction normal to the wall, i.e., in the b direction. So we can set

$$\frac{\partial P}{\partial n}=\frac{\partial P_0}{\partial n}=-\rho\frac{W_0^2}{R}$$

$$\mathbf{s}\cdot\frac{\mu}{\rho w^2}\nabla\,{}^2\boldsymbol{\zeta}=\frac{\mu}{\rho w^2}\frac{\partial^2 \zeta_s}{\partial b^2}$$

$$\mathbf{n}\cdot\frac{\mu}{\rho}\nabla\,{}^2\boldsymbol{\zeta}=\frac{\mu}{\rho}\frac{\partial^2 \zeta_n}{\partial b^2}$$

Furthermore, we can write

$$\frac{2\boldsymbol{\Omega}\cdot\nabla w}{w^2}=\frac{2}{w^2}\left(\Omega_s\frac{\partial w}{\partial s}+\Omega_n\frac{\partial w}{\partial n}+\Omega_b\frac{\partial w}{\partial b}\right)$$

In most practical situations, ζ_b is zero. Hence, $\partial w/\partial n = w/R$. Also, $\zeta_n = \partial w/\partial b$. Hence,

$$\frac{2\boldsymbol{\Omega}\cdot\nabla w}{w^2}=\frac{2}{w^2}\left(\Omega_s\frac{\partial w}{\partial s}+\Omega_n\frac{w}{R}+\Omega_b\zeta_n\right)$$

Assuming $\partial a_b/\partial s = 0$, and noting that the first term on the right side of equation (4) is very small (since $\zeta_b \approx 0$ and τ is usually very large with these assumptions), equations (3) and (4) reduce to,

Nomenclature

a_b = relative streamline spacing in the b direction
b_0 = height of the blades/height of the duct
P = static pressure
R = radius of curvature of relative streamline
$R_e = \dfrac{W_1 \cdot \delta_1 \cdot \rho_1}{\mu}$ = Reynolds number
S = width of the duct (or spacing in cascade)
s,n,b = intrinsic coordinate system (Fig. 1)
u,v = secondary velocities in b, n directions, respectively (Fig. 1)
w = relative velocity inside the shear layer
W_0 = free stream relative velocity
W_1 = free stream relative velocity at inlet
β = relative air angle measured from the axial direction
δ = boundary layer thickness
δ^* = boundary layer displacement thickness
ζ = relative vorticity/absolute vorticity for $\Omega = 0$
λ = stagger angle
μ = molecular viscosity
μ_e', μ_e'', μ_e = eddy viscosity (equations (10) and (11))
ν = kinematic viscosity
ρ = density
ρ_1 = reference density
τ = radius of torsion of the streamline
τ_0 = wall shear stress
ψ = secondary stream function
Ω = angular velocity
$\Delta s, \Delta n, \bar{\Delta} b$ = stepsize in s,n,b direction
$\Delta\alpha_2$ = change in outlet angle due to secondary vorticity

Subscripts

s,n,b = components in intrinsic coordinate system
0 = reference/inviscid/free stream values
1 = inlet of the blade row
2 = outlet of the blade row

Superscripts

—— = nondimensional quantities/passage averaged quantities/time averaged quantities
bold face = vector

$$\frac{\partial}{\partial s}\left(\frac{\zeta_s}{w}\right)=\frac{2\zeta_n}{wR}+\frac{W_0^2}{\rho w^2 R}\frac{\partial \rho}{\partial b}+\frac{2}{w^2}\left(\Omega_s\frac{\partial w}{\partial s}+\Omega_n\frac{w}{R}+\Omega_b\zeta_n\right)+\frac{\mu}{\rho w^2}\frac{\partial^2\zeta_s}{\partial b^2} \quad (5)$$

$$\frac{\partial}{\partial s}(\zeta_n w)=\frac{2\Omega_s w}{R}-2\Omega_n\frac{\partial w}{\partial s}+\frac{1}{\rho^2}\frac{\partial P_0}{\partial s}\frac{\partial \rho}{\partial b}+\frac{\mu}{\rho}\frac{\partial^2\zeta_n}{\partial b^2} \quad (6)$$

Equations (5) and (6) are valid for laminar flow. In case of turbulent flow the last term in equations (5) and (6) become, respectively,

$$\frac{1}{\rho w^2}\frac{\partial^2}{\partial b^2}\left[(\mu+\mu_e)\zeta_s\right] \quad , \quad \frac{1}{\rho}\frac{\partial^2}{\partial b^2}\left[(\mu+\mu_e)\zeta_n\right]$$

The derivation of these terms are given in Appendix 1.

One of the major assumptions of the present method is that the streamwise $w(s,b)$ velocity profile is assumed known. Since no boundary layer growth is allowed, it is reasonable to neglect the viscous term in the normal vorticity equation.

Equations (5) and (6) are nondimensionalized using the free stream velocity (W_1) at the inlet as the characteristic velocity, the inlet boundary layer thickness δ_1 as the characteristic length, and some reference density ρ_1. The boundary layer growth through the duct or blade row is neglected.

$$\bar{\zeta}=\zeta\frac{\delta_1}{W_1},\ \bar{\Omega}=\Omega\frac{\delta_1}{W_1},\ \bar{w}=\frac{w}{W_1},\ \bar{W}_0=\frac{W_0}{W_1},\ \bar{P}=\frac{P}{\rho_1 W_1^2},$$

$$\bar{\rho}=\frac{\rho}{\rho_1},\ \bar{s}=\frac{s}{\delta_1},\ \bar{b}=\frac{b}{\delta_1},\ \bar{n}=\frac{n}{\delta_1},\ \bar{R}=\frac{R}{\delta_1},$$

$$\bar{\psi}=\frac{\psi}{W_1\delta_1},\ \bar{\mu}=\frac{\mu_e+\mu}{\mu}$$

The resulting equations are given by

$$\frac{\partial}{\partial\bar{s}}\left(\frac{\bar{\zeta}_s}{\bar{w}}\right)=\frac{2\bar{\zeta}_n}{\bar{w}\bar{R}}+\frac{2}{\bar{w}^2}\left(\bar{\Omega}_s\frac{\partial\bar{w}}{\partial\bar{s}}+\bar{\Omega}_n\frac{\bar{w}}{\bar{R}}+\bar{\Omega}_b\bar{\zeta}_n\right)$$
(1) (2)
$$+\frac{1}{\bar{\rho}\bar{w}^2}(\bar{W}_0)^2\frac{1}{\bar{R}}\frac{\partial\bar{\rho}}{\partial\bar{b}}+\frac{1}{\mathrm{Re}}\frac{1}{\bar{\rho}\bar{w}^2}\frac{\partial^2}{\partial\bar{b}^2}[\bar{\mu}\,\bar{\zeta}_s] \quad (7)$$
(3) (4)

$$\frac{\partial}{\partial\bar{s}}(\bar{\zeta}_n\bar{w})=\frac{2\bar{\Omega}_s\bar{w}}{\bar{R}}-2\bar{\Omega}_n\frac{\partial\bar{w}}{\partial\bar{s}}+\frac{1}{\bar{\rho}^2}\frac{\partial\bar{P}_0}{\partial\bar{s}}\frac{\partial\bar{\rho}}{\partial\bar{b}} \quad (8)$$
(1) (2) (3)

where

$$\mathrm{Re}=\frac{W_1\cdot\delta_1\cdot\rho_1}{\mu}$$

Equations (7) and (8) can be solved for the values of $\bar{\zeta}_n$ and $\bar{\zeta}_s$ at any given location. Since these equations are decoupled, the value of $\bar{\zeta}_n$ can be derived from the solution of equation (8), which can then be substituted in equation (7) to derive the value of $\bar{\zeta}_s$. Solution of the inviscid terms of these equations is available for many simpler cases [1-4, 10], but the numerical or analytical solution of the streamwise and normal vorticity equations with the viscous terms has never been attempted before.

Knowing the value of $\bar{\zeta}_s$ along the mean streamline, the secondary velocities $\bar{u}$, $\bar{v}$ in the transverse plane can be derived from the numerical solution of the Poisson's equation for the secondary stream function

$$\nabla^2\bar{\psi}=-\bar{\zeta}_s(\bar{b},\bar{n}) \quad (9)$$

where $\bar{u}$ and $\bar{v}$ are perturbation velocities (from initially zero values in the primary flow) in b and n directions. Expressions for these are given respectively, by

$$\bar{u}=\frac{u}{W_1}=-\frac{\partial\bar{\psi}}{\partial\bar{n}} \quad , \quad \bar{v}=\frac{v}{W_1}=\frac{\partial\bar{\psi}}{\partial\bar{b}}$$

where $\bar{b}$ and $\bar{n}$ are rectilinear coordinates.

The change in the outlet angle (or deviation angle from the primary flow) can be obtained from the equation

$$\Delta\alpha_2=\tan^{-1}\frac{\bar{v}}{\bar{w}}$$

It should be emphasized that the calculation procedure outlined here assumes that the primary flow is known [$w(b,n,s)$]. Utilizing this value and equations (7), (8), and (9), the secondary vorticity ($\bar{\zeta}_s$), normal vorticity ($\bar{\zeta}_n$), and secondary velocities ($\bar{u}$, $\bar{v}$) are calculated. In the numerical scheme presented in the next section, it is assumed that the secondary vorticity is constant in the $\bar{n}$ direction (which is true in most practical situations), hence $\bar{\zeta}=\bar{\zeta}(b)$, and the equations are solved in the ($\bar{s}$ $\bar{b}$) plane along the mean streamline using a marching technique. The mean streamline is the streamline at the mid-passage and is the mean (vectorial) between the streamlines near the pressure and suction surfaces.

Turbulence Closure. To study the effect of turbulence in the development of secondary flow, eddy viscosity is used in equation (7). The eddy viscosity is modelled as follows [11]:

for $0 \le b \le b_k$

$$\mu_e'=\rho\left\{kb\left[1-\exp\left(-\frac{b\sqrt{\tau_0/\rho}}{\nu A}\right)\right]\right\}^2\frac{\partial w}{\partial b} \quad (10)$$

for $b_k \le b \le \delta$

$$\mu_e''=\rho k_2 W_0\delta^*/[1+5.5(b/\delta)^6] \quad (11)$$

where A, k, and k_2 are constants, given by values $k = 0.4$, $A = 26$, and $k_2 = 0.017$.

The value of b_k which delineates the range of validity of equation (10) from equation (11) is obtained from the requirement that the eddy viscosities must assume equal values there. Hence,

$$\mu_e'=\mu_e'' \quad \text{for} \quad b=b_k$$

Numerical Solution and Boundary Conditions

Equations (7) and (8) are solved along the mean streamline of the duct or the blade passage in the boundary layer region. The solution is marched in the downstream direction using Crank-Nicolson method. This procedure neglects any elliptical effects. This assumption is good provided there is no flow separation. The streamwise velocity profile (primary flow) is assumed to be known.

The s coordinate is the time-like variable. The equations are approximated at the location ($i + 1/2, j$), where the index i is the mesh point in the streamwise direction and j is the mesh point in the b direction. Since equation (8) is uncoupled from equation (7), the value of $(\bar{\zeta}_n)_{i+1,j}$ can be evaluated from the known value. The rest of the quantities in equation (8) are known either from the primary flow solution, geometry, or the fluid properties. The finite difference form of equations (7) and (8) are, respectively,

$$-A_1(\bar{\zeta}_s)_{i+1,j-1}+(B_1+2A_2)(\bar{\zeta}_s)_{i+1,j}-A_3(\bar{\zeta}_s)_{i+1,j+1}$$
$$=A_4(\bar{\zeta}_s)_{i,j-1}+(B_2-2A_5)(\bar{\zeta}_s)_{i,j}+A_6(\bar{\zeta}_s)_{i,j+1}+C_1 \quad (12a)$$

$$B_3(\bar{\zeta}_n)_{i+1,j}=B_4(\bar{\zeta}_n)_{i,j}+C_2 \quad (12b)$$

Constants $A_1 - A_6$, B_1, B_2 and C in the difference equation (12a) are given by

$$A_1=\left[\frac{1}{\mathrm{Re}\,\bar{\rho}\bar{w}^2}\right]_{i+1/2,j}\frac{\bar{\mu}_{i+1,j-1}}{2(\Delta\bar{b})^2}$$

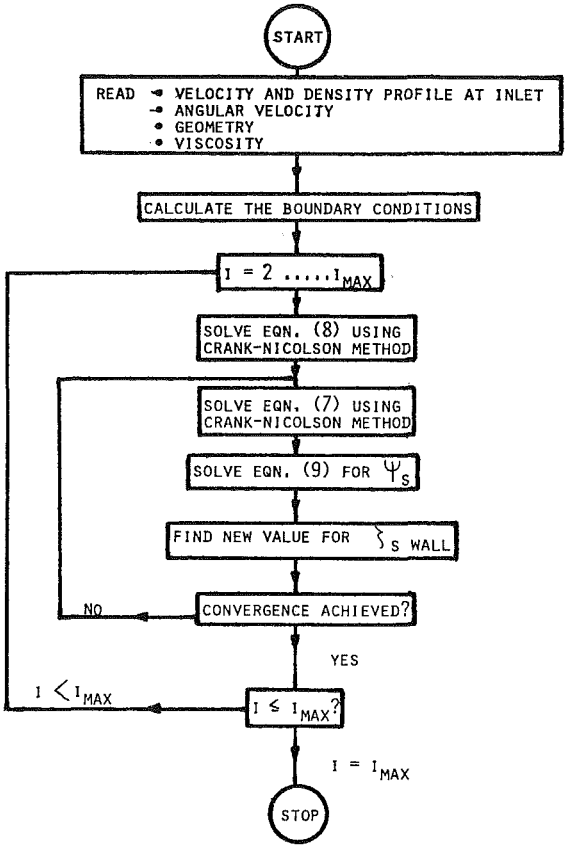

Fig. 2 Flow chart of the computer program

$$A_2 = \left[\frac{1}{\mathrm{Re}\ \bar{\rho}\bar{w}^2}\right]_{i+1/2,j} \frac{\bar{\mu}_{i+1,j}}{2(\Delta\bar{b})^2}$$

$$A_3 = \left[\frac{1}{\mathrm{Re}\ \bar{\rho}\bar{w}^2}\right]_{i+1/2,j} \frac{\bar{\mu}_{i+1,j-1}}{2(\Delta\bar{b})^2}$$

$$A_4 = \left[\frac{1}{\mathrm{Re}\ \bar{\rho}\bar{w}^2}\right]_{i+1/2,j} \frac{\bar{\mu}_{i,j-1}}{2(\Delta\bar{b})^2}$$

$$A_5 = \left[\frac{1}{\mathrm{Re}\ \bar{\rho}\bar{w}^2}\right]_{i+1/2,j} \frac{\bar{\mu}_{i,j}}{2(\Delta\bar{b})^2}$$

$$A_6 = \left[\frac{1}{\mathrm{Re}\ \bar{\rho}\bar{w}^2}\right]_{i+1/2,j} \frac{\bar{\mu}_{i,j+1}}{2(\Delta\bar{b})^2}$$

$$B_1 = \frac{1}{\Delta\bar{s}\ \bar{w}_{i+1,j}}, \quad B_2 = \frac{1}{\Delta\bar{s}\ \bar{w}_{i,j}}$$

$$C = \left[\frac{2\bar{\zeta}_n}{\bar{w}\bar{R}} + \frac{(\bar{W}_0)^2}{\bar{\rho}\bar{w}^2\bar{R}}\frac{\partial\bar{\rho}}{\partial\bar{b}} + \frac{2}{\bar{w}^2}\left(\bar{\Omega}_s\frac{\partial\bar{w}}{\partial\bar{s}} + \bar{\Omega}_n\frac{\bar{w}}{\bar{R}} + \bar{\Omega}_b\bar{\zeta}_n\right)\right]_{i+1/2,j}$$

Constants B_3, B_4, and C_2 for the difference equation (12*b*) are given by

$$B_3 = \frac{\bar{w}_{i+1,j}}{\Delta\bar{s}}, \quad B_4 = \frac{\bar{w}_{i,j}}{\Delta\bar{s}},$$

$$C_2 = \left[\frac{2\bar{\Omega}_s\bar{w}}{\bar{R}} - 2\bar{\Omega}_n\frac{\partial\bar{w}}{\partial\bar{s}} + \frac{1}{\bar{\rho}^2}\frac{\partial\bar{P}_0}{\partial\bar{s}}\frac{\partial\bar{\rho}}{\partial\bar{b}}\right]_{i+1/2,j}$$

Knowing the value of $(\bar{\zeta}_n)_{i+1,j}$, the value of $\bar{\zeta}_s$ at the new $\bar{s}$ station can be found from equation (7). The method is stable for all values of the ratio $\Delta\bar{s}/(\Delta\bar{b})^2$, where $\Delta\bar{s}$ and $\Delta\bar{b}$ are the step sizes in s and b directions, respectively. The method converges with discretization error $0[(\Delta\bar{s})^2 + (\Delta\bar{b}^2)]$.

Knowing $\bar{\zeta}_s$, equation (9) can be solved to derive the values of $\bar{u}$ and $\bar{v}$. Equation (9) is solved by the successive over-relaxation method. The boundary condition is $\bar{\psi} = 0$ along all the wall surfaces. The numerical method uses the following iteration scheme:

$$(\bar{\psi})_{i,j}^{(n+1)} = (\bar{\psi})_{i,j}^{(n)} + \frac{\omega}{4}\left[(\bar{\psi})_{i-1,j}^{(n+1)} + (\bar{\psi})_{i+1,j}^{(n)} + (\bar{\psi})_{i,j-1}^{(n+1)} + (\bar{\psi})_{i,j+1}^{(n)} - 4(\bar{\psi})_{i,j}^{(n)} - h^2(\bar{\zeta}_s)_{i,j}\right] \tag{13}$$

where h is the stepsize $h = \Delta\bar{n} = \Delta\bar{b}$ and ω is a relaxation parameter given by

$$\omega = \frac{8 - 4\sqrt{4-\alpha^2}}{\alpha^2}$$

with $\alpha = \cos(\pi/M) + \cos(\pi/N)$ where M and N are, respectively, the total number of increments into which the horizontal, i.e., n, and vertical, i.e., b, sides of the rectangular region are divided. More details of the solution for equation (13) can be found in reference [12].

Initial and Boundary Conditions. The initial conditions at the inlet of the passage are prescribed $[\bar{w}(\bar{b}), \bar{\zeta}_{n0}, \bar{\zeta}_{s0}, \bar{\rho}(\bar{b})]$, and the angular velocity is known.

The boundary conditions for equations (7) and (8) are as follows. In the inviscid or vortex free region, $\bar{\zeta}_s = \bar{\zeta}_n = 0$. The boundary conditions on the wall surface for $\bar{\zeta}_s$ are derived iteratively from the solution. Initially on the wall, $\bar{\zeta}_n = (\bar{\zeta}_n)_{\text{inlet}} = \text{constant}$ and $\bar{\zeta}_s = (\bar{\zeta}_s)_{\text{inlet}} + 2\bar{s}/\bar{R}\ (\bar{\zeta}_n)_{\text{wall}}$. Thus, the inviscid expression for the secondary vorticity derived by Squire and Winter [2] is prescribed initially. The values of $\bar{\zeta}_s$ on the wall surface are continuously updated during the computation. Utilizing these initial boundary conditions, equations (7) and (8) are solved in finite difference form (e.g., equation 12). Knowing $\bar{\zeta}_s$ everywhere, equation (9) for $\bar{\psi}$ is solved numerically. Utilizing this zeroth approximation, the boundary condition on the wall surface $[(\bar{\zeta}_s)_{\text{wall}}]$ can be updated using the equation

$$(\bar{\zeta}_s)_{\text{wall}} = (-7\bar{\psi}_{\text{wall}} + 8\bar{\psi}_{\text{wall}+1} - \bar{\psi}_{\text{wall}+2})/2(\Delta\bar{b})^2$$

where $\bar{\psi}_{\text{wall}+1}$, $\bar{\psi}_{\text{wall}+2}$ represents values at the grid points away from the wall. The first term on the right-hand side is zero. This form is of second-order accuracy [13]. With this new information, values of $\bar{\zeta}_s$, $\bar{\psi}$, $\bar{v}$, $\bar{u}$ can be determined. This procedure is repeated until the convergence is achieved. The calculation then proceeds to the next $\bar{s}$ station. The secondary vorticity and secondary flow field throughout the passage is thus determined. The computational flow chart is shown in Fig. 2.

In the present analysis, the boundary condition on the wall for the secondary vorticity is unknown and should come out of the solution. Since the secondary vorticity peaks near the wall, the accuracy of the solution depends on the accuracy of ζ_s calculation near the wall. The presence of large gradients in eddy viscosity makes the problem very sensitive to the calculations near the wall. To overcome these difficulties a large number of grid points were chosen near the wall.

Prediction and Comparison With Experimental Data

To check the analysis, assumptions, and numerical technique, the results of the computer program are compared with the following experimental and analytical results.

(*a*) Hawthorne's [14] analytical results.

(*b*) Experimental data from curved duct [2,15].

(*c*) The compressor and turbine cascade data [16,17,18].

(*d*) Model rotors are used to study the effects of rotation and the inlet density stratification.

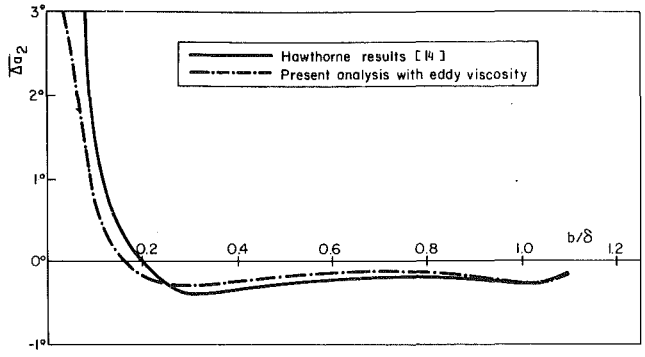

Fig. 3 Comparison between Hawthorne's [14] theoretical results and the predicted change in average outlet angle for $\delta/S = 2$

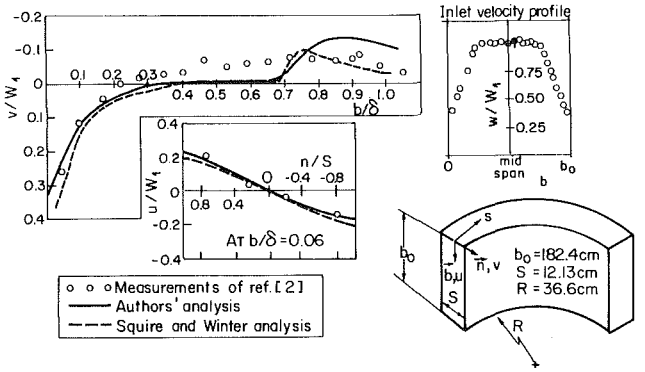

Fig. 4 Comparison between experimental and predicted *v*, *u* for Squire and Winter duct [2]

Comparison With Hawthorne's Analytical Results. Hawthorne, using Squire and Winter's expression [2] for the secondary vorticity [$\bar{\zeta}_s = (2\bar{s}/\bar{R})(\bar{\zeta}_n)_{\text{inlet}}$], solved equation (9) for a duct with a large span using a series expansion technique. He assumes a (1/7)th power boundary layer coming into the duct. The analysis is valid for incompressible, inviscid, homogeneous flow in a non-rotating duct. In this case, the second and third terms in equation (7) and the corresponding terms in equation (8) are zero. He predicts very large secondary vorticity at the wall. The results of Hawthorne are not accurate near the wall, since the viscous effects are neglected. His results are compared with the authors' results for $\Delta\alpha_2$ for $\delta/S = 2$ in Fig. 3.

The authors' results agree very well with Hawthorne's inviscid theory away from the wall. The departure between solutions is large (for $b < 0.2\ \delta$) near the wall where the effects of viscosity cannot be neglected. It is thus clear that inviscid analyses are not valid near the wall, and that effects of viscosity should be considered for accurate prediction.

Comparison With Experimental Data From Curved Ducts. Squire and Winter [2] carried out detailed measurements in a curved duct with 94 deg flow turning and a 36.6 cm radius. The width (S) and height of the channel were 12.13 cm and 182.4 cm, respectively. The measured inlet velocity (primary flow) profile as well as the predicted and measured secondary velocity profiles are shown in Fig. 4. In this case, the second and third terms in equation (7) and the corresponding terms in equation (8) are zero. The flow is assumed laminar. The measured values of u (spanwise or b direction) at $b/\delta = 0.06$, which is very near the wall, agree very well with the authors' prediction. The prediction from Squire and Winter's [2] analysis also is shown. This confirms the earlier conclusion that the viscous effects should be included to accurately predict the secondary flow near the wall regions. The prediction of the secondary velocity (v) in the n direction shows good agreement with the data.

Lewkowicz [15] carried out comprehensive measurements

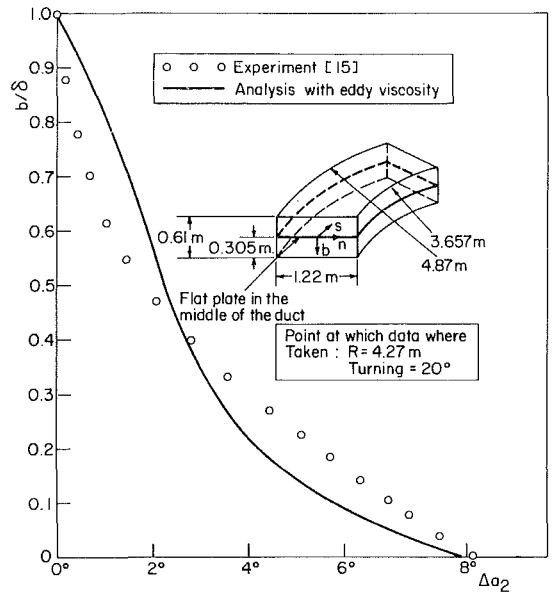

Fig. 5 Comparison between experimental and predicted $\Delta\alpha_2$ for Lewkowicz bend [15]

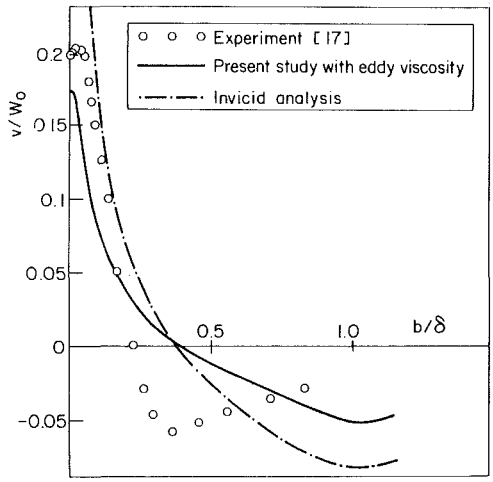

Fig. 6 Comparison between experimental and predicted cross flow velocity profile at the exit of the cascade [17]

in a curved duct shown as insert in Fig. 5. The predicted deviation angle ($\Delta\alpha_2 \approx v/w$) variation across the boundary layer is in excellent agreement with the predictions from the authors' analysis. It is thus evident that the development of cross flow in the three-dimensional boundary layer is predicted accurately from this analysis. Since the turning is small (20 deg) and the radius of the bend is large, this test case falls within the realm of a small cross-flow assumption. Hence, good agreement between the theory and experiment is as expected. The inviscid classical analysis predicts nearly twice the measured $\Delta\alpha_2$ (not shown in Fig. 5).

Comparison With the Compressor and Turbine Cascade Data. The first and fourth terms in equation (7) and the corresponding terms in equation (8) are retained for the prediction of the flow through cascades described in this section.

Papailiou et al. [17] carried out experiments in a compressor cascade consisting of blades with a NACA 65-12-A_{10}-10 profile. Other parameters of the cascade were as follows: inlet free stream velocity = 44.9 m/s, space chord ratio = 0.8, aspect ratio = 2.1, stagger angle = 15 deg, inlet air angle = 20.4 deg, and outlet air angle = −23.8 deg. The experimental results of Papailiou et al. [17] are compared with

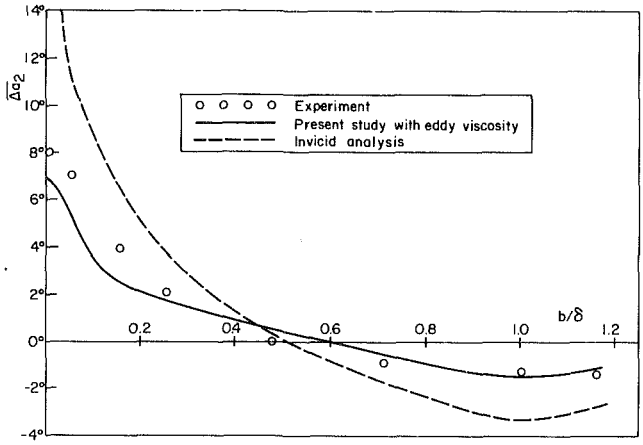

Fig. 7 Comparison between experimental and predicted change in outlet angle for Marchal and Sieverding's cascade [16]

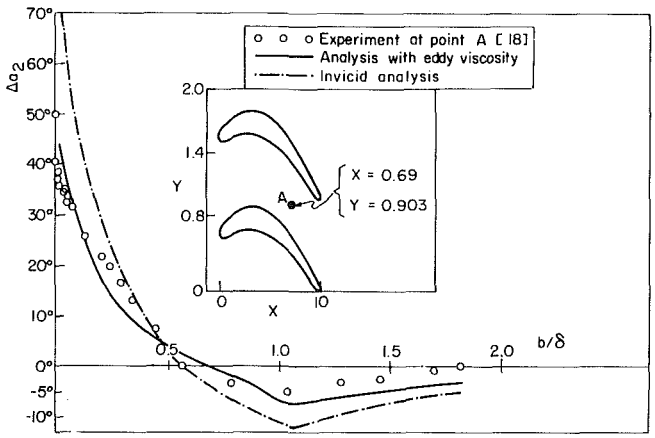

Fig. 8(a) Comparison between experimental and predicted change in angle for Langston's cascade [18]

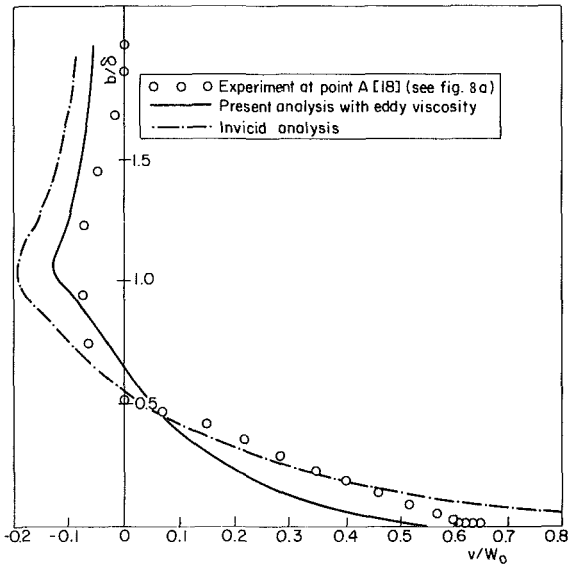

Fig. 8(b) Comparison between experimental and predicted cross flow velocity profiles for Langston's cascade [18]

the results of the present analysis for the secondary velocity v at the exit of the cascade in Fig. 6. The prediction of the present study is better near the wall than the inviscid analysis. This provides a validation of the authors' approach in updating the boundary condition for $(\bar{\xi}_s)_{\text{wall}}$ near the wall.

Marchal and Sieverding [16] carried out experiments for a turbine cascade. The cascade geometry was as follows: chord = 12 cm, space to chord ratio = 0.725, stagger angle =

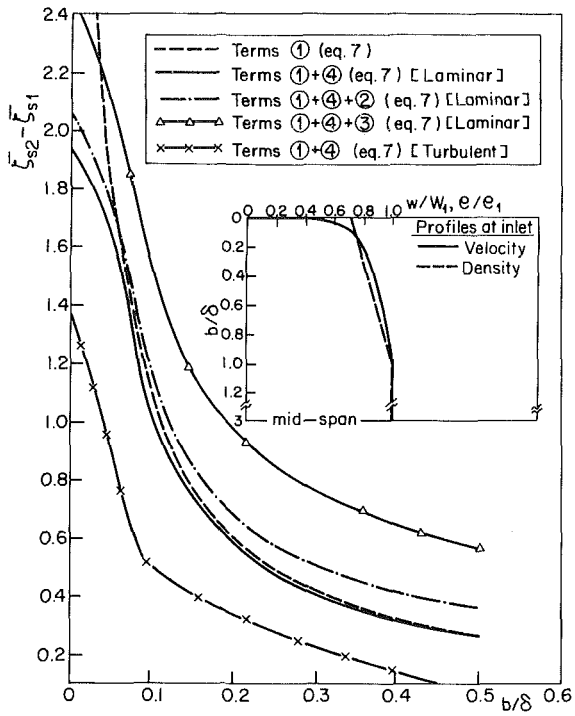

Fig. 9 Relative secondary vorticity at the exit of the model compressor rotor in the casing region

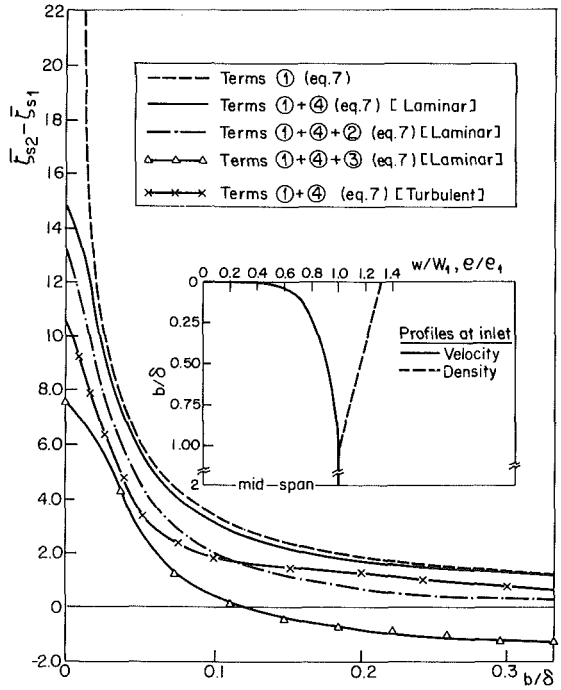

Fig. 10 Relative secondary vorticity at the exit of the model turbine rotor in the casing region

-42.5 deg, blade height = 10 cm. The inlet and outlet air angles were 0 deg and -67.8 deg, respectively. The Reynolds number based on the chord and the exit velocity was 2.61×10^5. The experimental results for $\Delta\alpha_2$ are compared with the predictions of the present analysis and the predictions from the inviscid analysis in Fig. 7. The inviscid analyses provides poor predictions near the wall. The authors' analysis gives much better predictions in the entire flow field.

Langston [18] recently carried out measurements of the subsonic flow in a large-scale rectilinear turbine cascade. The cascade geometry was as follows: chord = 34 cm,

pitch/chord ratio = 0.78, aspect ratio = 0.81, camber angle = 70 deg. The inlet boundary layer thickness, displacement thickness, and momentum thickness were 3.3 cm, 0.376 cm, and 0.279 cm, respectively.

The predictions of the cross-flow velocity and the yaw angle deviation for Langston's [18] cascade is compared with the data in Fig. 8. The measurements at station A (Fig. 8(*a*)) near mid-passage at 69 percent of axial chord are used for this comparison. The results are quite good since this station is away from the suction side of the airfoil, where the separation occurs. The authors' prediction is not valid near a separated flow. The analysis predicts maximum cross flow at the middle of the passage, decaying as we go near the blade surfaces. Langston's measurements show an increase in the cross-flow velocity when going from $Y = 0.903$ to $Y = 0.766$. The present analysis gives much better results than the inviscid analysis near the wall.

Model Rotors. Calculations have been made for a model compressor rotor and a model turbine rotor in order to study the effect of rotation and density stratification on the development of relative secondary vorticity. The model rotors have the following features. Compressor rotor: $\beta_1 = 40$ deg, $\beta_2 = 10$ deg, $\lambda = 25$ deg, $W_2/W_1 = 0.78$, $2\delta/b_0 = 0.33$, $\Omega\delta/W_1 = 0.188$. Turbine rotor: $\beta_1 = 20$ deg, $\beta_2 = -70$ deg, $\lambda = 25$ deg, $W_2/W_1 = 2.74$, $2\delta/b_0 = 0.75$, $\Omega\delta/W_1 = 0.56$.

The velocity and density profiles employed in this computation are shown as inserts in Figs. 9 and 10 for the compressor and turbine rotors, respectively. The assumed density profile for a compressor rotor (Fig. 9) is of the type encountered in thermal boundary layers near the hub and annulus walls. The density profile for the turbine (Fig. 10) represents the non-uniformity in temperature at the exit of the combustion chamber. The assumed magnitude and profiles of velocity and density are arbitrary.

The contribution to the secondary vorticity development in a compressor rotor from various terms in equation (7) is shown in Fig. 9. The laminar viscous term has a dominant effect near the wall. The turbulence reduces the secondary vorticity drastically across the entire boundary layer. The rotation and density stratification have appreciable influence in this case. It should be remarked here that the contribution due to the density stratification will be reversed if the density gradients are opposite to those shown in Fig. 9. Such a case may occur due to inherent design features of the preceding blade row. A similar trend is observed in the case of a turbine rotor as shown in Fig. 10. The dominant effect of the term $\Omega_n \partial w/\partial s$ is evident from this figure. The rotation effect is opposite to those of a compressor for this particular case.

Concluding Remarks

The present analysis employs the classical approach of uncoupled primary and secondary flow fields so it cannot predict any transport of the secondary vorticity and subsequent roll up near the suction side of the passage. However, it goes beyond the classical approach by introducing the effects of viscosity, rotation, and density stratification on the development of secondary vorticity.

The agreement between the analysis and several sets of data in a duct, compressor, and turbine cascade is good in all regions. Earlier theories had poor predictions near the wall (up to approximately 2/10 of the boundary layer), and this has been rectified by introducing the viscous effects on secondary flow and vorticity development. Excellent agreement between experimental data and the present analysis near the wall emphasizes not only the need for a viscous analysis for accurate prediction, but also confirms the validity of the method of updating of the boundary condition developed in this paper.

The present method can be improved by allowing for the change in the streamwise velocity and development of the wall boundary layers.

Acknowledgments

This work was sponsored by the National Aeronautics and Space Administration through the grant NSG 3212, with Dr. P. Sockol as the Technical Monitor. The authors wish to thank Dr. J. Galmes for his help in the derivation of the vorticity equation for turbulent flow (Appendix 1).

References

1 Hawthorne, W. R., "Secondary Circulation of Fluid Flow," *Proceedings of the Royal Society*, Series A, Vol. 206, 1951, p. 374.

2 Squire, H. B., and Winter K. G., "The Secondary Flow in a Cascade of Airfoils in a Non-Uniform Stream," *Journal of Aeronautical Sciences*, Vol. 18, 1951, p. 271.

3 Horlock, J. H., and Lakshminarayana, B., "Secondary Flows: Theory, Experiment, and Application in Turbomachinery Aerodynamics," *Annual Review of Fluid Mechanics*, Vol. 5, 1973, pp. 247–280.

4 Lakshminarayana, B., and Horlock, J. H., "Effect of Shear Flows on Outlet Angle in Axial Flow Compressor Cascades," ASME *Journal of Basic Engineering*, Vol. 89, 1967, pp. 191–200.

5 Barber, T. J., "Analysis of Shearing Internal Flows," AIAA Paper 81-0005, Jan. 1981.

6 Abdallah, S., and Hamed, A., "An Inviscid Solution for the Secondary Flow in Curved Ducts," AIAA Paper 80-1116, 1980.

7 Pratrap, V. S., and Spalding, D. B., "Fluid Flow and Heat Transfer in Three-Dimensional Duct Flows," *International Journal of Heat and Mass Transfer*, Vol. 19, 1976, pp. 1183–1188.

8 Briley, W. R., and McDonald, H., "Computation of Three-Dimensional Turbulent Subsonic Flow in Curved Passages," UARL Report R75-911596-8, 1975.

9 Briley, W. R., and McDonald, H., "Analysis and Computation of Viscous Subsonic Primary and Secondary Flows," AIAA Paper 79-1453, 1979.

10 Lakshminarayana, B., and Horlock, J. H., "Generalized Expressions for Secondary Vorticity Using Intrinsic Coordinates," *Journal of Fluid Mechanics*, Vol. 59, Part 1, 1973, pp. 97–115.

11 Schlichting, H., *Boundary Layer Theory*, Seventh Edition, McGraw-Hill.

12 Chow, Chuen-Yen, *An Introduction to Computational Fluid Mechanics*, Wiley, 1979.

13 Roache, P. J., *Computational Fluid Dynamics*, Hermosa Publishers, 1972.

14 Hawthorne, W. R., "Some Formulas for the Calculation of Secondary Flows in Cascades," British Aeronautical Research Council Report 17519, 1955.

15 Lewkowicz, A. K., "Two- and Three-Dimensional Incompressible Turbulent Boundary Layers," Ph.D. thesis, University of Liverpool, 1965.

16 Marchal, Ph., and Sieverding, C. H., "Secondary Flows Within Turbomachinery Bladings," AGARD CP 214, 1977.

17 Papailiou, K., Flot, R., and Mathieu, J., "Secondary Flows in Compressor Bladings," ASME Paper 76-GT-57, 1976.

18 Langston, L. S., "Crossflows in a Turbine Cascade Passage," ASME *Journal of Engineering for Power*, Vol. 102, Oct. 1980, pp. 866–874.

APPENDIX 1

Vorticity Equation for Turbulent Flow

The Reynolds equation for a turbulent flow field is given by

$$(\mathbf{V}\cdot\nabla)\mathbf{V} + \overline{(\mathbf{u}'\cdot\nabla)\mathbf{u}'} = -\frac{\nabla P}{\rho} - \frac{\mu}{\rho}\nabla\times(\nabla\times\mathbf{V}) + \frac{4}{3}\mu\nabla(\nabla\cdot\mathbf{V}) \tag{A1}$$

where, $\mathbf{V}$ is the mean velocity vector and $\mathbf{u}'$ is the fluctuating velocity vector.

The vorticity equation can be derived by taking the curl of equation (A1). All the terms in equation (A1) except the expression $[\overline{(\mathbf{u}'\cdot\nabla)\mathbf{u}'}]$ are expanded in reference [10]. Expansion of this term follows.

The fluctuating velocity vector is written as,

$$\mathbf{u}' = q_s'\mathbf{s} + q_n'\mathbf{n} + q_b'\mathbf{b}$$

where q_s', q_n', q_b' are fluctuating components in s, n, b directions. Hence,

$$\overline{(\mathbf{u}'\cdot\nabla)\mathbf{u}'} = \overline{q_s'\frac{\partial \mathbf{u}'}{\partial s}} + \overline{q_n'\frac{\partial \mathbf{u}'}{\partial n}} + \overline{q_b'\frac{\partial \mathbf{u}'}{\partial b}} \tag{A2}$$

Expanding the above expression in intrinsic coordinate system [10] and assuming that the flow is incompressible, it can be proved

$$\begin{aligned}\overline{(\mathbf{u}'\cdot\nabla\mathbf{u}')} = \mathbf{s}\Big[&\frac{\partial}{\partial s}(\overline{q_s'^2}) + \frac{\partial}{\partial n}(\overline{q_s'q_n'}) + (\overline{q_s'q_b'}) - \frac{\overline{q_s'q_n'}}{R}\Big] \\ &+ \mathbf{n}\Big[\frac{\overline{q_s'^2}}{R} + \frac{\partial}{\partial s}(\overline{q_s'q_n'}) + \frac{\partial}{\partial n}(\overline{q_n'^2}) + \frac{\partial}{\partial b}(\overline{q_n'q_b'}) \\ &- \overline{q_s'q_b'}\frac{1}{\tau} + \overline{q_n'q_s'}\Big(\frac{1}{a_n}\frac{\partial a_n}{\partial s}\Big)\Big] + \mathbf{b}\Big[\frac{\partial}{\partial s}(\overline{q_s'q_b'}) \\ &+ \frac{\partial}{\partial n}(\overline{q_n'q_b'}) + \frac{\partial}{\partial b}(\overline{q_b'^2}) + \overline{q_s'q_n'}\frac{1}{\tau} \\ &+ \overline{q_b'q_s'}\frac{1}{a_b}\frac{\partial a_b}{\partial s}\Big]\end{aligned}$$

The above expression is simplified by assuming that τ and R are very large, and by neglecting all terms involving derivatives in the streamwise and normal direction. The final result is

$$\overline{(\mathbf{u}\cdot\nabla\mathbf{u}')} \approx \mathbf{s}\frac{\partial}{\partial b}(\overline{q_s'q_b'}) + \mathbf{n}\frac{\partial}{\partial b}(\overline{q_n'q_b'}) + \mathbf{b}\Big(\frac{\partial}{\partial b}\overline{q_b'^2}\Big) \tag{A3}$$

Taking the curl of the above quantity and utilizing the assumptions made earlier, equation (A3) simplifies to,

$$\overline{(\mathbf{u}'\cdot\nabla\mathbf{u}')} = -\mathbf{s}\frac{\partial^2}{\partial b^2}(\overline{q_n'q_b'}) + \mathbf{n}\frac{\partial^2}{\partial b^2}(\overline{q_s'q_b'}) \tag{A4}$$

The terms $(\overline{q_n'q_b'})$ and $(\overline{q_s'q_b'})$ can be modeled using the eddy viscosity concept

$$\overline{q_n'q_b'} = -\frac{\mu_e}{\rho}\frac{\partial v}{\partial b}\quad,\quad \overline{q_s'q_b'} = -\frac{\mu_e}{\rho}\frac{\partial w}{\partial b} \tag{A5}$$

The secondary vorticity can be written as,

$$\zeta_s = \frac{\partial u}{\partial n} - \frac{\partial v}{\partial b}$$

In most of the cases $\partial v/\partial b >> \partial u/\partial n$, hence $\zeta_s \approx -\partial v/\partial b$. Since $\partial w/\partial b = \zeta_n$, the correlations in equation (A5) can be expressed as

$$\overline{q_n'q_b'} = \frac{\mu_e}{\rho}\zeta_s\quad,\quad q_s'q_b' = -\frac{\mu_e}{\rho}\zeta_n \tag{A6}$$

Substituting expressions (A6) in equation (A4) it follows that

$$\overline{(\mathbf{u}'\cdot\nabla\mathbf{u}')} = -\mathbf{s}\frac{\partial^2}{\partial b^2}\Big(\frac{\mu_e}{\rho}\zeta_s\Big) - \mathbf{n}\frac{\partial^2}{\partial b^2}\Big(\frac{\mu_e}{\rho}\zeta_n\Big) \tag{A7}$$

Transferring these terms to the right-hand side of equation (A2), the additional terms that appear on the right-hand side of equations (A5) and (A6) are, respectively,

$$\Big[\frac{1}{w^2}\frac{\partial^2}{\partial b^2}\Big(\frac{\mu_e}{\rho}\zeta_s\Big)\Big] \qquad \Big[\frac{\partial^2}{\partial b^2}\Big(\frac{\mu_e}{\rho}\zeta_n\Big)\Big] \tag{A8}$$

Modification of Vortex Shedding in the Synchronization Range

M. M. Zdravkovich
Reader,
University of Salford,
Salford, U.K.

One aspect of the synchronization phenomenon, which has attracted little attention so far, is the timing of vortex shedding in relation to the displacement of a bluff body. Systematic analysis of flow visualization within the synchronization range revealed that the jump in fluctuating forces had a simple fluid mechanics origin. The oscillating cylinder imposed not only its frequency to the wake behind it but also the timing of the vortex shedding. In the lower region of the synchronization range, the vortex formed on one side of the cylinder was shed when the cylinder was near to the maximum amplitude on the opposite side. This timing changed suddenly in the upper synchronization range where the vortex of the same circulation as before was shed when the cylinder reached the maximum amplitude on the same side.

Introduction

General Aspects. When a bluff body is flexible, the vortex shedding excites oscillations and the oscillations control the vortex shedding. This peculiar interaction is reflected in a synchronization of the frequency of vortex shedding to the natural frequency of oscillation over a range of free stream velocities. The constant frequency of vortex shedding within the range of synchronization leads to a continuous decrease of the Strouhal number. The maximum amplitude of oscillation occurs in the middle of the synchronization range where the Strouhal number is significantly reduced in comparison with that found behind the rigid cylinder.

The extent of the synchronization range strongly depends on the amplitude of oscillation, buoyancy and shape of bluff body, to mention only a few. Only bluff bodies having a cross-section either circular or semicircular (D-section) will be considered in this paper. The mean feature of synchronized vortex shedding is a large magnification of fluctuating forces on the oscillating cylinder in comparison with those measured on the stationary one. The cause of magnification is attributed to three different origins:

(*i*) the shortening of the length of the vortex formation region, [1, 2],

(*ii*) the increase in correlation length along the span of the cylinder [3, 4],

(*iii*) the increased period of vortex shedding [5].

Even a small amplitude of oscillation can considerably reduce the length of the formation region in the nearwake and thus magnify the fluctuating and time averaged forces. This effect was documented by Gerrard [1] for turbulent wakes and by Griffin [2] for laminar wakes.

The cyclic displacement of the oscillating cylinder enhances remarkably the spanwise correlation of the vortex formation and shedding. This correlation was measured by Toebes [4] on a cylinder forced to oscillate at constant frequency and amplitude. Finally, the constancy of the synchronized frequency means a constant period of time available for the vortex formation. Hence, more vorticity is generated with increased velocity within and along the synchronization range which leads to stronger vortices. Sarpkaya [5] quantified that effect in a computer simulation of vortex shedding behind an oscillating cylinder. All three effects combined to produce stronger and more regular vortex shedding behind the oscillating cylinder than that behind the stationary one.

Specific Aspects. Bishop and Hassan [6] forced the cylinder to oscillate at constant amplitude throughout the synchronization range and found an increase at first followed by a discontinuous fall of the fluctuating and time-averaged forces in the middle of the synchronization range. Ramamurthy and Toebes [7] verified that discontinuous fall for the fluctuating lift force. Stansby [8] found a similar discontinuity in base pressure and Bearman and Currie [9] in fluctuating side pressure.

Parkinson and his students [10, 11] discovered that the maximum amplitude of a freely oscillating cylinder in the middle of the synchronization range coincided with a discontinuous jump in phase angle measured between the cylinder displacement and pressure fluctuation on its side. It is evident that the discontinuity of fluctuating pressures and forces in the middle of the synchronization range cannot be explained by the three effects discussed earlier.

Object. One aspect of the synchronized vortex shedding, which may have a dominant role within the synchronization range, is the timing of vortex shedding in relation to the cylinder displacement. It is the main object of this paper to analyse flow visualization photographs and try to establish two different modes of the synchronized vortex shedding. If the two modes exist, then a sudden change from one mode to another will lead to a discontinuous change in fluctuating

Contributed by the Fluids Engineering Division of THE AMERICAN SOCIETY OF MECHANICAL ENGINEERS and presented at the Winter Annual Meeting, Washington, D.C., November 15-20, 1981. Manuscript received by the Fluids Engineering Division, December 1, 1981. Paper No. 81-WA/FE-25.

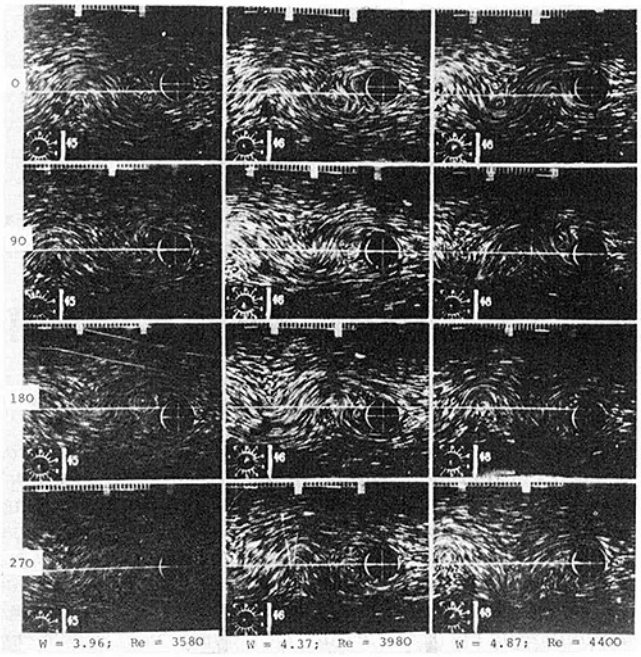

Fig. 1 Synchronized wake of mechanically oscillating cylinder under various conditions (after Den Hartog, 1934)

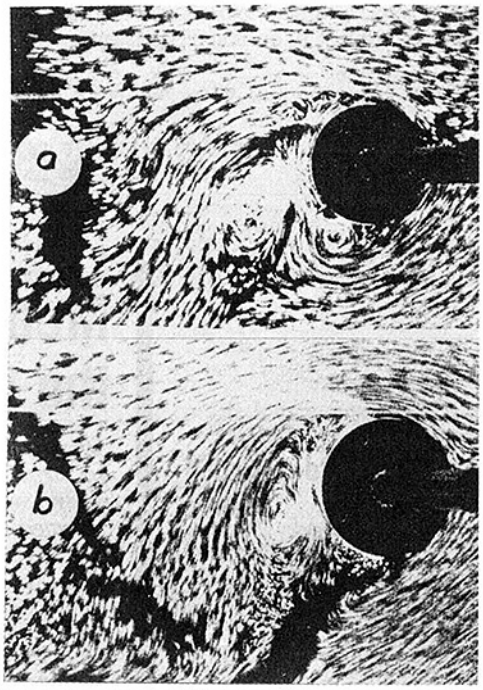

Fig. 2 Sychronized wake of freely oscillating cylinder under (*a*) steady and (*b*) unsteady conditions (after Meier-Windhorst, 1939)

pressure around the cylinder and to a discontinuity in resulting fluctuating and time-averaged forces. The hysteresis effect found by Bishop and Hassan [6] can be explained then as the persistence of one mode up to a higher velocity when the velocity increases and the other mode overlaps to a lower velocity when the velocity decreases. The hysteresis loops were found for both, the amplitude of oscillation and phase angle for the freely oscillating cylinder [10, 11].

Flow Visualization Experiments

Forced Oscillating Cylinder. The earliest flow visualization experiments have been carried out by Den Hartog [12]. The flow pattern was photographed around a mechanically oscillated cylinder towed in a water tank. The synchronization region was determined after some preliminary tests "on a single-degree-of-freedom vibrating system, having the elastic and inertia forces much greater than the fluctuating wind forces." The system oscillated at its natural frequency within the range of reduced velocities $3.9 < W < 4.9$ and the maximum amplitude occurred at $W_{cr} = 4.4$. It has not been stated in the paper whether the same system was forced to oscillate in the towing tank where flow visualization was carried out.

Figure 1 is Den Hartog's original selection of photographs which summarizes his observations. Four photographs in any vertical column represent four consecutive positions of the forced oscillating cylinder with a phase angle of 90 degrees between each photograph. In the middle column test 46, the reduced velocity coincided with that at which maximum amplitude was found in free oscillations in air. In the left column, test 45 was carried out at the reduced velocity 10% below that of test 46, and in test 48 the reduced velocity was about 10% above that of test 46. Hence the three regimes represented the beginning, middle, and end of the synchronization range. Den Hartog remarked that in all three cases the flow was completely periodic, i.e., after each period of oscillation of the cylinder the same flow pattern was photographed. He added that outside the synchronization range ($W > 4.9$ or $W < 3.9$) the flow was nonperiodic.

The common feature seen in all three columns in Fig. 1 is that the formation of vorticies occurred in the nearwake very close to the cylinder. For that range of Reynolds numbers the length of the formation region is now known to be at least two diameters behind the stationary cylinder. At the beginning of the synchronization range, test 45, the timing of the lower vortex shedding seems to take place after the top maximum amplitude was reached. Photograph 45.2 clearly shows that the lower vortex is engulfed in the flow coming from the upper side of the cylinder and a small new vortex having the same sense of circulation is formed adjacent to the cylinder. The upper vortex is almost ready to be shed when the cylinder is at the lower maximum amplitude as seen in photograph 45.3.

Similar flow patterns at slightly different phasing are seen

Nomenclature

A = maximum amplitude of oscillation of either forced or free cylinder
D = diameter of circular cylinder
L = maximum fluctuating lift force
N_c = natural or forced frequency of cylinder
N_v = natural vortex shedding frequency
$N_c = N_v$ = only within synchronization range
R_e = Reynolds number $= VD/\nu$
S_t = Strouhal number $= N_v D/V$
V = free stream velocity
W = reduced velocity $= V/N_c D$
W_{cr} = critical reduced velocity: at A for free oscillating cylinder and at L for forced oscillating cylinder
ν = kinematic viscosity of fluid
ϕ = phase angle

in the middle column. Test 46 was carried out in the middle of the synchronization range but presumably at a reduced velocity still less than the critical. Photograph 46.1 shows that the lower vortex was shed when the cylinder reached the upper maximum amplitude. It is also evident that the upper vortex is closer to the apparent axis of the wake than it was in test 45. Photograph 46.2 reveals that an almost fully grown upper vortex occupies the center of the nearwake suppressing the growth of the new lower vortex. Finally, in photograph 46.3, the upper vortex is shed while the lower vortex fills the center of the nearwake. The location of the shed vortex is below the apparent wake axis. Thus, in order to form a correct staggered vortex street it has to cross the wake axis and travel to the upper side of the far-wake.

The new feature of the test 48 near the end of synchronization range is a change in the phase of vortex shedding. Photograph 48.1 in Fig. 1 shows that when the cylinder reaches the upper maximum amplitude the upper vortex (having anticlockwise circulation) is shed by engulfment of the flow. This 180 degrees change in phase becomes obvious by comparing photographs 46.3 and 48.1 or 46.1 and 48.3. Photograph 48.2 reveals the rapid growth of the lower vortex positioned above the apparent wake axis. It is instructive to follow the displacement of the location of that vortex in 45.4, 46.4 and 48.2 for the later discussion of the path of shed vortices.

It can be concluded that two modes of synchronized vortex shedding exist. In the lower region of the synchronization range, the vortex located on the opposite side to the displacement of the cylinder is shed when the cylinder is just about to reach or has reached its maximum amplitude. In the upper part of the synchronization range the vortex adjacent to the cylinder's displacement is shed when that maximum amplitude is reached. Whether the change from the lower mode to the upper one is continuous or discontinuous cannot be deduced from the flow visualization shown in Fig. 1.

Freely Oscillating Cylinder. Another crucial question also remains unresolved. That is whether the synchronized wake behind a mechanically oscillated cylinder is similar to that of a freely oscillated one. The two synchronized wakes should be similar at the same reduced velocity if both have the same relative amplitude of oscillation. The latter, however, is always kept constant throughout the synchronization range for the mechanically oscillating cylinder.

The mechanical displacement of the cylinder at constant amplitude triggers the synchronization of the vortex shedding frequency before it becomes equal to the forced frequency and maintains the synchronization beyond the reduced velocity found for the same cylinder freely suspended [3, 6, 8]. This is an indication that the synchronized vortex shedding becomes more regular and stronger with the increase in amplitude i.e., that the phenomenon is fluidelastic as Toebes called it [7].

Systematic experiments have been carried out by Meier-Windhorst [13] by using a freely oscillating cylinder attached to a swinging arm and submerged in a uniform water stream. The variation of amplitude of oscillation was measured as affected by the flexibility, buoyancy and external damping of the cylinder arrangement, and was complemented with flow visualization on the water surface. Figure 2 shows a selection of two photographs from [13]. The top photograph shows the synchronized wake as the cylinder approaches the upper maximum amplitude. The superimposed white line denotes a tangent to the cylinder when it is in the upper extreme of its oscillation. Hence the timing of the synchronized wake shown in Fig. 2(*a*) is slightly ahead of the synchronized wakes shown in Fig. 1, first row. The flow pattern resembles closely that in photograph 48.1. The large anticlockwise vortex is almost at the same location in both photographs. The small clockwise one is squeezed in 48.1 but well rounded in Fig. 2(*a*). Meier-

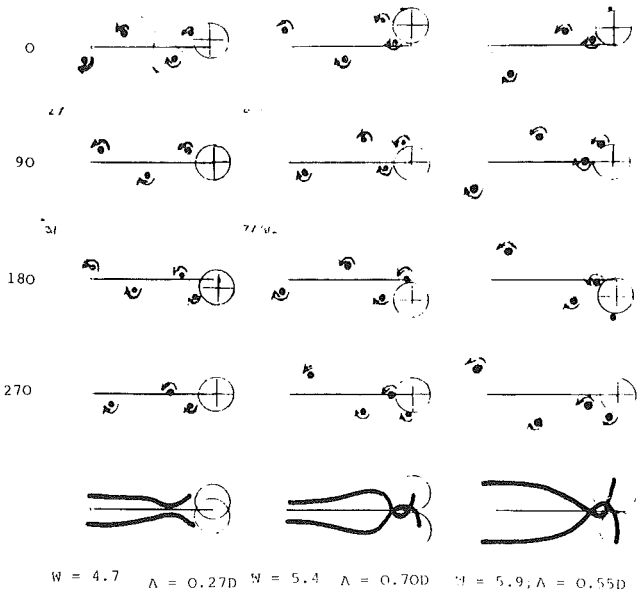

Fig. 3 Instantaneous positions and paths of vortices in synchronized wake of freely oscillating cylinder under various conditions (derived from Angrilli et al. 1974)

Windhorst argued that the dragging of that small vortex during the upward stroke reduced the lift force on the cylinder. When the same cylinder was stopped and then released to build up the oscillation again the flow pattern was changed in as much as the small vortex did not appear, as seen in Fig. 2(*b*). This feature supports Meier-Windhorst's [13] argument that, in the unsteady regime of the amplitude build-up, the maximum fluctuating lift force is generated in the absence of the small vortex. This modification of the synchronized vortex shedding will be discussed in the next section.

Timing of Initiation and Shedding of Vortices in Synchronized Range

Turbulent Synchronized Wakes. The excellent flow visualization sequences recorded by Den Hartog [12] are incomplete in two important respects:

(*i*) the timing of the initial formation of individual vortices cannot be deduced, and

(*ii*) the paths of the vortices with opposite circulation cannot be traced.

Angrilli et al. [14] carried out flow visualization of the synchronized wake of a freely oscillating cylinder. The experimental arrangement was identical to that used by Meier-Windhorst [13] except that the cylinder was not fitted with end plates.[1]

Four cine films were shot at various reduced velocities within the synchronization range. One cycle of oscillation was depicted in at least 16 consecutive frames of the cine film. This gave a sufficient number of points to trace the path of each vortex from its first appearance until it was carried away downstream. For a freely oscillating cylinder there was always some modulation of the response due to cycle-to-cycle variations in vortex formation and shedding, due to free stream turbulence and three-dimensional end effects. The simultaneous measurement of the displacement of the cylinder and pressure fluctuations on its surface were coupled with the cine-camera. This enabled to distinguish the sequence of frames depicting regular or irregular oscillation. The consecutive vortices did not follow the same path at the fixed

[1] Length to diameter ratio was only 1.8 in (13) and 8.6 in (14).

reduced velocity during the irregular period of oscillation. In one cycle chosen near the end of the synchronization range, it was found that a newly formed vortex moved in the wrong direction and quickly broke down.

The plots showing the instantaneous location of vortices in the synchronized wakes were not suitable for direct comparison with Den Hartog's data. Figure 3 was derived from Angrilli's et al. [14] Fig. 5. The instantaneous location of vortices at 1/4 periods of one cycle are depicted for three values of reduced velocity. The actual relative maximum amplitude and reduced velocity are shown under each column. Finally below each column the average paths of vortices are shown starting from the first appearance of each vortex.

By comparing the first columns in Fig. 1 and 3, it can be seen that all vortices are formed and shed in almost the same positions in all four sequences. The same similarity is evident by inspecting the third columns in Figs. 1 and 3. The middle column which was chosen to represent the maximum amplitude of oscillation shows a distinct jump in the timing of vortex shedding and appears similar to the sequences shown in the last column. This might have been caused either by reaching the maximum amplitude by decreasing the reduced velocity in the experiment or if the actual maximum amplitude occurred at slightly lower reduced velocity.

The change in timing of vortex shedding was accompanied by a distinct change in the path of the vortices along the nearwake, as seen in the bottom row in Fig. 3. At the beginning of the synchronization range the path of the vortices is very similar to that found behind the stationary cylinder. The typical "neck" and "origin" marked by the shedding and initiation of vortices respectively are moved closer to the cylinder. The change in timing beyond the critical reduced velocity gives rise to completely different paths of the vortices. The vortices are formed first above or below the cylinder on its way from the upper or lower maximum amplitude, respectively. The timing of the vortex initiation at $W = 5.42$ is estimated to be between 40-50 degrees after the cylinder passed its maximum amplitude. The timing of the initiation gradually decreased to about 10 degrees at $W = 5.9$, where the amplitude of oscillation was reduced to 0.55D. Hence it seems that the timing of the initiation of the vortex formation reduces the lift force towards the end of the synchronization range as argued by Meier-Windhorst [13].

Two aspects of the second mode of vortex shedding will be emphasized. Firstly the paths as shown in Fig. 3 cross each other twice. The vortices are formed in such a way that the two alternate vortices reach the crossing points at different times, half a period apart. Secondly, the actual position of the first appearance of the vortex, at the upper or lower side of the cylinder, requires that the instantaneous separation points move upstream towards the apparent stagnation point. If this requirement is not fulfilled, the second mode of synchronized vortex shedding cannot commence. One example is the 'anomalous' behaviour of the D-shaped cylinder [11]. The flat upstream side widened the wake and reduced the Strouhal number to 0.14 for the stationary D-cylinder. The sharp corners fixed the position of separation and prevented the switch to the second mode of synchronized vortex shedding. The result was that as soon as the maximum amplitude was reached the synchronization ceased [11]. The phase shift of fluctuating pressure and displacement of the cylinder was not found by Feng [11].

Laminar Synchronized Wakes. Griffin [15] carried out an extensive set of experiments on laminar wakes of a forced oscillating cylinder. Flow-visualization of the synchronized wake behind a mechanically oscillating cylinder was performed in air at low Reynolds numbers. A variable-phase channel on the sine-wave generator allowed the vortex street to be photographed at any instant within a cycle of cylinder oscillation. The initial position of the cylinder was also adjustable by means of a time delay system.

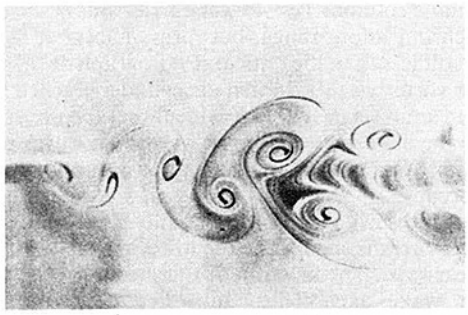

Fig. 4(*a*) $W = 5.14$

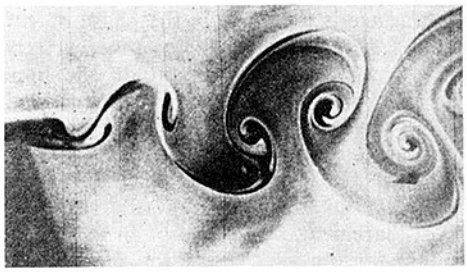

Fig. 4(*b*) $W = 6.00$

Fig. 4 Laminar synchronized wake at Re = 190 of mechanically oscillating cylinder at constant amplitude of 0.3D (After Griffin and Ramberg, 1974)

Figure 4 shows the instantaneous appearance of a synchronized laminar wake at the same relative position of the cylinder in the oscillating cycle. The maximum amplitude and Reynolds number were kept constant at 0.3D and 190, respectively. The reduced velocity of 5.14 corresponded to a lower synchronization range and $W = 6.00$ to the upper synchronization range.

The most important aspect of these synchronized wakes is the timing of vortex initiation. The two photographs show a distinct almost mirror like image of the two vortex streets due to the change in phase of about 180 deg.

Conclusions

Systematic analysis of the available flow visualization photographs of the synchronized wakes revealed that two modes of vortex shedding exist:

(*i*) the vortex formed on one side of the cylinder was shed when the cylinder was near to the maximum amplitude on the opposite side.

(*ii*) the vortex formed on one side of the cylinder was shed when the cylinder was near to its maximum displacement on the same side.

The first mode was found in the lower region of the synchronization range while the second appeared in the upper region. The two modes were separated by the critical reduced velocity which marked a discontinuous change of fluctuating and time averaged forces for the forced oscillating cylinder. A similar discontinuity in phase angle between the cylinder displacement and fluctuating pressure on it was found for a freely oscillating cylinder at the maximum amplitude. The hysteresis effect can be explained by the two modes of timing of the synchronized vortex shedding.

References

1 Gerrard, J. H., "The Mechanics of the Formation Region of Vortices

behind Bluff bodies," *Journal of Fluid Mechanics*, Vol. 25, 1966, pp. 401–413.

2 Griffin, O. M., and Votaw, C. W., "The Vortex Street in the Wake of a Vibrating Cylinder," *Journal of Fluid Mechanics*, Vol. 51, 1972, pp. 31–48.

3 Koopmann, G. H., "The Vortex Wakes of Vibrating Cylinders at Low Reynolds Numbers," *Journal of Fluid Mechanics*, Vol. 28, 1967, pp. 501–512.

4 Toebes, G. H., "The Unsteady Flow and Wake Near an Oscillating Cylinder," ASME *Journal of Basic Engineering*, Vol. 91, Sept. 1969, pp. 493–505, Discussion pp. 859–862.

5 Sarpkaya, T., "Vortex-Induced Oscillations - A Selective Review," ASME *Journal of Applied Mechanics*, Vol. 46, 1979, pp. 241–258.

6 Bishop, R. E. D., and Hassan, A. Y., "The Lift and Drag Forces on a Circular Cylinder Oscillating in a Fluid Flow," *Proc. Roy. Soc. A*, Vol. 277, 1964, pp. 51–75.

7 Toebes, G. H., and Ramamurthy, A. S., "Fluidelastic Forces on Circular Cylinders," *Proc. Amer. Soc. Civil Eng., J. Eng. Mech. Div.*, Vol. 93, EM6, 1967, pp. 1–20.

8 Stansby, P. K., "Base Pressure of Oscillating Circular Cylinders," Amer. Soc. Civil Eng., *J. Eng. Mech Div.*, Vol. 102, EM4, 1976, pp. 591–600.

9 Bearman, P. W., and Currie, I. C., "Pressure Fluctuation Measurements on an Oscillating Circular Cylinder," *J. Fluid Mech.*, Vol. 91, 1979, pp. 661–677.

10 Ferguson, N., and Parkinson, G. V., "Surface and Wake Flow Phenomena of the Vortex-Excited Oscillation of a Circular Cylinder," ASME *Journal of Engineering for Industry*, 1967, pp. 831–38.

11 Feng, C. C., "The Measurement of Vortex Induced Effects in Flow Past Stationary and Oscillating Circular and D-Section Cylinders," MSc thesis, Univ. Brit. Columbia, 1968.

12 Den Hartog, J. P., "The Vibration Problems in Engineering," *Proc. 4th Int. Congr. Appl. Mech.*, Cambridge, U. K., 1934, pp. 36–53.

13 Meier-Windhorst, A., "Flatterschwingungen von Zylindern im gleichmassigen Flussigkeitsstrom" (Flutter Oscillations of Cylinder in Uniform Liquid Flow), Mitteillungen des Hydraulischen Instituts der Technischen Hochschule, Munchen, Heft 9, 1939, pp. 3–39.

14 Angrilli, F., Di Silvio, G., and Zanardo, A., "Hydroelasticity Study of a Circular Cylinder in a Water Stream," in *Flow Induced Structural Vibrations*. Ed. E. Naudascher, Springer, Berlin, 1974, pp. 504–512.

15 Griffin, O. M., and Ramberg, S. E., "The Vortex-Street Wakes of Vibrating Cylinders," *Journal of Fluid Mechanics*, Vol. 66, 1974, pp. 553–576.

F. Angrilli

S. Bergamaschi

V. Cossalter

Institute of Applied Mechanics,
Padua University,
Padua, Italy.

Investigation of Wall Induced Modifications to Vortex Shedding From a Circular Cylinder[1]

In this paper the influence of a wall on vortex shedding frequency, geometrical pattern, and velocity field are investigated. Frequency measurements were carried out with three circular cylinders at Reynolds numbers of 2860, 3820, and 7640. Mean and fluctuating velocities at several traverses were also measured at Re = 3820 both for an isolated cylinder and for an arrangement with a gap from the wall equal to one cylinder diameter. The modifications of the wake pattern are shown in several figures. It is also shown that the proximity of the wall induces a slight increase of vortex shedding frequency.

Introduction

The history of investigations on wakes past bluff bodies is a clear demonstration that the understanding of vortex shedding has not yet been completely achieved.

Moreover, in many engineering problems the wake is in close proximity to a plane boundary or to other wakes. Therefore, the simplifying assumption that the fluid extends to infinity in any direction and that the body under investigation is the only cause of perturbation on the fluid is no longer appropriate. Practical examples can be found in different engineering areas. Heat exchangers, pipelines near sea bottom, multiple conductor transmission lines are some significant cases.

While the wake past an isolated circular cylinder has been studied extensively, only few investigations have been carried out to understand the modifications induced on a confined wake. As it is well known, in certain geometrical conditions, it is possible, according to potential flow theory, to establish an equivalence between the wake behind a pair of adjacent parallel cylinders and the wake past a cylinder near a wall [1].

In a real flow viscosity induces differences between the two cases; this point has been critically discussed by Bearman and Zdravkovich [2].

The interaction between the wakes behind a pair of circular cylinders in various arrangements has been extensively reviewed by Zdravkovich [3]. More recently, the frequency of vortex shedding from two circular cylinders in staggered arrangements has been experimentally investigated by Kiya et al [4]. With cylinders placed side by side they found a large variation of shedding frequency when the gap was in the range $0.5 \div 1$ cylinder diameters.

The experimental investigations on vortex shedding from a cylinder placed near a surface seems to have received the proper attention only in recent years. Bearman and Zdravkovich [2] studied the flow around a circular cylinder near a plane boundary in a wind tunnel at $Re = 4{,}5 \cdot 10^4$. For various gap values, they measured the mean pressure distribution, around the cylinder and along the wall, and the velocity fluctuations by means of a hot wire anemometer. They found that the vortex shedding frequency, as computed by digital spectral analysis, was remarkably constant with respect to gap variations. However, in the same paper some results are reported from Goktun's M.Sc. thesis, where the Strouhal number was found to increase from 0.198 to 0.206 when the cylinder was moved from the free stream to a gap of one half diameter. Buresti and Lanciotti [5] carried out an experimental investigation of predominant frequencies in a wake near a plane surface at $Re = 0{,}8 \cdot 10^5 \div 3 \cdot 10^5$. They did not find any significant frequency dependence on the wall distance.

From the references cited above it appears that most of the experiments have been carried out in wind tunnels at $Re \geq 2{,}5 \cdot 10^4$. The purposes of the present study are:

(*a*) to investigate wall effects on vortex shedding frequency in water in the low subcritical Reynolds range

(*b*) to compare the wake structures both with and without the wall.

General Method

The adopted procedure consisted of:

(*a*) computing the shedding frequency by measuring the velocity fluctuations downstream a cylinder placed at various distances from a wall;

(*b*) estimating the wake structure by measuring the mean and the fluctuating velocity at various downstream traverses, both without the wall and with the cylinder placed at one diameter from the wall.

Experiments (*a*) were performed using three cylinders having different diameters, corresponding to Re values of 2860, 3820 and 7640, respectively. Experiments (*b*) were performed at $Re = 3820$.

The frequency was computed averaging the spectra of the anemometer signal. The velocity transducer was placed 2.5

[1] This work has been partly sponsored by the Italian National Research Council.

Contributed by the Fluids Engineering Division for publication in the JOURNAL OF FLUIDS ENGINEERING. Manuscript received by the Fluids Engineering Division, March 30, 1981.

diameters behind the cylinder in the outer row with respect to the wall (Fig. 1). The time average of the flow velocity U was measured at 5 traverses placed at 1.5, 2.5, 3.5, 5.5, 8.0 diameters downstream the 0.02 m cylinder. At the same distances downstream, the rms values of velocity fluctuations were measured.

Experimental Arrangement

The experiments were carried out in the open water channel of the Institute of Applied Mechanics at Padua University. The channel is long about 4.5 m and its working section is 0.35 m wide; the experiments were performed with 0.18 m water depth. In additions to the regularization system, a properly sized honeycomb filter was installed upstream the test section. In this way a more uniform velocity field and a lower turbulence level were obtained in the test section. In fact, the velocities measured at several points of the test area were found to differ from their mean value by at most ± 2 percent and the rms of the velocity fluctuations was less than 1.5 percent of the local value. The hot film anemometer was used to measure the boundary layer on the bottom; its thickness in the test area was found to be 0.008 m.

In every test a cylinder was placed at the center of the flow and the velocity transducer was placed 0.05 m below the free surface. During the tests, water temperature was monitored, its value being between 18° and 20°C. The wall effect was obtained mounting a polished stainless steel sheet parallel to the flow at different distances from the cylinder. The sheet, whose thickness was 0.001 m, was clamped to a rigid frame, external to the flow, which enabled its exact positioning. The test cylinders were situated 10 diameters from the leading edge of the wall.

The boundary layer thickness originated by the wall, measured by means of the hot-film anemometer, was found to be thick less than 0.005 m in the test area.

A mechanism was employed to control the positioning of the velocity sensors, both in the transverse and longitudinal directions, in the area downstream of the cylinder. The displacements could be red on the toothed guide bars by means of a vernier. The transverse movement was driven by means of a d-c motor connected to a ten turn potentiometer, which allowed remote sensing of the probe position. The transducer used to detect the transverse displacement was a 7270 Beckman ten turn wire-wound potentiometer. The overall nonlinearity error was less than 0.2 percent.

The transverse section of the channel and the arrangement are shown in Fig. 2.

Measurement Apparatus

The velocity fluctuations in the flow and the frequency of vortex shedding have been measured by means of a DISA 55M constant temperature hot film anemometer with a 55R41 conical probe. In order to measure the mean velocity at traverses across the wake the anemometer was accurately calibrated. Some preliminary measurements of the undisturbed free stream in the velocity range from 0.05 to 0.4 m/s were performed both with the anemometer and with a Kent miniflow probe.

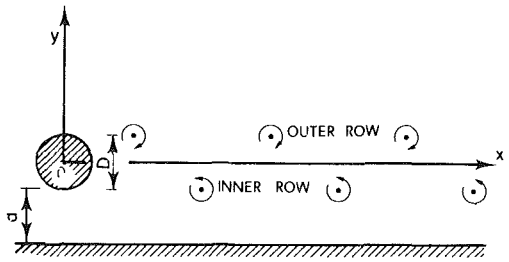

Fig. 1 Reference system

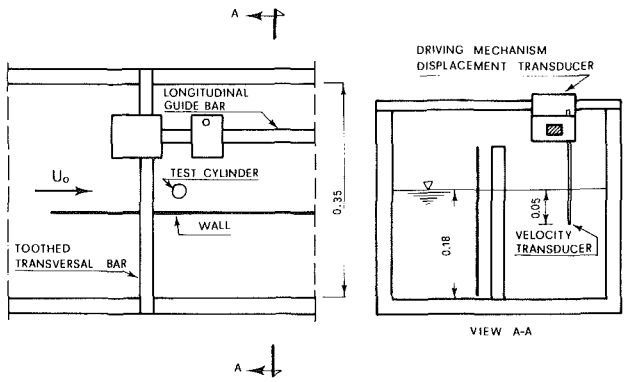

Fig. 2 Sketch of the test section and velocity measurement arrangement

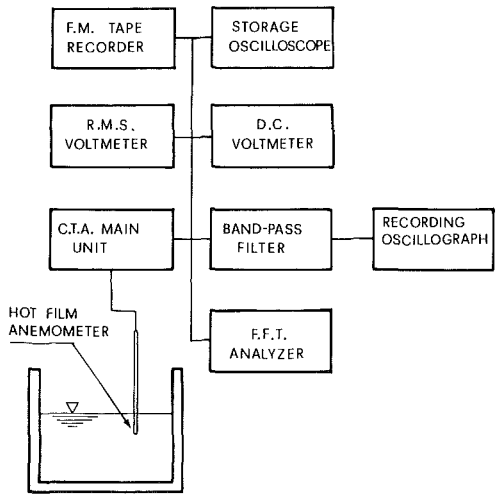

Fig. 3 Instrumentation associated to the hot film anemometer

The results obtained, read on a 55D30 DISA D.C. Voltmeter, have been compared with those given by the current flow-meter. The current flow-meter was previously calibrated in the calibration tank of the Hydraulics Institute of Padua University. Its standard deviation with respect to a regression curve was found to be $2.5 \cdot 10^{-3}$ m/s.

The output of the anemometer was stored in a magnetic tape recorder and processed by a 2031 Bruel-Kjaer F.F.T.

Nomenclature

d = gap between the cylinder and the wall
D = diameter of the cylinder
f = vortex shedding frequency
f_0 = vortex shedding frequency for isolated cylinder
U_{rms} = time average of velocity fluctuations
U = time average velocity of water
U_0 = undisturbed stream velocity
x,y = axes of the reference system measured from the cylinder center
$\theta = \frac{U_{rms}}{U_0}$ = a dimensionalized velocity fluctuation

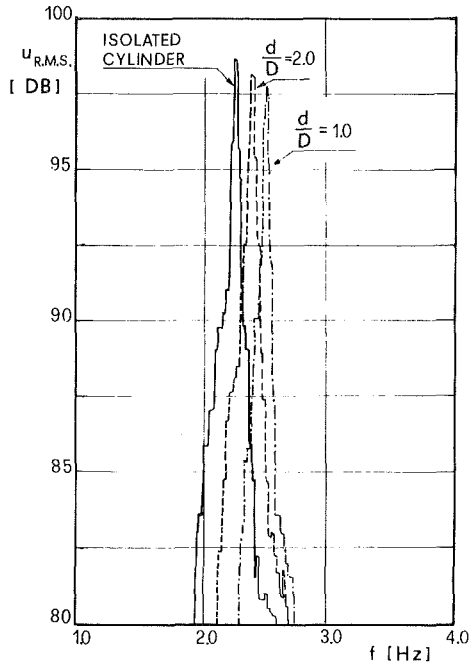

Fig. 4 Example of frequency spectrum

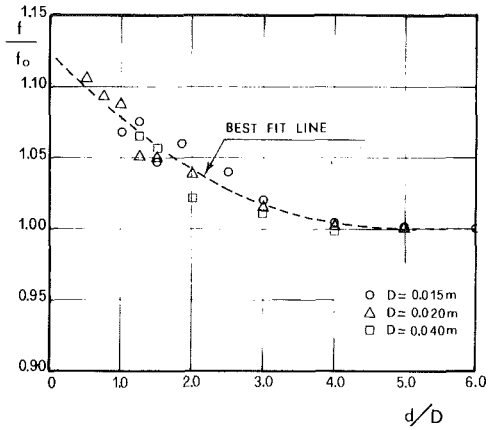

Fig. 5 Variation of vortex shedding frequency as a function of wall distance from the test cylinder

analyzer. Because the frequency of vortex shedding was not quite distinct, the peak value of the average of 16 spectra was assumed as the best one. The resolution was 0.025 Hz. The amplitude of velocity fluctuations due to eddies was computed taking the average of the spectral density in a range of 0.250 Hz centered around the peak frequency. The maximum value of uncertainty of velocity measurements was estimated to be ±4 percent. Experimental results have not been corrected for blockage effect because, in the most unfavourable case, the ratio between the cross section of the cylinders and the section of the channel was 0.11. Moreover, the thickness of the plate was very little and a gap was allowed between its lower edge and the bottom, so that the blockage effect was independent from the position of the plate.

Results and Discussion

(*a*) Shedding Frequency Analysis. A typical pattern of the averaged frequency spectra obtained with the technique mentioned above is shown in Figure 4. It is observed that the band of shedding frequencies around the dominant value is quite narrow. The values of the frequencies of the vortices shed by the three test cylinders, at several distances from the

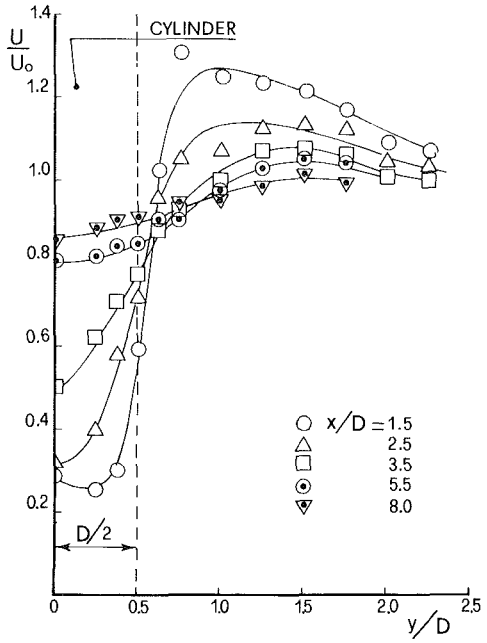

Fig. 6 Isolated cylinder. Plots of U/U_o taken from traverses across the wake

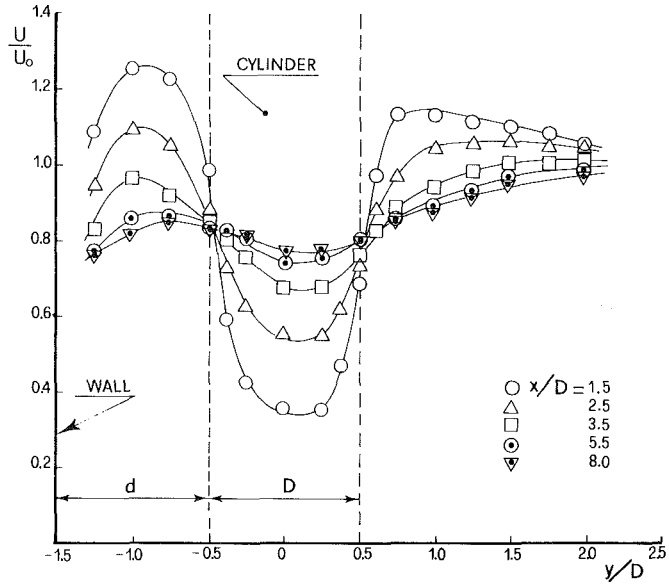

Fig. 7 Cylinder near the wall ($d/D = 1$). Plots of U/U_o taken from traverses across the wake.

wall, have been plotted in Fig. 5, together with their best fit line. Frequencies have been non-dimensionalized with respect to the value obtained from the isolated cylinder. It is clearly seen that frequency increases when the wall is placed closer to the cylinder. It is reasonable to assume that this modification is originated by the reduction of the scale of the vortex formation region induced by the proximity of the wall. As pointed out by Gerrard [6], and confirmed by Sarpkaya [7], when the shear layers are brought closer, their interaction is facilitated and the shedding period is shortened.

These results are in agreement with those obtained by Göktun, although the frequency increase found by him is less pronounced. In fact, as reported in [2], he finds a frequency ratio $f/f_0 = 1.04$ for a gap $d/D = 0.5$; our result for the same gap is $f/f_0 = 1.10$. On the contrary, our results are in contrast with Bearman and Zdravkovich [2] and Buresti and Lanciotti [3] measurements.

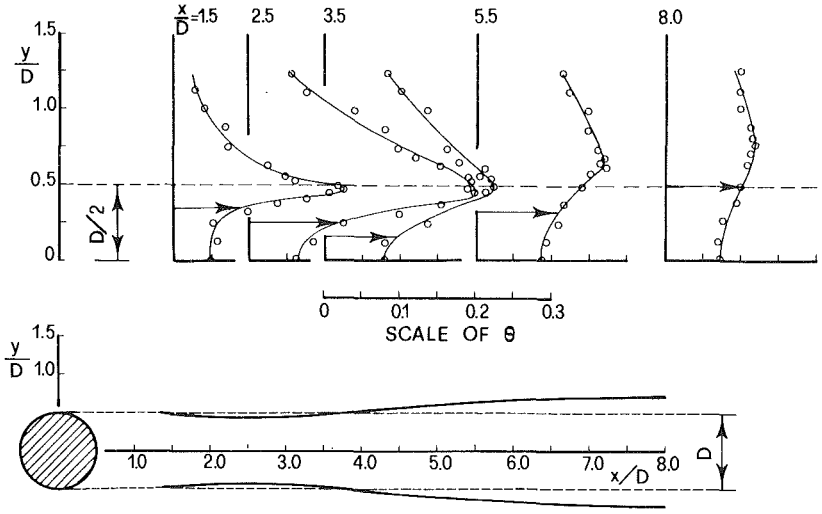

Fig. 8 Isolated cylinder. Velocity fluctuation θ at traverses across the wake. Plots of positions of maximum θ taken from traverses along the wake.

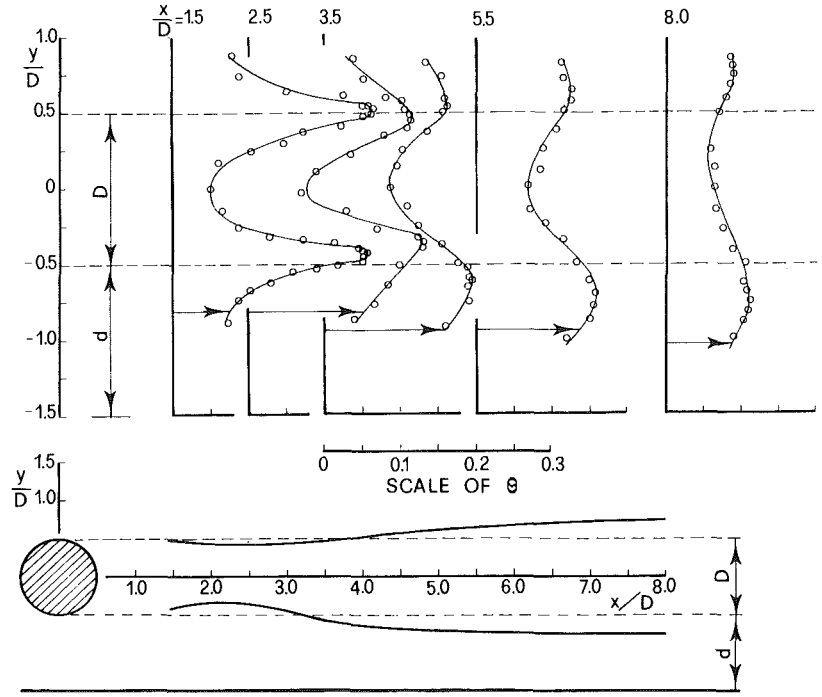

Fig. 9 Cylinder near the wall ($d/D = 1$). Velocity fluctuation θ at traverses across the wake. Plots of positions of maximum θ taken from traverses along the wake.

This difference may be due to various reasons:

- our investigation has been carried out at Re values in the low subcritical range. It can be expected that at higher Re the influence of the wall be less pronounced, because the length of the formation region is shorter
- our experiments have been carried out in water and not in air. Even though the Mach numbers at which the experiments in [2] and [5] have been carried out are small, it cannot be excluded that air compressibility is not negligible. The different mechanical behaviour of air and water may be appreciable in this case, because frequency variations are small.
- The minimum value of the gap in our experiments was more than twice the boundary layer thickness on the wall. On the contrary, some of the results reported in [2] were obtained with gap values less than the thickness of the boundary layer. It seem plausible that the frequency increase due to the wall may be cancelled by the velocity defect in the boundary layer.

(*b*) Wake Pattern Analysis. The time averaged velocity of water, U, has been measured at traverses placed at different distances downstream of the 0.02 m diameter cylinder. Figs. 6 and 7 show the ratio U/U_0 versus y/D, at five downstream positions x/D in a case without wall and with the wall placed at a distance of one diameter from the cylinder. The pattern is quite similar to others reported in the literature [8, 9].

Comparing the two plots it is seen:

- The wall causes the mean velocity distribution to be asymmetric. Near downstream the velocity is greater at the wall side, while at distances $x/D > 2.5$ the converse is true.

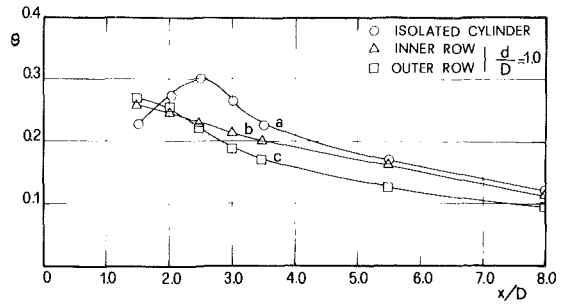

Fig. 10 Maximum θ along the wake for the isolated cylinder and for the cylinder near the wall ($d/D = 1$).

– At the wake centerline, for distances x/D less than about 3.5, the velocity defect is greater if the wall is absent.

At the same distances downstream, the rms values of velocity fluctuations were also measured. The variation of fluctuating velocity $\theta = U_{rms}/U_0$ with distance from the street centerline is presented in Figs. 8 and 9 in both the arrangements without and with the wall. In the same figures, the loci of the maximum values of θ are also shown. From Fig. 9 the lack of symmetry induced by the wall is readily apparent. In the arrangement without the wall it can be seen that the traverse of minimum spacing between the curves of maximum θ values is nearly coincident with the traverse corresponding to the absolute maximum value of θ. This result is in agreement with Schaefer and Eskinazi [8] and with Bearman [10].

The positions of maximum intensity at seven traverses are evidenced in Fig. 10. From plot (*a*) of the same figure it can be seen that the maximum value of θ for the isolated cylinder occurs at $x/D \simeq 2.5$. This result is in agreement with Bloor and Gerrard [9]. On the contrary, plots *b* and *c* relative to θ values of the vortices of the rows shed near the wall exhibit negative slope everywhere in the range from 1 to 8 diameters downstream. It is also seen that, for $x/D > 2$, the fluctuating velocity component of the outer row is weaker than that of the inner one. It seems reasonable to assume that this result is due to the circumstance that the wall increases dissipation and decreases diffusion of the eddies of the inner row, if compared with those of the outer one. Obviously, in the results presented in Fig. 10, the latter mechanism is more efficient than the former.

Conclusions

As a wall is placed closer and closer to a cylinder, the following major effects have been observed:

– the vortex shedding frequency increases
– an asymmetric distribution of the mean velocity across the wake
– the position of the maximum velocity fluctuation is displaced from $x/D = 2.5$ to about or less than 1.5.

References

1 Landweber, L., "Flow About a Pair of Adjacent Parallel Cylinders Normal to a Stream," David Taylor Model Basin Report 485, 1942.

2 Bearman, P. W., and Zdravkovich, K. M., "Flow Around a Circular Cylinder Near a Plane Boundary," *Journal of Fluid Mechanics*, Vol. 89, Part 1, 1978, pp. 33-47.

3 Zdravkovich, K. M., "Review of Flow Interference Between two Circular Cylinders in Various Arrangements," ASME JOURNAL OF FLUIDS ENGINEERING, Vol. 99, No. 4, 1977 pp. 618-633.

4 Kiya, M., et al., "Vortex Shedding From Two Circular Cylinders in Staggered Arrangements," ASME JOURNAL OF FLUIDS ENGINEERING, Vol. 102, No. 2, 1980, pp. 166-173.

5 Buresti, G., and Lanciotti, A., "Vortex Shedding from Smooth and Roughened Cylinders in Cross-Flow near a Plane Surface," *The Aeronautical Quarterly*, Vol. 30, 1979, pp. 305-321.

6 Gerrard, J. H., "The Mechanisms of the Formation Region of Vortices Behind Bluff Bodies," *Journal of Fluid Mechanics*, Vol. 25, Part 2, 1966, pp. 401-413.

7 Sarpkaya, T., "Vortex-Induced Oscillations. A Selective Review," ASME *Journal of Applied Mechanics*, Vol. 46, 1979, pp. 241-258.

8 Schaefer, J. W., and Eskinazi, S., "An Analysis of the Vortex Street Generated in a Viscous Fluid," *Journal of Fluid Mechanics*, Vol. 6, Part 2, 1959, pp. 241-260.

9 Bloor, M. S., Gerrard, J. H., "Measurements on Turbulent Vortices in a Cylinder Wake," *Proceedings of the Royal Society*, London A., Vol. 294, 1966, pp. 319-342.

10 Bearman, P. W., "Investigation of the Flow Behind a Two Dimensional Model with a Blunt Trailing Edge and Fitted with Splitter Plates," *Journal of Fluid Mechanics*, Vol. 21, Part 2, 1965, pp. 241-255.

An Experimental Evaluation of Drag Coefficient for Rectangular Cylinders Exposed to Grid Turbulence

J. Courchesne
Graduate Student.

A. Laneville
Associate Professor.

Mechanical Engineering Department,
University of Sherbrooke,
Sherbrooke, Quebec, Canada

This paper describes an experimental evaluation of the effects of the intensity and scale of turbulence on the drag coefficient of two-dimensional rectangular cylinders exposed to grid turbulence. It is observed that the mean drag coefficient is principally influenced, for a given cylinder, by the intensity of turbulence and that the scale of turbulence plays a secondary role.

Introduction

Turbulence contained in the atmospheric boundary layer, influences the wind loads experienced by buildings and structures in two ways. As approaching the structure, turbulence induces unsteady buffeting loads and interacts in a complex fashion with the flow around the body which leads to changes in the mean and unsteady flow patterns. In order to estimate the magnitude of these effects, special wind tunnels are designed to produce thick boundary layers, but the resultant simulation is restricted as to the generated scale of turbulence and as to the Reynolds number. This paper reports an investigation of the relative importance of the turbulence characteristics and is concerned with two of the independant variables describing the neutral boundary layers: the intensity ($u'/\bar{U}$) and the macroscale (Lx) of turbulence. The effect of these two variables on the dependant variable, the mean (time average sense) drag coefficient, is examined for different geometries of two-dimensional rectangular cylinders.

Previous Investigations

Schubauer and Dryden [1] were the first to notice that turbulence increased the mean drag of horizontal flat plates. Vickery [2] measured a thirty percent reduction in the drag coefficient of a two-dimensional square cylinder exposed to turbulence superimposed on an otherwise smooth flow. Bearman [3] observed that the mean base pressure of normal square and circular plates in turbulent grid flow ($u'/\bar{U} = 0.083$ and $Lx/D = 0.375$) was considerably lower than that measured in smooth flow ($u'/\bar{U} = 0.002$). Bearman suggested that the principal reason for this was that, compared to smooth flow, there was extra entrainment of fluid out of the wake resulting from the mixing of the near wake with the free stream turbulence. In support of this argument, the base pressure coefficients were shown to correlate well with the turbulence parameter ($u'/\bar{U}$) (Lx^2/A). Laneville et al. [4], in the range $0.5 < Lx/D < 5$, observed no effect of the scale of turbulence on the mean drag coefficients (and on the galloping oscillations [5]) for two-dimensional rectangular cylinders at zero incidence with $H/D = 0.5$, 1 and 2. Nakamura et al. [6], in a wider range of longitudinal lengths ($0.1 < H/D < 3$), also observed no integral scale effects for a similar range of scale ratios. On the other hand, Nakamura et al. [6] and Laneville et al. [4] observed that the mean drag coefficient and the mean base pressure coefficient were largely influenced by the intensity of turbulence and the "afterbody length" H/D. Petty [7], using Lee's results [8] and Allen and Vincenti's blockage correction, confirmed these results. In more recent tests, Laneville and Williams [13] investigated the effect of large scale turbulence ($6 \leq Lx/D \leq 18$) on the base pressure coefficient of 2-D rectangular cylinders exposed to a fixed intensity of turbulence. With small models mounted in a large test section (blockage less than 1 percent), they concluded that the integral scale of turbulence did not measurably influence the base pressure coefficient and consequently the drag coefficient of the models. In view of the limited data available, an experimental program was set up to systematically investigate the effect of grid turbulence (with well defined $u'/\bar{U}$ and Lx) on the mean drag coefficient of two-dimensional rectangular cylinder.

Experimental Program

All the tests were conducted in a closed jet open circuit type (N.P.L.) wind tunnel with two ft (61 cm) octogonal test section. The turbulence intensity in the empty tunnel was measured as 0.6 percent.

The models for this investigation had D ranging from 1.25 in. (3.175 cm) to 2.5 in. (6.35 cm) and H/D from 0.3 to 3.0. The models were 18 in. (46 cm) long, with end plates, and located in the central core of the flow. Care was taken to machine sharp corners. Dummy spacers with the same cross section as the models were mounted between the wind tunnel walls and the end plates to insure the uniformity of the flow around the tested models. The clearance between the end plates and the dummy spacers was kept to the minimum. The

Contributed by the Fluids Engineering Division for publication in the JOURNAL OF FLUIDS ENGINEERING. Manuscript received by the Fluids Engineering Division, September 22, 1980.

diameter of the end plates was 3 times the model face D. The resulting additional drag was less than 0.005 of the total drag of the model.

The models were attached at their center downstream face to a circular tube. This tube was parallel to the flow and contained a small force balance. The drag force was measured using an Interface Mini Beam strain gauge load cell. The base pressure was measured on the centerline (2 in. away from absolute center) of the model's downstream face via a Tygon tube that was connected to a Barocell type 572D pressure transducer. The pressure readout was achieved with a Datametrics Electronic Manometer type 1018.

Turbulence was generated using biplanar square mesh grids installed at the wind tunnel test section entrance. Four grids were constructed allowing for a variation of the intensity of turbulence from 1.2 percent to 13 percent and a variation of the non-dimensional integral scale of turbulence, Lx/D, from 0.3 to 1.6. The model was located at a distance of over 30 bar sizes downstream of the grid. Table 1 gives a summary of the physical characteristics of the grids. All the turbulence properties were measured with hot wire anemometry (DISA D generation system with linearizer). The linearity was maintained within 1 percent and the precision on $u'/\bar{U}$ was 5 percent. The longitudinal scale of turbulence was determined via a real time spectral analysis (Spectral Dynamics Corps SD300A R.T.A.) of the linearized output.

In smooth flow, the Reynolds number (based on $\bar{U}$ and D) varied from $2 * 10^4$ to $1 * 10^5$ while in turbulent flow, the maximum for the Reynolds number was reduced to $7 * 10^4$. Since a Reynolds number effect was observed on the mean drag coefficient up to $4 * 10^4$, only the results with larger Reynolds numbers were considered in the present analysis. In the case of models with H/D in the vicinity of 0.6, the Reynolds number had to be larger than $6 * 10^4$. A similar effect was observed by Bearman and Trueman [9].

Blockage Correction Procedures

Previous work [10] in smooth flow has shown that Maskell's method [12] underestimates the corrected drag coefficient of models with $H/D > 1$. Moreover, because it includes the ratio of the mean base pressure coefficient to the mean drag coefficient, this method was inapplicable to models with $H/D > 2$. In reference [10], it was also shown that the drag correction coefficient for models with $H/D > 1$ was independent of H/D and that a simple empirical method gives accurate results for blockage ratios less than 13 percent. The equation used for correction was

$$C_{DC}/C_D = 1 - \zeta(AM/AS), \quad (1)$$

where ζ is the drag correction coefficient which was function of H/D for models with $H/D < 1$. In the absence of validated blockage correction procedures for turbulent flows, a method based on several observations was developed to take into account the blockage produced by the models. The first observations by [4 and 5] in turbulent flows indicate that a model with a given H/D exposed to an increased turbulence intensity behaves as a model with increased H/D in smooth flow. Correction procedure developed in smooth flow could be used if the equivalent H/D was known. The determination of the equivalent H/D is not required for models with $H/D > 1$ since ζ is not a function of H/D in this range [10]. Equation (1) can be used directly in this case with $\zeta = 1.19$. For models with $H/D < 1.0$ where ζ is a function of H/D, the procedure used to correct for data was the one suggested by Maskell [12] for smooth flow exposition. From [10], the overestimate of the correction by the method suggested by Maskell is not severe for blockage ratio less than 10 percent for models with $H/D < 1.0$. In view of the equivalent elongation of the models' afterbody by turbulence, this method was applied as long as the correction of the drag coefficient was less than the correction for the $H/D = 1$ model in smooth flow. When the correction on C_D by Maskell's method was larger than the one for square section models in smooth flow, equation (1) was used with $\zeta = 1.19$.

Table 1

Grid no.	b (in.)	M (in.)	Remarks
1	0.08	0.5	uniplanar (round bars)
2	0.25	1.25	biplanar (rectangular bars)
3	0.50	2.00	biplanar (rectangular bars)
4	0.75	4.00	biplanar (rectangular bars)

Results

In order to discuss the effect of turbulence on models subjected to blockage, care must be taken to validate the correction procedure when the correction itself is function of turbulence. The previous work by [4, 5 and 13] has indicated the secondary role of the turbulence integral scale and at the same time uncoupled the blockage effect from the scale effect. Thus it is admitted here that the intensity of turbulence is the essential variable affecting the blockage correction along with H/D. Figures 1 and 2 compare the blockage correction technique used for low and high levels of turbulence with the extrapolation of the data for several blockage ratios. Most of the predicted C_{DC} by the procedure are within 3 percent of the C_{DC} obtained by the extrapolation of the C_D. This comparison gave sufficient confidence in the procedure and in its application to all the data. Figure 3 shows the resulting drag curve for the H/D variable when the turbulence level was 11.2 percent.

Figure 4 shows the effect of the longitudinal scale of turbulence on the mean drag coefficient in the cases of the models with $H/D = 0.75$ and 1.0 exposed to grid turbulence with $I = 3.1$ and 7.5 percent. The lines enveloping the results are separated by a total deviation of 5 percent. Similar results were obtained for models with different H/D (0.5, 0.63, 0.75, 1.0, 1.5, and 3.0) and different levels of turbulence (0.006, 0.083, and 0.112). In the case of 2-D rectangular cylinders

Nomenclature

A = plate area
AM = model area
AS = wind tunnel test section cross-sectional area
b = grid bar size
C_D = measured mean drag coefficient = mean drag force/($q \times AM$)
C_{DC} = corrected mean drag coefficient
D = frontal dimension of the rectangular cylinder perpendicular to the flow direction
H = lateral dimension of the rectangular cylinder parallel to the flow direction
I = intensity of turbulence $= u'/\bar{U}$
Lx = longitudinal integral scale
M = grid mesh size
q = freestream dynamic pressure
u' = rms value of the longitudinal velocity component
$\bar{U}$ = mean value of the longitudinal velocity component

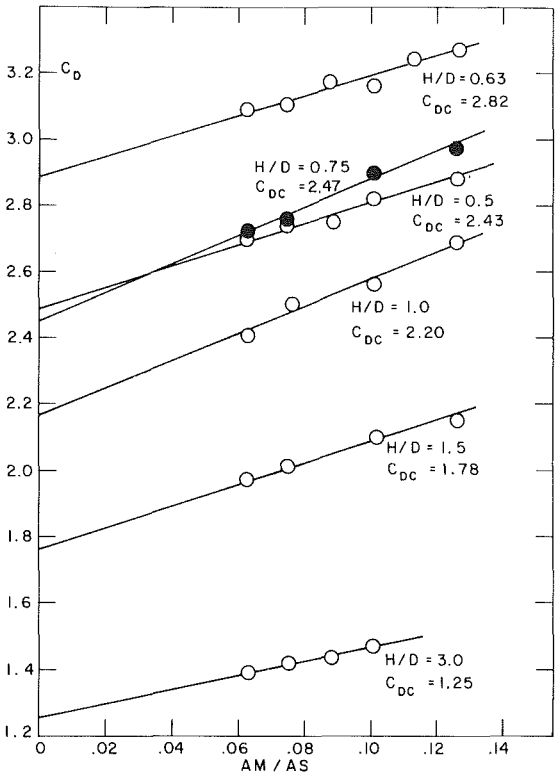

Fig. 1 Comparison of blockage correction technique with data extrapolation (I = 0.6 percent)

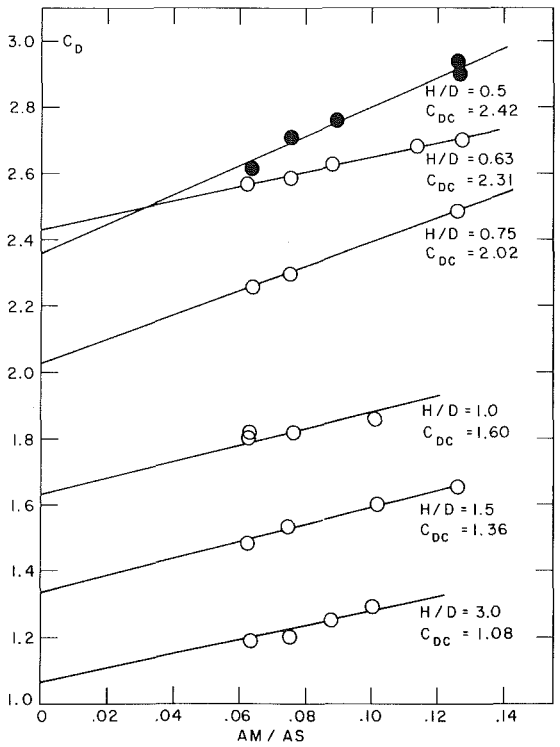

Fig. 2 Comparison of blockage correction technique with data extrapolation (I = 11.2 percent)

with $H/D > 0.31$, it confirms that the scale of turbulence ratio, Lx/D, plays a secondary role in the mean flow about rectangular cylinders. This was also observed by [4, 5 and 13]. Figures 5, 6, 7, and 8 summarize the effect of the intensity of turbulence on the C_{DC} for different H/D models. The lines

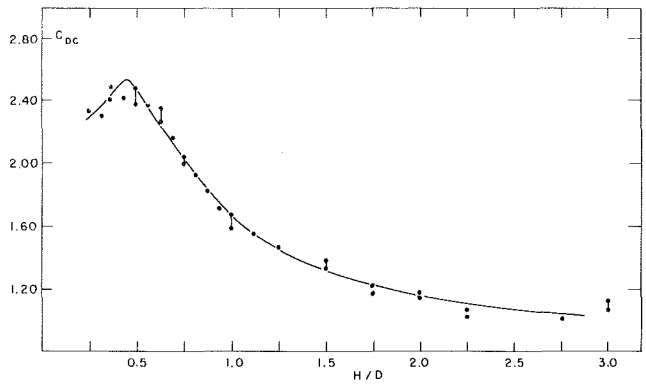

Fig. 3 Drag curve for I = 11.2 percent

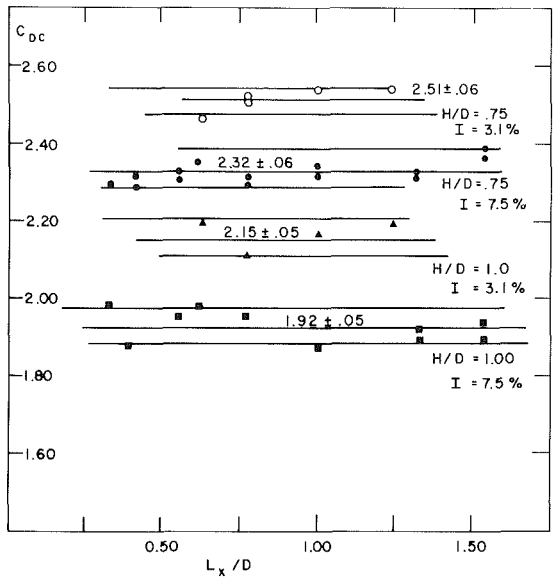

Fig. 4 Effect of the macroscale of turbulence on the drag coefficient for the models with H/D = 0.75 and 1.0 exposed to I = 3.1 and 7.5 percent

drawn on these figures are fitted lines through the data and represent the mean values of the corrected drag coefficient for cylinders with different afterbody length, H/D, as the intensity of turbulence is varied. Rectangular cylinders with H/D larger than 0.63 see their C_{DC} reduced as the turbulence level is increased. In smooth flow, the maximum C_{DC} of 2.90 occurs for the cylinder with $H/D = 0.63$, which agrees with [9, 10, 6]. In grid turbulence, models with $0.5 < H/D < 0.63$ see their drag coefficient reach the smooth flow maximum C_{DC} and decrease as the level of turbulence is increased. Models with $0.3 < H/D < 0.5$ show a similar trend but the peak is much less pronounced and the smooth flow maximum C_{DC} is not reached.

Figure 9 gives a summary of all the results and includes the results obtained by Nakamura and Tomonari [6]. Again here the effect of turbulence intensity is clearly to shift the C_{DC} versus H/D curve to the left and to reduce the maximum C_{DC} progressively as the level of turbulence is increased. Nakamura and Tomonari results are not corrected for blockage effects that were small in their test. The agreement as seen is good.

Discussion

As indicated by Figs. 5 to 9, and 9 principally, the behavior of the mean flow around rectangular bluff bodies is a strong function of the afterbody length H/D and the level of tur-

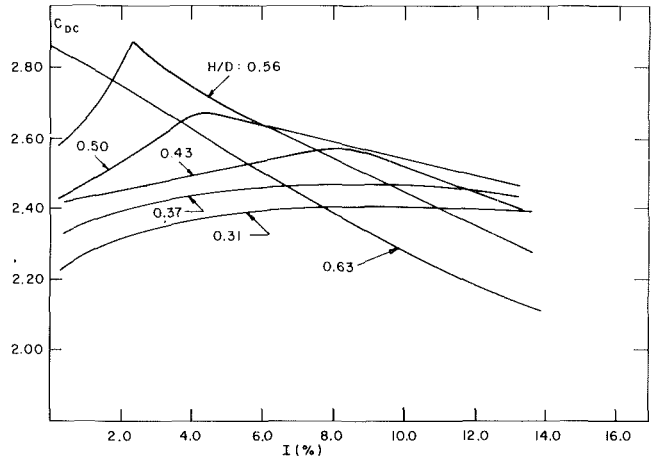

Fig. 5 Effect of the intensity of turbulence on the drag coefficient

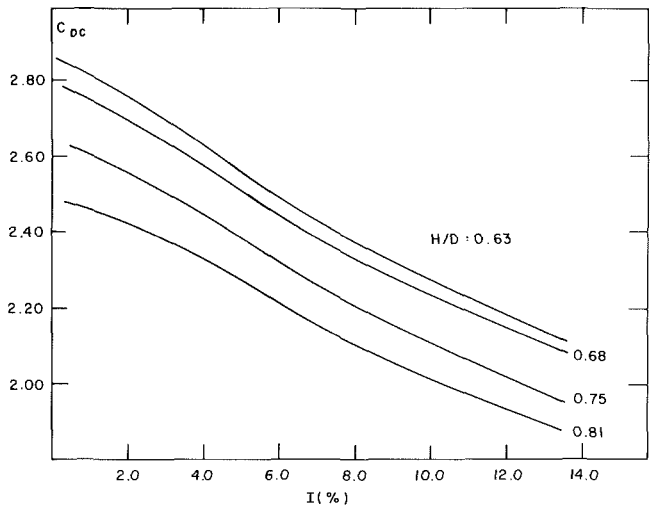

Fig. 6 Effect of the intensity of turbulence on the drag coefficient

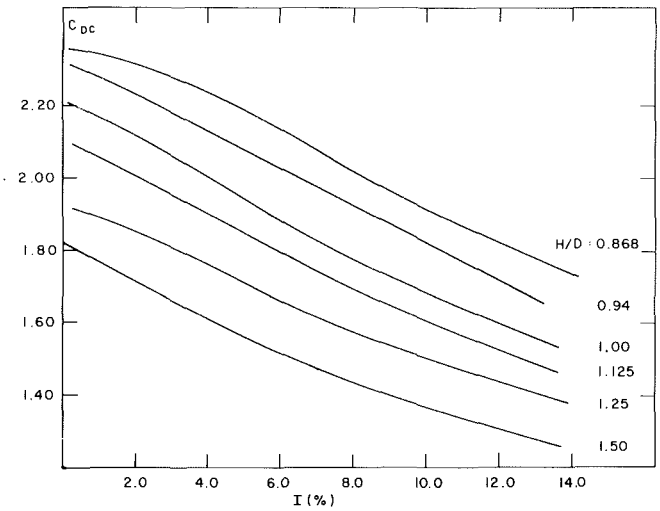

Fig. 7 Effect of the intensity of turbulence on the drag coefficient

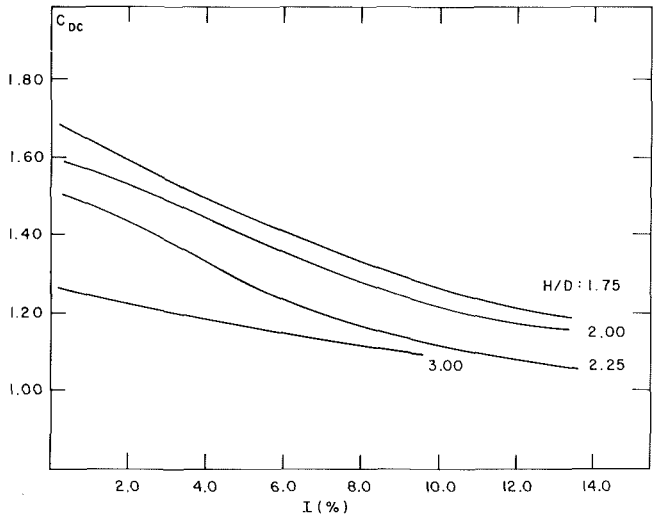

Fig. 8 Effect of the intensity of turbulence on the drag coefficient

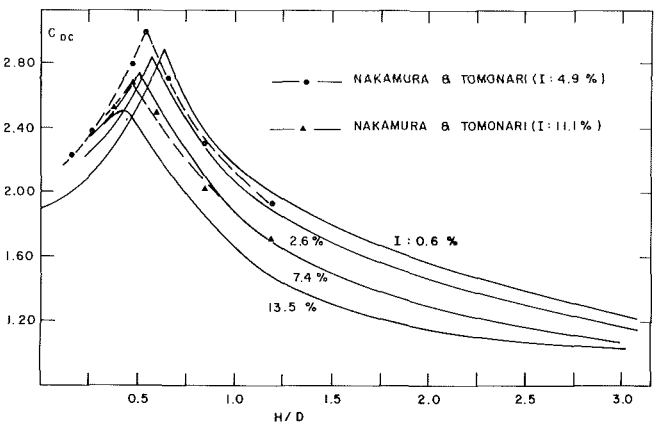

Fig. 9 Effect of the afterbody length (H/D) on the drag coefficient for different levels of turbulence

turbulence. In smooth flow with very low levels of turbulence, Nakaguchi et al. [11], as well as Bearman and Trueman [9], did a flow visualization and found a correlation between the curvature of the shear layer and the drag coefficient to explain the peak drag at $H/D \simeq 0.6$. High curvature implied high drag coefficient. Bearman and Trueman argued that for small values of H/D, the effect of the body downstream of separation is to reduce the size of the separated wake cavity, thus leading to an increase in drag. They also suggested that in the case of $H/D > 0.6$, the vortices are forced to form further downstream because of the influence of the trailing edge corners, thus occasioning a reduction in drag. It is not clear if the vortices are forced to form further downstream in the flow direction or in the lateral direction. Pressure distributions in the base region for the $H/D = 0.6$ cylinder indicate a peak negative pressure in the model center [9]. The location of this peak suction would indicate rather a lateral displacement of the locus of formation of the vortices and this would also explain the high curvature of the streamlines when the vortex forms in the base area.

A complex equilibrium must prevail between the vorticity shed form the cylinder, the distance to vortex formation and the base pressure (or drag). In turbulent flow, this complex equilibrium is measurably influenced by the level of turbulence, as indicated by the present results. It was suggested that the distortion of turbulence by the mean flow field of the bluff body and the subsequent modification (or increased mixing) in the shear layer structure by this distorted turbulence could be a plausible explanation of the effects observed here. With this increased mixing, the complex equilibrium is modified and the reattachment of the shear layer occurs at an earlier angle of incidence than in smooth flow [4].

Conclusion

The purpose of the present investigation was to systematically define the effect of turbulence on the drag. The results offer a semi-consistent behavior. Cylinders with $H/D > 0.5$ follow a regular influence with turbulence, that is, an increased in the level of turbulence seems to move the smooth flow C_{DC} of a given H/D section to the C_{DC} of an equivalent increased H/D section. Cylinders with $H/D < 0.5$ do not reach the maximum C_{DC} of 2.9 as the level of turbulence is increased. It also suggests that the vortices strength as well as their formation and the afterbody length H/D remain predominant variables in turbulent flow with the additional turbulence intensity. The complex equilibrium in the near wake is a concept that has to be more investigated and how perturbations, as turbulence contained in main stream, play a role in this equilibrium remains to be investigated more fully.

Acknowledgment

This research was supported by an N.R.C. Scholarship given to the junior author and by N.R.C. Grant No. 002-588-0 given to the senior author. The authors wish to thank D. Lambert, R. Joubert and Mrs. P. Jutras for their collaboration in this research.

References

1 Schubauer, G. B., and Dryden, H. L., NACA Rep. no. 546, 1935.

2 Vickery, B. J., "Fluctuating Lift and Drag on a Long Cylinder of Square Cross Section in a Smooth and in a Turbulent Stream," *Journal of Fluid Mechanics*, Vol. 25, Part 3, 1966, pp. 481-494.

3 Bearman, P. W., "An Investigation of the Forces on Flat Plates Normal to a Turbulent Flow," *Journal of Fluid Mechanics*, Vol. 46, Part 1, 1971, pp. 117-198.

4 Laneville, A., Gartshore, I. S., and Parkinson, G. V., "An Explanation of Some Effects of Turbulence on Bluff Bodies," *Proceedings of the 4th Int. Conf. on Wind Effects on Buildings and Structures*, Heathrow, London, U.K. 1975, pp. 333-342.

5 Laneville, A., and Parkinson, G. V., "Effects of Turbulence on Galloping of Bluff Cylinders," *Proceedings of the 3rd Int. Conf. on Wind Effects on Buildings and Structures*, Tokyo,, 1971, pp. 787-797.

6 Nakamura, Y., and Tomonari, Y., "The Effect of Turbulence on the Drag of Rectangular Prisms," *J. Japan Soc. Aeronaut. Space Sci.*, Vol. 19, No. 44, June 1976, pp. 81-86.

7 Petty, D. G., "The Effect of Turbulence Intensity and Scale on the Flow Past Square Prisms," *Proceedings of the 3rd Colloquium on Industrial Aerodynamics*, Part 2, Aachen, Germany, June 1978, p. 287.

8 Lee, B. E., "Some Effects of Turbulence Scale on the Mean Forces on Bluff Bodies," *Journal of Industrial Aerodynamics*, Vol. 1, 1975/1976, pp. 361-370.

9 Bearman, P. W., and Trueman, D. M., "An Investigation of the Flow Around Rectangular Cylinders," *Aeronaut. Q.*, Vol. XXIII, Part 3, 1972, pp. 229-237.

10 Courchesne, J., and Laneville, A., "A Comparison of Correction Methods Used in the Evaluation of Drag Coefficient Measurements for Two-Dimensional Rectangular Cylinders," ASME JOURNAL OF FLUIDS ENGINEERING, Vol. 101, Dec. 1979, pp. 506-511.

11 Nakaguchi, H., Hashimoto, K., and Muto, S., "An Experimental Study on Aerodynamic Drag of Rectangular Cylinders," *J. Japan Soc. Aeronaut. Space Sci.*, Vol. 16, 1968, pp. 1-5.

12 Maskell, E. C., "A Theory of the Blockage Effects on Bluff Bodies and Stalled Wings in a Closed Wind Tunnel," R.A.E. Aero-Rep. 2685, No. 1965.

13 Laneville, A., and Williams, C. D., "The Effect of Intensity and Large Scale Turbulence on the Mean Pressure and Drag Coefficients of 2-D Rectangular Cylinders," *Proceedings of the 5th Int. Conf. on Wind Engineering*, Fort Collins, Colo., 1979.

Conclusion

The purpose of the present investigation was to systematically define the effect of turbulence on the drag. The results offer a semi-consistent behavior. Cylinders with $H/D > 0.5$ follow a regular influence with turbulence, that is, an increased in the level of turbulence seems to move the smooth flow C_{DC} of a given H/D section to the C_{DC} of an equivalent increased H/D section. Cylinders with $H/D < 0.5$ do not reach the maximum C_{DC} of 2.9 as the level of turbulence is increased. It also suggests that the vortices strength as well as their formation and the afterbody length H/D remain predominant variables in turbulent flow with the additional turbulence intensity. The complex equilibrium in the near wake is a concept that has to be more investigated and how perturbations, as turbulence contained in main stream, play a role in this equilibrium remains to be investigated more fully.

Acknowledgment

This research was supported by an N.R.C. Scholarship given to the junior author and by N.R.C. Grant No. 002-588-0 given to the senior author. The authors wish to thank D. Lambert, R. Joubert and Mrs. P. Jutras for their collaboration in this research.

References

1 Schubauer, G. B., and Dryden, H. L., NACA Rep. no. 546, 1935.

2 Vickery, B. J., "Fluctuating Lift and Drag on a Long Cylinder of Square Cross Section in a Smooth and in a Turbulent Stream," *Journal of Fluid Mechanics*, Vol. 25, Part 3, 1966, pp. 481-494.

3 Bearman, P. W., "An Investigation of the Forces on Flat Plates Normal to a Turbulent Flow," *Journal of Fluid Mechanics*, Vol. 46, Part 1, 1971, pp. 117-198.

4 Laneville, A., Gartshore, I. S., and Parkinson, G. V., "An Explanation of Some Effects of Turbulence on Bluff Bodies," *Proceedings of the 4th Int. Conf. on Wind Effects on Buildings and Structures*, Heathrow, London, U.K. 1975, pp. 333-342.

5 Laneville, A., and Parkinson, G. V., "Effects of Turbulence on Galloping of Bluff Cylinders," *Proceedings of the 3rd Int. Conf. on Wind Effects on Buildings and Structures*, Tokyo,, 1971, pp. 787-797.

6 Nakamura, Y., and Tomonari, Y., "The Effect of Turbulence on the Drag of Rectangular Prisms," *J. Japan Soc. Aeronaut. Space Sci.*, Vol. 19, No. 44, June 1976, pp. 81-86.

7 Petty, D. G., "The Effect of Turbulence Intensity and Scale on the Flow Past Square Prisms," *Proceedings of the 3rd Colloquium on Industrial Aerodynamics*, Part 2, Aachen, Germany, June 1978, p. 287.

8 Lee, B. E., "Some Effects of Turbulence Scale on the Mean Forces on Bluff Bodies," *Journal of Industrial Aerodynamics*, Vol. 1, 1975/1976, pp. 361-370.

9 Bearman, P. W., and Trueman, D. M., "An Investigation of the Flow Around Rectangular Cylinders," *Aeronaut. Q.*, Vol. XXIII, Part 3, 1972, pp. 229-237.

10 Courchesne, J., and Laneville, A., "A Comparison of Correction Methods Used in the Evaluation of Drag Coefficient Measurements for Two-Dimensional Rectangular Cylinders," ASME JOURNAL OF FLUIDS ENGINEERING, Vol. 101, Dec. 1979, pp. 506-511.

11 Nakaguchi, H., Hashimoto, K., and Muto, S., "An Experimental Study on Aerodynamic Drag of Rectangular Cylinders," *J. Japan Soc. Aeronaut. Space Sci.*, Vol. 16, 1968, pp. 1-5.

12 Maskell, E. C., "A Theory of the Blockage Effects on Bluff Bodies and Stalled Wings in a Closed Wind Tunnel," R.A.E. Aero-Rep. 2685, No. 1965.

13 Laneville, A., and Williams, C. D., "The Effect of Intensity and Large Scale Turbulence on the Mean Pressure and Drag Coefficients of 2-D Rectangular Cylinders," *Proceedings of the 5th Int. Conf. on Wind Engineering*, Fort Collins, Colo., 1979.

DISCUSSION

B. E. Lee[1]

The authors of this paper are to be encouraged in their efforts to shed more light on the unknown influences which effect the modelling criteria used in the investigation of building aerodynamics problems. Generally such investigations as this embody a complex problem where the investigators may attempt to quantify the effects of incident flow turbulence intensity on the forces acting on a bluff body, where the ratio of integral turbulence scale to body size is an additional variable, whilst simultaneously making proper allowances for blockage ratio effects, end effects and aspect ratio effects. The kind of difficulties the authors face are illustrated by their use of circular end plates which have presumably been used to nullify end effects but whose effectiveness in dealing with bluff bodies of this shape may be in doubt, [14, 15].

One potential source of error in an investigation of this type is in the existence of lateral non-uniformities in a supposedly two dimensional central core region. Although the authors do not give complete information in their paper regarding which grids produce which turbulence characteristics at which grid to model streamwise separation distances some reason to suspect the presence of non-uniformities exists. With the use of the larger models Grid 4, which presumably produces the hightest turbulence levels, is only 5.6 mesh lengths upstream of the model and Grid 3 only 7.5 mesh lengths upstream. Earlier work by this reviewer [16] has shown that at these distances lateral nonuniformities of the mean velocity and turbulence characteristics of the flow will occur behind such grids. Indeed one could go further and say that it is not at all possible to use square mesh grids to simulate the turbulence characteristics appropriate to large buildings in the lower part of the earths boundary layer without the introduction of such lateral nonuniformities into the flow. The aspect ratios of the bodies used in the current tests may also cause axial nonuniformities to occur in the force distributions along the body. The aspect ratios used in the present tests are as low as 9.6 for frontal ratio and for the case of $H/D = 3.0$, only 3.2 for side aspect ratio. Values as low as these may well be beyond the ability of end plates to simulate two-dimensional flow over a central region of the body.

Finally it may be worthwhile to reconsider some of the questions posed when many of the results given in this paper were first presented, [13]. Since the use of a turbulence intensity term is a global way of referring to the energy contained within the turbulence spectrum over a wide range of frequencies, and hence eddy sizes, it may be considered whether or not there is some way in which the part of this spectrum effective in inducing the observed changes in mean drag could be isolated from the whole. One may suspect that in order to do this a more detailed picture of the incident flow – shear layer interaction process will be necessary and that possibly another form of "scale" effect may emerge from such studies.

Additional References

14 Obasaju, E. D., "On the Effect of End Plates on the Mean Forces on Square Sectioned Cylinders," *Jnl. Ind. Aero.*, Vol. 5, 1979, pp. 179-186.

15 Lee, B. E., Discussion "On the Effect of End Plates on the Mean Forces on Square Sectioned Cylinders," *Jnl. Ind. Aero*, Vol. 5, 1979, pp. 187-188.

16 Lee, B. E., "The Susceptibility of Tests on Two Dimensional Bluff Bodies to Incident Flow Variations, *Jnl. Ind. Aero.*, Vol. 2, 1977, pp. 133-148.

Authors' Closure

The authors thank Dr. B. E. Lee for his words of encouragement and his interest for this work. We will try to answer the questions relative to the experimental set up and then discuss the question of integral scales.

[1] Lecturer, Department of Building Science, University of Sheffield, Sheffield, S10 2TN, England.

In the choice of the endplates dimensions, care was taken to insure that the boundary layer they generate upstream of the models was as small as possible. Also, in the wake region downstream of the model, the endplate had to be long enough to prevent any communication of this region with one a different pressure. Obasaju, E. D. and Lee, B. E. discussed earlier the effectiveness of these plates to nullify end effects. In the tests reported here, the use of dummy spacers with the models' section installed between the tunnel floor and ceiling and the "live" portion of the model, ensured the correct base pressure and wake simulation. The fact that the measured base pressure and drag coefficients compared well in the smooth flow cases with data obtained by Nakaguchi et al and Bearman and Trueman, where end effects and aspect ratios were presumably insignificant, removed any major doubt concerning the experimental set up. The turbulence characteristics although not reported in detail, were measured and the data indicated that for all the models' locations, the profiles of the mean velocity and the longitudinal turbulence intensity were uniform within ± 1.5 percent except in the wall boundary layer. The models were indeed located at a distance generally larger than 7.5 mesh length.

The authors agree with Dr. Lee's comment on the simulation of the earth's boundary layer. Square mesh grids were used to produce a quasi-isotropic turbulence superimposed on an otherwise uniform flow, a flow certainly different from a boundary layer flow. The purpose of this research being to conclude on the relative importance of the turbulence intensity and macroscale, grid flow was appropriate to simulate 2-D flow.

With respect to the integral scale, Laneville, A. and Williams, C. D. have shown that the longitudinal integral scale of turbulence was not as significant a variable as the intensity of turbulence (in the range $L_x/d<20$) for the mean base pressure and drag coefficients of 2-D rectangular cylinders. Melbourne, W. H. [17] reached the same conclusion and suggested that the length scale should be associated to a wavelength smaller than the typical frontal body dimension. Earlier, Gartshore, I. S. [18] has attempted to isolate the part of the spectrum that induces the observed changes in mean drag, concluded that the small perturbations on the stagnation line were responsible for most of the changes in the mean properties. There is a clear need for more research in the determination of the interaction between the shear layer, the external turbulence, the cylinder afterbody length and the vortex formation, interaction regulated by a certain equilibrium.

NOTE: Corresponding Author: Andre Laneville, Dept. of Mechanical Engineering University of Sherbrooke (Quebec) CANADA J1K 2R1

Additional References

17 Melbourne, W. H., "Turbulence Effects on Maximum Surface Pressures – A Mechanism and Possibility of Reduction," *Proc. of the Fifth Int. Conf. on Wind Engineering*, Fort Collins, 1979, Pergamon Press.

18 Gartshore, I. S., "The Effects of Free Stream Turbulence on the Drag of Rectangular Two-Dimensional Prisms," Research Report BLWT-4-73, University of Western Ontario, London, Canada.

ERRATA

"Flow Aerodynamic Modeling of an MHD Swirl Combustor: Calculation and Experimental Verification," by A. K. Gupta, J. M. Beer, J. F. Louis, A. A. Busnaina, and D. G. Lilley, **Journal of Fluids Engineering**, September, 1982, pp. 385–392.

Figs. 11(*a*) and 11(*b*) were incorrectly printed in the above paper. The correct figures appear below.

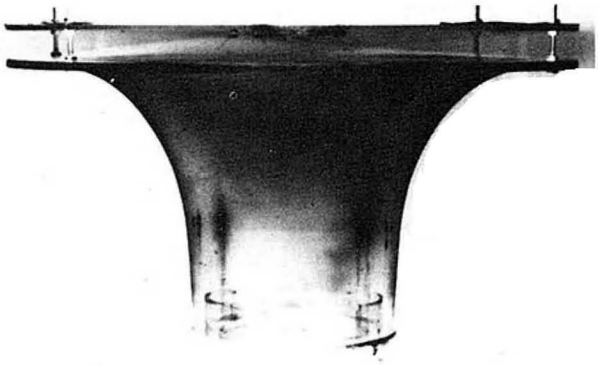

Fig. 11(a) Dissipation of colored dye injected centrally at entrance to the second stage with flow through tangential and axial inlets in the first state and all inlets in the second stage at S = 1.83.

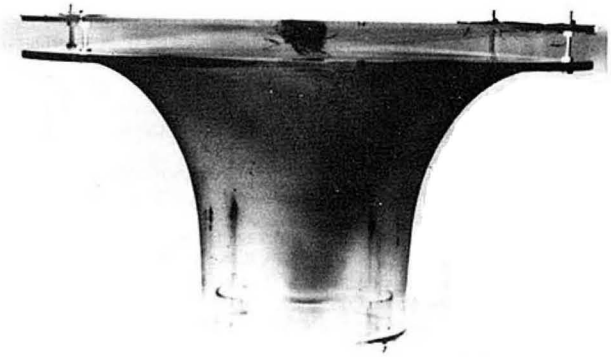

Fig. 11(b) Dissipation of colored dye injected centrally at entrance to the second state with flow through tangential inlet in the first stage and all inlets in the second stage at S = 1.83.

S. Taniguchi
Associate Professor,
Department of Applied Mechanical Engineering.

H. Sakamoto
Professor,
Department of Mechanical Engineering.

Kitami Institute of Technology,
Kitami 090, Japan

M. Arie
President,
Hokkaido University,
Sapporo 060, Japan

Interference Between Two Circular Cylinders of Finite Height Vertically Immersed in a Turbulent Boundary Layer

Measurements were made of the circumferential pressure distributions around two cylinders of finite height h and diameter d, spaced a distance s apart and vertically immersed in a turbulent boundary layer. The angle of attack ϕ and the dimensionless spacing s/d were varied. Drag and lift characteristics of both cylinders were classified into three regions divided by two zero-lift lines, namely $0 \lesssim \phi \lesssim 30$ deg, $30 \lesssim \phi \lesssim 120$ deg, and $120 \lesssim \phi \lesssim 180$ deg, in which interference between the two cylinders was found to be almost negligible for $s/d \gtrsim 4.0$, except for an influence in the wake region of the upstream cylinder.

Introduction

Interference takes place between adjacent structural members subjected to fluid flow. It generally induces drag and lift forces, parallel to and normal to an oncoming flow, which vary considerably in magnitude with the relative position of the members. This fluid dynamic interaction presents an important engineering problem relevant to the design of chimney stacks, offshore structures, tubes of heat exchangers, open towers and other structures standing side by side. A number of researchers [1-9] have thoroughly investigated the fluid forces and wake formations resulting from interference between two circular cylinders of infinite height in uniform flow and recently Zdravkovich [10] reviewed and categorized their experimental results.

It is expected that the interference between a pair of circular cylinders of finite height vertically placed on a plane wall is substantially different from that of two infinite cylinders because of the effects of shear flow, tip flow and presence of a plane wall. Zdravkovich [11] reported on the aerodynamics of two circular cylinders of finite height, but his data cover only a small range of angles of attack and spacings, thus calling for further efforts to look into aerodynamic forces for varied spacings and angles of attack.

The present paper describes an experiment and classifies aerodynamic forces computed from the time-averaged circumferential pressure distributions around two cylinders of finite height placed vertically on a smooth plane floor, on which a turbulent boundary layer was fully developed under zero pressure gradient. The cylinder spacing and the angle of attack were successively changed. Two cylinders of finite height were chosen because they were considered as representing a typical arrangement of offshore structures, smokestacks, or cooling towers on the ground. The paper also incorporates the observations on the flow patterns around the two cylinders by the smoke wire technique.

Contributed by the Fluids Engineering Division for publication in the JOURNAL OF FLUIDS ENGINEERING. Manuscript received by the Fluids Engineering Division, February 25, 1981.

Experimental Apparatus

Wind Tunnel. The pressure distributions on the cylinder surface were measured in a test section 0.4m (width), 0.4m (height), and about 4m (length) of a closed circuit wind tunnel. The ceiling of the test section was made of a flexible sheet of steel, in which were drilled 18 pressure taps of 0.5mm diameter, so that a given longitudinal pressure gradient was obtained by adjusting its shape. The floor of the test section was made of smooth acrylic resin plate, excepting a part

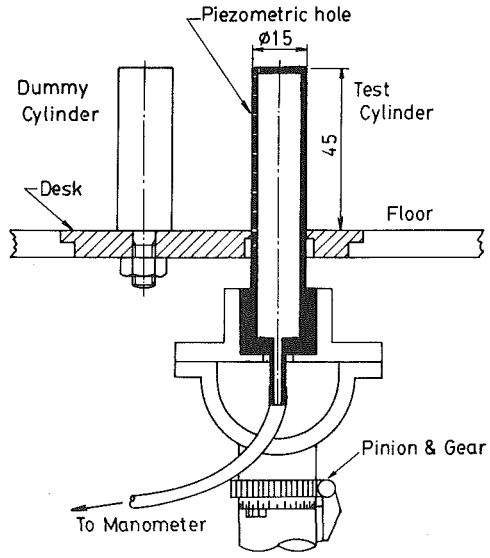

Fig. 1 Cross section of two circular cylinders of finite height

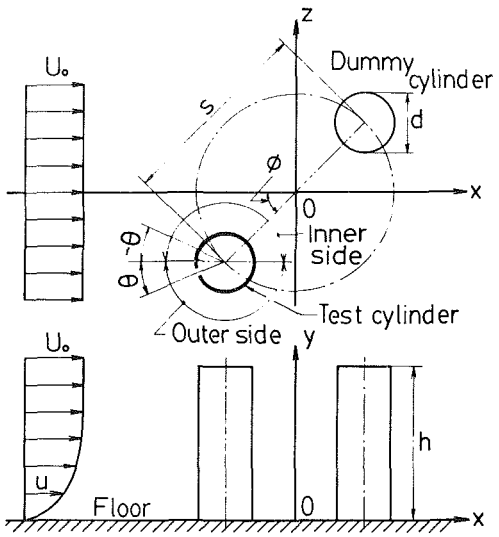

Fig. 2 Definition sketch and coordinate system of two cylinders

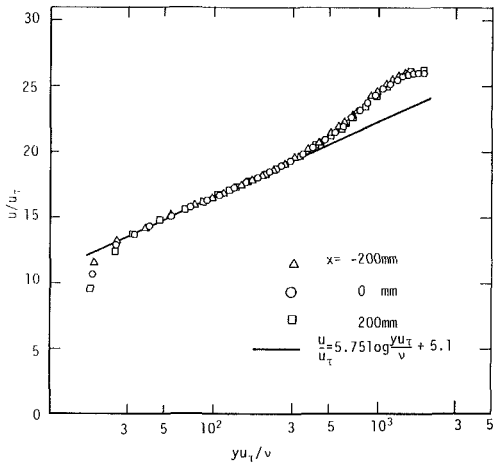

Fig. 3 Wall law plot of the mean velocity profiles in the boundary layer. ——Coles [12]. The uncertainty in u/u_τ is ±0.1 and that in yu_τ/δ is ±30 at most.

covered with a steel plate 460mm long and 400mm wide. The two circular cylinders of identical size and finite height were installed on the steel plate. The two cylinders were located at a position 2.255m downstream from the entrance of the test section, where the mean velocity was uniform to the accuracy of 99.8 percent, except the boundary layers along the walls. The free-stream turbulence level measured at this position by a constant-temperature hotwire anemometer was about 0.3 percent at the velocity 16m/s, which was the velocity employed in the present experiment. In addition, a wind channel was used to visualize the flow by means of the smoke wire technique. The channel was a through-flow type with a test section of 0.18m (width), 0.18m (height), and 1.6m (length).

Visualization Equipment. The smoke wire consisted of a discharge circuit which produced a current pulse, a retarder which received the pulse and arbitrarily delayed it so as to send the pulse as a signal to a stroboscope illuminating the smoke produced by a wire element, and a camera. The wire element of 0.12mm diameter was set up in a probe. Smoke was emitted by a mixture of liquid paraffin, kerosene, and silicon oil.

Two Cylinders of Finite Height. Two smoothly-machined brass cylinders of diameter $d=15$mm and height $h=45$mm were installed on a turn table, as seen in Fig. 1. One of them was used as a test cylinder to measure pressure on its surface

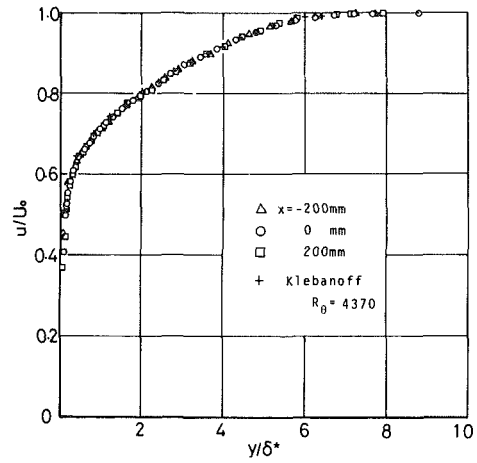

Fig. 4 Mean velocity profile in the boundary layer. + Klebanoff and Diehl [13]. The uncertainty in u/U_0 is ±0.01 and that in y/δ^* is ±0.02.

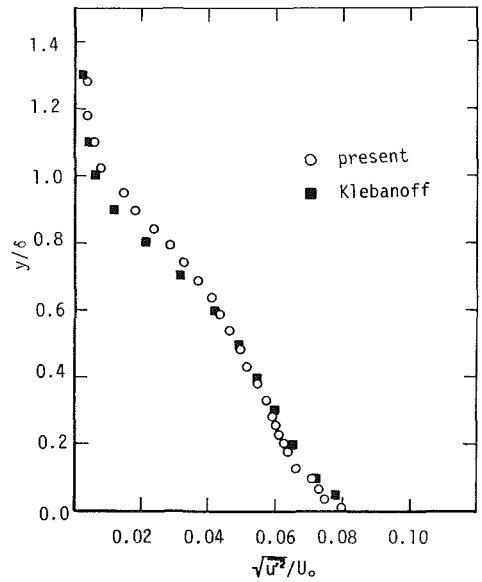

Fig. 5 Distribution of the longitudinal turbulent intensities. ■ Klebanoff and Diehl [13], ○ present experiment. The uncertainty in $\sqrt{\overline{u'^2}}/U_0$ is ±0.01 and that in y/δ is ±0.02.

Table 1 Angles of attack and spacings of two cylinders

Angle of attack ϕ deg.	0, 15, 30, 45, 60, 75, 90, 105,120,135,150,165,170,175,180
Spacing s/d	1.2,1.35,1.50,1.75,2.0,3.0,4.0

Table 2 Characteristics of the turbulent boundary layer used in this experiment

Velocity of the free stream	U_o m/s	16
Thickness of the boundary layer	δ mm	39.0
Displacement thickness	δ^* mm	6.26
Momentum thickness	θ mm	4.53
Reynolds number	$R_\theta=U_o\theta/\nu$	4286
Nondimensional shear velocity	u_τ/U_o	0.0384
Shear velocity	u_τ m/s	0.614
Shape factor	$H=\delta^*/\theta$	1.38

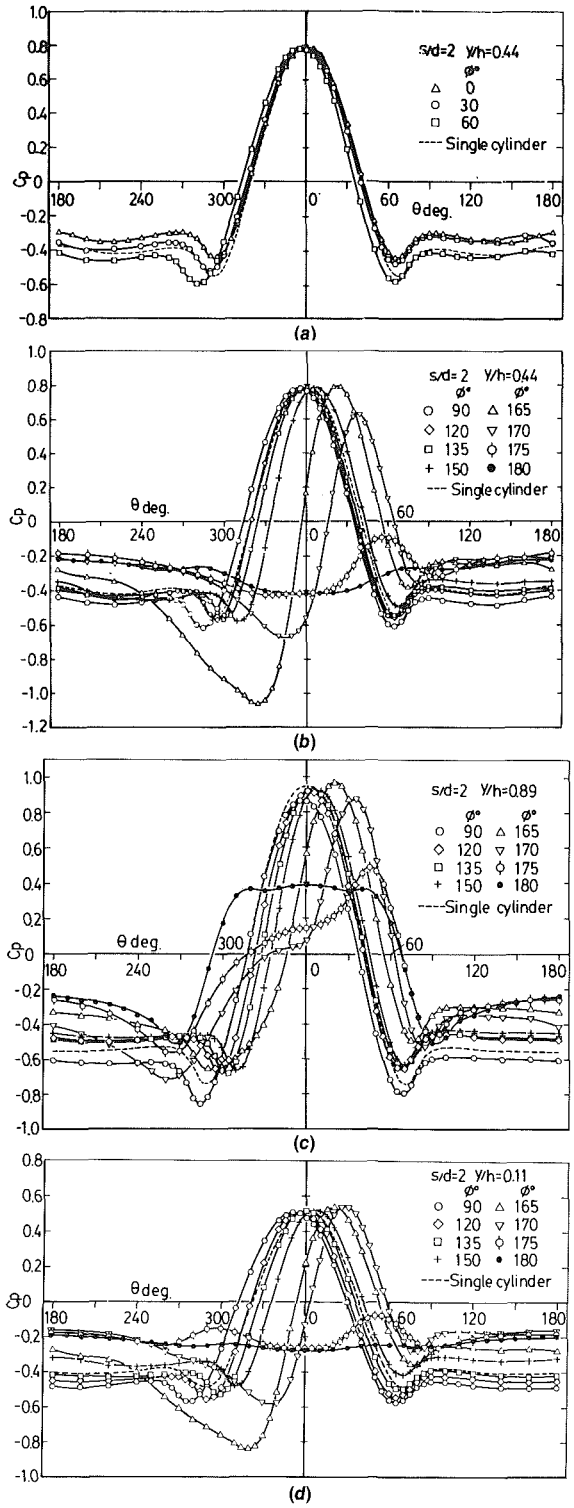

Fig. 6(*a*) $y/h = 0.44$, 0 deg $\lesssim\phi\lesssim$60 deg, Fig. 6(*b*) $y/h = 0.44$, 90 deg $\lesssim\phi\lesssim$180 deg, Fig. 6(*c*) $y/h = 0.89$, 90 deg $\lesssim\phi\lesssim$180 deg, Fig. 6(*d*) $y/h = 0.11$, 90 deg $\lesssim\phi\lesssim$180 deg.

Fig. 6 Pressure distributions on the cylinder surface. The uncertainty in c_p is ± 0.02 and that in θ ± 0.5 deg.

and the other was a dummy. Ten piezometric holes 0.4 ~ 0.5mm in diameter were drilled into the surface of the test cylinder equidistant along one spanwise axis except the top part of the cylinder. The pressure was read on a Betz manometer (with an accuracy 0.05mmAq). The cylinders were vertically mounted a distance s apart on a steel turn table 100mm in diameter, which was placed flush with the floor of the wind tunnel. Rotation of the table allowed the angle of

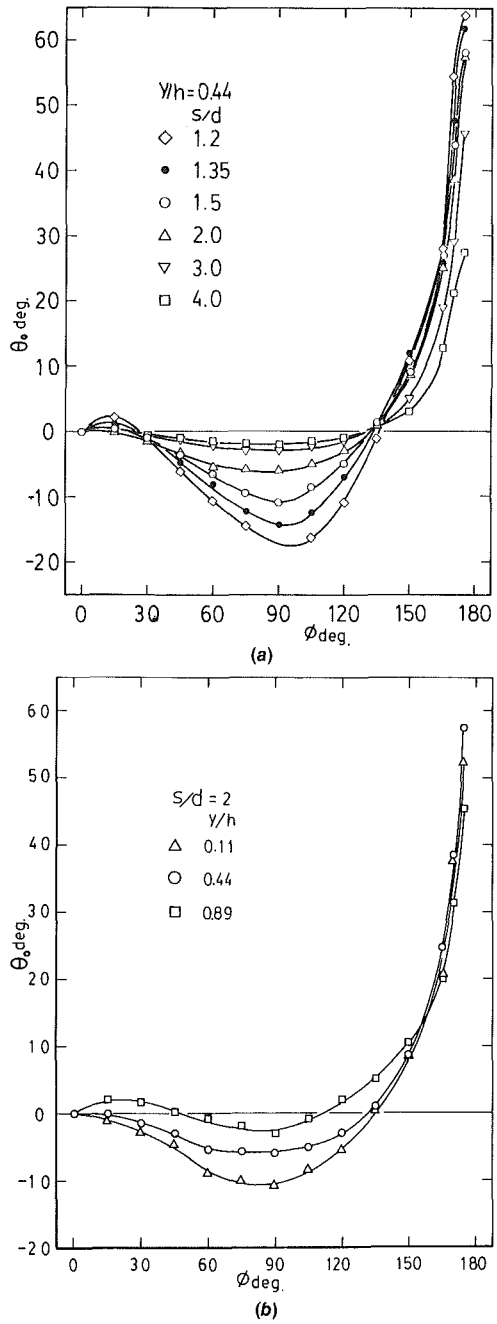

Fig. 7(*a*) Comparison among several spacings at $y/h = 0.44$, Fig. 7(*b*) Comparison among three different heights of the cylinder, $y/h = 0.11$, 0.44 and 0.89.

Fig. 7 Relation between location of the maximum pressure and angle of attack. The uncertainty on θ_0 is ± 0.5 deg and that in ϕ is ± 0.5 deg.

attack ϕ to be changed from 0 to 180 deg in intervals of 5 or 15 deg, the uncertainty in ϕ being 0.5 deg at most. The spacing between the two cylinders was varied between 1.2 and 4.0 diameters. Table 1 shows the variations of the angle of attack and the spacing between the two cylinders employed in the pressure experiment. The uncertainty in the distance s was determined to be 0.2mm by direct measurements using a micrometer. The test cylinder was able to rotate about its axis by the equipment under the floor of the tunnel, as shown in Fig. 1, in which the range $0 \lesssim\theta\lesssim 180$ deg represents the outer side of the cylinder and the range $180 \lesssim\theta\lesssim 360$ deg (or $0 \gtrsim\theta\gtrsim -180$ deg) the inner side (see Fig. 2), the uncertainty in θ also being 0.5 deg.

Figure 2 shows a definition sketch of the two cylinders in a turbulent boundary layer.

Characteristics of the Boundary Layer

The present experiment adopted the turbulent boundary layer which fully developed along the smooth floor under zero pressure gradient because such a boundary layer shear flow has been well investigated. The mean velocity distribution near the floor satisfied the logarithmic law suggested by Coles [12], as shown in Fig. 3. It was also confirmed that the mean velocity profile and distribution of longitudinal turbulent intensity in the boundary layer followed Klebanoff's data [13], as shown in Figs. 4 and 5, respectively. An examination by Pitot-tube traverses in the z direction showed that the boundary layer realized a satisfactory two-dimensionality at the location of the two cylinders in the region 100mm wide on each side of the center line of the test section. Accordingly, it is concluded that the turbulent boundary layer employed in the present investigation has the same characteristics as the fully developed equilibrium turbulent boundary layer. The Reynolds number Re based on the velocity U_0 and the diameter of the cylinder d was 1.55×10^4. The characteristics of the undisturbed turbulent boundary layer at the location of the two cylinders are summarized in Table 2. The ratio of the cylinder height to the boundary layer thickness was 1.15, so the top of the cylinder protruded slightly above the boundary layer. This configuration of the two cylinders and the boundary layer could serve as a model of extremely tall structures such as smoke stacks, cooling towers and other offshore structures. Accodingly, the results of this study will be applicable qualitatively to such structures, although not quantitatively to full scale models because there are great differences between this experimental situation and a full scale one.

Further, the flow around the two cylinders was visualized by the smoke wire technique at a fixed free-stream velocity $U_0 = 0.7$m/s in the wind channel. This observation showed that the boundary layer was laminar and its thickness was about 18mm at the location of the two cylinders.

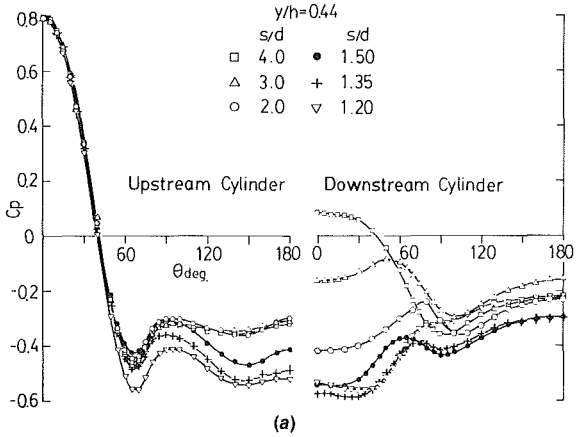

Pressure Distribution

Pressure Distribution as a Function of Angle of Attack. Pressure distributions on the cylinder surface are given in Figs. 6(a)-(d) with the pressure coefficient Cp as the ordinate and the angle of attack ϕ as the abscissa, for non-dimensional cylinder heights $y/h = 0.11$, 0.44, and 0.89. The noticeable phenomena as follows are seen in the pressure distributions at $y/h = 0.44$: First, the maximum value of the pressure on the front surface of the cylinder is almost constant in the range $0 \lesssim \phi \lesssim 165$ deg. However, this value decreases rapidly beyond $\phi \simeq 165$ deg. The pressure on the whole surface finally becomes negative in the range $175 \lesssim \phi \lesssim 180$ deg. Secondly, the location θ_0 of the maximum pressure shifts with

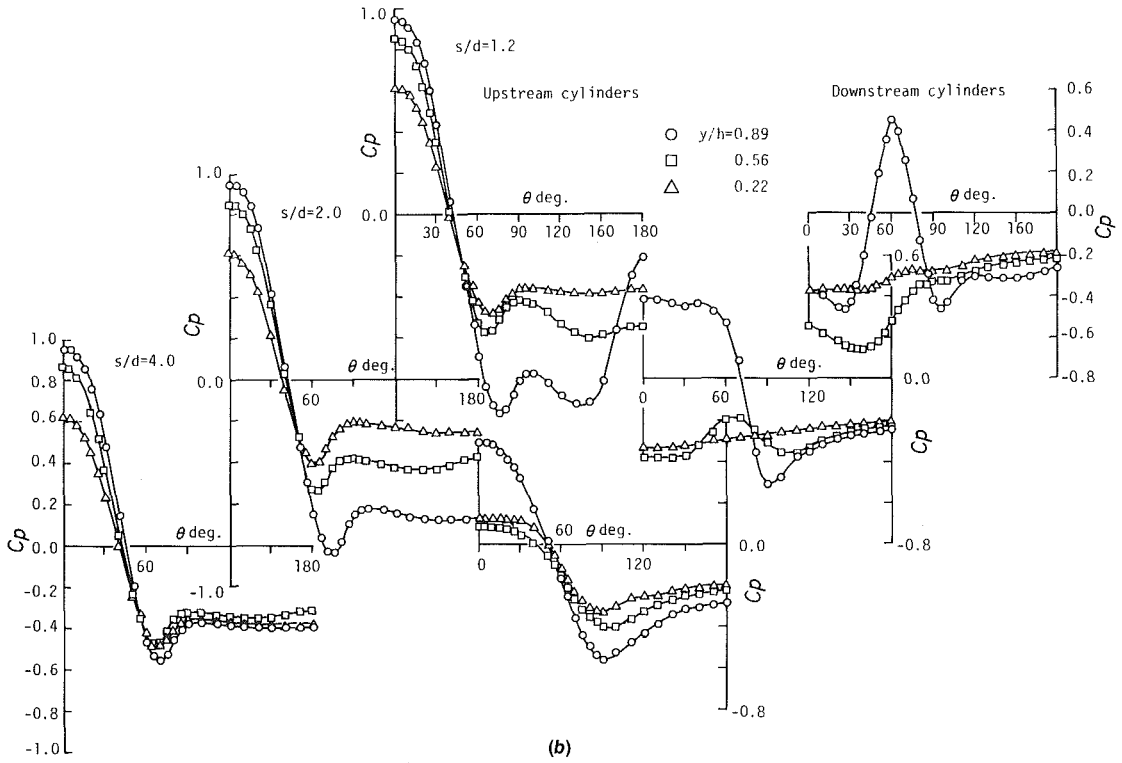

Fig. 8(a) Comparison among several spacings at $y/h = 0.44$, Fig. 8(b) Comparisons among three different heights of the cylinders, $y/h = 0.22$, 0.56 and 0.89.

Fig. 8 Pressure distributions of two cylinders in a tandem arrangement. The uncertainty in s/d is ± 0.013. For further informations, see the caption of Fig. 6.

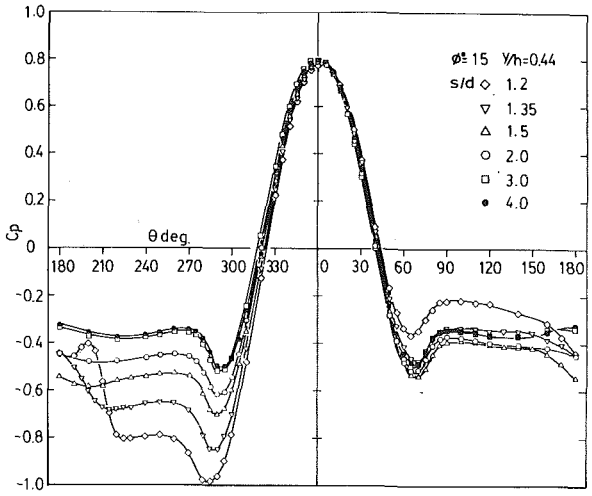

Fig. 9(a)

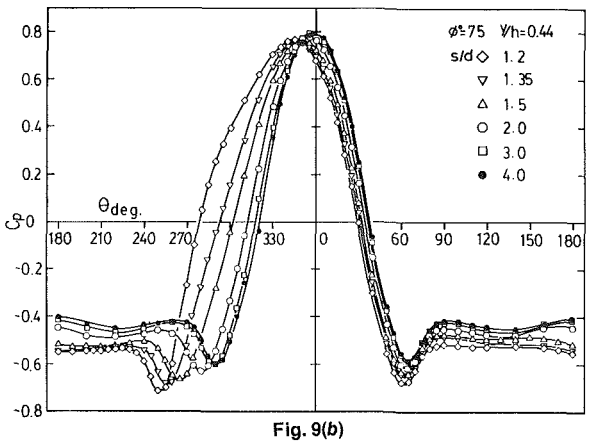

Fig. 9(b)

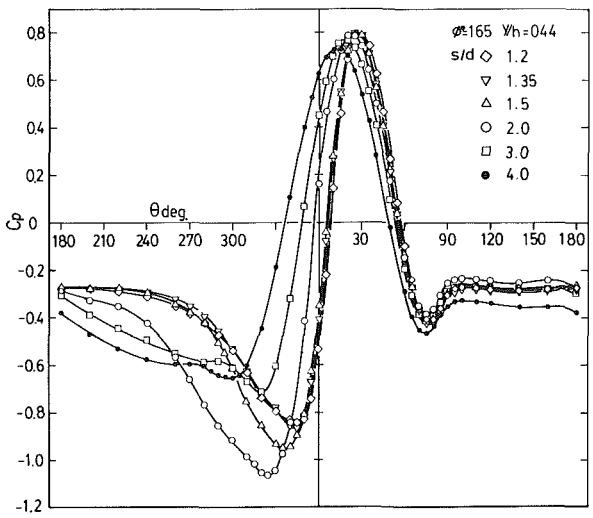

Fig. 9(c)

Fig. 9 Variation in pressure distributions. For further information, see the captions of Figs. 6 and 9.

respect to the variation in angle of attack, as shown in Fig. 7(*a*). This location moves to the inner side of the cylinder with increasing angle of attack and attains its minimum value when $\phi \simeq 90$ deg. Then θ_0 shifts to the outer side in the range $\phi \gtrsim 90$ deg. Figure 7(*b*) shows the variations of θ_0 at the other height of the cylinder $y/h = 0.11$ and 0.89 in the case of $s/d = 2.0$. The trends in the variations of θ_0 are much alike to that of $y/h = 0.44$ except for their magnitudes. The asymmetry of the pressure distributions about $\theta = 0$ deg induced by such a shift of the maximum pressure location is one of the primary factors in the occurrence of lift. Thirdly regarding the values and features of the pressure distributions on both sides of the cylinder, it is noted that the rate of influence by the dummy cylinder is larger on the inner side of the cylinder than on the outer side, as shown in Fig. 6(*b*) (also see Fig. 9). As a result, the asymmetry of the pressure distributions about $\theta = 0$ deg becomes larger with increasing angle of attack. Figures 6(*c*) and (*d*) show the pressure distributions at the heights $y/h = 0.89$ and 0.11. For $y/h = 0.89$, the values of the pressure on the front part of the cylinder are larger than those at $y/h = 0.44$ and are positive even in the tandem arrangement, because the tip flow from the upstream cylinder influences the upper part of the cylinder. On the other hand, the shapes of the pressure distributions at $y/h = 0.11$ are much alike to those at $y/h = 0.44$.

Pressure Distribution as a Function of Spacing. In this section, the variations of the pressure distributions with respect to spacing s/d between the two cylinders are presented. As shown in Fig. 8(*a*), the pressure distributions around the two cylinders in a tandem arrangement are almost independent of s/d when $s/d \gtrsim 2.0$. However, the pressure of the rear surface of the upstream cylinder decreases gradually as the spacing reduces and this value of pressure finally attains the same value as the corresponding one on the side of the downstream cylinder which faces the gap between the two cylinders. It follows that the flow in the gap is almost stagnant at the height $y/h = 0.44$. Hori [1] studied the same phenomenon in two-dimensional flow around two circular cylinders. On the other hand, the downstream cylinder is affected by the wake of the upstream cylinder. Two symmetric peaks are found in the pressure distributions of the downstream cylinder when $s/d \lesssim 3.0$, presumably corresponding to the reattachment points of the streamlines separated from the upstream cylinder, which were also found in the two dimensional case.

Figure 8(*b*) shows several comparisons of the pressure distributions at three different cylinder heights in the tandem arrangement. For the upstream cylinder, the value of the pressure on the back surface decreases as the height of the cylinder increases. There always exists a range of positive values of the pressure at $y/h = 0.89$ on the front surface of the downstream cylinder. The reason is that the separated flow from the upstream cylinder reattaches to the front part of the downstream cylinder in the cases of $s/d = 1.2$ and 2.0. However, in the case of $s/d = 4.0$, the effect of the upstream cylinder decreases and the pressure on the front part of the downstream becomes positive as a result.

Pressure distributions at the height $y/h = 0.44$ when $\phi = 15$, 75 and 165 deg are presented in Figs. 9(*a*), (*b*), and (*c*), respectively. In the case $\phi = 15$ deg, the pressure of the inner side of the cylinder decreases and therefore the pressure distributions become more asymmetric about $\theta = 0$ deg as the two cylinders approach each other. This feature of the pressure compares well with the flow visualizations, as seen in Fig. 10. The downstream cylinder is directly in the wake of the upstream cylinder, when $\theta = 0$ deg. However, in the case $\theta = 15$ deg, a flow is observed between the two cylinders, that is, a gap flow is produced by a winding of the flow on the front surface of the downstream cylinder. As for inviscid fluid, it is well known that a pressure gradient acts toward the center of the curvature of the flow when the flow bends. This pressure gradient ∇p is expressed by

$$\nabla p = \frac{\rho}{2} \frac{\partial q^2}{\partial s} t - \rho \frac{q^2}{R} n \tag{1}$$

where ρ is the density of fluid, q the velocity of the flow, s the coordinate to the streamwise direction, $\mathbf{t}$ and $\mathbf{n}$ unit vectors to the streamwise and normal direction of the flow, respectively, and R the radius of curvature, as shown in Fig. 11. Accordingly to equation (1), the pressure gradient is in inverse

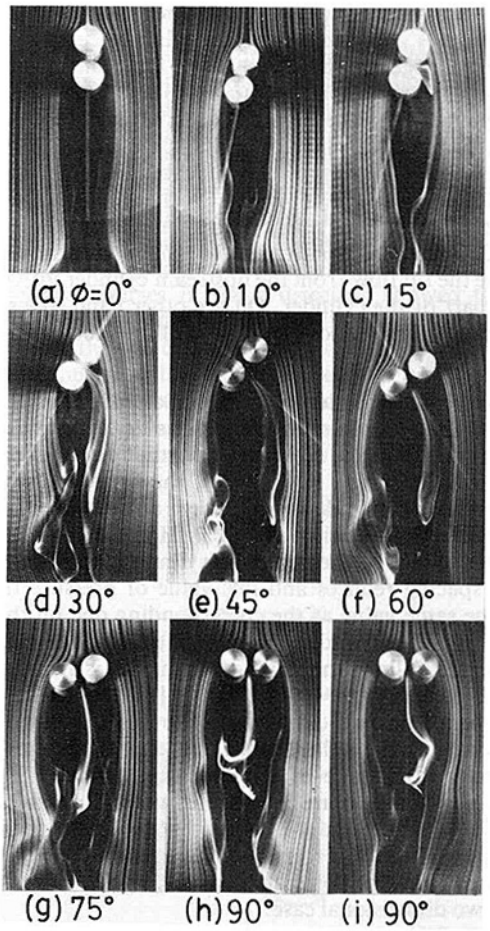

Fig. 10(i) s/d = 1.2

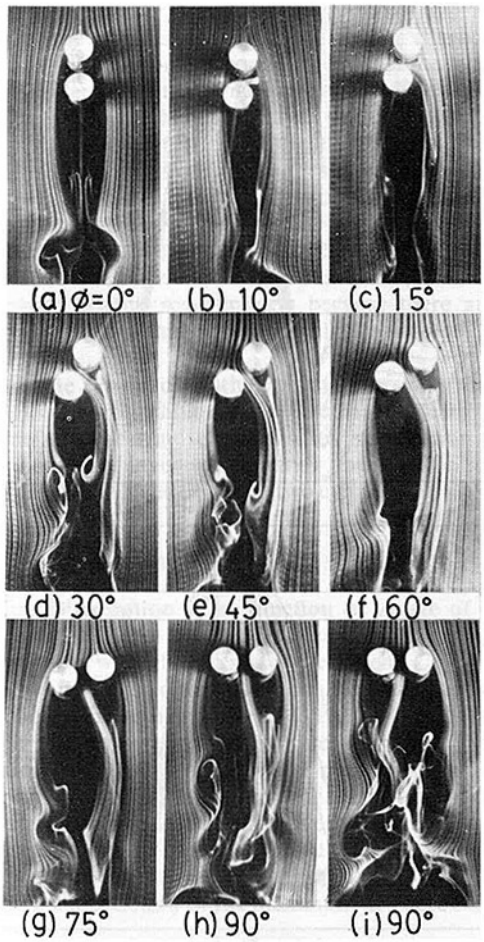

Fig. 10(ii) s/d = 1.5

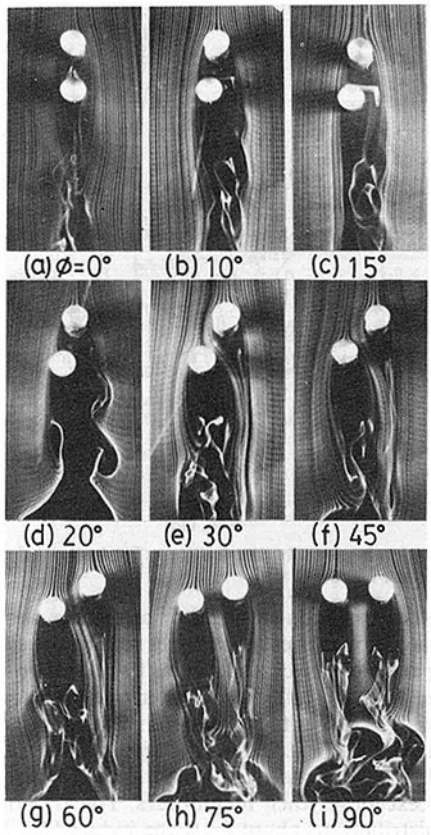

Fig. 10(iii) s/d = 2.0

Fig. 10 Flow patterns around two cylinders (by smoke wire technique).

proportion to R. Consequently, a primary factor of such a decrease in pressure with reduced spacing between the two cylinders is due to the variation in curvature of the gap flow. As Zdravkovich [10] pointed out, bistable flows between two cylinders of finite height can be observed in the case of the side by side arrangement $\phi = 90$ deg when $s/d = 1.2$ and 1.5, as shown in Fig. 10(i) and (ii).

Pressure distributions are also shown in Fig. 9(b) as a function of s/d for $\phi = 75$ deg. In this case, the pressure on the front part of the inner side of the upstream cylinder increases as the spacing reduces. Further, it is observed that the gap flow is markedly more retarded than the outer flow surrounding the two cylinders, as shown in Fig. 10. The pressure increment on the front part of the inner side of the cylinder seems to be induced by a blockage effect, which becomes larger as the two cylinders approach each other.

Finally, Fig. 9(c) shows pressure distributions at an angle of attack $\phi = 165$. In this case, the downstream cylinder is affected by the wake of the upstream cylinder as intensely as in the case in which the two cylinders are positioned in a tandem arrangement. The pressure variation of the inner side of the downstream cylinder has no systematic change with respect to the spacing. However, pressure distributions of the inner side are lower than those of the outer side and exhibit some complicated features.

Lift and Drag

A fluid force acting on a cylinder consists of two parts: one is the pressure force and the other is the viscous force. Attention is paid only to the former, however, because it has a much larger order of magnitude than the latter.

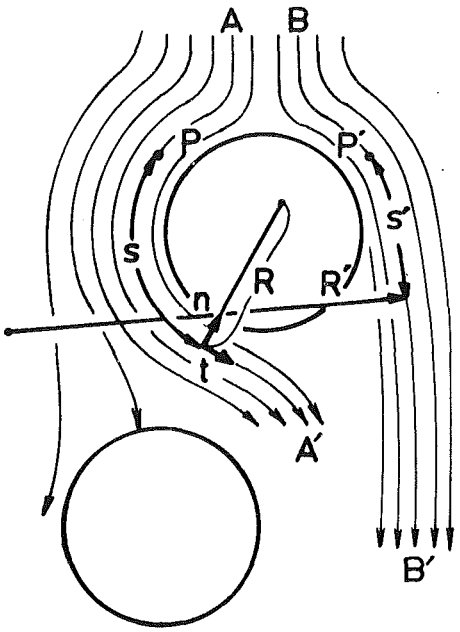

Fig. 11 Curvature of the gap flow between two cylinders

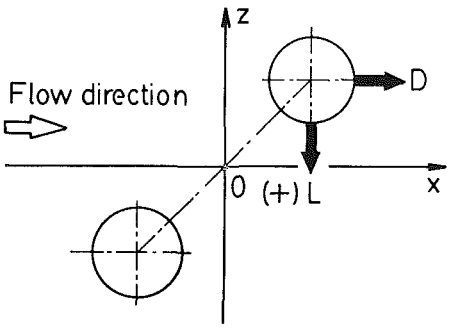

Fig. 12 Definition of fluid forces

The local drag and lift coefficients at each height of the two cylinders can be obtained by

$$C_{Dy} = \frac{1}{2}\int_0^{2\pi} \frac{p-p_0}{(1/2)\rho U_0^2}\cos\theta d\theta = \frac{1}{2}\int_0^{2\pi} C_p \cos\theta d\theta \qquad (2)$$

$$C_{Ly} = \frac{1}{2}\int_0^{2\pi} \frac{p-p_0}{(1/2)\rho U_0^2}\sin\theta d\theta = \frac{1}{2}\int_0^{2\pi} C_p \sin\theta d\theta \qquad (3)$$

respectively. Accordingly, the total drag and lift in the form of coefficient C_D and C_L can be integrated as

$$C_D = \int_0^1 C_{Dy} d\left(\frac{y}{h}\right) \qquad (4)$$

$$C_L = \int_0^1 C_{Ly} d\left(\frac{y}{h}\right) \qquad (5)$$

where the positive value of the lift is in the direction to the gap between the two cylinders in this arrangement, as shown in Fig. 12.

The lift described above is summarized in a single figure, as seen in Fig. 13, in which the curves of equilift coefficient C_L are drawn by the interpolation between the measured values of the lift. All of the possible arrangements of the two cylinders are classified into three regions by taking into account whether the lift is greater or smaller than zero; (1) $0 \lesssim \phi \lesssim 30$ deg, (2) $30 \lesssim \phi \lesssim 120$ deg and (3) $120 \lesssim \phi \lesssim 180$ deg. In region (1), the lift is positive and increases as the spacing reduces. The reason is that the pressure of the inner side of the upstream cylinder decreases with reduced spacing between the

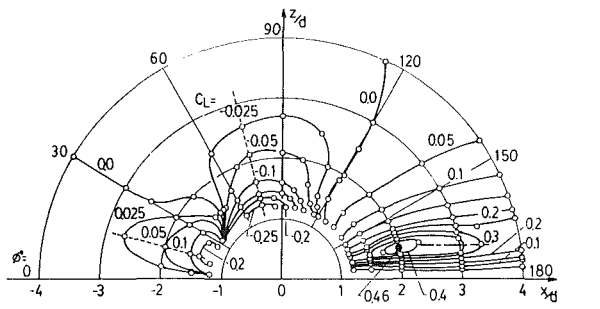

Fig. 13 Equilift lines. The uncertainty in ϕ is ± 0.5 deg and that in x/d is ± 0.013.

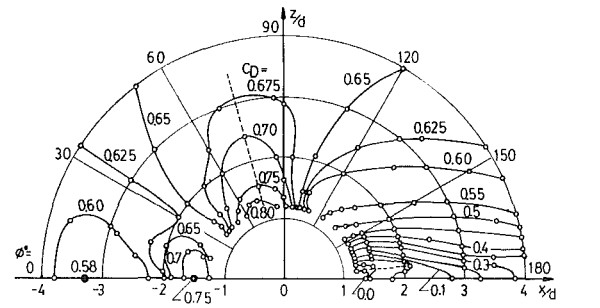

Fig. 14 Equidrag lines. For further information, see the caption of Fig. 13.

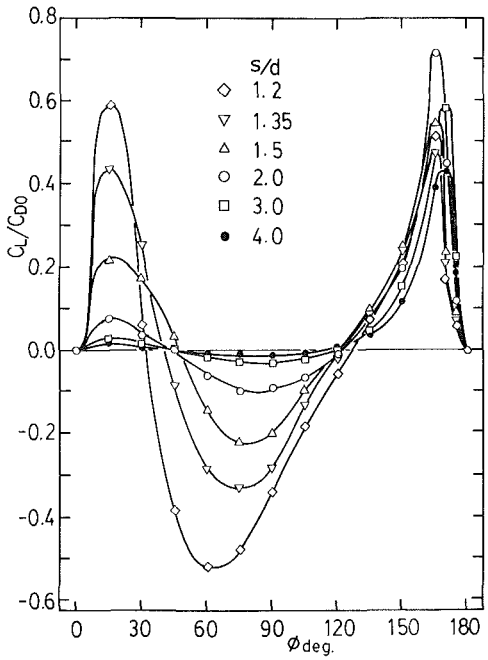

Fig. 15 Relation between lift and angle of attack. The uncertainty in C_L/C_{D_0} is ± 0.04 and that in ϕ ± 0.5 deg.

two cylinders. Further, a peak line of the lift exist at $\phi = 15$ deg. Meanwhile, the lift is negative and decreases as the spacing reduces in the region (2). As described in the preceding section, the pressure increment on the inner side of the cylinder resulting from a blockage effect produces a negative lift, always corresponding to a repelling force between the two cylinders. Finally, in region (3), in which the downstream cylinder is strongly affected by the wake of the upstream cylinder, the equilift lines are almost parallel to the x axis. It is also seen that the lift changes considerably when the downstream cylinder shifts slightly in the transverse direction. The maximum value in this region exists at $s/d \simeq 2.0$ and $\phi \simeq 165$ deg, and a peak line of the lift parallel to the x axis is well compared with the result of the two dimensional case of two cylinders [1].

Equidrag lines are shown in Fig. 14 in the form of a drag

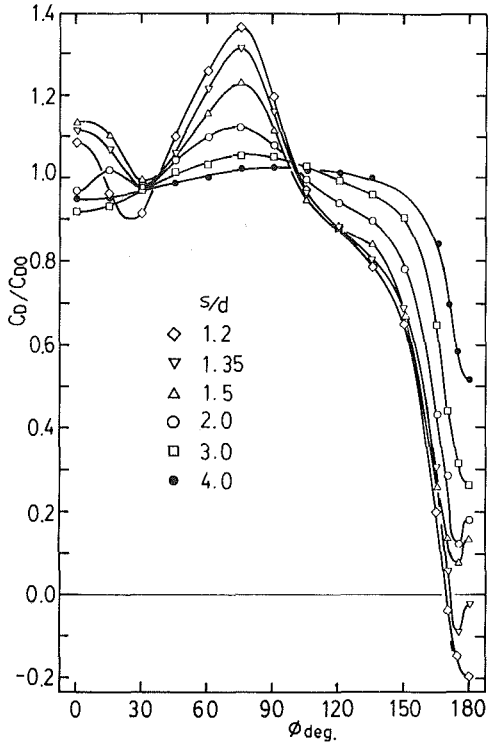

Fig. 16 Relation between drag and angle of attack. The uncertainty in C_D/C_{D_0} is ± 0.04 and that in 6c ± 0.5 deg.

coefficient C_D. This chart is similar to that of the equilift chart. It is also classified into three regions which are divided by constant lines $C_D = 0.625$, which is almost the same value as that of a single cylinder, $C_{D0} = 0.64$. The single cylinder had the same dimensions as the two cylinders of finite height. The main result of C_D in region (1) are as follows: The maximum and the minimum values of C_D are found at $x/d = 1.5$ and -3.3 in a tandem arrangement, respectively. Further, the variation in C_D in this region is not so large as those in the other regions. The drag in region (2) increases with reduced spacing and has a bottom line at $\phi \simeq 75$ deg, which links the minimum values of each drag line. In region (3), the equidrag lines are almost parallel to the x axis, similar to the equilift lines. As a result, these charts of lift and drag correspond qualitatively to those of the two dimensional case of the two cylinders reported by Hori [1] and Zdravkovich [10].

In order to make clearer the variations in lift and drag induced by interference between the two cylinders, the ratio of C_L/C_{D0} and C_D/C_{D0} with respect to angle of attack ϕ for various parameters s/d should be investigated. The value of C_L/C_{D0} attains a maximum when $\phi \simeq 15$ and 165 deg for each value of s/d, as shown in Fig. 15. Taking the relative position of the two cylinders into account, the line between the centers of the two cylinders makes an angle 15 deg to the free stream direction. In this position, high values of lift occur on the two cylinders and their magnitude attains $0.6 \sim < 10.7$ times the magnitude of C_{D0} when $s/d = 1.2$. Moreover, the variation in C_L attains 1.1 times the magnitude of C_{D0} and its direction turns inversely when angle of attack changes from 15 to 60 deg at the same spacing. Meanwhile, the value of C_D/C_{D0} attains a maximum when $\phi \simeq 75$ deg and decreases with increasing ϕ beyond $\phi \simeq 75$ deg, as seen in Fig. 16. The value of C_D/C_{D0} is almost a unit in the range $0 \lesssim \phi \lesssim 135$ deg when $s/d = 4.0$. Further, in this region C_L/C_{D0} is almost zero, as seen in Fig. 15. Consequently, it is considered that the effect of the interference between the two cylinders is negligible in the region $0 \lesssim \phi \lesssim 135$ deg and $s/d \gtrsim 4.0$.

Conclusions

Time-averaged fluid forces acting on the two circular cylinders of finite height which were placed vertically and arranged differently on the plane floor were experimentally investigated, with the following major results:

1) The trend of lift is classified into three regions: (1) $0 \lesssim \phi \lesssim 30$ deg, (2) $30 \lesssim \phi \lesssim 120$ deg and (3) $120 \lesssim \phi \lesssim 180$ deg. In region (1) lift has a positive value and increases with reduced spacing; in region (2) it has a negative value and its absolute value tends to increase with reduced spacing; in region (3) equilift lines are almost parallel to the direction of the free stream.

2) The trend of drag is also classified into three regions similar to those of lift: In region (1) the variation in drag is not so large as those of the other regions; in region (2) the drag increases with reduced spacing; in region (3) the equidrag lines are parallel to the x axis, similar to the equilift lines.

3) The effect of interference between the two cylinders becomes almost negligibly small when $0 \lesssim \phi \lesssim 135$ deg and $s/d \gtrsim 4.0$. Accordingly, time-averaged fluid forces of the two cylinders in this region are regarded as similar to those observed in the case of a single cylinder.

Acknowledgment

The authors are indebted to Messr. Y. Obata, T. Miura, and M. Fujita for their assistance in conducting the experiment and constructing the experimental apparatus.

References

1 Hori, E., "Experiments on Flow Around a Pair of Parallel Circular Cylinders," *Proc. 9th Japan National Congress for Applied Mech.*, Tokyo, 1959, pp. 231-234.

2 Price, S. J., "The Origin and Nature of the Lift Force on the Leeward of Two Bluff Bodies," *Aero. Quart.*, Vol. XXVI, 1976, pp. 154-168.

3 Bearman, P. W., and Wadcock, A. J., "The Interaction Between a Pair of Circular Cylinders Normal to a Stream," *J. Fluid Mech.*, Vol. 61, No. 3, 1973, pp. 499-511.

4 Kiya, M., Arie, M., Tamura, H., and Mori, H., "Vortex Shedding from Two Circular Cylinders in Staggered Arrangement," ASME JOURNAL OF FLUIDS ENGINEERING, Vol. 102, No. 2, 1980, pp. 166-173.

5 Ishigai, S., Nishikawa, E., Nishimura, K., and Cho, E., "Experimental Study of Structures of Gas Flow in Tube Banks with Tube Axis Normal to Flow (Part 1, Kármán Vortex Flow around Two Tubes at Various Spacings)," *Bulletin of the Japan Society of Mechanical Engineers*, Vol. 15, No. 86, 1972, pp. 949-956.

6 Spivac, H. M., "Vortex Frequency and Flow Pattern in the Wake of Two Parallel Cylinders at Varied Spacings Normal to an Air Stream," *Journal of Aeronautical Sciences*, Vol. 13, 1946, pp. 289-297.

7 Okajima, A., "Flow Around Two Tandem Circular Cylinders at Very High Reynolds Numbers," *Bulletin of the Japan Society of Mechanical Engineers*, Vol. 22, No. 166, 1974, pp. 504-511.

8 Biermann, D., and Herrnstein, W. H., "The Interference Between Struts in Various Combinations," National Advisory Committee for Aeronautics, Report No. 468, 1933, pp. 515-524.

9 Dalton, C., and Szabo, J. M., "Drag on a Group of Cylinders," ASME *Journal of Pressure Vessel Technology*, Vol. 199, No. 1, 1977, p. 152-157.

10 Zdravkovich, M. M., "Review of Flow Interference Between Two Circular Cylinders in Various Arrangement," ASME JOURNAL OF FLUIDS ENGINEERING, Vol. 99, No. 4, 1977, pp. 618-633.

11 Zdravkovich, M. M., "Aerodynamics of Two Parallel Circular Cylinders of Finite Height at Simulated High Reynolds Numbers," *Journal of Wind Engineering and Industrial Aerodynamics*, Vol. 6, 1980, pp. 59-71.

12 Coles, D., "The Law of the Wake in the Turbulent Boundary Layer," *J. Fluid Mech.*, Vol. 1, No. 1, 1956, pp. 191-226.

13 Klebanoff, P. S., and Diehl, Z. W., "Some Features of Artificially Thickened Fully Developed Turbulent Boundary Layer with Zero Pressure Gradient," NACA TR, No. 1110, 1952.

J. H. Ferziger

A. A. Lyrio

J. G. Bardina

Department of Mechanical Engineering,
Stanford University,
Stanford, Calif. 94305

New Skin Friction and Entrainment Correlations for Turbulent Boundary Layers

A new correlation for the skin friction and two new correlations for the entrainment rate in turbulent boundary layers are presented. Relative to previous correlations, the new ones are at least as accurate, simpler to use, and applicable to separated flows.

I Introduction

A great many methods for the prediction of boundary layer behavior can be found in the literature; a number of good ones were tested in the 1968 conference (Kline et al. [1]) and more have appeared since. Although recent trends favor methods based on partial differential equations, there is an important role to be played by methods based on integral equations, i.e., ordinary differential equations derived by integrating the partial differential equations over the boundary layer. Such methods allow greater use of physical insight and intuition and have recently been shown by the authors and their colleagues (Kline et al. [2]; Bardina et al. [3]) to be able, with proper precautions, to handle separated flows more straightforwardly. Their principal disadvantage lies in the fact that integral methods require correlations which are highly empirical and therefore need to be rechecked and perhaps extended every time a new phenomenon is introduced into the set of flows to be considered.

Kline et al. [2] showed that a wide variety of boundary layer profiles are well fit by the Coles [4] wall-wake law. Furthermore, by introducing the new parameters,

$$h=\frac{H-1}{H},\ \Lambda=\delta^*/\delta \tag{1}$$

where H is the conventional shape factor, they were able to show that $h \equiv h(\Lambda, \mathrm{Re}^*)$, and that the dependence on the displacement thickness Reynolds number Re^* is weak, especially near separation. They were also able to make a distinction between incipient and full separation based on these parameters.

The $h-\Lambda$ correlation can be used to simplify the momentum integral equation, but, as in any integral method, a correlation is needed for the skin-friction coefficient, C_f, and an auxiliary equation is necessary. The latter can be any of a number of possibilities, but the most popular choice is the entrainment equation, which is essentially an integral form of the continuity equation for the boundary layer. A recent report (Childs et al. [5]) shows that this is the best choice among the equations in common use.

Contributed by the Fluids Engineering Division for publication in the JOURNAL OF FLUIDS ENGINEERING. Manuscript received by the Fluids Engineering Division, September 28, 1981.

We thus need a skin-friction correlation and an entrainment correlation. Several of these already exist, but they also have weaknesses that leave room for improvement. Several skin-friction correlations were reviewed by Escudier et al. [6] The Ludwieg-Tillman correlation is one of the better ones available, but it is not capable of dealing with reversed flows. Consequently, we shall seek a method which is as accurate as the Ludwieg-Tillman correlation for attached flows but which is capable of dealing with reversed flows as well. This is taken up in the next section.

We have used the Bradshaw et al. [7] entrainment correlation with considerable success. Its major drawback is that it was found to consume most of the computing time in the boundary layer programs that we developed. This is not a serious difficulty for steady flows for which the computation time is almost trivial, but it does cause problems when applied to the unsteady case (Lyrio et al. [8]). Consequently, in Section III we shall present new correlations which seem to be as accurate as Bradshaw's and which are much simpler to use.

These new correlations have been built into programs for computing both boundary layer and diffuser behavior for both steady and unsteady cases. The results, given in publications cited above, are quite satisfactory.

II Skin-Friction Correlation

Coles' profile can be written in the form,

$$\frac{u}{u_\tau}=\frac{1}{\kappa}\ln\frac{yu_\tau}{\nu}+5.0+\frac{\Pi}{\kappa}(1-\cos\pi y/\delta). \tag{2}$$

As stated above, it is capable of fitting a very wide range of boundary layer profiles, including ones with reverse flow if u_τ is allowed to be negative; this modification was first pointed out by Kuhn and Nielsen [9].

By integrating equation (2) over the boundary layer and using the fact that $u = u_\infty$ at the edge of the boundary layer, it is not difficult to derive an implicit relation for the skin friction,

$$V_T=\frac{1-2\Lambda}{0.05+\ln|V_T|+\ln(\kappa\mathrm{Re}^*/\Lambda)} \tag{3}$$

where $V_T = u_\tau/\kappa u_\infty = (\mathrm{sgn}(\tau_w)/\kappa)\sqrt{C_f/2}$. This relation can

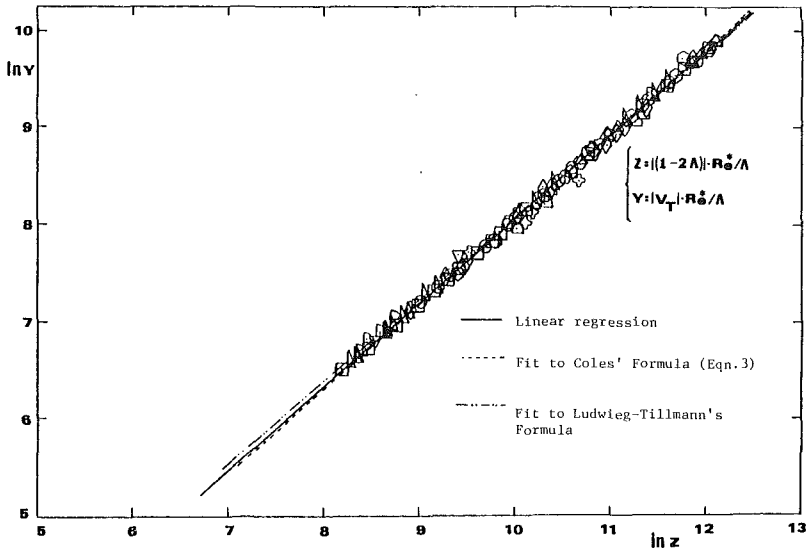

Fig. 1 Skin friction correlation. Eleven data sets have been used including cases of separating and separated flow. All of the data except those marked ✣ are from the 1968 Conference [1]; the latter are due to Ashjaee et al. For details of the other sources, see the authors' report (Lyrio et al. [8]).

be used for the skin friction, but it has the disadvantages of being implicit (thus requiring iterative solution) and of behaving badly in the neighborhood of separation (for which $\Lambda = 0.5$ and $V_T = 0$). Thus we shall look for a simplification.

The path to simplifying equation (2) is made easier by recognizing that equation (2) can be cast in terms of the nondimensional variables,

$$Y = V_T \mathrm{Re}^*/\Lambda,\ Z = (1-2\Lambda)\mathrm{Re}^*/\Lambda. \tag{4}$$

This suggests plotting the experimental data in the form Y versus Z, and this is done in Fig. 1. This plot clearly suggests a correlation of the form

$$Y = AZ^N. \tag{5}$$

There are a number of methods one can use to get the fitting constants A and N. The first is simply to use a linear regression to fit a curve to the data. A second is to plot the Ludwieg-Tillman correlation in these coordinates and fit a curve of the type (5) to the result. Finally, one can plot the relationship (3) on this figure and fit a curve of the form (5) to it. As can be seen in the figure, all of these give good fits to the data, and all work quite well in practice. The constants obtained are given in Table 1 below. Illustrative results will be given later.

Table 1 Constants for the skin-friction curve fit

Method	A	N
Linear regression on data	0.55	0.866
Ludwieg-Tillman	0.62	0.855
Coles' profile	0.44	0.885

The coefficients obtained using the linear regression lie between those corresponding to the Ludwieg-Tillman and Coles' correlations. The linear regression yields an explicit equation for the skin friction coefficient,

$$C_f = 0.1017\ |1-2\Lambda|^{1.732}\left(\frac{\Lambda}{\mathrm{Re}^*}\right)^{0.268}\ \mathrm{sign}(1-2\Lambda) \tag{6}$$

Figure 2 compares the prediction of C_f with the experimental data of Simpson, et al. [10].

III Entrainment Correlation

The entrainment rate is defined by

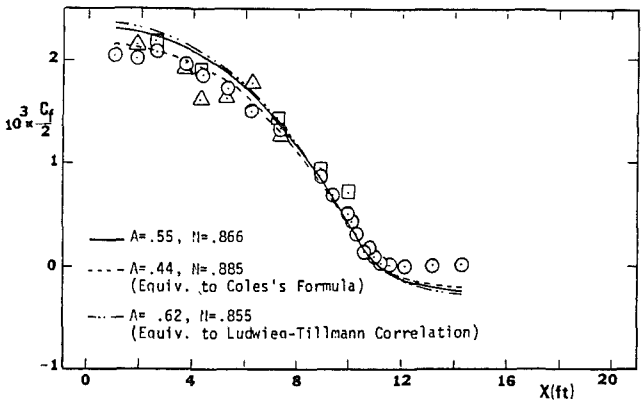

Fig. 2 Skin-friction coefficient. Comparison to Simpson's experimental results.

$$E = \frac{1}{u_\infty}\frac{d}{dx}\int_0^\delta u\,dy = \frac{1}{u_\infty}\frac{d}{dx}[u_\infty(\delta-\delta^*)] \tag{7}$$

Experimental evaluation of the entrainment usually relies on the last expression. Because this requires one to evaluate δ, for which the uncertainty may be fairly high, and then differentiate the result, the uncertainty in the measured entrainment is always quite large. The situation is especially poor for separated flows for which both δ and δ^* grow rapidly and for which there are few reliable measurements of these parameters. This means that any entrainment correlation is quite uncertain for separated flows.

Several entrainment correlations have been presented in the literature. Head's [11] and Michel's [12] correlations are both based on shape factors and are easy to use and quite accurate for attached flows. However, they are not designed to deal with separated flows and do not fare well when applied to them. In a longer report (Lyrio et al. [8]) we have shown that Bradshaw's [7] method works well for both attached and separated flows but requires a considerable amount of computation for the evaluation of the maximum shear stress at each location.

To account for nonequilibrium turbulent boundary layers, including upstream history and delay responses to abrupt changes in the pressure gradient, several authors have proposed the use of a lag equation,

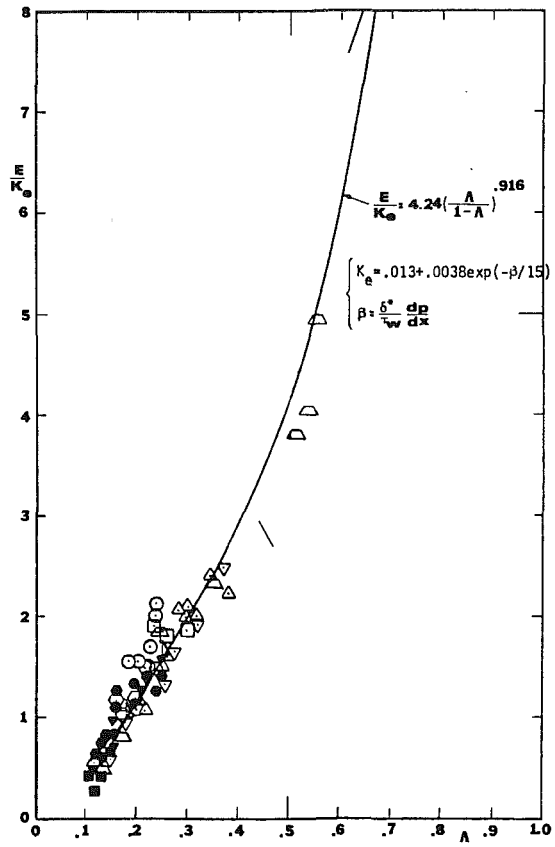

Fig. 3 Entrainment correlation. The recommended correlation is the smooth curve. Eleven data sets were used; all but two are from the 1968 Conference [1]. The data denoted by □ are from Simpson et al. [14], while those denoted by ▽ are by Ashjaee et al. [15]; for the identity of the others see the authors' report (Lyrio et al. [8]). The data were differentiated to obtain the entrainment, and the uncertainty is estimated as 20–30 percent.

$$\frac{dQ}{dx} = \frac{C}{\delta}(Q_{eq} - Q), \tag{8}$$

where Q is any of the quantities used in the model and Q_{eq} is the "equilibrium" value (the one obtained if the boundary is maintained in its present state for a long time). Q may be the entrainment rate itself or some intermediate quantity used in the calculation. Lag equations of this type have been used by many previous authors; one of the earliest appears to have been Goldberg [13].

A common assumption in the derivation of entrainment methods is that the entrainment, which occurs in the outer part of the boundary layer, ought to be sensitive to parameters which measure the behavior of that part of the flow. In our case, the parameter Λ (or what is nearly equivalent, h) is the one which essentially does this. Consequently, we plotted the entrainment data vs. Λ, as shown in Fig. 3, and the assumption of a functional relationship between E and Λ appears to be valid. It was found that the function,

$$E = 4.24\, Ke\left(\frac{\Lambda}{1-\Lambda}\right)^{0.916}, \tag{9}$$

where Ke is the pressure gradient parameter introduced by Kuhn and Nielsen [9],

$$Ke = 0.13 + 0.0038\, e^{-\beta/15},\ \beta = \frac{\delta^*}{\tau_w}\frac{dp}{dx}, \tag{10}$$

fits quite well. We found further that this equation should be used together with the lag equation (8), where $Q = E$ and $C = 0.025$. After separation (for $\Lambda > 0.5$), no lag need be used.

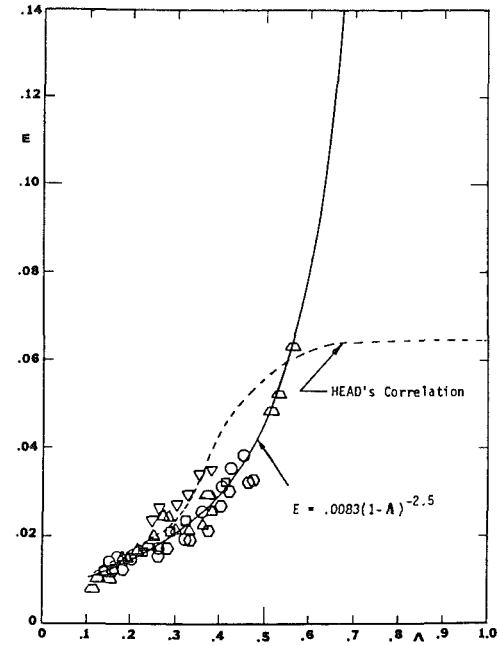

Fig. 4 Entrainment correlation. Six data sets are shown.

An even simpler correlation which can be used without a lag is

$$E = 0.0083(1-\Lambda)^{-2.5} \tag{12}$$

and this is shown in Fig. 4. However, this correlation does not work well for accelerated flows. We have used it with considerable success in diffuser calculations (Bardina et al. [3]) and recommend its use in such flows.

We have not included examples of flows computed with these methods, as some of these have been presented elsewhere. A wide range of flows from the 1968 Conference [1] as well as those used in the 1980–81 Stanford Conferences [16], including separated flows, have been computed without serious discrepancy, and methods based on the correlations presented in this paper have been found to be at least as accurate as any of the methods previously available, applicable to a wider range of flows, and faster computationally.

IV Conclusions

We have derived a new correlation for the skin friction coefficient and two new correlations for the entrainment rate in turbulent boundary layers. Relative to earlier methods, the new ones have the advantages that they are at least as accurate, are capable of treating separated flows, and are simpler to apply.

Acknowledgments

This work was supported by the Air Force Office of Scientific Research under Contract AF-F49620-79-C-0010. The authors are indebted to a number of colleagues for important contributions to this work. Prof. S. J. Kline provided the spark that initiated this work and contributed heavily to it. R. E. Childs and R. J. Strawn and Prof. J. P. Johnston and other members of the Separated Flow Research Group made important comments during the course of the work.

References

1 Kline, S. J., Morkovin, M. V., Sovran, G., and Cockrell, D., "Com-

putation of Turbulent Boundary Layers," 1968 AFOSR-IFP-Stanford Conference, Dept. of Mech. Engrg., Stanford Univ., 1968.

2 Kline, S. J., Bardina, J. G., and Strawn, R. C., "Correlation and Computation of Detachment and Reattachment of Turbulent Boundary Layers on Faired Surfaces," AIAA-81-1220, 1981.

3 Bardina, J., Lyrio, A., Kline, S. J., Ferziger, J. H., and Johnston, J. P., "A Prediction Method for Planar Diffuser Flows," ASME JOURNAL OF FLUIDS ENGINEERING, Vol. 103, 1981, p. 315.

4 Coles, D. E., "The Law of the Wake in Boundary Layers," *J. Fluid Mech.*, Vol. 1, 1956, p. 191.

5 Childs, R. E., Ferziger, J. H., and Kline, S. J., "A Method of Prediction for Subsonic Compressible Diffusers," Report PD-24, Dept. of Mech. Engrg., Stanford Univ., 1981.

6 Escudier, M. P., Nicoll, W. B., and Spalding, D. B., "An Explicit Drag Law for Uniform Density Boundary Layers in Smooth, Impermeable Walls," Report, Mech. Engrg. Dept., Imperial College, 1966.

7 Bradshaw, P., Ferriss, D. H., and Atwell, N. P., "Calculation of Boundary Layer Development Using the Turbulent Energy Equation," *J. Fluid Mech.*, Vol. 28, 1967, p. 593.

8 Lyrio, A. A., Ferziger, J. H., and Kline, S. J., "An Integral Method for the Computation of Steady and Unsteady Boundary Layer Flows, Including Transitory Stall in Diffusers," Report PD-23, Dept. of Mech. Engrg., Stanford Univ., 1981.

9 Kuhn, G. D., and Nielsen, J. N., "An Analytical Method for Calculating Turbulent Separated Flows Due to Adverse Pressure Gradient," *AIAA Journal*, Vol. 12, 1974, p. 881.

10 Simpson, R. L., Chew, Y. T., and Shivaprasad, B. G., "Measurements of a Separating Turbulent Boundary Layer," Project SQUID Report TR SMU-4-PU, 1980.

11 Head, M. R., "Entrainment in Turbulent Boundary Layers," Aero Res. Council Report and Memo 3152, 1958.

12 Michel, R., Quemard, C., and Durant, R., "Hypothesis on the Mixing Length and Application to the Calculation of the Turbulent Boundary Layers in Kline et al. (1968)."

13 Goldberg, P., "Upstream History and Apparent Stress in Turbulent Boundary Layers," Report 85, MIT Gas Turbine Lab, 1966.

14 Simpson, R. L., Strickland, J. H., and Barr, P. W., "Laser and Hot-Film Anemometer Measurements in Separating Turbulent Boundary Layers," Rpt. WT-3, Southern Methodist University, 1974. Also *Journal of Fluid Mechanics*, Vol. 79, 1977, pp. 553–594.

15 Ashjaee, J., Johnston, J. P., and Kline, S. J., "Subsonic Turbulent Flow in Plane-Wall Diffusers: Peak Pressure Recovery and Transitory Stall," Rpt. PD-21, Dept. of Mechanical Engineering, Stanford University, 1980. Also ASME JOURNAL OF FLUIDS ENGINEERING, Vol. 102, 1978, p. 180.

16 Kline, S. J., Cantwell, B. J., and Lilley, G. M., eds., *Proceedings of the 1980-81 AFOSR-HTTM-Stanford Conference on Complex Turbulent Flows—Comparison of Computation and Experiment*, Vol. I, Dept. of Mechanical Engineering, Stanford University, 1982.

putation of Turbulent Boundary Layers," 1968 AFOSR-IFP-Stanford Conference, Dept. of Mech. Engrg., Stanford Univ., 1968.

2 Kline, S. J., Bardina, J. G., and Strawn, R. C., "Correlation and Computation of Detachment and Reattachment of Turbulent Boundary Layers on Faired Surfaces," AIAA-81-1220, 1981.

3 Bardina, J., Lyrio, A., Kline, S. J., Ferziger, J. H., and Johnston, J. P., "A Prediction Method for Planar Diffuser Flows," ASME JOURNAL OF FLUIDS ENGINEERING, Vol. 103, 1981, p. 315.

4 Coles, D. E., "The Law of the Wake in Boundary Layers," *J. Fluid Mech.*, Vol. 1, 1956, p. 191.

5 Childs, R. E., Ferziger, J. H., and Kline, S. J., "A Method of Prediction for Subsonic Compressible Diffusers," Report PD-24, Dept. of Mech. Engrg., Stanford Univ., 1981.

6 Escudier, M. P., Nicoll, W. B., and Spalding, D. B., "An Explicit Drag Law for Uniform Density Boundary Layers in Smooth, Impermeable Walls," Report, Mech. Engrg. Dept., Imperial College, 1966.

7 Bradshaw, P., Ferriss, D. H., and Atwell, N. P., "Calculation of Boundary Layer Development Using the Turbulent Energy Equation," *J. Fluid Mech.*, Vol. 28, 1967, p. 593.

8 Lyrio, A. A., Ferziger, J. H., and Kline, S. J., "An Integral Method for the Computation of Steady and Unsteady Boundary Layer Flows, Including Transitory Stall in Diffusers," Report PD-23, Dept. of Mech. Engrg., Stanford Univ., 1981.

9 Kuhn, G. D., and Nielsen, J. N., "An Analytical Method for Calculating Turbulent Separated Flows Due to Adverse Pressure Gradient," *AIAA Journal*, Vol. 12, 1974, p. 881.

10 Simpson, R. L., Chew, Y. T., and Shivaprasad, B. G., "Measurements of a Separating Turbulent Boundary Layer," Project SQUID Report TR SMU-4-PU, 1980.

11 Head, M. R., "Entrainment in Turbulent Boundary Layers," Aero Res. Council Report and Memo 3152, 1958.

12 Michel, R., Quemard, C., and Durant, R., "Hypothesis on the Mixing Length and Application to the Calculation of the Turbulent Boundary Layers in Kline et al. (1968)."

13 Goldberg, P., "Upstream History and Apparent Stress in Turbulent Boundary Layers," Report 85, MIT Gas Turbine Lab, 1966.

14 Simpson, R. L., Strickland, J. H., and Barr, P. W., "Laser and Hot-Film Anemometer Measurements in Separating Turbulent Boundary Layers," Rpt. WT-3, Southern Methodist University, 1974. Also *Journal of Fluid Mechanics*, Vol. 79, 1977, pp. 553-594.

15 Ashjaee, J., Johnston, J. P., and Kline, S. J., "Subsonic Turbulent Flow in Plane-Wall Diffusers: Peak Pressure Recovery and Transitory Stall," Rpt. PD-21, Dept. of Mechanical Engineering, Stanford University, 1980. Also ASME JOURNAL OF FLUIDS ENGINEERING, Vol. 102, 1978, p. 180.

16 Kline, S. J., Cantwell, B. J., and Lilley, G. M., eds., *Proceedings of the 1980-81 AFOSR-HTTM-Stanford Conference on Complex Turbulent Flows—Comparison of Computation and Experiment*, Vol. I, Dept. of Mechanical Engineering, Stanford University, 1982.

DISCUSSION

H. L. Moses[1]

The authors describe some new correlations that lead to a simple method of calculating turbulent boundary layers. Since a large amount of data has been used to develop and check these correlations, one would expect the resulting method to be quite reliable.

The significant contribution, however, is the extension of the correlations to separated and unsteady flow. Although detailed measurements in separated flow are quite limited, the author's experience in this area is extensive and has, no doubt, entered into the correlations.

It is not clear whether the authors simply integrated their equation (2) or included the viscous sublayer in forming the integral parameters. The difference is only important for low Reynolds numbers, but in that case it can be significant [1].

It is also not clear what the limitations of the correlations are. As the separated region becomes large, the assumed velocity profiles result in an unresonably large negative velocity. In fact, the skin friction correlation very quickly exceeds the limited data for separated flow. This limitation was briefly discussed by Childs, et al. and reference [2], where these profiles have been used. A modification for large areas of separated flow was suggested in reference [3], which was similar to that sketched by Childs et al. Has this effect been included in the correlations?

This writer takes a mild exception to the statement that Childs et al. *show* that the entrainment method is the "best" choice (over methods based on the monentum equation). This conclusion, however, which was based on an examination of the coefficients in the resulting ordinary differential equations, is certainly worthy of note. The implications that the coefficients are significantly different for the entrainment method and give better results with separated flow raises some interesting questions. Perhaps a correlation is better than attempting to satisfy the momentum equation with a model for reversed flow.

Additional References

1 Moses, H. L., "A Strip-Integral Method for the Turbulent Boundary Layer," *Proceedings, Computation of Turbulent Boundary Layers—1968 AFOSR-IFP-Stanford Conference*, Vol. I, Ed. Kline, Cockrell, Morkovin, and Sovran, Stanford Univ. Press, 1968.

2 Moses, H. L., and Chappell, J. R., "Turbulent Boundary Layers in Diffusers Exhibitng Partial Stall," ASME *Journal of Basic Engineering*, Vol. 89, Sept. 1967, pp. 655-665.

3 Moses, H. L., Sparks, J. F., and Jones, R., R., III, "An Integral Method for the Turbulent Boundary Layer with Separated Flow," in *Turbulent Boundary Layers*, Weber, H. E., Ed., ASME, 1979.

Authors' Closure

Professor Moses has correctly pointed out a number of things that may not have been explained with sufficient clarity in out paper and we would like to take this opportunity to try to clarify them.

Professor Moses is correct that one of the advantages of our method is the ability to deal with separation; another advantage is that it is *much* simpler computationally and leads to significant cost reductions. In the separated region our entrainment correlation (as indeed all other entrainment correlations) is extremely uncertain and we have found that, in some applications (not including the one in this paper), an ad hoc modification is necessary in order to obtain correct predictions.[2]

The model of this paper does not incude a viscous sublayer. This is not a serious defect except, as Professor Moses points out, at low Reynolds number and, as shown in the paper, at high frequencies for which the Stokes layer thickness becomes the same size as the sublayer. We believe that the problem can be corrected without great difficulty.

Finally, we should perhaps have been more careful about the statement that the entrainment method is *the* best method. Childs et al. show that this method performs somewhat better in the neighborhood of separation. However, other methods can be used with success.

[1] Professor of Mechanical Engineering, Virginia Polytechnic Institute and State University, Blacksburg, Va.

[2] Bardina et al. (reference [3] of paper).

Journal of Fluids Engineering

Discussion

Draining of Tanks With Submerged Outlets or Without Vacuum Relief[1]

J. Kubie.[2] The authors' work is an important contribution to the understanding of this difficult problem. However, further insight into an area of their work which deals with the problem of tank draining with air ingestion can be gained by reinterpreting their experimental results. The authors argue that the inception of air ingestion depends on the momentum of the draining liquid, and obtain the following condition for the inception.

$$\frac{P_u - P_a}{P_a} + \frac{\rho_l g (z_l - z_0)}{P_a} = K_1 \tag{1}$$

The dimensionless parameter K_1 was obtained experimentally as $0.001 \leq K_1 \leq 0.002$. The authors also suggest that K_1 does not depend on the diameter of the outlet D or on ρ_l, but in view of the limited experimental evidence and large experimental uncertainty this is inconclusive.

An alternative hypothesis can be made by suggesting that the inception of air ingestion depends on the relative velocity of incoming air bubbles v_B and the draining liquid v.

Velocity of air bubbles in liquid-filled pipes was investigated previously [3]. Using the results of that study, and assuming that they are applicable also in this case, the velocity of air bubbles which could potentially be ingested is given as

$$v_B = k(gD)^{1/2} \tag{16}$$

where k is a constant of the order of unity. The mean velocity of the draining liquid can be obtained as

$$v = 2^{1/2}\left(g[z_l - z_0] + \frac{P_u - P_a}{\rho_l}\right)^{1/2} \tag{17}$$

Finally, it is assumed that air ingestion commences when $v = v_B$, from which the parameter K_1 is obtained as

$$K_1 = \frac{k^2}{2}\frac{g\rho_l D}{P_a} \tag{18}$$

For the cases investigated $K_1 \approx 0.001$, as was observed experimentally.

The importance of this hypothesis is not in the, perhaps fortuitous, agreement between the theoretical and experimental values of K_1, but in that K_1 appears to be a function of the dimensionless parameter $g\rho_l D/P_a$, which has implications for the extrapolation of the results to larger scales.

Additional Reference

3 Zukoski, E. E., "Influence of Viscosity, Surface Tension, and Inclination Angle on Motion of Long Bubbles in Closed Tubes," *J. Fluid Mech.*, Vol. 25, No. 4, 1966, pp. 821-837.

Authors' Closure

The authors appreciate the complimentary remarks by the discusser and agree with him that the conditions required to initiate bubble ingestion have not yet been settled. Equation (1) was a working hypothesis that correlated our data. Since both the density of the liquids used in the tests and the diameter of the relatively small hole were varied by only about 50 percent, it is possible that any dependency of K_1 on these parameters was masked by the scatter in the test data. The correlation suggested by the discusser (equation (16)) represents a physically plausible mechanism and also fits our data. Clearly, tests covering a much wider range of parameters are needed to decide between the two correlations. It should be noted, however, that the hole diameter cannot be greatly increased, because then air would enter only through the upper part of the hole, thus violating one of the assumptions upon which both equations (1) and (16) are based.

[1] By F. T. Dodge and E. B. Bowles, published in the March, 1982, issue of the JOURNAL OF FLUIDS ENGINEERING, Vol. 104, pp. 67-71.

[2] Nuclear Safety Branch, Central Electricity Generating Board, Health and Safety Department, London EC4, England.

Journal of Fluids Engineering

Book Reviews

Advances in Transport Processes, edited by A. S. Mujumdar, Halstead Press/Wiley Eastern Limited, New Delhi. Vol. I, 1980, 263 pp., price $27.95. Vol. II, 1982, 432 pp., price $37.95.

REVIEWED BY FRANK M. WHITE

These two volumes mark the beginning of a new cloth-bound series of review articles on fluid dynamics and other aspects of transport processes. The articles are wide-ranging, with a diverse international authorship. The books are printed in India with excellent type composition and clear, sharp figures. However, the paper is of rather poor quality – thin, rough, and porous – the benefit to the reader being a considerably lower price than comparable review series.

Volume I presents five reviews of about 50 pages each: Blood Flow, by V. L. Shah; Two-Phase Gas Non-Newtonian Flow, by R. Mahalingam; Mass Transport in Electrochemical Systems, by T. Z. Fahidy and S. Mohanta; Numerical Methods for Viscous Flow Problems, by M. M. Gupta; and Mixing of Viscous Newtonian and Non-Newtonian Fluids, by V. V. Chavan and R. A. Mashelkar. In general, the articles are less general than they sound. For example, Shah's blood flow review is primarily concerned with entrance and diffusion effects in straight tube flow. Similarly, Gupta's numerical methods review concentrates on the traditional stream function/vorticity technique plus a brief discussion of the MAC method. One senses that these articles, though very interesting to the nonexpert such as this reviewer, are not presenting the state of the art as described, say, in the program of the last ASME Winter Annual Meeting. They do serve the goal expressed by the editors that engineer readers learn about scientific advances in transport processes while scientists learn about the practical problems to be faced.

Volume II contains six reviews: Modelling of Aquatic Systems, by L. T. Fan et al.; Non-Newtonian Circular Entry Flows, by D. V. Boger; Electrohydrodynamic Enhancement of Convective Transfer, by F. A. Kulacki; Dust Removal from Gas Streams by Filters, by S. C. Saxena and W. M. Swift; Multiphase Flow Models, by R. W. Lyczkowski et al.; and Movement of Particles in Flow Fields, by H. Brauer. Again the work may be somewhat dated and not too general. Brauer's review of particle motion, for example, leans heavily on simple drag correlations and flow field descriptions and is much less general than a gas-particle textbook we reviewed here in December 1981. The review of multiphase flow models does seek generality at the expense of being utterly uncritical: model after model is thrown at us without recommendations or judgments. Kulacki's review of electrohydrodynamic enhancement was especially interesting and educational.

This new review series serves a good purpose of educating engineers to new fields of fluids engineering. They are recommended especially for library acquisition.

How to Write and Publish Engineering Papers and Reports, by H. B. Michaelson, ISI Press, Philadelphia, 1982, 158 pp., price $17.95.

REVIEWED BY FRANK M. WHITE

A how-to-do-it book on this topic is normally a turn-off for research engineers, who might typically grumble, "I don't need no double-dome English teachers to show me how to write good." And they are often right. Further, a positive review by myself might be interpreted merely as an act of self-defense in my role as a *Transactions* editor.

But this book is a jewel. There is no one I know who would fail to benefit from it. This author has put so much thought and insight into the manuscript and knows so much more about writing and publishing than the rest of us that it isn't funny. The reviewer is filled with editor-envy.

The title only hints at the broad scope of the book. There are 22 chapters covering every phase of engineering communications, beginning with the selection of the proper journal and audience. There is a chapter on writing abstracts – did you know there are three different kinds of abstract, each with a different purpose? There is a chapter on organizing and writing as you go, thus preserving the excitement of the research as it occurred. There is a chapter on how to select and draw proper illustrations.

A chapter on word processing and home computers conveys the subtle power of these new tools, in addition to describing the newest software packages which correct spelling, replace poor words with better synonyms, punctuate, proofread, and improve the style of manuscripts. And there is a very useful chapter showing how to compile a bibliography either by hand or by computer search. What not to do is explained also.

There are chapters on how to deal with journal editors and how to rebut critical reviewers. There is a complete list of proofreading symbols and how to use them. And there is a long section on how to prepare and deliver an oral presentation, including tips on visual aids.

A softcover version is also available at $11.95. If every reader and contributor to the JFE would read this book, a measurable improvement in our meetings and journals would be predicted by this reviewer.

An Album of Fluid Motion, edited by Milton van Dyke, The Parabolic Press, PO Box 3032, Stanford CA 94305, 1982, 176 pp, price $10.00 (paperback).

REVIEWED BY FRANK M. WHITE

One of the glories of fluid mechanics is its ready adaptability to flow visualization techniques. This book celebrates that fact with an album of 282 photographs of flow